Stony Brook University

Measurement of Dielectron Invariant Mass Spectra in $Au + Au$ Collisions at $\sqrt{s_{NN}} = 200 GeV$ with HBD in PHENIX

A Dissertation presented

by

Jiayin Sun

to

The Graduate School

in Partial Fulfillment of the

Requirements

for the Degree of

Doctor of Philosophy

in

Physics

Stony Brook University

May 2016

Stony Brook University

The Graduate School

Jiayin Sun

We, the dissertation committe for the above candidate for the

Doctor of Philosophy degree, hereby recommend

acceptance of this dissertation

Barbara Jacak - Dissertation Advisor
Professor of Physics, Lawrence Berkeley National Laboratory

Axel Drees - Dissertation Advisor
Professor, Department of Physics and Astronomy

Derek Teaney - Chairperson of Defense
Associate Professor, Department of Physics and Astronomy

Robert McCarthy
Professor, Department of Physics and Astronomy

Gabor David
Physicist, Brookhaven National Laboratory

This dissertation is accepted by the Graduate School

Charles Taber
Dean of the Graduate School

Abstract

Measurement of Dielectron Invariant Mass Spectra in $Au + Au$ Collisions at $\sqrt{s_{NN}} = 200 GeV$ with HBD in PHENIX

by

Jiayin Sun

Doctor of Philosophy

in

Physics

Stony Brook University

2016

Dileptons are emitted throughout the entire space-time evolution of heavy ion collisions. Being colorless, these electromagnetic probes do not participate in the final-state strong interactions during the passage through the hot medium, and retain the information on the conditions of their creation. This characteristic renders them valuable tools for studying the properties of the Quark Gluon Plasma created during ultra-relativistic heavy ion collisions. The invariant mass spectra of dileptons contain a wealth of information on every stage of the evolution of heavy ion collisions. At low mass, dilepton spectra consist mainly of light meson decays. The medium modification of the light vector mesons gives insight on the chiral symmetry restoration in heavy ion collisions. At intermediate and high mass, there are significant contributions from charm and bottom, with a minor contribution from QGP thermal radiation. The region was utilized to measure cross sections of open charm and open bottom, as well as quarkonium suppression as demonstrated by PHENIX.

An earlier PHENIX measurement of dielectron spectra in heavy ion collisions, using data taken in 2004, shows significant deviations from the hadronic decay expectations. The measurement, however, suffered from an unfavor-

able signal to background ratio. Random combination of electron-positron pairs from unrelated sources, mostly Dalitz decay of π^0 and external conversion of decay photon to electrons, is the main contributor to the background. Mis-identified hadrons are another major background source.

To improve the situation, the Hadron Blind Detector (HBD), a windowless proximity focusing Cerenkov detector, is designed to reduce this background by identifying electron tracks from photon conversions and π^0 Dalitz decays. The detector has been installed and operated in PHENIX in 2009 and 2010, where reference p+p and Au+Au data sets were successfully taken. We will present the dielectron results from the analysis of the Au+Au collisions, and compare the measured mass spectra to theoretical expectations.

To my parents,
and my grandmother.

Contents

非人磨墨墨磨人，瓶应未罄罍先耻。

Acknowledgements
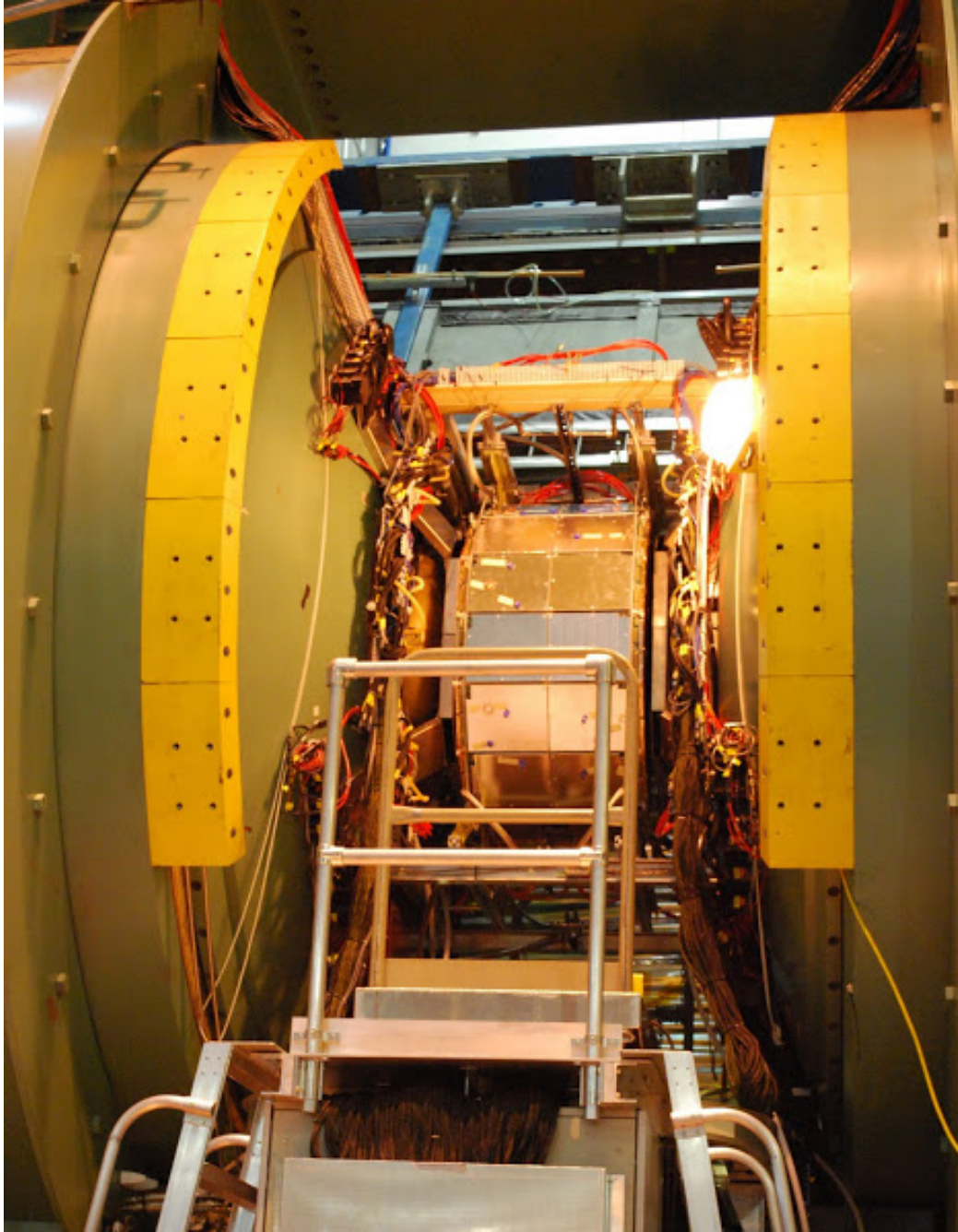
Chapter 1

Introduction to Dilepton Measurements in Heavy-Ion Collisions

1.1 High Energy Heavy-Ion Collision Overview

1.1.1 QCD and Quark Deconfinement

The universe consists of matter from atoms, whose cores are nuclei, which are built of nucleons, namely protons and neutrons. The nucleons, in turn, are composed of quarks.

The quarks are fermions. They have six degrees of freedom in flavor: up, down, strange, charm, top and bottom. There are three degrees of freedom in color as well: red, green and blue. The quarks always form color-less (white) bound states as experiments have never observed single color states in nature. Such bound states of quarks take the form of hadrons, which are divided into two families: the mesons and the baryons. The mesons are formed of $q\bar{q}$ pair, and the baryons are formed of three valence quarks qqq.

Quantum Chromodynamics(QCD) gives a description of how quarks interact with each other. Akin to quantum electrodynamics(QED), QCD has spin 1 gauge bosons, i.e. the gluons, as the carrier of strong force between quarks, just like the role of photons between charged particles. The gluons carry color-anticolor charge, which leads to eight gluon color states in total.

"Asymptotic freedom" is one of the results obtained from the Yang-Mills gauge theory, and is a unique feature of the QCD. It describes the decreasing strength of the strong interaction at decreasing distance. This is related to the fact that gluons carry color charge, so that a bare color charge is diluted away in space by the cloud of gluons. By contrast, at low energy, the
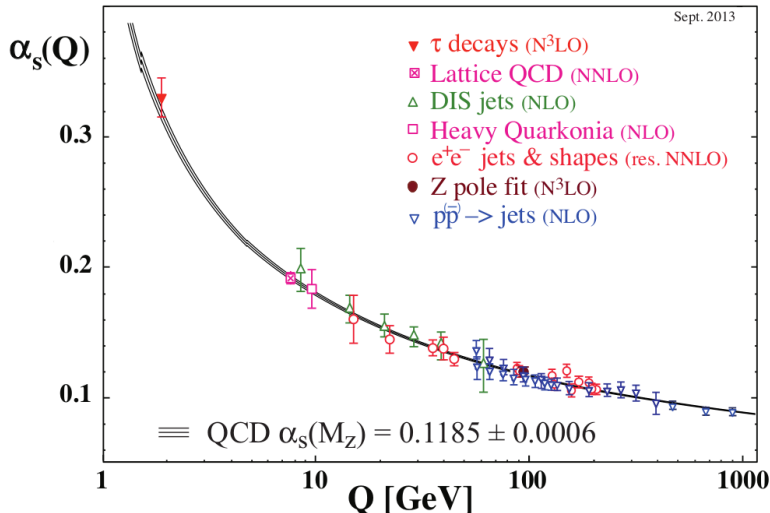
Figure 1.1: Effective QCD coupling constant α_s as a functoin of the momentum exchange Q. [68]

interaction strength becomes so strong that it leads to the confinement of quarks. Phenomenologically, the potential between a quark anti-quark pair increases linearly with the distance between the pair. As a result, when the quarks in a $q\bar{q}$ pair move away from each other, the interaction between them pulls them close. If their separation is far enough that the total energy of the system exceeds a critical value, a new pair of $q\bar{q}$ is created from the QCD vacuum, and the four quarks regroup into two new $q\bar{q}$ pairs. Thus the quarks are always confined in bound states.

The running coupling constant of the QCD, α_s, which describes the strength of the interaction, takes the following form,

$$\alpha_s(Q) = \frac{\alpha_s(\Lambda)}{1 + \alpha_s(\Lambda)\frac{33-2N_f}{12\pi}ln(\frac{Q^2}{\Lambda^2})} \tag{1.1}$$

where Q is the momentum transfer in a strong interaction, Λ is a scale, $\alpha_s(\Lambda)$ can be determined from experiment, N_f is the number of flavors. Fig. 1.1 illustrates the running α_s as a function of momentum tranfer Q, determined from experimental data. α_s decreases logarithmically at large Q (corresponding to high energy or short distance). This is the so-called *asymptotic freedom* described above. The interaction strength is weak and

perturbation theory is applicable in this regime. At small Q (corresponding to low energy or long distance), α_s rises rapidly. It becomes large enough that perturbation theory is no longer valid in this strong interaction region. A commonly used method is lattice gauge theory, which treats four-dimensional space-time as a lattice, with quarks occupying lattice points and gluons act as the lattice links. Based on the lattice discretization, Monte Carlo numerical simulation can be used to compute QCD problems.

Intuitively, a bag model can be used to interpret the quark confinement. Consider a hadron in which the quarks are confined inside a bag, the inward bag pressure is balanced with the outward pressure arising from the quarks' wavefunctions. If the outward pressure from the quarks is increased and exceeds the inward bag pressure, the bag will be broken and the quarks will spill out. This would lead to a new phase consisting of deconfined, free-moving quarks and gluons. Such a novel state of matter is given the name *quark-gluon-plasma*.

To achieve this, there are two ways:

- **High temperature.** The color-white hadrons are thermally excited when the QCD matter is heated. When the temperature reaches a critical value T_c, the hadrons begin to overlap with each other. At $T > T_c$, the hadrons melt into a matter of deconfined quarks and gluons. The critical temperature T_c estimated from different models, ranges from $\sim 150\ MeV$ to $\sim 200\ MeV$ [83] [80] [118]. For example, the bag model with a bag pressure $B^{1/4} = 206\ MeV$ yields a critical temperature at 144 MeV [118]. Lattice QCD calculation for a system with massless quarks gives $T_c \sim 175\ MeV$ for $N_f = 2$, and $T_c \sim 155\ MeV$ for $N_f = 3$. The critical energy density is estimated to be $\epsilon_{crit} \sim 1\ GeV\ fm^{-3}$ [80].

- **Large baryon density, or, high pressure.** The pressure of quarks arises from the Pauli exclusion principle, as no two fermions can occupy the same quantum state. As the density of quarks increases, the quarks must occupy higher momentum states. The pressure of quarks increases with the quark density, which corresponds to baryon density as each quark carries a baryon number $\frac{1}{3}$. Thus quark deconfinement becomes possible when the baryon density is large enough. Based on the simple bag model and a bag pressure of $B^{1/4} = 206\ MeV$, Ref. [118] gives an estimation of $\rho_B(quark - gluon\ plasma) = 0.72/fm^3$ for the critical

3

baryon density at $T = 0$. The number is several times higher than $\rho_{nm} = 0.16\,fm^{-3}$, the baryon density of normal nuclear matter.

At high temperature, the energy density of the system can be estimated by the bag model. Using massless quarks and non-interacting ideal gas, the energy density for pion gas is obtained as

$$\epsilon_H = 3d_\pi \frac{\pi^2}{90} T^4,$$

and for the deconfined phase,

$$\epsilon_{QGP} = 3d_{QGP} \frac{\pi^2}{90} T^4 + B$$

The degeneracy factor for pion gas $d_\pi = N_f^2 - 1 = 8$ for $N_f = 3$. For the deconfined quark-gluon-plasma phase, the degeneracy factor is $d_{QGP} = d_g + \frac{7}{8} d_q$, where

$$d_g = 2_{spin} \times (N_c^2 - 1), \qquad d_q = 2_{spin} \times 2_{q\bar{q}} \times N_c \times N_f$$

For $N_c = 3$ and $N_f = 3$, $d_{QGP} = 47.5$. The number of degrees of freedom increases greatly from the hadron gas to the quark-gluon-plasma phase, as quarks are released from bound states.

The energy density of the system ϵ/T^4 computed as a function of T/T_c [83] is presented in Fig. 1.2. "2 flavor" represents a system of up and down quarks with $m_{u,d}/T = 0.4$ and $N_f = 2$. "3 flavor" has $m_{u,d,s}/T = 0.4$ and $N_f = 3$. "2+1 flavor" uses $m_{u,d} = 0.4$ and $m_s/T = 1.0$. A phase transition is manifest when the energy density undergoes a sudden increase at critical temperature T_c, corresponding to the sudden increase of the degrees of freedom discussed with the bag model above. When T is above T_c, the energy density behaves as a constant. The constant is below the Stefan-Boltzman limit for a non-interacting gluon gas (denoted by arrows in Fig. 1.2), and implies an interacting system of gluons and quarks.

Fig. 1.3 is a schematic phase diagram of QCD obtained with using 2 quarks (up and down) with observed quark mass [115]. Normal matter(hadron states) occupy the lower temperature T and lower baryon chemical potential μ_B region while the QGP phase exists in higher T and μ_B. The X(μ_B) and Y(T) dimensions represent the two recipes of achieving quark deconfinement: increasing baryon density or increasing temperature. The phase transition

4
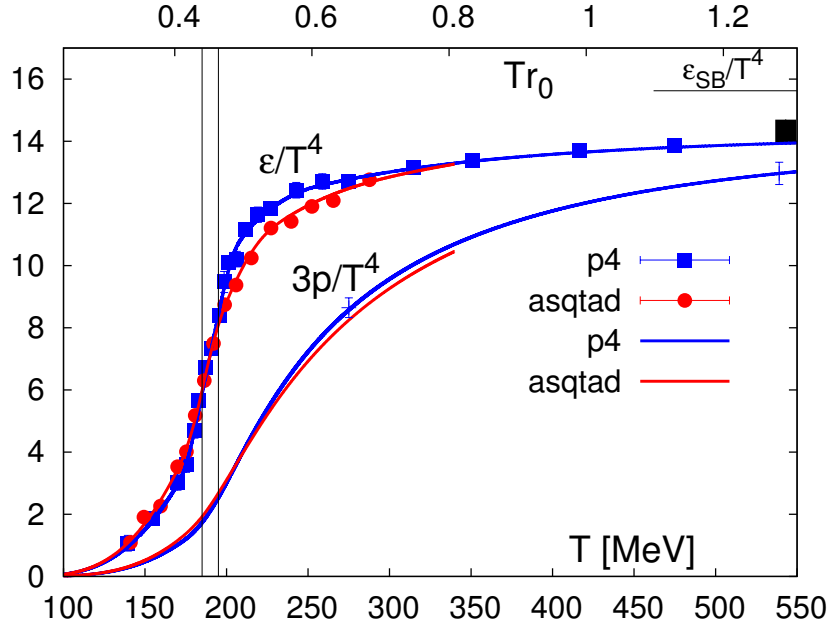
Figure 1.2: Lattice QCD calculation of energy density ε as a function of temperature T. ε_{SB}/T^4 is the Stefan-Boltzmann limit for non-interacting gluon gas [67].
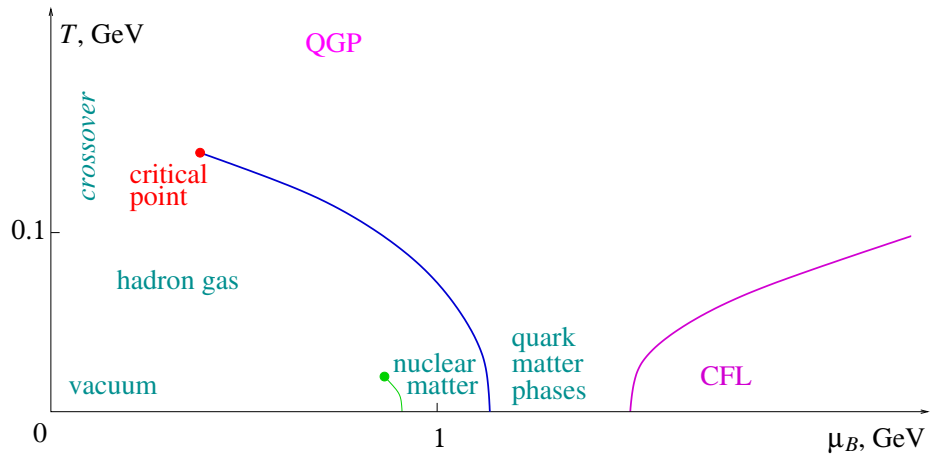
Figure 1.3: Schematic phase diagram of QCD matters as a function of baryonic chemical potential μ_B and temperature T. [115]

boundary between the hadron phase and QGP phase is denoted by a blue curve. Many theoretical models conclude the blue line is a first order transition [115]. At high T and lower μ_B, the blue line ends at a critical point of the second order. Beyond the critical point, at high T and small μ_B, lattice calculation has confirmed that the transition is a crossover [75].

In nature, the phase of QGP can exist in an environment of high temperature or(and) high baryon density. There are two places satisfying these conditions: the early universe 10^{-5} s after the big bang when the temperature $T \sim T_c$, and in the core of neutron or quark stars if the core density of the super dense star reaches $5 \sim 10$ ρ_{nm}.

Also, the regime of QGP is accessible via high energy heavy-ion collisions.

1.1.2   Ultra-Relativistic Heavy-Ion Collisions

In ultra-relativistic heavy-ion collisions, two heavy nuclei are accelerated to very high energies and collide head-on, thereby creating momentarily a small regime of extremely high temperature and energy density. Taking the example of the Relativistic Heavy Ion Collider (RHIC) at Brookhaven National Lab, which is designed to carry out such an experiment, we consider a head-on collision of two ^{197}Au nuclei at center of mass energy $\sqrt{s} = 200$ GeV per nucleon. Because of the Lorentz factor $\gamma = \sqrt{s}/2m_{nucleon} \sim 106$, the two incoming Au nuclei are flattened into two thin sheets of nucleons. The center of mass collision energy $\sqrt{s} = 200$ GeV is high enough that the two nuclei tend to pass through each other, local high temperature and energy density are achieved in the overlapping region. It also has a low baryon density. On the QCD phase diagram, such heavy ion collisions in RHIC are positioned at high T and low μ_B region, where hadron state transits into the QGP state through a smooth crossover. On the other hand, when the center of mass collision energy $\sqrt{s}$ is lower, e.g. under 100 GeV, the incoming nuclei tend to stop one another move. Both high temperature and high baryon density are obtained in this case, and such collisions are positioned at higher μ_B and slightly lower T. Fig. 1.4 illustrates the RHIC heavy ion collisions on the QCD phase diagram. As the RICH beam energy increases, the collisions take place at increasing temperature and decreasing baryon chemical potential μ_B.

Physically, a heavy-ion collision proceeds through several stages. The system's space-time evolution is described by a Bjorken picture [44]. Fig. 1.5 is a lightcone presentation of the evolution of the collision. At the time of
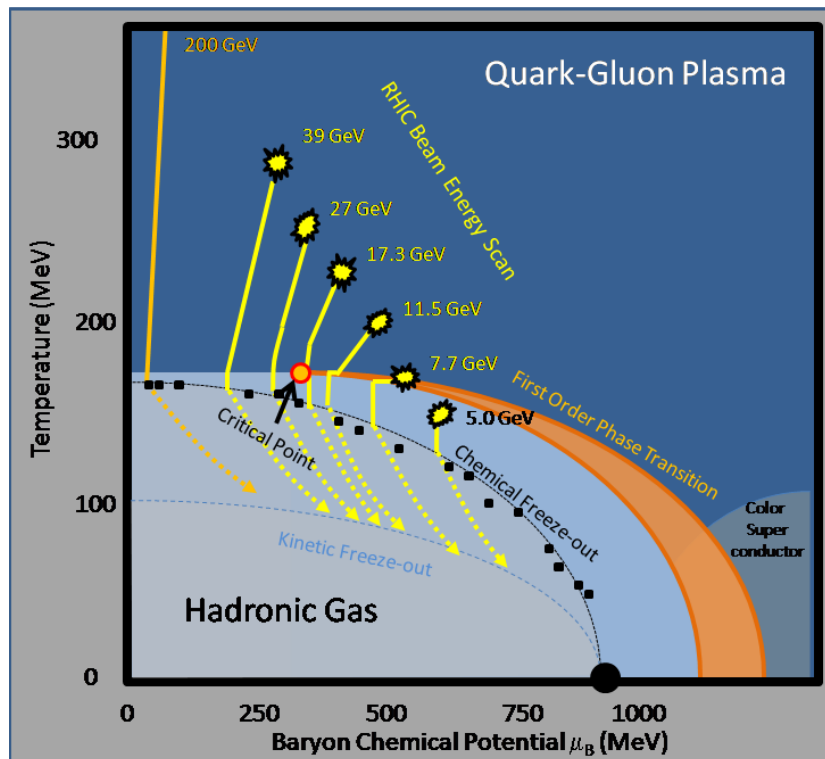
Figure 1.4: Heavy ion collisions at different RHIC energies are shown on the schematic phase diagram of QCD matters as a function of baryonic chemical potential μ_B and temperature T.

collision illustrated by the origin point, the two incoming nuclei pass through each other and create huge amount of entropy. The space between the receding nuclei is filled with highly excited vacuum with a small baryon density. When the system becomes de-excited, real quarks and gluons emerge and interact with each other. At proper time τ_{form}, the produced partons establish local equilibrium. This period at $0 < \tau < \tau_{form}$ is termed *pre-equilibrium stage*. Ref. [69] gives an estimation of $\tau_{form} \sim 0.35 fm/c$ based on the Bjorken picture and PHENIX measurements of $dE_T/d\eta$ and $dN^{ch}/d\eta$, which leads to an estimation of the energy density at τ_{form} to be $15 GeV/fm^3$, as shown on Fig. 1.6.

After achieving local equilibrium, the second stage is the expansion of the partonic system. As the mean free path is small compared to the system size, the expanding motion can be approximated to be that of a fluid, and relativstic hydrodynamics can be utilized for calculation. The motion is governed by the conservation of the energy-momentum tensor and baryon number:

$$\partial_\mu \langle T^{\mu\nu} \rangle = 0, \qquad \partial_\mu \langle j_B^\mu \rangle = 0$$

As the system expands, the temperature cools down. At around the critical temperature, the phase transition from QGP to hadron gas takes place. A mixed phase with coexisting partons and hadrons can occur during the phase transition if it is first order. After that, the quarks are all bound in confined states and the system becomes hadronic gas. As everything continues expanding, the interaction becomes weaker and the mean free path becomes larger. Finally, chemical freeze-out takes place and the number of each particle species becomes fixed. Thermal freeze-out occurs when the mean free path is comparable to the size of the system. Hydrodynamics is no longer applicable; at this stage the hadrons are still interacting in a non-equilibrium way. Transport models such as UrQMD [87] can be employed to describe the stage.

1.1.3 Dileptons from Heavy-Ion Collisions

Dileptons are emitted throughout the entire time-space evolution of ultrarelativistic heavy ion collisions. They are termed "penetrating probes", as the lack of color charge prevents them from participating in strong interactions. In contrast to hadronic probes, the information encoded in these electro-magnetic probes on the conditions of their creation is not smeared by
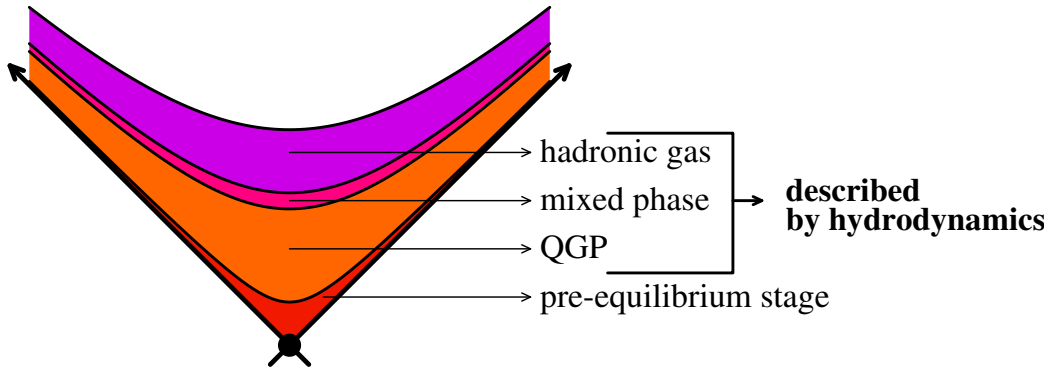
Figure 1.5: Schematic plot representing the evolution in a heavy ion collision where QGP is created [92].

strong final-state interactions during their passage through the hot and dense medium. Thus the ability to preserve information on the medium properties, including the hottest stage, makes dileptons valuable probes to study the QGP.

The information from dileptons is rich, since they are produced at every stage, from the initial hard scattering to the final freeze-out. A dilepton mass spectrum from heavy ion collisions is a composite of dilepton productions from all the sources, with varying creation conditions. During the medium evolution, the temperature cools down from the hottest stage to below the critical temperature T_c. The medium constituents also vary from free moving quarks and gluons to bound hadron states. Furthermore, the spectrum is also affected by early-time transverse anisotropy [101]. Generally speaking, there are three main stages of dilepton production, the Drell-Yan process in the initial hard scattering; the thermal radiation from the thermalized partonic medium and after the phase transition, from the hadronic gas; and lastly, the decays of the produced hadrons after freeze-out. Dilepton spectra are useful to study the QGP temperature and lifetime inferred from the thermal radiation, the production and dynamics of various neutral vector mesons in the medium, such as ρ, ω and ϕ, with relevance to chiral symmtry restoration, the production of heavy flavor quarks and the in-medium suppression of J/ψ.

The dilepton spectrum can be sectioned into 3 mass regions. Each region is dominated by different physics sources, which will be explained below. The low mass region(LMR) ranges between $0 \leqslant m_{ee} \leqslant m_\phi \sim 1.2 \ GeV/c^2$. The intermediate mass region(IMR) is set to be $1.2 \leqslant m_{ee} \leqslant 2.8 \ GeV/c^2$, which

9
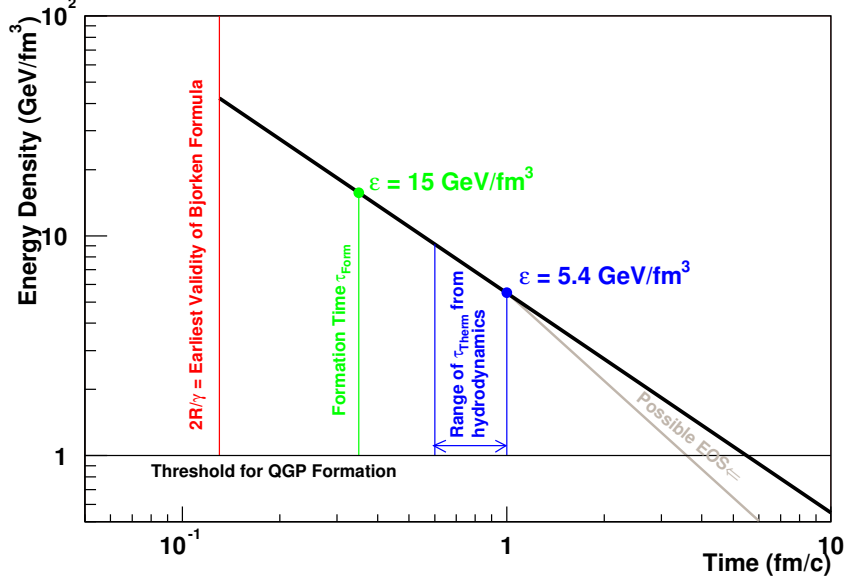
Figure 1.6: Schematic plot of the evolution of energy density ε with respect to time in heavy ion collisions derived from the Bjorken picture [69].

includes the mass window above the ϕ meson and below the J/ψ. The high mass region(HMR) is for $m_{ee} \geqslant 2.8\ GeV/c^2$.

Initial Hard Scattering

During the initial hard scattering of the partons, dileptons produced by the Drell-Yan process $q\bar{q} \to \gamma^* \to l^+l^-$ are well understood by the perturbative QCD. Thus the Drell-Yan production can be treated as a reference, to compare with dilepton rates from other processes. To leading order in QCD, the Drell-Yan cross section from a parton-parton collision is obtained as

$$\sigma(q\bar{q} \to l^+l^-) = \frac{1}{3} \cdot Q_q^2 \cdot \frac{4\pi\alpha^2}{3\hat{s}} \tag{1.2}$$

where Q_q is the charge of a quark, q. The factor of 3 is the number of quark colors. Symbol ˆ denotes the two-body scattering processes at the parton level. $\sqrt{s}$ is the center-of-mass energy of the collision.

For a $p+p$ collision, the Drell-Yan cross section is the sum over all partons weighted by the parton momentum distribution function of the proton.

10

$$\frac{d^2\sigma_{DY}^{pp}}{dM^2dy} = \sum_{q\bar{q}} x_1 f_q(x_1) x_2 f_{\bar{q}}(x_2) \cdot \frac{1}{3} Q_q^2 \cdot \frac{4\pi\alpha^2}{3M^4} \tag{1.3}$$

where x is the quark's momentum fraction of the proton, M and y are the invariant mass and rapidity of the pair, $M^2 = \hat{s} = x_1 x_2 s$ and $y = \frac{1}{2} ln(\frac{x_1}{x_2})$. $f_q(x)$ is the parton momentum distribution function of proton.

The Drell-Yan cross section for $N + N$ collisions can be written as,

$$\frac{d^2\sigma_{DY}^{AB}}{dM^2dy}(b) = \frac{d^2\sigma_{DY}^{pp}}{dM^2dy} T_{AB}(b) \tag{1.4}$$

where b is the impact parameter and $T_{AB}(b)$ is the nuclear overlap function. $T_{ab}(b)$ effectively counts the number of nucleon-nucleon collisions.

The higher order corrections to the Drell-Yan production consider gluon radiation from quarks and anti-quarks. The correction turns out to be on the same order of the leading order result, and it brings the theory in accord with the experiment.

In a dilepton mass spectrum, the Drell-Yan pairs show up in the high mass region, where the pair mass is greater than the J/ψ.

Thermal Radiation

After rapid thermalization, local equilibrium in the plasma is achieved. Thermal radiation from the partonic medium and after the phase transition, from the hadron gas, becomes the predominant dilepton production process.

In the partonic phase, to lowest order, the primary dilepton production is through basic quark anti-quark scattering: $q\bar{q} \rightarrow \gamma^* \rightarrow l^+l^-$ in finite temperature QCD plasma. Higher order processes are a small correction [94].

Later, in the hadronic phase, the main contributors are pion annihilation $\pi^+\pi^- \rightarrow l^+l^-$ as well as kaon annihilation and collisions between hadrons. At small pair mass, dileptons are also produced by soft virtual photons from bremstrahlung-type emissions. At high pair mass, productions from annihilation processes of $h\bar{h} \rightarrow \gamma^* \rightarrow l^+l^-$ are well below the Drell-Yan yield [80]. Due to vector-meson dominance [112] [113] [114], these two-body annihilation processes in the hadron gas are coupled with the formation and decay of the vector mesons such as the ρ, ω and ϕ: e.g. $\pi^+\pi^- \rightarrow \rho \rightarrow \gamma^* \rightarrow l^+l^-$.

The dilepton thermal emission rate is determined by the spectral function. Due to restoration of chiral symmetry and hadronic interactions in the hot

hadron gas, the in-medium spectral function in the hadron gas is expected to be modified. Thus the change would be reflected in the dilepton spectrum, making it a focus of interest to study medium properties.

To illustrate the relation between the thermal emission rate and the spectral function, we can first look at the transition matrix element S_{fi} from the initial state $|i\rangle$ to the final state $|f\rangle$,

$$S_{fi}(p_1, p_2) = -i\frac{e^2}{p^2}[\bar{u}(p_1)\gamma_\mu v(p_2)] \int d^4x e^{ipx} \langle f|j_{em}^\mu(x)|i\rangle. \qquad (1.5)$$

where $p_i^\mu = (E_i, \mathbf{p_i})$ is the momentum for the lepton pair. The total pair momentum is $q^\mu = (\omega, \mathbf{p}) = p_1^\mu + p_2^\mu$. $e\bar{u}(p_1)\gamma_\mu v(p_2)$ is the electromagnetic current of the outgoing lepton pair. The dilepton rate is defined as:

$$R_{l^+l^-} = \frac{1}{\int d^4x} \int \frac{d^3p_1}{2E_1(2\pi)^3} \int \frac{d^3p_2}{2E_2(2\pi)^3} \frac{1}{Z} \sum_{f,i} e^{-(E_i-\mu N_i)/T}|S_{fi}|^2 \qquad (1.6)$$

where Z is the grand-canonical partition function, E_i is the initial state energy, N_i is the initial state particle number, T is the temperature, μ is the chemical potential. All possible final states are summed and the thermal average is taken for the initial state.

Hence the general form of dilepton emission rate from a hot medium at rest with fixed temperature T is derived to be, [80]

$$\frac{d^4R_{l^+l^-}}{d^4p} = \frac{-\alpha^2}{3\pi^2p^2} \frac{\rho_\mu^\mu(\omega, \mathbf{p})}{e^{\omega/T} - 1} F(m_l^2/p^2) \qquad (1.7)$$

where $\rho(\omega, \mathbf{p})$ is the spectral function, $F(x) = (1+2x)(1-4x)^{1/2}\theta(1-4x)$ is a kinematical factor. This local emission rate, Equation 1.7, is a general form valid for both the partonic and hadronic phase, as it describes dilepton emission from two-body scattering, regardless of the characteristics of the participating particles. To describe emission from an expanding and cooling plasma in a real heavy ion collision, hydrodynamical evolution needs to be combined with the local emission rate. Assuming u^μ is the local four-velocity at a fluid cell in the expanding hot matter, local Lorentz transformation is used to calculate emissions from fluid cells with different local velocities. Hence ω can be replaced with $p \cdot u$. In the case of $p \cdot u \gg T$, and neglecting the lepton mass [80]

$$\frac{d^2N_{l+l-}}{d^4p} = \int d^4x S_{l+l-}(M^2, p \cdot u; T(x))e^{-p \cdot u/T(x)} \tag{1.8}$$

where $T(x)$ is the temperature at fluid cell x, S_{l+l-} contains the spectral function: $S_{l+l-}(p^2, p \cdot u; T) \equiv -(\alpha^2/3\pi^2 p^2)\rho_\mu^\mu(p^2, p \cdot u; T)$, and it is a function of M, local temperature, and other local properties of the medium. The difference between the QGP and hadron thermal emission lies in S_{l+l-}. Because of S_{l+l-} dependence on M, in central rapidity the thermal dilepton exhibits peak structures associated with $q\bar{q}$ resonances.

Observation of the QGP thermal dileptons would be especially useful in determining the QGP's temperature [109]. Thermal dilepton emission from the QGP is expected to be a structure-less continuum. Because the QGP precedes the hadronic phase, the emission from QGP is from a higher temperature than from the hadron gas, and therefore has a smaller slope in dilepton spectrum (harder spectrum). At RHIC energy according to theoretical prediction [102], the yield of QGP thermal dileptons is dominating over both the hadron gas thermal dileptons and the Drell-Yan dileptons in the intermediate mass region. Since the medium has small effects in this region, the dilepton rate is approximately $dR_{l+l-}/dM \propto (MT)^{3/2}exp(-M/T)$. As $M \gg T$ for $1.5 < M < 2.5$ GeV/c^2, the thermal emissions from lower temperature is suppressed. Hence the total yield is more sensitive to early high temperature stage and can be used accordingly as a thermometer to extract early temperature [109]. However, at this mass range this QGP signal is still small compared to the semi-leptonic decays of open charm mesons, which occur mainly after freeze-out. These heavy flavor decay products may largely overwhelm the QGP thermal signals in this mass region.

After a period of expansion and cooling, the partonic phase becomes a hot hadron gas. The thermal emissions from the hadron phase dominate in the low mass region. Since the spectral function S_{l+l-} is dependent on M, the dilepton spectrum displays peak structures from resonances such as ρ, ω, and ϕ. A key characteristic of hadron gas thermal emission is medium modifications of these mesons, seen as changes to the meson peaks, such as broadening, enhancement or mass shift.

Of particular interest is the medium modification of these light vector mesons. According to the Vector Meson Dominance model [105], dileptons are produced through hadron-hadron scattering via coupling to vector mesons, e.g. $\pi^+\pi^- \to \rho \to \gamma^* \to l^+l^-$. In ultra-relativistic heavy ion collisions, vector meson spectral functions are altered through interactions

with the hot hadronic gas. Furthermore, this alteration may very well be connected with the restoration of chiral symmetry, which is theoretically predicted to occur in coincidence with the phase transition [49] [107]. With the dynamics of the light vector mesons governed by chiral symmetry, the in-medium spectral function should be imprinted with the consequence of the chiral symmetry restoration, especially around the ρ mass. To consider the effect of chiral symmetry, the classical Lagrangian for QCD is,

$$\mathcal{L}_{QCD} = \bar{\psi}(i\slashed{D} - \mathcal{M}^0)\psi - \frac{1}{4}G^a_{\mu\nu}G^{\mu\nu}_a \tag{1.9}$$

where, ψ denotes spin $1/2$ colored fields with N_f flavors, i.e. the quarks, $\slashed{D} \equiv \gamma^\mu D_\mu = \gamma^\mu(\partial_\mu - ig(\lambda_a/2)A^a_\mu)$ is the Dirac operator, with A^a_μ representing spin-1 gauge field with 8 colors (a = 1,2,..8), λ_a SU(3) Gell-Mann matrices and g the strong interaction coupling constant such that $\alpha_s \equiv \frac{g^2}{4\pi}$; $\mathcal{M}^0$ denotes the diagonal $N_f \times N_f$ matrix of current quark masses,

$$\mathcal{M}^0 = \begin{pmatrix} m_u & & & \\ & m_d & & \\ & & m_s & \\ & & & ... \end{pmatrix}$$

The term $-\frac{1}{4}G^a_{\mu\nu}G^{\mu\nu}_a$ represents gluon interactions with gluons, with the non-abelian gluonic field-strength tensor, (f^{abc} are structure constants of group SU(3)),

$$G^a_{\mu\nu} = \partial_\mu A^a_\nu - \partial_\nu A^a_\mu + igf^{abc}A^b_\mu A^c_\nu$$

In the limit of quark mass $\rightarrow 0$, which is a good approximation for the up, down and to a lesser degree strange quarks, the Lagrangian is invariant under global vector and axialvector transformation in SU(3)-flavor space

$$\psi \rightarrow e^{-i\alpha^i_V \frac{\lambda^i}{2}}\psi, \qquad \psi \rightarrow e^{-i\alpha^i_A \frac{\lambda^i}{2}\gamma_5}\psi \tag{1.10}$$

where $i = 0, 1, ..., N_f^2 - 1$. As a result, the vector and axialvector Noether currents are conserved quantities,

$$j^\mu_{V,i} = \bar{\psi}\gamma^\mu \frac{\lambda_i}{2}\psi, \qquad j^\mu_{A,i} = \bar{\psi}\gamma^\mu\gamma_5\frac{\lambda_i}{2}\psi. \tag{1.11}$$

The chiral operator γ_5 has two eigenstates with eigenvalue ± 1: the left-handed and the right-handed quarks:

$$\psi_{L,R} = \frac{1}{2}(1 \mp \gamma_5)\psi$$

14

Thus, the QCD Lagrangian Eq. 1.9 can be decomposed with left and right chirality components:

$$\mathcal{L}_{QCD} = \bar{\psi}_L i \slashed{D} \psi_L + \bar{\psi}_R i \slashed{D} \psi_R - \frac{1}{4} G^a_{\mu\nu} G^{\mu\nu}_a - (\bar{\psi}_L \mathcal{M} \psi_R + \bar{\psi}_R \mathcal{M} \psi_L) \quad (1.12)$$

Then the above transformation in eq. 1.10 takes the following form in terms of left and right-handed quarks:

$$\psi_L \rightarrow e^{-i\alpha^i_L \frac{\lambda^i}{2}} \psi_L, \qquad \psi_R \rightarrow \psi_R \quad (1.13)$$

$$\psi_R \rightarrow e^{-i\alpha^i_R \frac{\lambda^i}{2}} \psi_R, \qquad \psi_L \rightarrow \psi_L \quad (1.14)$$

where $\alpha_V = \alpha_L = \alpha_R$ and $\alpha_A = -\alpha_L = \alpha_R$. Hence the Lagrangian $\mathcal{L}_{QCD}$ is invariant under $SU_L(N_f) \times SU_R(N_f)$ global transformation. The left and right-handed quarks do not mix dynamically at the limit $\mathcal{M}^0 \rightarrow 0$.

This is termed the chiral symmetry. In the QCD vacuum, the quark condensate $\langle \bar{\psi}\psi \rangle$ (as well as gluon condensate $\langle G^2 \rangle$) has finite expectation value, which leads to the spontaneous breaking of the chiral symmetry. While the vector current is still conserved, the QCD vacuum as a result is no longer invariant under axialvector transformations. One of the perceptible consequences of chiral symmetry breaking is the mass splitting of vector and axialvector mesons. The chirality is equivalent to helicity $\sigma \cdot \hat{\mathbf{p}}$ for massless quarks, and eigenstates of helicity should be parity eigenstates as well. The hadronic isospin multiplets of opposite parity, for example the vector meson ρ and its chiral partner a_1 meson, are expected to be degenerate in mass when chiral symmetry is preserved. Experimentally, the observed mass is $775.26 \pm 0.25 \ MeV/c^2$ for the ρ meson and $1230 \pm 40 \ MeV/c^2$ for the a_1 meson [68], clearly indicating chiral symmetry breaking.

However in a hot medium with finite temperature T and chemical potential μ_q, the quark condensate $\langle \bar{\psi}\psi \rangle$ is expected to be different. Results from lattice QCD show that the thermal averaged quark condensate $\langle\langle \bar{\psi}\psi \rangle\rangle$ quickly decreases to 0 when temperature $T > 0.9 \ T_c$, T_c being the critical temperature [106]. The "melting" of the quark condensate is found to take place at the phase transition temperature. Thus the restoration of chiral symmetry would coincide with the QGP and hadron phase transition.

The restoration of the chiral symmetry at the phase boundary would alter the spectral function of the light vector mesons, i.e. ω, ρ and ϕ. In principle

these mesons are produced not in the QGP phase but in the subsequent mixed phase or in the hadronic phase close to the phase boundary. In essence, the in-medium modification on the spectral function of the vector mesons reflects the medium properties in vicinity to the chiral symmetry restoration. The ρ meson in particular, due to its short lifetime ($\sim 1.3\ fm/c$), decays into dilepton pairs inside the hot and dense matter. Hence the dilepton mass spectrum around the ρ mass directly reflects the in-medium ρ spectral function. Whereas for ω and ϕ mesons, with much longer lifetimes ($23fm/c$ and $46fm/c$, respectively), a large fraction of them decay into dileptons outside the hot medium where their spectral functions have regained the vacuum properties, making them less sensitive probes than ρ.
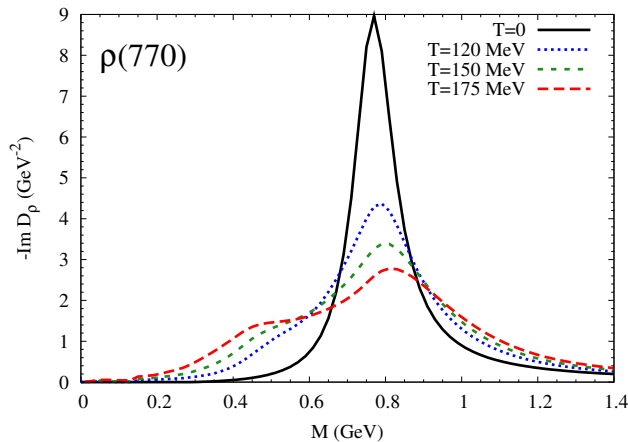
Figure 1.7: In-medium ρ spectral function as calculated with collisional broadening scenario. The ρ resonance peak "melts" as temperature increases to $\simeq 175\ MeV$ [103] [76].

There are two common theoretical schemes modeling ρ modification. (a) is the dropping mass scenario. Based on Chiral Symmetry Restoration, Brown and Rho proposed that the mass of ρ meson should drop to almost 0 at the phase boundary [48] [49] [88]. (b) is the collisional broadening scenario, referring to the broadening of ρ spectral function by its rescattering on constituents of the hadronic medium [106] [99] [102] [53]. It takes into account two main medium modification effects. One is the pion cloud of the ρ, modified by the pion interaction with the medium; the other is direct interactions between the ρ and mesons (π, K, ρ,...) as well as between ρ and baryons (N, Λ, Δ...) in a hot environment. These effects cause strong

broadening of the vector meson spectral function, and slight shift in mass. When extrapolated to $T_c \simeq 175\ MeV$, the broadening leads to a complete "melting" of ρ resonance peak [98], as shown in Fig. 1.7. Unlike the dropping mass scenario, which is explicitly based on Chiral Symmetry Restoration, the collisional broadening scenario relies on "conventional" hadronic scatterings. Yet a recent paper [77] argues that the ρ melting is compatible with chiral restoration.

Both scenarios, when translated into dilepton emission rate, show a distinct enhancement at around and below the ρ mass. This makes the low mass region in the dilepton mass spectrum, especially around the ρ mass, a highly interesting place for experimental observation of the restoration of chiral symmetry at the phase boundary. Results from past experiments, and comparison with theoretical predictions from the two scenarios, will be introduced later in Sec. 1.2.

Last but not least. the total thermal radiation is also a measure of the total system lifetime. Ref. [109] proposes to use the excess yield region below the ρ/ω, $0.3 < M < 0.7\ GeV/c^2$, to track the total lifetime, where the thermal yield is found be proportional to the total lifetime within a $\sim 10\%$ uncertainty across a large range of heavy-ion collision energies.

Fig. 1.8 is an example of theoretical calculation of thermal dilepton yield in the low mass region [74]. The calculation is done for the most central $Au + Au$ collisions in mid rapidity at full RHIC energy. The QGP thermal radiation is seen in a smooth distribution well below the yield of the hadronic medium at $M < 1\ GeV$. The radiation from the hadronic medium exhibits a resonance peak at ϕ mass, and an enhancement at around ρ mass where $M \sim 0.7\ GeV$. The calculation incorporates viscous correction to the hydro evolution.

Freeze-Out

At the end of the fireball evolution, when thermal freeze-out is reached, hadrons decouple from the system. After this point, the dilepton production is dominated by decays from produced hadrons. Dalitz decays from π^0, η and ω populates the low mass region. In the intermediate mass region, dilepton pairs come from semi-leptonic decays of open charm mesons, e.g. D and $\bar{D}$. Contributions from bottom reside at higher mass.

Neutral vector mesons such as heavy quarkonium states J/ψ and ψ' decay largely after freeze-out because of their long lifetimes. The shape of their

17
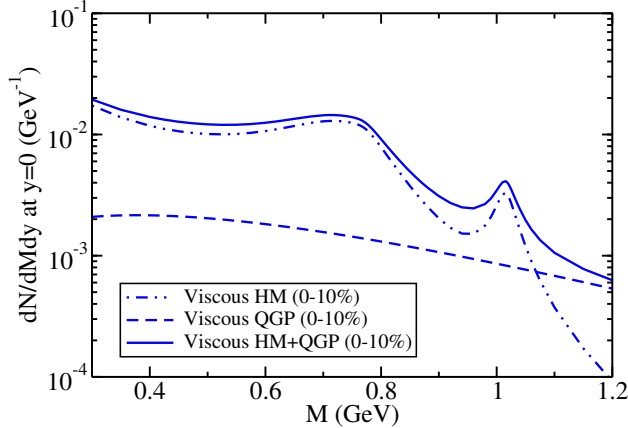
Figure 1.8: Theoretical calculation of thermal dilepton yield from QGP and hadronic medium(HG) with respect to the pair invariant mass [74] in mid rapidity, for RHIC energy in the most central collisions ($0-10\%$ centrality class). The calculation incorporates viscous correction to the hydro evolution.

mass spectrum does not carry information from in-medium interactions, however their absolute yield is relevant to deconfinement in the QGP.

It is predicted first in 1986 [91] that the yield of J/ψ is suppressed in the deconfined QGP because of color Debye screening. In a simple picture, since the charm quark mass $m_c \gg \Lambda_{QCD}$, where $\Lambda_{QCD} \sim 200\ MeV$ is the QCD scale parameter, the Schrödinger equation can be used for a charmonium bound state,

$$(-\frac{\nabla^2}{2(m_Q/2)} + V(r))\Psi(r) = E\Psi(r) \tag{1.15}$$

where $\frac{m_Q}{2}$ is the reduced mass, and the potential takes the form,

$$(x_+ y)(x_+ + exp[-\mu_q/T])V(r) = Kr - \frac{4}{3}\frac{\alpha_s}{r} + \frac{32\pi\alpha_s}{9}\frac{\mathbf{s}_1 \cdot \mathbf{s}_2}{m_Q^2}\delta(\mathbf{r}) + \cdots \tag{1.16}$$

The first term is the linear confining potential. The second is Color Coulomb potential term and the third is the color magnetic spin interaction. In the hot QCD plasma, the strength of the confining potential, K, vanishes when $T > T_c$, and the second term is Debye screened in the partonic plasma. $V(r)$ becomes a Yukawa potential,

$$V(r) \to -\frac{4}{3}\frac{\alpha_s}{r}e^{-r/\lambda_D} \tag{1.17}$$

18

where λ_D is the Debye screening length. When the Debye screening mass

$$\omega_D = 1/\lambda_D = gT\sqrt{N_c/3 + N_f/6}$$

[80] is large enough at high temperature, the potential no longer holds bound states and as a result, charmonium states become dissolved in the plasma.

In the dilepton mass spectrum, since the J/ψ production cross section is much larger compared to the thermal production, the J/ψ resonance peak dominates the thermal radiation, making the dilepton J/ψ signals relatively straightforward to observe. However, past experiments [42] have noted that J/ψ is also absorbed in cold nuclear matter without the presence of QGP, due to final state interactions with the surrounding hadrons. Thus the suppression from hadronic interactions must be disentangled in order to observe the J/ψ suppression from the QGP [117].

1.2 Prior Measurements of Dileptons

There have been various experiments outside RHIC that have measured dilepton spectra in Heavy Ion Collisions with many ion species and energies. The HADES collaboration at GSI SIS has taken data with collision energies as low as $1-2AGeV$ per nucleon in fixed target collisions [31] [32], which confirmed an dilepton enhancement in low mass region previously seen by DLS collaboration [97]. At SPS with higher energy, CERES has reported an enhancement at $0.2 < M < 0.6~GeV/c^2$ in $Pb + Au$ at 40 and 158 AGeV [61] [5] [60]. Recent NA60 dimuon measurement with $158A~GeV~In+In$ collisions [38] [39] [96] [37] provides precision high enough to discriminate the two different scenarios for medium modification. These experiments and their findings will be discussed together with the RHIC results in the coming sections.

Over the years of RHIC operation, both PHENIX and STAR experiments at RHIC have measured dielectron mass spectra with a variety of ion species and collision energies. PHENIX has gathered a collection of dielectron spectra of different ion species, from very light systems such as $p + p$ [20] [10] and $d + Au$ [19], to a medium system like $Cu + Cu$ [50], and to a heavy system like $Au + Au$ [10], all at collision energy $\sqrt{s} = 200~GeV$. The STAR experiment, in contrast, has measured $Au + Au$ dielectron spectra with a series of collision energy ranging from 19.6 GeV to 200 GeV [4] [2] [3].

The PHENIX experiment has measured e^+e^- pairs in $p + p$ collisions at $\sqrt{s} = 200~GeV$ using data taken in Run5 (year 2005) as a baseline for dielectrons at RHIC energy [20] [10]. The measured spectra show excellent agreement with hadronic decay expectations, demonstrating that the hadronic sources are well understood. In the meanwhile, a measurement of $Au+Au$ collisions at the same energy with Run4 (2004) data has been carried out [10]. In contrast to the $p + p$ measurement, the heavy ion result shows a remarkable excess at the ρ mass regions. The magnitude of the enhancement is so large that theoretical calculations have not been able to reproduce the yield. A $d + Au$ measurement using Run8 (2008) data [19] was performed in order to veto any effect of cold nuclear effect in the formation of the large excess seen in the $Au+Au$ data. The $d+Au$ shows no enhancement, thereby excludes any cold nuclear effect, so the excess must come from effects of the hot dense medium. A $Cu + Cu$ measurement [50], using Run5 (2005) data, provides a point of reference for an intermediate system where the medium is somewhat less hot and less dense due to the smaller energy density. An

enhancement is again observed at ρ mass.

With a time-of-flight upgrade in the STAR experiment in 2009, the STAR collaboration has developed the ability to carry out e^+e^- measurements and has reported results in recent years. In addition to a baseline of $p + p$ dielectron measurement at $\sqrt{s} = 200~GeV$ in year 2009 [1], STAR has undertaken measurements with $Au + Au$ collisions at collision energy 19.6, 39, 62.4 and 200 GeV in 2010. As of now, STAR has recently published the 200 GeV results [4] [2], and preliminary results from energy scan of 19.6, 39, 62.4 and 200 GeV are work in progress [3]. The STAR $Au + Au$ dielectron spectra from all these energies exhibit an enhancement at the same ρ mass region as the PHENIX results. Yet the enhancement is found to have a significantly lower magnitude and is in agreement with theoretical calculations. A slight dependence on both centrality and collision energy was observed.

1.2.1 Measurements Outside RHIC

High Acceptance DiElectron Spectrometer (HADES), using a fixed target, measured dielectrons from $C + C$ collisions at 1 and 2 AGeV per nucleon [29] [30]. At higher energies, the ChErenkov Ring Electron Spectrometer (CERES) at CERN SPS has measured electron pairs at mass < 1.6 GeV in $S + Au$ collisions at 200 GeV [72], $Pb + Au$ collisions at 40 and 158 GeV [5] [61]. Another experiment at CERN, NA60, equipped with a silicon vertex tracker which improves mass resolution at the ρ mass and reduces the combinatorial background, provided high statistics data with $In + In$ collisions at 158 GeV [38] [39] [96]. It measured dimuon mass from 0.2 GeV to up to 5 GeV.

CERES observed an excess in the mass region 0.2-0.6 GeV in Pb+Au collisions at 158 GeV (Fig. 1.9) [61] [60] [70]. By contrast, in p+Be and p+Au collisions [73], the spectra were in good agreement with decays from known hadron sources. The enhancement factor over a mass range between 0.2 to 1.1 GeV, was found to be 2.45±0.21(stat)±0.35(syst)±0.58(decays). Soft p_T pairs are the main contributor to this excess.

Fig. 1.9 compares CERES e^+e^- mass spectrum with hadronic decay expectations in the left panel, and an enhancement between 0.2 and 0.6 GeV/c^2 is clearly visible. The right panel compares the data with the two medium modification scenarios described in Sec. 1.1.3. Both the dropping ρ mass and collisional broadening scenarios reproduce the magnitude of the enhancement within uncertainties. The collisional broadening calculations demonstrates a
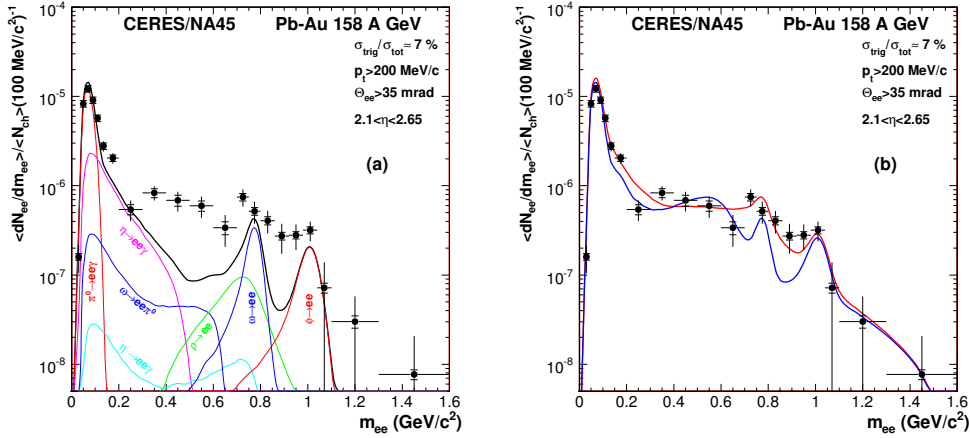
Figure 1.9: Dielectron mass spectrum measured by CERES experiment in $Pb+Au$ collisions at 158 GeV [60]. Left panel: Invariant e^+e^- mass spectrum compared to hadronic decay expectations. Right panel: same spectram compared to dropping ρ mass scenario (blue dashed) and collisional broadening scenario (red solid).

better agreement in shape.

In 2009, the NA60 experiment published high precision dimuon invariant mass spectra with $In + In$ collisions at 158 GeV [38] [39] [96] [37]. It is the first time data had sufficient accuracy to discriminate the two medium modification scenarios. As shown in Fig. 1.10, the collisional broadening scenario displays excellent agreement with the data while the dropping mass scenario is ruled out.

The intermediate mass region is expected to be populated with QGP radiation and semi-leptonic decays from open charm mesons, with the open charm being the predominant source. There are several measurements of dileptons in this mass range at SPS: HELIOS-3 using S+W at 200 GeV [90], NA38 with p+W, S+U at 200 GeV [95], NA50 with Pb+Pb at 158 GeV [95] [62], and NA60 with In+In at 158 GeV [38] [39]. All these experiments have seen an excess in this region above the open charm and Drell-Yan yields. Theoretical studies suggest it is created through either enhanced charm production or thermal radiation. NA60, which has a vertex resolution at the order of 10-15 microns, ruled out charm enhancement as the source of the excess, and pointed to thermal radiation from an early stage of the collision as the
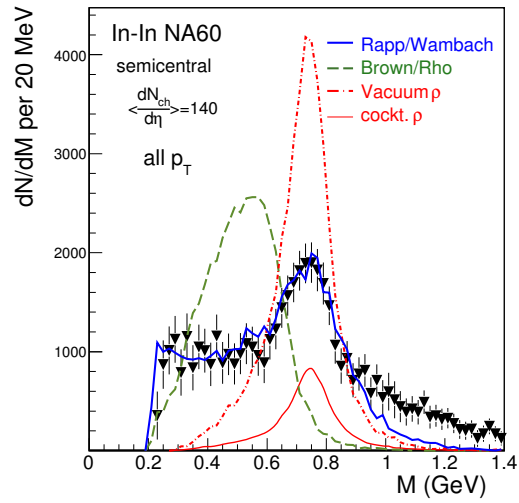
Figure 1.10: Excess dimuon yield in LMR measured by NA60 experiment in $In + In$ collisions at 158 GeV [39] [96] [76], compared with theoretical predictions from (a) vacuum ρ spectral function in dashed red, (b) dropping ρ mass in dashed green, (c) collisional broadening in solid blue, labeled *Rapp/Wambach*.

origin. Fig. 1.11 illustrates the NA50 dimuons in IMR described by the sum of Drell-Yan, correlated Charm decay and thermal radiation from QGP and hadron gas [58].
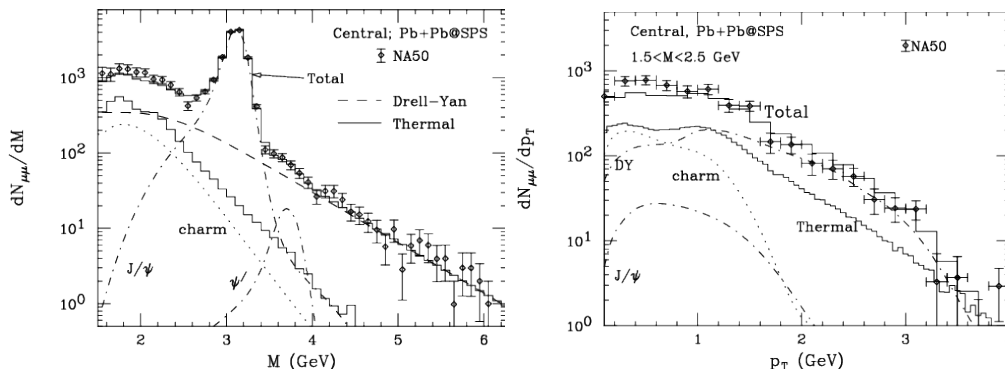
Figure 1.11: Dimuon spectra in mass(left panel) and p_T(right panel) in $1.5 < M < 2.5\ GeV/c^2$ measured by NA50 experiment in $In + In$ collisions. The dimuon yields are described by Drell-Yan, correlated Charm decay and thermal radiation from QGP and hadron gas [58].

1.2.2 PHENIX Dielectron Results

$p + p$ dielectrons

Now, moving up to RHIC experiments, a baseline measurement with p+p collisions at $\sqrt{s} = 200$ GeV using the data taken in 2005 was analyzed by PHENIX [20] [10]. The di-electron invariant mass spectrum is shown in Fig. 1.12. In addition to the blue data points, the expected contributions from various hadronic sources, the so-called cocktails, are plotted together for easy comparison. At very low mass below $150 MeV/c^2$, dielectrons arise dominantly from π^0 Dalitz decays. In the low mass region between $150 MeV/c^2$ and $750 MeV/c^2$, Dalitz decays from various light mesons form a smooth continuum. The mesons include η, η', ω, and ϕ mesons. Contributions from open charm semi-leptonic decay are also present. Between mass $750 MeV/c^2$ and $1.10 GeV/c^2$, peaks of ω and ϕ are visible above the underlying yield. Contributions from ρ are shown to sit mostly under the ω peak. In the intermediate mass region between $1.1 GeV/c^2$ and $2.8 GeV/c^2$, open charm decays are shown to be the dominant source. Heavy flavors dominate the

24
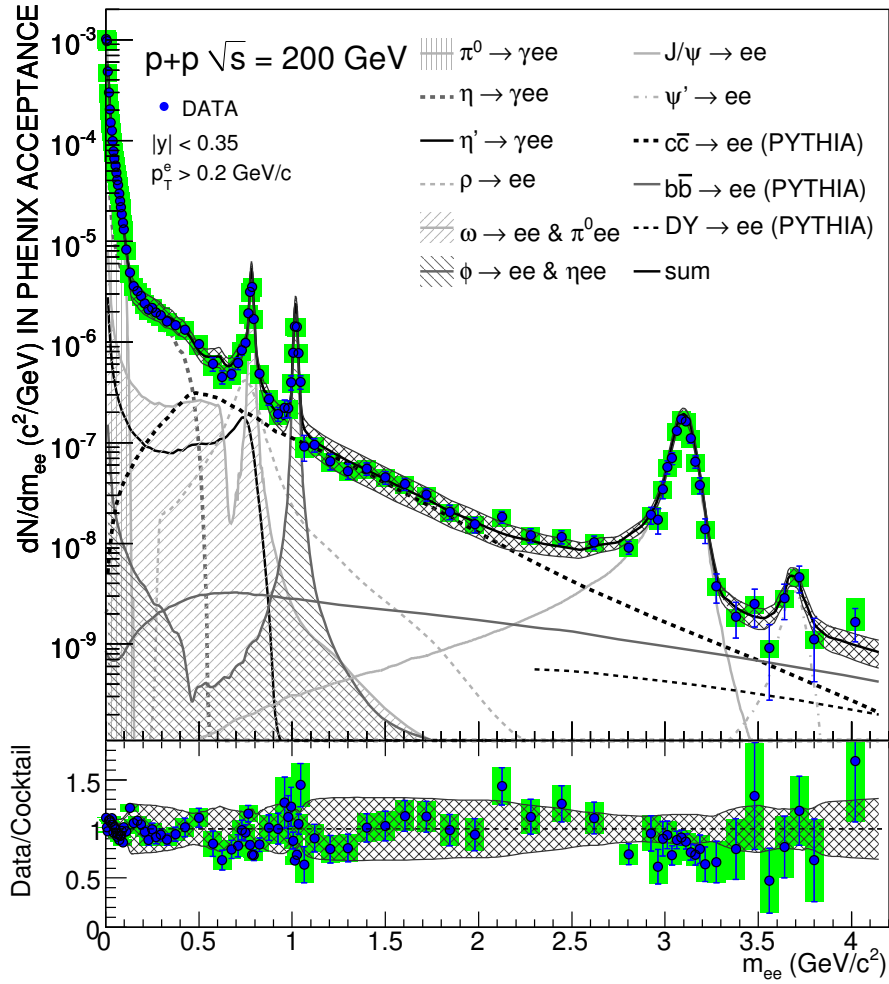
Figure 1.12: PHENIX dielectron mass spectrum of $p + p$ collisions at $\sqrt{s} = 200\ GeV$. Upper panel: spectrum with expected yield from various hadronic sources. Lower panel: the ratio of measured spectrum to hadronic expectation. [20] [10]

high mass region. Open bottom decays are the major contributor beyond the J/Ψ and Ψ' peaks. Yields from the Drell-Yan process would overtake bottom contribution at still higher mass.

In Fig. 1.12, the sum of the various sources is plotted as a solid black line and compared to the data points. The ratio of the two, shown in the lower panel, demonstrates excellent agreement between data and hadronic decay expectations. The agreement validates our knowledge of the hadronic sources and their spectral shapes when the hot and dense medium is absent. The $p + p$ spectrum serves as a starting point to investigating the heavy ion case.

$Au + Au$ dielectrons

In 2004, PHENIX measured of dielectron spectra in Au+Au collisions at $\sqrt{s} = 200$ GeV [10]. A remarkable feature in the final spectra shows an unexpectedly large excess localized between 0.15 GeV and 0.75 GeV in the minimum bias collisions. The minimum bias result (Fig. 1.13) shows an excess with a factor of 4.7±0.4(stat)±1.5(syst)±0.9(model) over expected yield from the hadronic cocktail expectations. Furthermore, the excess is shown to be strongly centrality dependent, as seen in Fig. 1.14. It increases when the collisions are more central and dwindles when the collisions become peripheral. This trend with centrality is an indication that this excess is linked with the formation of the hot fireball. A study of the excess in transverse momentum slices (Fig. 1.15), which compares the $Au+Au$ spectra in p_T slices to those from $p + p$, demonstrates that soft pairs under 1 GeV are the main contributor to the excess.

While similar enhancement has been observed in many experiments in the same mass region, the magnitude of the excess in the PHENIX result exceeded theoretical expectations. Current theoretical models have been unable to explain the discrepancy. This measurement, however, suffers from a huge combinatorial background. Improved S/B ratio, increased statistics and a more precise background subtraction are called for, in order to improve this significant result and to shed light on the discrepancy between experiment and theory.

In the intermediate mass region where radiation from QGP is predicted, the lower energy experimental observations discussed in Sec. 1.2.1 found an excess likely to originate from early thermal radiation. The PHENIX intermediate mass region shows little distinct excess over open charm expectations
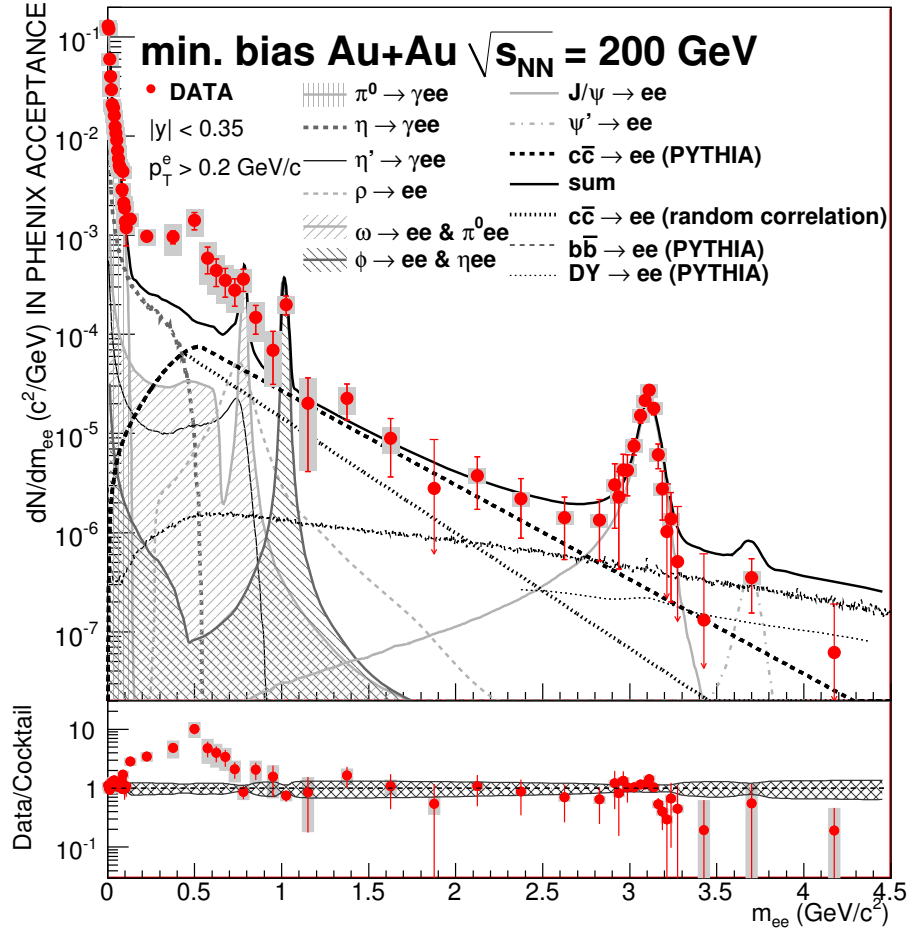
Figure 1.13: PHENIX dielectron mass spectrum of $Au+Au$ min bias collisions at $\sqrt{s} = 200\ GeV$. Upper panel: min bias spectrum compared to hadronic cocktails. Lower panel: the ratio of data to hadronic expectation. [10]
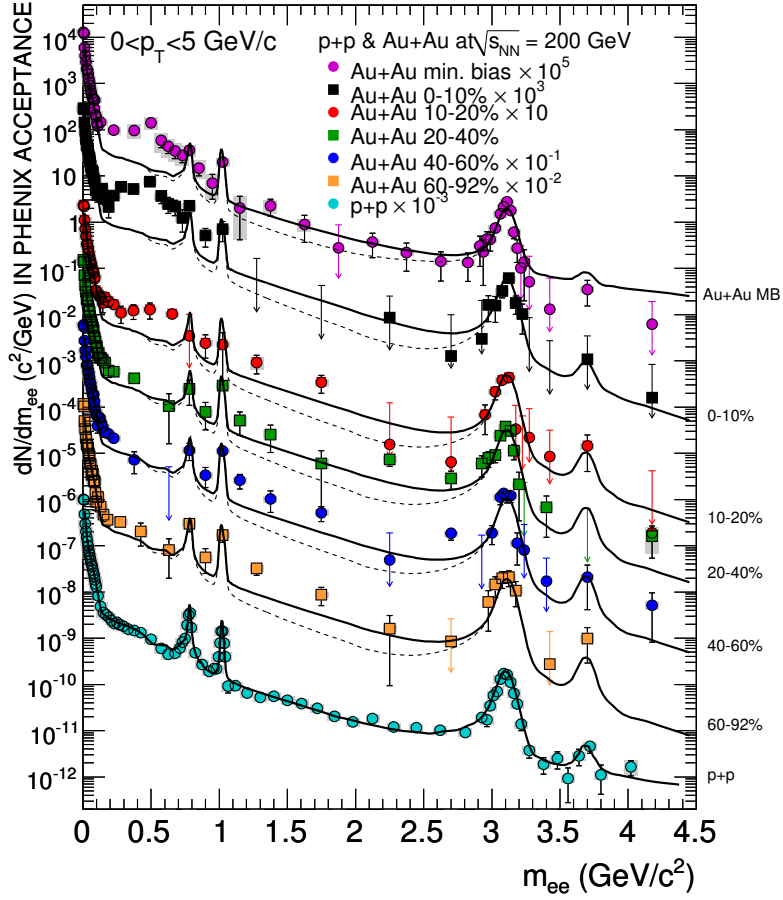
Figure 1.14: PHENIX $Au + Au$ spectra with split centrality bins. The centrality selections from the top are: min bias, $0 - 10\%$, $10 - 20\%$, $20 - 40\%$, $40 - 60\%$ and $60 - 92\%$, with the bottom one being result from $p + p$ collisions. [10]
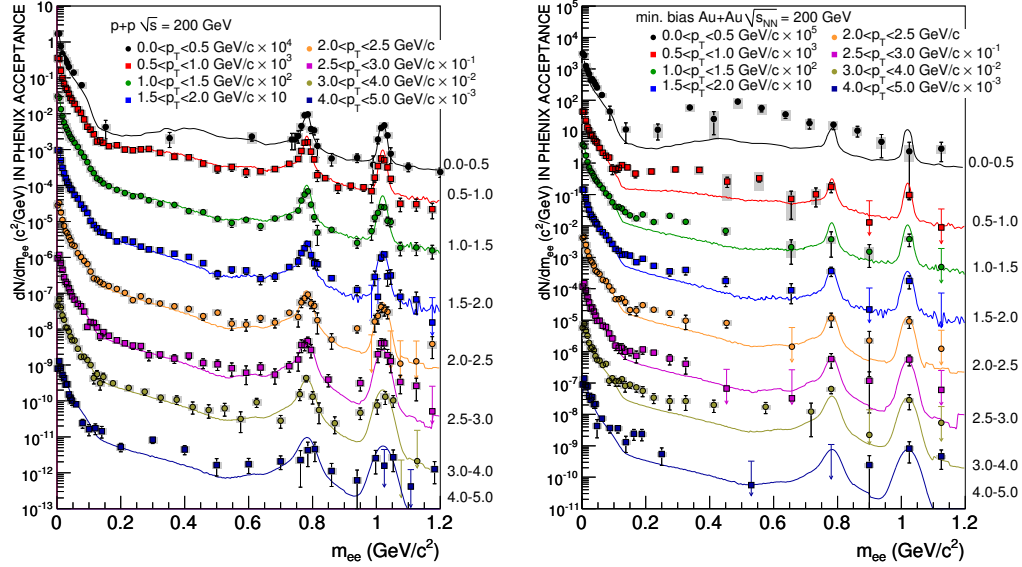
Figure 1.15: Left: PHENIX $p+p$ spectra in low mass region with split p_T bins. Right: PHENIX $Au + Au$ spectra in low mass region with split p_T bins. [10]
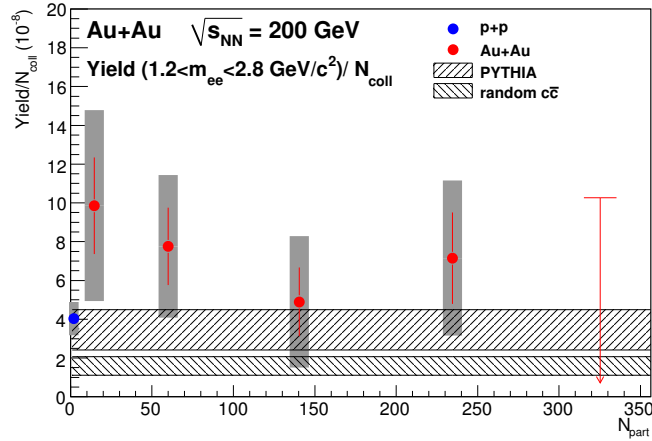
Figure 1.16: PHENIX $Au+Au$ dielectron yield between $1.2\ GeV/c^2 < m_{ee} < 2.8\ GeV/c^2$, with comparison to PYTHIA [116] simulation of charm contribution. Plotted as a function of N_{part}. [10]

within experimental uncertainties. Within the relatively large uncertainty on the data points, the yield in the region is consistent with N_{coll} scaling of c-$\bar{c}$ yield based on PYTHIA [116] simulation of open charm production, as shown in Fig. 1.16. In the dielectron spectra measured by STAR, a hint of suppression is seen in the most central collisions (see Fig. 1.21, Fig. 1.22), leading to speculations of possible charm de-correlation effect. Given the current experimental uncertainties, both STAR and PHENIX results are consistent with hadron cocktail expectation. A more precise measurement would add useful information to this mass region.

$Cu + Cu$ dielectrons
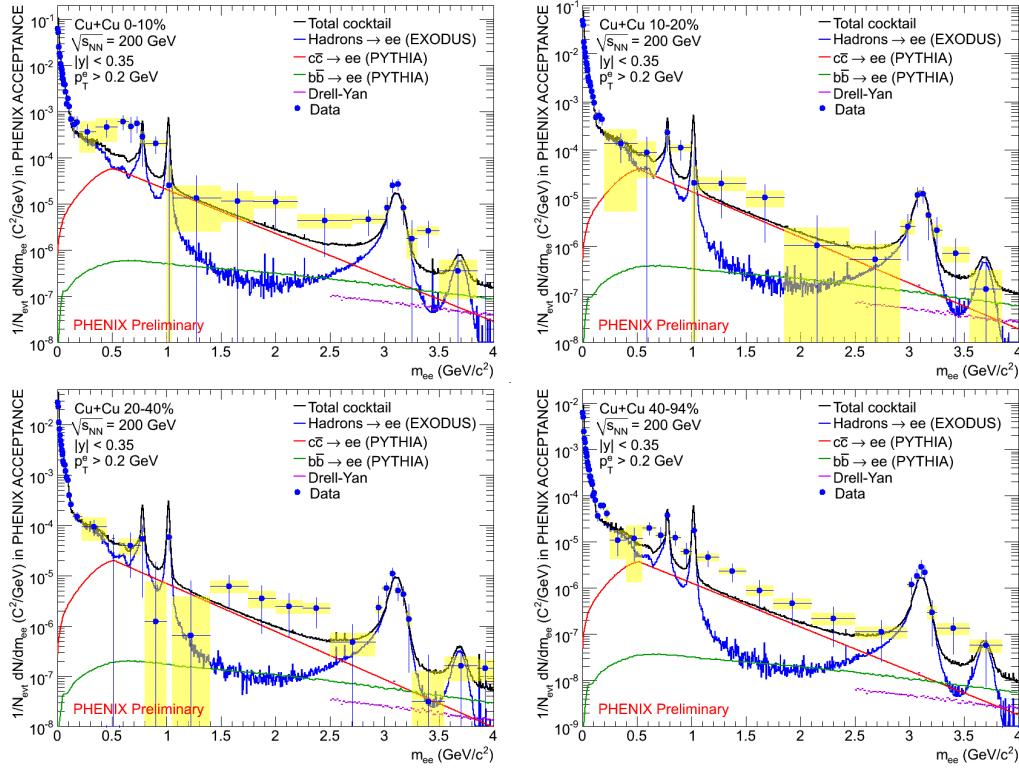
Figure 1.17: Dielectrum spectra of $Cu + Cu$ collisions in centrality bins: $0 - 10\%$, $10 - 20\%$, $20 - 40\%$ and $40 - 94\%$. [50]

The $Cu + Cu$ dielectron mass spectra provide a look into an intermediate system with somewhat lower energy density, lower temperature and

smaller volume. Fig. 1.17 shows the mass spectra from 4 centrality classes in $Cu + Cu$ collisions [50]. The plot for the most central collisions illustrates a clear enhancement at the ρ mass region. However the enhancement fades for the other, more peripheral centrality classes. In all centrality selections, an enhanced yield in the intermediate mass region was observed.

$d + Au$ dielectrons
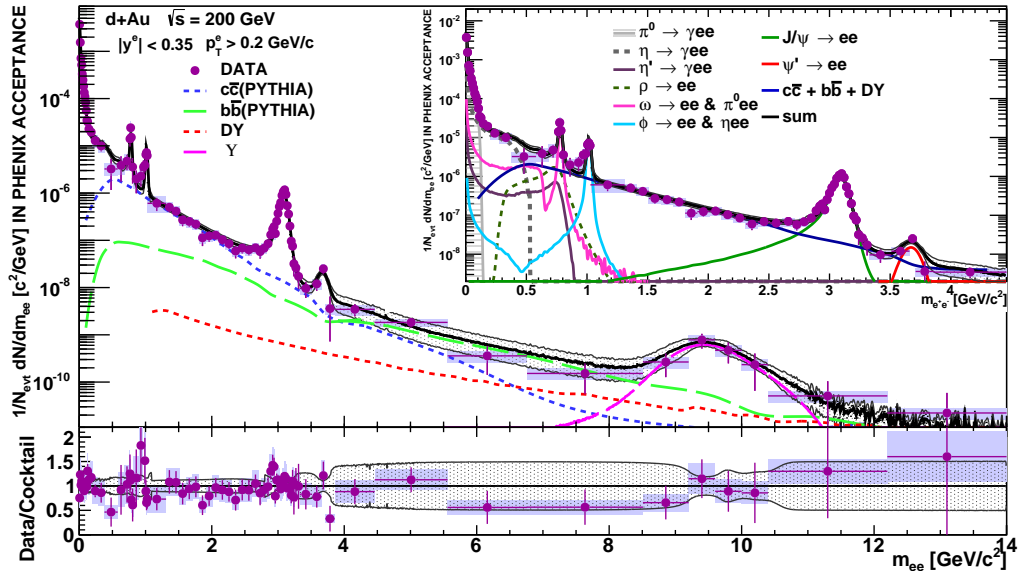
Figure 1.18: PHENIX result of $d + Au$ collisions at $\sqrt{s} = 200\ GeV$. The corresponding hadronic cocktail is plotted against the spectrum in the upper panel. The lower panel shows the ratio of data to the cocktail. [82] [19]

It is essential to disentangle cold nuclear effect from the observed low mass enhancement in $Au+Au$ spectra. A subsequent PHENIX measurement using d+Au collisions at the same energy, excludes any cold nuclear effects on the enhancement [19]. Fig. 1.18 is the $d + Au$ spectra overlaid with the hadronic cocktail, while Fig. 1.19 shows $d + Au$ data with the $p + p$ spectrum scaled up by a factor so that the $\frac{dN^\pi}{dy}$ in $p + p$ matches that measured in $d + Au$. The d+Au spectrum exhibits good consistency in full mass range with both hadronic expectations and the $p + p$ results. With only cold nuclear matter present the initial state of $d+Au$ collision, there is no low mass enhancement,

confirming that the enhancement in $Au + Au$ collisions is indeed an effect from hot and dense matter.
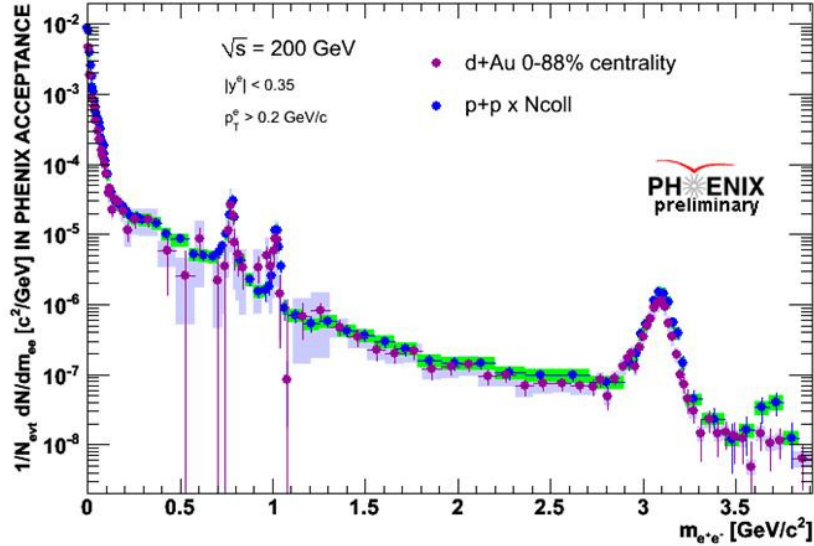
Figure 1.19: The $d + Au$ spectrum compared to the $p + p$ spectrum scaled up by N_{coll} to match the multiplicity in $d + Au$ collisions. [82]

Fig. 1.20 [82] illustrates the integrated dielectron yield per participating nucleon pair in the low mass region for the four different collision systems($p+ p$, $d + Au$, $Cu + Cu$ and $Au + Au$), plotted as a function of the number of participating nucleons (denoted by N_{part}) in selected centrality classes. The grey bands denote expectations from hadronic cocktails. The lower panel is the yield for mass under $100 MeV/c^2$ where π^0 Dalitz decay is the dominant source. It exhibits consistency between different measurements as well as between data and hadronic expectations over all four systems. The upper panel is the yield for mass between $150 MeV/c^2$ and $750 MeV/c^2$. The enhancement above the hadronic cocktail is shown to grow with N_{part} across the four systems.

1.2.3 STAR Dielectron Results

Recently STAR has also published dielectron mass spectra in Au+Au collisions at $\sqrt{s} = 200$ GeV [4] [2], measured with Time Projection Chamber and
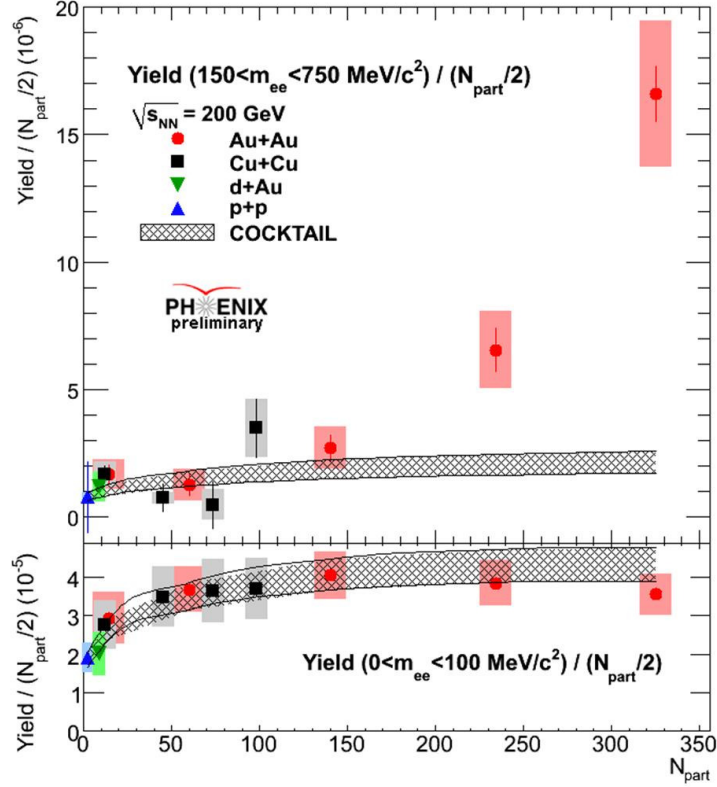
Figure 1.20: The dielectron yield in low mass region $0.15\ GeV/c^2 < M_{ee} < 0.75\ GeV/c^2$ in collision systems $p + p$, $d + Au$, $Cu + Cu$ and $Au + Au$ at $\sqrt{s} = 200\ GeV$, plotted as a function of N_{part}. The grey band represents expectations from hadronic cocktails. [82]

Time-of-Flight detectors. They also reported an excess at the ρ region (0.30-0.76 GeV), though the enhancement factor is $1.76\pm0.06(\mathrm{stat})\pm0.26(\mathrm{syst})\pm0.29(\mathrm{cocktail})$ in Minimum Bias collisions, which is significantly lower than the PHENIX result. Moreover, STAR has demonstrated that the enhancement has a mild dependence on both centrality and p_T, contrary to the PHENIX conclusion that the enhancement comes mainly from soft particles in more central collisions. Fig. 1.21 depicts the STAR dielectron spectra in centrality bins $0 - 10\%$, $10 - 40\%$, $40 - 80\%$ and the min bias. Fig. 1.22 shows the spectra divided into a few p_T windows. The plots display only a small dependence on centrality and p_T.

The STAR excess is compared with two theoretical models, one an ef-
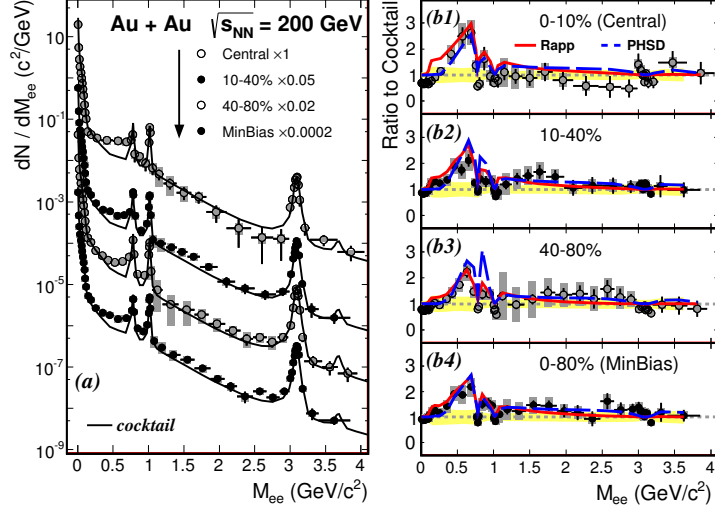
Figure 1.21: Left: dielectron mass spectra from STAR experiment with $Au+$ Au collisions at $\sqrt{s} = 200\ GeV$ in several centrality bins. Right: the ratio of STAR data to STAR cocktails in the 4 respective centrality bins compared to two theoretical models. [4]
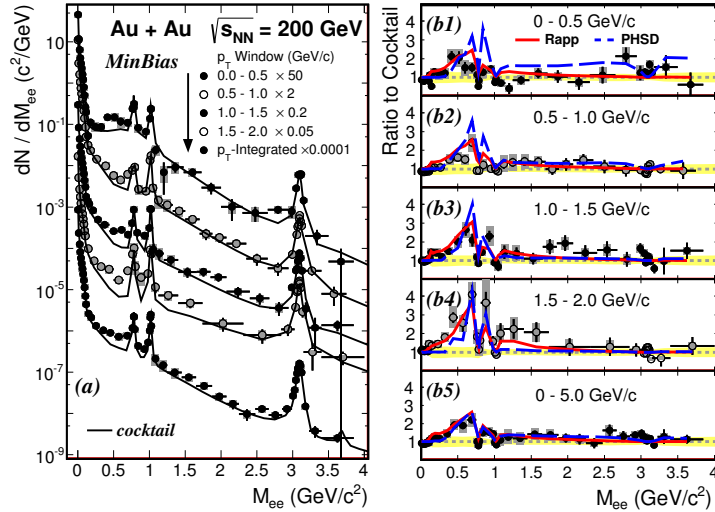
Figure 1.22: Left: STAR dielectron mass spectra with $Au + Au$ collisions at $\sqrt{s} = 200\ GeV$ in selected p_T bins. Right: the ratio of STAR data to STAR cocktails in the 5 respective p_T bins compared to two theoretical models. [4]
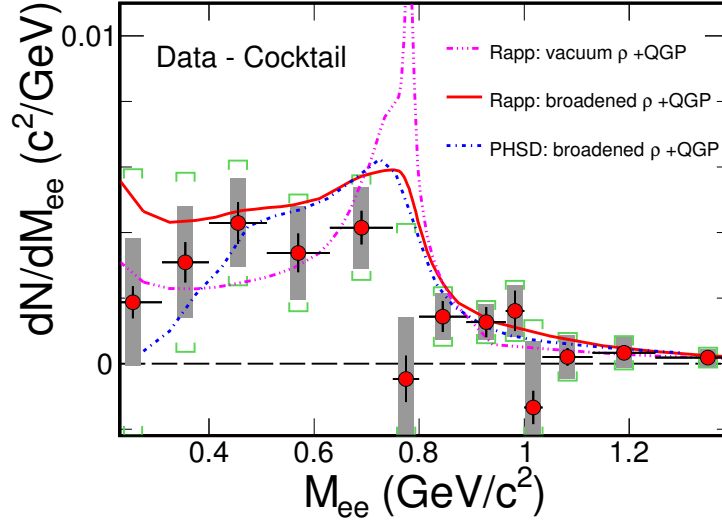
Figure 1.23: STAR excess in the low mass region compared to results from theoretical models. The data show agreement with the effective many-body model by Rapp as well as the PHSD, a microscpic transport model. [4]

fective many-body model from Rapp et al. [104], the other a microscopic transport model from O.Lynnik et al. [53] [55] [84]. Both based on the ρ broadening scenario, are able to obtain good agreement with STAR data within uncertainty, as shown in Fig. 1.23. A third theoretical curve with vacuum ρ properties by Rapp fails to reproduce the data.

In addition to the $Au + Au$ measurement at $\sqrt{s} = 200\ GeV$, STAR has also been able to carry out $Au + Au$ dielectron measurements at lower energies [3]. Fig. 1.24 lists dielectron spectra at collision energy 19.6, 39, 62.4 and 200 GeV. An excess is observed in all the energies with a similar magnitude. The dielectron yield after subtracting a ρ-less cocktail for each collision energy is shown in Fig. 1.25. It shows that this excess, resulting from medium modification of ρ mesons, exists in a wide range of collision energy from 19.6 to 200 GeV, and its absolute yields appear to bear little dependence on $\sqrt{s}$.

1.2.4 Motivation For The Dissertation

The discrepancy between the STAR and PHENIX $Au+Au$ results, as well as the disagreement between theory and the PHENIX enhancement, call for
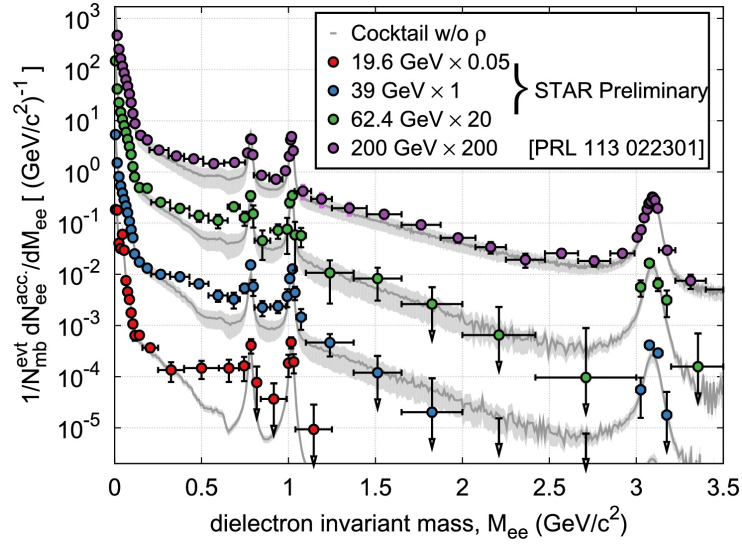
Figure 1.24: STAR $Au + Au$ dielectron mass spectra at several collsion energies: 19.6 GeV, 39 GeV, 62.4 GeV and 200 GeV. The grey bands denote the hadronic cocktails with uncertainties. [4]
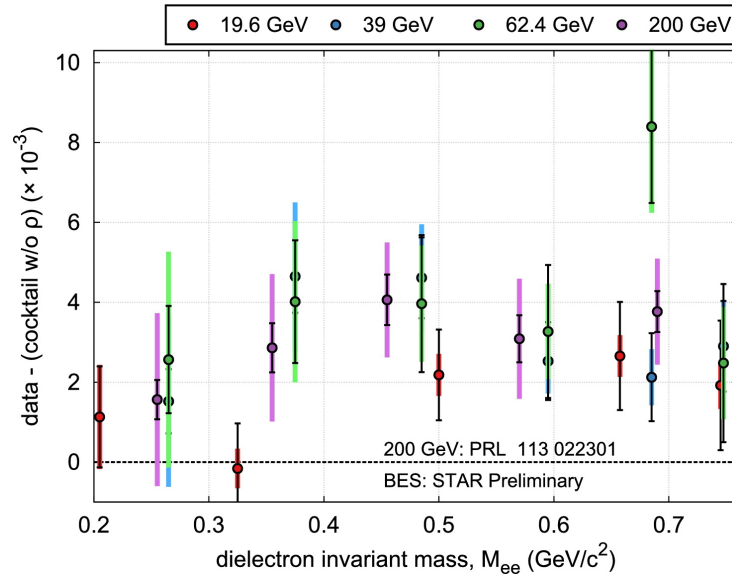
Figure 1.25: Comparison of STAR excess observed at different collision energies: 19.6, 39, 62.4 and 200 GeV. [3]

an improved measurement with better precision. The major difficulty from the past $Au + Au$ result of 2004 stemmed from the huge combinatorial background as a result of random pairing of e^+ and e^- of unidentified ancestry. Most of these tracks are from π^0 Dalitz decays and photon conversions, and about 30% of the tracks in the central collisions are mis-identified hadrons.

To address this issue, a novel detector named the Hadron Blind Detector (HBD) was designed and constructed. Detailed description of the HBD will be followed in the next chapter. It is a windowless Cherenkov proximity focused detector, aiming to reduce the level of combinatorial background significantly.

The HBD was installed as a PHENIX upgrade in 2009 and 2010. In 2009, PHENIX successfully took data on $p + p$ collisions at $\sqrt{s} = 200 \ GeV$ with the HBD. The $p + p$ HBD measurement provided a simple environment for understanding the HBD performance, and established a baseline for the $Au + Au$ HBD results, which are the subject of the present thesis.

In 2010, a large dataset of $Au + Au$ collisions at $\sqrt{s} = 200 \ GeV$ was recorded by PHENIX with the HBD running successfully. With significantly increased statistics and enhanced background rejection power, the new measurement aims to improve the previous PHENIX measurement of $Au + Au$ collisions.

Chapter 2

PHENIX Experiment at RHIC

2.1 RHIC
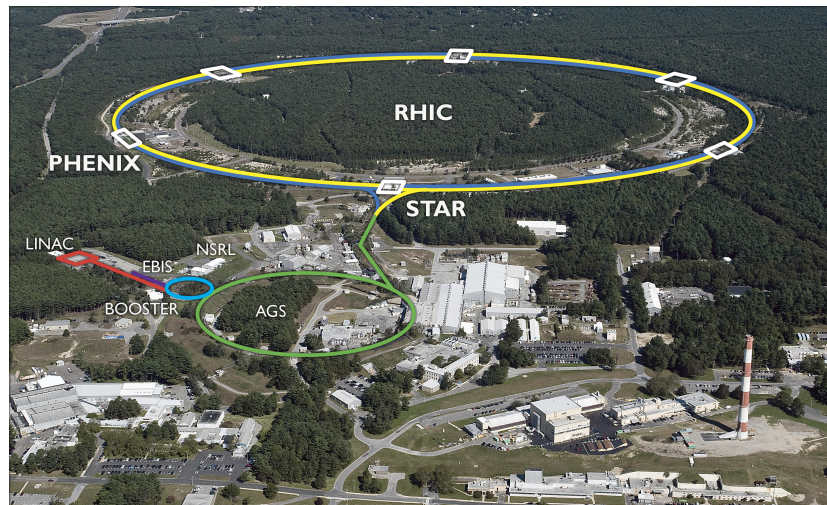
Figure 2.1: Aerial view of RHIC facility with PHENIX and STAR experiments.

The Relativistic Heavy Ion Collider (RHIC) is located at Brookhaven National Laboratory on Long Island, New York. It is one of the two heavy ion colliders currently in operation - the other being the Large Hadron Collider (LHC) in CERN - and the only collider capable of colliding spin polarized $p + p$ ions. The primary objective of RHIC is to investigate the formation and property of the QGP. It is designed to accelerate, store and collide

particle species ranging from protons to gold. Recently it successfully collided uranium ions. The top energy for heavy ion beam can reach as high as 100 GeV/u, and 250 GeV for proton beams. The design luminosity is $2 \times 10^{26} cm^{-2} s^{-1}$ for $Au + Au$ beams, and $1.4 \times 10^{31} cm^{-2} s^{-1}$ for $p + p$.

Fig. 2.1 presents an overview of the RHIC facility. The RHIC collider has a diameter of 3.7km. It consists of two concentric accelerator/storage rings, named the blue and the yellow ring. The beam in the blue ring travels clockwise and in the yellow counter-clockwise. The two beams are brought to intersect with each other at six collision locations. Experiments have been built at four of them, BRAHMS, PHOBOS, STAR and PHENIX. Out of the four, BRAHMS and PHOBOS are smaller experiments and completed data taking by 2005 and 2006, respectively. STAR and PHENIX, at 6 o'clock and 8 o'clock on the RHIC ring, have been actively taking physics data to date.

Run	Year	Species	$\sqrt{s}$ GeV	Run	Year	Species	$\sqrt{s}$ GeV
1	2000	$Au + Au$	130			$Au + Au$	62.4
2	2001/02	$Au + Au$	200			$Au + Au$	39
		$p + p$	200			$Au + Au$	7.7
3	2002/03	$d + Au$	200			$Au + Au$	11.5
		$p + p$	200	11	2010/11	$p + p$	500
4	2003/04	$Au + Au$	200			$Au + Au$	19.6
		$Au + Au$	62.4			$Au + Au$	200
5	2004/05	$Cu + Cu$	200			$Au + Au$	27
		$Cu + Cu$	62.4	12	2011/12	$p + p$	200
		$Cu + Cu$	22.5			$p + p$	510
		$p + p$	200			$U + U$	193
6	2005/06	$p + p$	200			$Cu + Au$	200
		$p + p$	62.4	13	2012/13	$p + p$	510
7	2006/07	$Au + Au$	200	14	2013/14	$Au + Au$	14.6
8	2007/08	$d + Au$	200			$Au + Au$	200
		$p + p$	200			$^{3}He + Au$	200
9	2008/09	$p + p$	500	15	2014/15	$p + p$	200
		$p + p$	200			$p + Au$	200
10	2009/10	$Au + Au$	200			$p + Al$	200

Table 2.1: Table of RHIC operating modes for the past years.

A list of RHIC collision modes from the past years to the present are

given in Table. 2.1. The dataset used for this thesis work is from the $Au+Au$ collisions at $\sqrt{s} = 200\ GeV$ taken during Run10 in 2010.

2.2 PHENIX

PHENIX stands for Pioneering High Energy Nuclear Interaction eXperiment [23]. It is a large multipurpose detector specializing in the measurement of rare, electromagnetic probes in heavy ion collisions, in particular the photons, electrons and muons.

PHENIX is composed of many subsystems. It has two central arms designed to detect photons, electrons and charged hadrons at mid-rapidity, each covering $90°$ in ϕ and $-0.35 < \eta < 0.35$ in pseudo-rapidity. Two muon arms are situated at rapidity $1.2 < |y| < 2.4$ with full azimuthal acceptance, specializing in muon detection. Fig. 2.2 illustrates the PHENIX configuration during Run10. The upper panel portrays the central arm detector arrangement viewed in the direction of the beam. The lower panel shows the muon arms and three PHENIX magnets viewed from the side. The various detector subsystems relevant to the dielectron analysis are summarized below,

- **The Central Magnet** provides a uniform magnetic field for momentum measurement of charged particles in the central arms. The "+-" field configuration produces a needed field-free region inside the Hadron Blind Detector.

- **Global Detectors** include the Beam-Beam counters (BBC), the Zero Degree Calorimeter (ZDC) and the Reaction Plane Detector (RXNP). In addition to providing a minimum bias trigger, the BBC measures the collision time and vertex position along the beam direction. When multiplicity information from the BBC and the ZDC are combined, event centrality can be determined. The RXNP measures the event plane orientation, which is essential for the elliptic flow[1] measurement.

- **The Central Arm Tracking System** consists of the Drift Chambers (DC) and the Pad Chambers (PC). The trajectory of charged tracks

---

[1]In a two-nuclei collision, the overlapping area is much more often an almond shape than a perfectly round disk. The almond shape leads to an azimuthal anisotropy of the particle distribution. The elliptic flow, defined as the seond Fourier coefficient v_2 of the particle azimuthal distribution, is used to describe the anisotropy.

can be reconstructed from DC hits. The PC has three layers, PC1, PC2 and PC3. Hits from PC1, PC2 and PC3 define the approximately straight track trajectory through the central spectrometer outside DC, and help resolving ambiguities in EMCal hits. The track trajectories and magnetic field map are used to reconstruct each particle's momentum. PC1 determines the z position of each trajectory.

- **Electron Identification Detectors** includes the Ring Imaging Cherenkov Counter (RICH), the Electromagnetic Calorimeter (EMCal) and Time-of-Flight East detector (TOF-E). Utilizing electron Cherenkov radiation in CO_2 gas, the RICH acts as the primary electron identification detector by searching for Cherenkov light near charged tracks. Charged tracks shower in the EMCal; electron showers are entirely contained in the EMCal, but hadronic showers are not. Electrons can be identified by matching the track momentum to the energy deposited in the EMCal. Finally, the time of flight measured by the EMCal or the TOF-E provides additional discriminating power for hadron rejection.

- **The Hadron Blind Detector Upgrade** is a novel Cherenkov proximity focused detector upgrade to PHENIX in 2009-2010. It is designed to reject π^0 Dalitz decay electrons and photon conversion electrons, thereby reducing the huge combinatorial background in the dielectron spectra.

2.3 PHENIX Magnet System

The PHENIX magnet system [40] has three magnets with warm iron yokes and water-cooled copper coils, namely the Central Magnet, and the north and south Muon Magnets. They are shown in the lower panel of Fig. 2.2. Each provides a field integral of 0.8 $T \cdot m$. The Central Magnet, which is relevant to this analysis, is composed of two sets of concentric coils, known as the outer and the inner coils. They provide a reasonably uniform magnetic field parallel to the beampipe up to the Drift Chamber. Such field configuration is designed for momentum analysis of charged particles in the polar angle ranging from 70 to 110 degrees.

Fig. 2.3 is a drawing of PHENIX magnetic field from the three magnets. The field lines parallel to the z-axis (the beam direction) in the center are

2010   PHENIX Detector

PC3
PbSc
PC2
Central
Magnet
PC3
TEC
PbSc

PbSc
PbSc

TOF-W
DC   DC

PbSc
RICH   RICH
PbGl

HBD
MPC RxNP

PbSc
PC1   PC1
PbGl

Aerogel
TOF-E

7.9 m = 26 ft

West   Beam View   East

South Muon Magnet   Central Magnet   North Muon Magnet

ZDC South
MPC
BBC
ZDC North

MuID
MuID

10.9 m = 36 ft
MuTr
RxNP
HBD

South   Side View   North

18.5 m = 60 ft
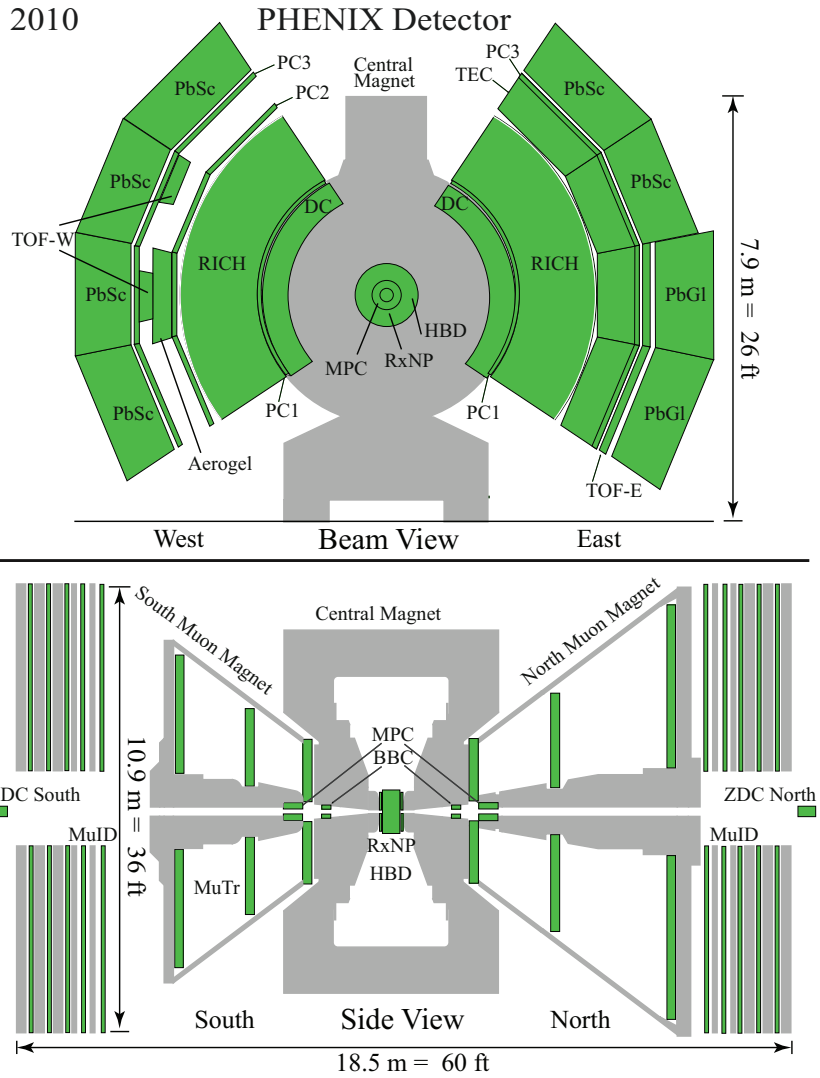
Figure 2.2: PHENIX configuration for Run10.

42
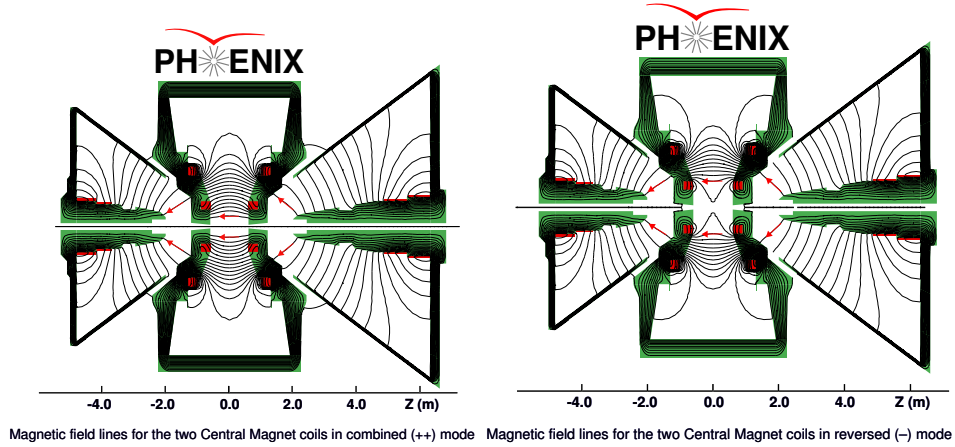
Figure 2.3: Left: PHENIX Magnet field lines in "++" configuration. Right: PHENIX Magnetic field lines in "+-" configuration.

created by the Central Magnet. The two sets of coils allow for two kinds of magnetic field configurations, the "++" (left panel) and the "+−" (right panel) field.

The "++" is a field-adding configuration where the total field is the outer coil field plus the inner coil field. The "+−" is a "bucking" configuration where the total field is the outer coil field minus the inner coil field. In "+-" field, the currents in the coils are adjusted so that the field integral in the region $0 < R < 50$ cm is approximately zero. This field-free region at small radial space is essential for the Hadron Blind Detector operation. This keeps an electron-positron pair from Dalitz decays or conversions in the beam pipe from opening its angle.

2.4   Global Detectors

2.4.1   Beam Beam Counter

The Beam Beam Counter (BBC) [34] serves several purposes. It provides the minimum bias trigger that signals the occurance of a collision, measures the collision vertex point along the beam axis, and determines the time of beam-beam collisions for Time-of-Flight measurements.

The BBC has two identical counters installed on the north and the south
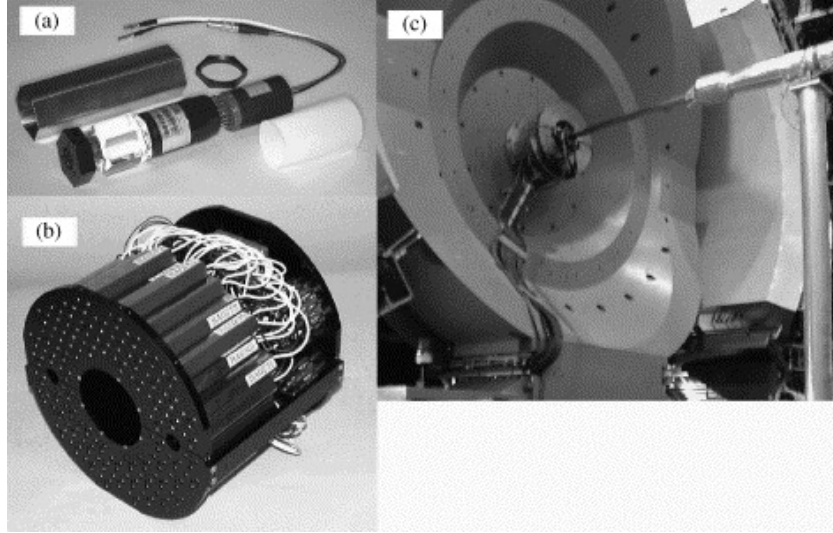
Figure 2.4: Picture of PHENIX Beam Beam Counter [34].

side of the collision point on the beam axis. Fig. 2.4 shows photographs of the detector. The counters have a cylinder shape, with an outer radius of 30 cm, and an inner radius of 10 cm, which provides room for the beam pipe to go through. Each counter consists of 64 photomultiplier tubes with quartz Cherenkov radiators installed in front. The timing resolution for a single PMT module is 52 ps. Both counters are positioned at 144 cm from the collision point, leading to a coverage of $3.0 < |\eta| < 3.9$ over the full azithmuth. The BBC has a broad dynamic range which allows for a capacity to operate in collisions ranging from $p + p$ to $U + U$.

When a collision occurs, both the north and south BBC are hit by charged particles. The time of the collision is calculated to be the average arrival time of charged particles at the two counters:

$$t_0 = \frac{t_{BBCN} + t_{BBCS}}{2} - \frac{L}{c} \tag{2.1}$$

where L is the length from $z = 0$ to the BBC, namely 144 cm, and c is the speed of light, t_{BBCN} and t_{BBCS} are hit time of BBC North and South, respectively. t_0 is used as the start time for track time-of-flight measurement. The collision vertex location along the z-axis (beam direction) is given by:

$$z_{vertex} = c\frac{t_{BBCN} - t_{BBCS}}{2} \tag{2.2}$$
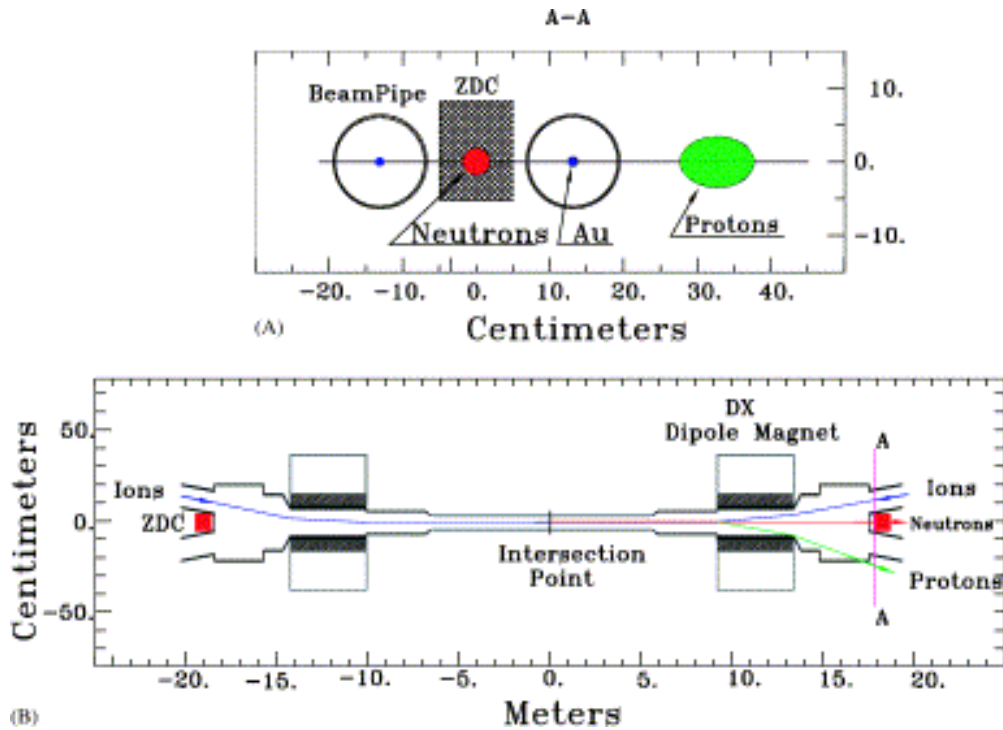
Figure 2.5: Schematic plot of ZDC configuration in RHIC [25].

A collision with vertex $|z_{vertex}| \leq 38\ cm$, together with a coincidence in both BBCs would cause the PHENIX level-1 trigger to fire. A typical z_{vertex} resolution for $Au + Au$ collisions is $\sim 3\ mm$.

2.4.2 Zero Degree Calorimeter

All four experiments on the RHIC ring are equipped with Zero Degree Calorimeters (ZDC) [25] [24]. It is a pair of sampling hadronic calorimeters located 18 m from the collision point behind the DX dipole magnet. As shown in Fig. 2.5, the ZDC is situated at a great distance from the beam intersection point behind DX Dipole Magnet, which bends the beams away, so that their acceptance is essentially limited at "zero degrees".

The ZDC is used for measuring the energy and arrival time of spectator neutrons. Those neutrons do not participate in the collisions and fly out without scattering. Thus, it monitors the beam luminosity, contribute to a minimum bias trigger selection for peripheral events, and measures the

collision vertex. The difference distribution in the measurement of the collision vertex from the BBC and the ZDC has a width of $\sim 2\ cm$, which is dominantly from the ZDC.

The spectator neutrons measured by the ZDC can be combined with the charge sum in the BBC to determine event centrality. For the data taken in Run10, however, only the BBC charge sum is used for centrality determination.

2.4.3 Reaction Plane Detector

Reaction Plane Detector(RXNP) [110] measures the event plane orientation in the heavy ion collisions. It is composed of two identical sets of scintillators, the north and the south, located at $\pm 39\ cm$ from the nominal vertex position and in front of the central magnet's nosecone.

Each scintillator set is installed perpendicular to the beam pipe with 2π coverage in ϕ. It circles around the beampipe with a 10 cm inner diameter and is sectioned into an inner and an outer ring. Each ring is divided into 12 equal scintillator paddles, which leads to a total of 24 scintillators in one side, as shown in Fig. 2.6. The inner ring covers a rapidity range of $1.5 < \eta < 2.8$ and the outer ring covers $1.0 < \eta < 1.5$.

One RXNP set is built with 4 aluminum structures. Each of these covers $90°$ in ϕ and mechanically holds 3 inner and 3 outer scintillators, as shown in Fig. 2.6. These plastic paddle scintillators are 2 cm thick and are connected to readout photomultipliers via embedded fiber light guide. A 2 cm thick Pb converter is placed in front of the paddle scintillators to enhance the particle flux into the detector. The RXNP detector achieves a 2nd harmonic reaction plane resolution of 0.75 [110].

2.5 Central Arm Tracking System

The two major detectors for PHENIX central arm tracking system are the Drift Chamber and the Pad Chamber [22]. The Drift Chamber is the first layer of PHENIX central arm detectors. Its purpose is to provide high precision p_T measurements of charged particles. Another major function is pattern recognition in a high multiplicity environment, so that tracks can be linked in various PHENIX detectors by Drift Chamber position information. Three
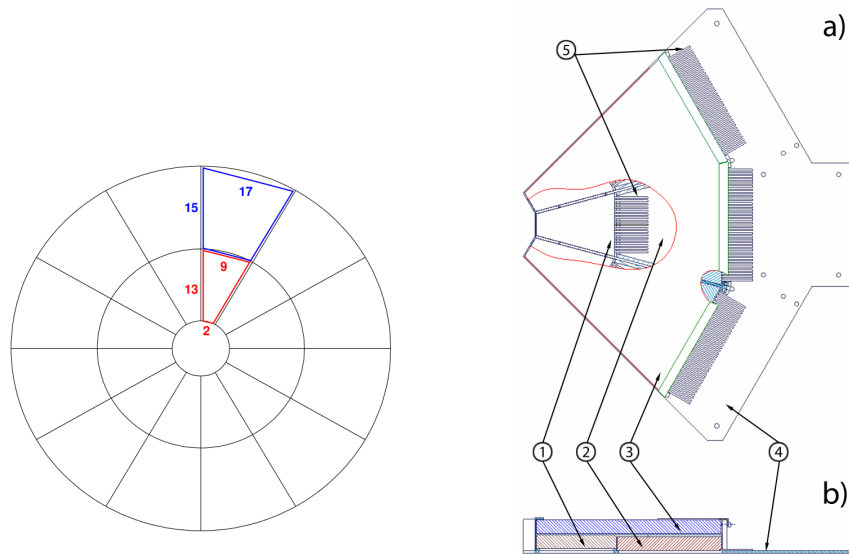
Figure 2.6: Left: Schematic view of one Reaction Plane Detector side with 24 plastic scintillators. The numbers denote the lengths of the scintillator side in cm. Right: a) Schematic sketch of one assembled RXNP aluminum tray in top view. b) The RXNP aluminum tray in side view. (1) and (2) are inner and outer scintillators, respectively. (3) denotes the Pb converter. (4) is the aluminum support tray. (5) shows the optical fibers connected to the rear of the scintillators [110].

layers of Pad Chambers(PC1, PC2 and PC3) provide three-dimensional space points and longitudinal momentum fraction p_z/p_T for charged tracks.

2.5.1 The Drift Chamber

The Drift Chamber [22] is the most important detector for charged particle tracking and momentum determination. It has two identical multiwire gas chambers installed as the first layer in each Central Arm of the PHENXI spectrometer, each covering $90°$ in azimuth and 2m in z direction. It is located at $2.02\ m < R < 2.46\ m$ in radial distance. Fig. 2.7 shows the side view of one Drift Chamber.

The DC is supported by a cylindrical titanium frame, which is sectioned into 20 equal parts. These are called keystones, each of which has a coverage of $4.5°$ in azimuth. There are 6400 anode wires in each keystone. Fig. 2.8 shows the layout of wire position in one keystone. There are four anode (sense) wire planes and four cathode planes. Every keystone consists of six types of wire modules: X1, U1, V1 and X2, U2, V2. The X1 and X2 wires are parallel to the beam direction, while the U and V stereo wires are oriented at $\sim 6°$ relative to the X wires. The U and X wires provides the z coordinate of the tracks. Additionally, "gate" and "back" wires are installed close to the anode and cathode wires. They regulate the electric field in such a way that the "gate" wires restrict the ionization collection region to improve precision of drift time, and the "back" wires make the sense wires sensitive to drift charges from only one side to reduce left-right ambiguity. The potential wires help maintain the electric field.

The DC uses a gas mixture of 50% Argon and 50% Ethane, allowing for high gain, stable ionization drift velocity and low diffusion coefficient. The single wire efficiency is found to be 96%. It has a single wire position resolution of $\sim 150\ \mu m$, and single wire two track separation better than 1.5 mm.

The DC measures the trajectories of charged particles in the $r - \phi$ plane. The track charge and its transverse momentum can be reconstructed from the trajectory information. The reconstruction uses DC hits to calculate DC coordinates ϕ and α of the track as illustrated in Fig. 2.9. ϕ is the angle between x direction and a vector pointing from the vertex to the point where the particle intersects the DC at a reference radius of $r = 2.20\ cm$. α is the track inclination angle, defined by the angle between the vector and the particle direction at the reference radius. ϕ and α are used to determine the

48

R = 2.02 m

90°

R = 2.46 m

2.5 m

Ti frame

mylar window

Figure 2.7: DC side view

49

4.5 degr.

V2 – planes

U2 – planes

X2 – planes

Termination wires

Back wire

V1 – planes

X

Gate wires

U1 – planes

X

Potential wire

X

sense (anode)
wire

X1 – planes

anode plane

cathode plane

Sector, side view

Wire orientations, top view

~ 1800 mm

U   X   V
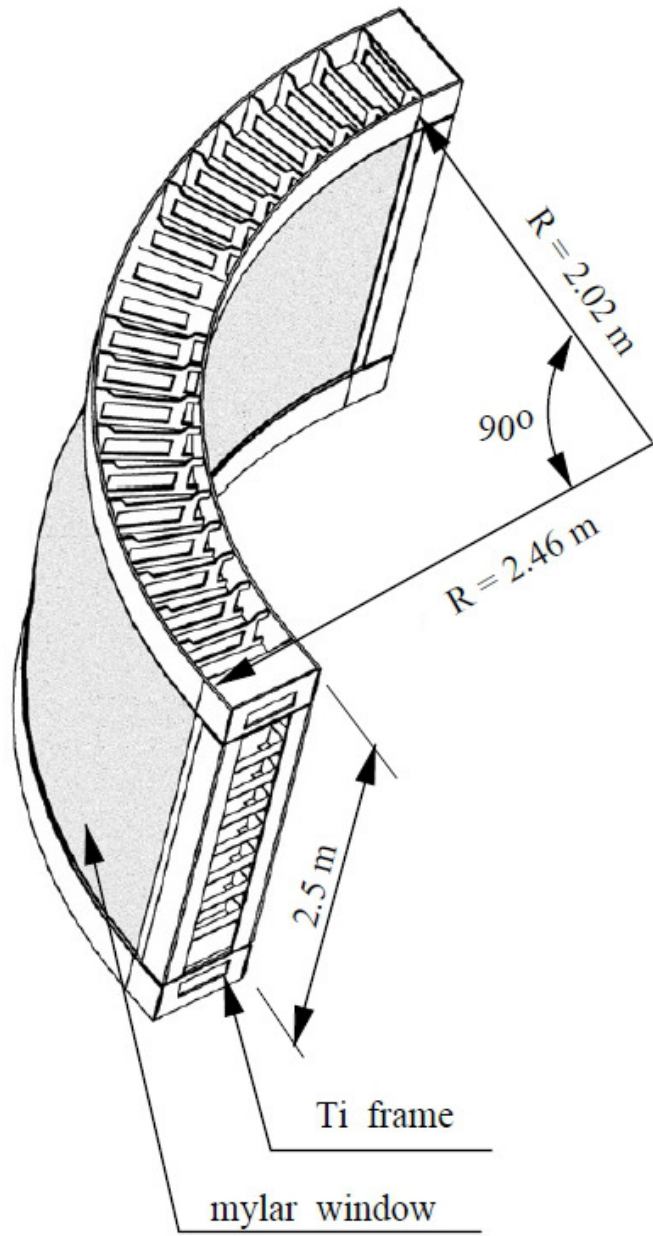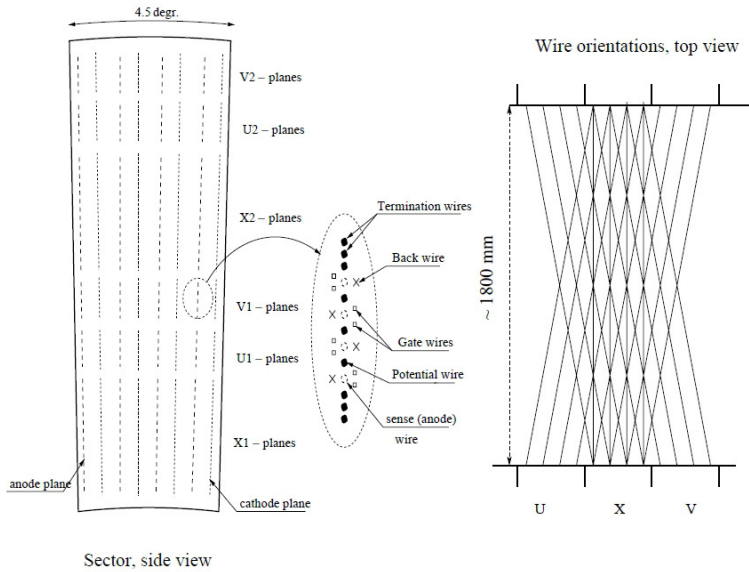
Figure 2.8: DC wire layout

track charge and the transverse momentum.

2.5.2 The Pad Chambers

The Pad Chambers [21] [22] are multiwire proportional chambers. They are installed in three layers (PC1, PC2 and PC3) at three locations in the PHENIX central arms. PC1 is positioned between the Drift Chamber and the Ring Imaging Cherenkov Counter. PC3 is located in front of the Electromagnetic Calorimeter. Both are present in the two PHENIX arms. PC2 is installed only in the west arm behind the RICH.

Fig. 2.10 shows the inner structure of a Pad Chamber. Each Pad Chamber is constructed with a single plane of anode and field wires in the middle of two cathode planes in a gas chamber. One of the cathode planes is made of solid copper while the other is finely segmented into pixels. The readout electronics collect signals from the pixels when a charged particle induces an avalanche on the anode wire. Three pixels are grouped into a cell. A valid signal requires all three pixels in a cell to fire in order to reject false signals.

The PC has a uniquely designed pad and pixel layout to avoid costly electronic channels, as illustrated in Fig. 2.11. Interleaved pixels are linked together nine by nine and connected to a common readout channel. The three
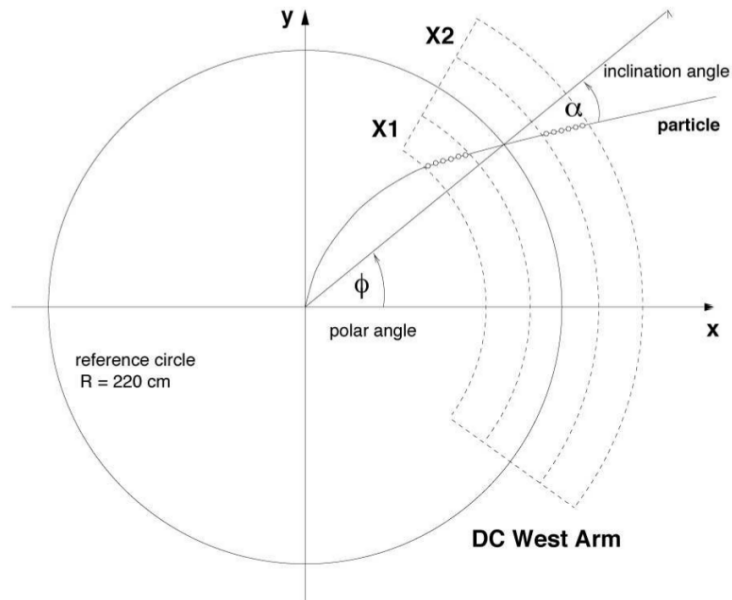
Figure 2.9: Definition of DC ϕ and α for a given track.
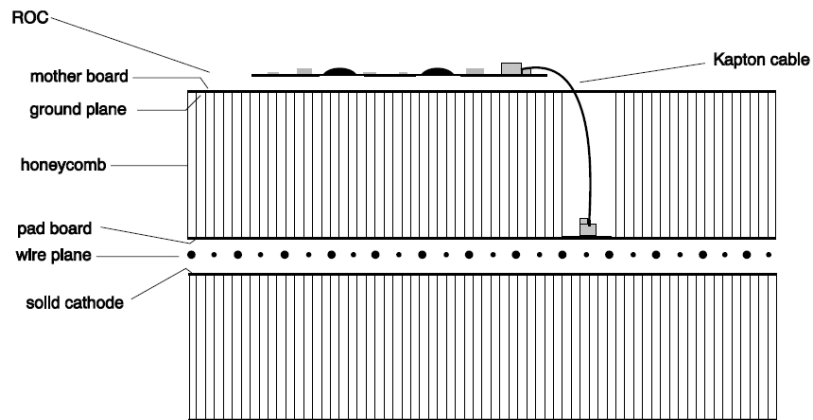
Figure 2.10: Pad Chamber structure
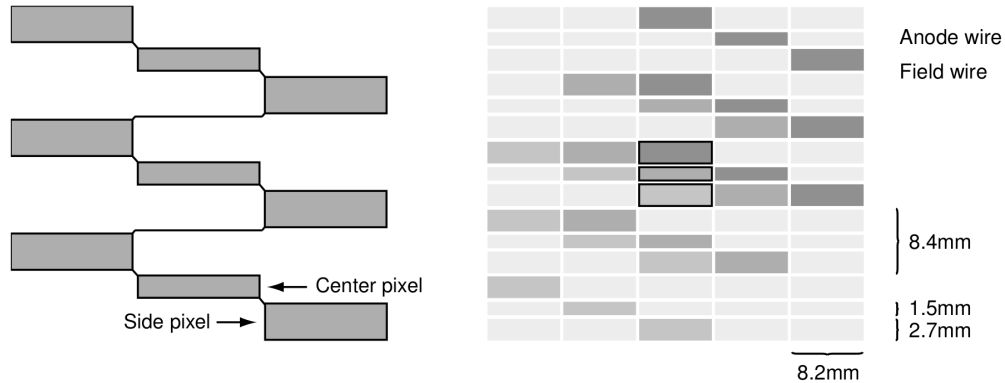
Figure 2.11: Left: the pad and pixel geometry. Right: a cell defined by three pixels is highlighted in the center.

pixels in a cell are always connected to different but neighboring channels so that each cell can be uniquely identified from its channel triplet.

The PC1 determines the z coordinate when a charge particle exits the Drift Chamber, which is essential for reconstructing p_z of the track's three-dimensional momentum. The information is especially useful for electron identification, as it provides the trajectory in the z direction pointing into the RICH. The PC2 and PC3 are useful in resolving ambiguities in the EMCal. About 30% of the particles seen by the EMCal are either secondary particles produced outside the Drift Chamber and PC1 aperture, or low momentum tracks that curve around PC1 in the magnetic field but strikes PC2 or PC3. The PC layers provide three points in a straight line track through the whole detecting system. It ensures that the signals from the electron identification detectors, such as RICH and EMCal, and the momentum measurement from the DC are correctly linked.

2.6 Electron Identification Detectors

2.6.1 RICH

The Ring Imaging Cherenkov Counter [33] is the primary detector for electron identification in PHENIX. It is located behind PC1 in both arms. The detector can obtain e/π discrimination for momenta less than 4 GeV/c

52
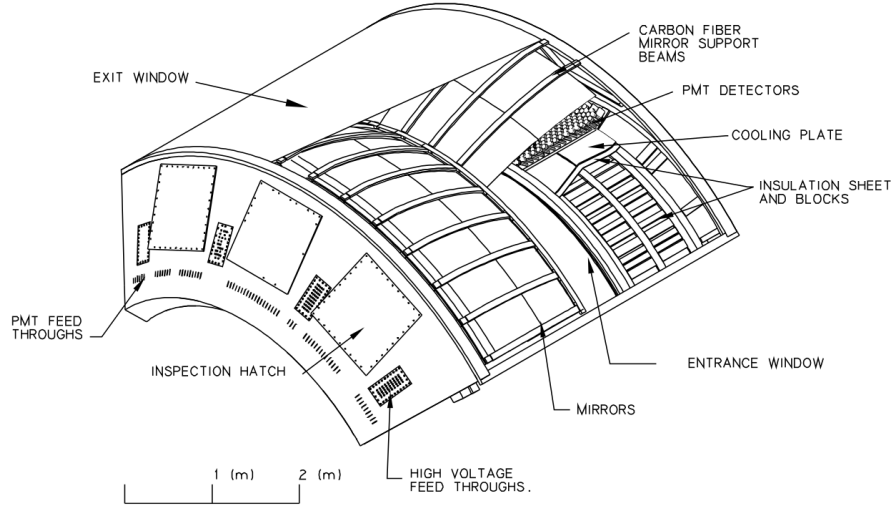
Figure 2.12: layout of the RICH structure

so that no more than 1 per 10^4 hadrons can be misidentified as electrons.

The RICH detects light from electron Cherenkov radiation in CO_2 gas. Each RICH detector has a gas volume of 40 m^3, with an 8.9 m^2 entrance window and a 21.6 m^2 exit window. Fig. 2.12 displays the structure of a RICH detector. There are two intersecting spherical mirror surfaces, pieced together by 48 mirror panels, forming a total reflecting area of 20 m^2. The spherical mirrors focus Cherenkov light onto two arrays of 1280 photomultiplier tubes, with one array on each side of the RICH entrance window.

The radiator gas, CO_2 in the RICH has a refractive index of $n = 1.00045$. It corresponds to a Cherenkov turn-on threshold of 18 MeV/c for electrons, and 4.65 GeV/c for pions. Thus for tracks with $p_T < 4 \, GeV/c$, Cherenkov radiation is dominated by electrons. The spherical mirrors focus the Cherenkov light radiated by a particular track into a ring on the PMT arrays. In such radiator gas, a particle with $\beta = 1$ and path length 1.2 m, typically produces a RICH ring of about 12 photon-electrons, with a ring diameter of 11.8 cm. e/π discrimination is achieved by asking whether a RIHC Cherenkov ring is detected in the vicinity of the track projection onto the RICH detector.
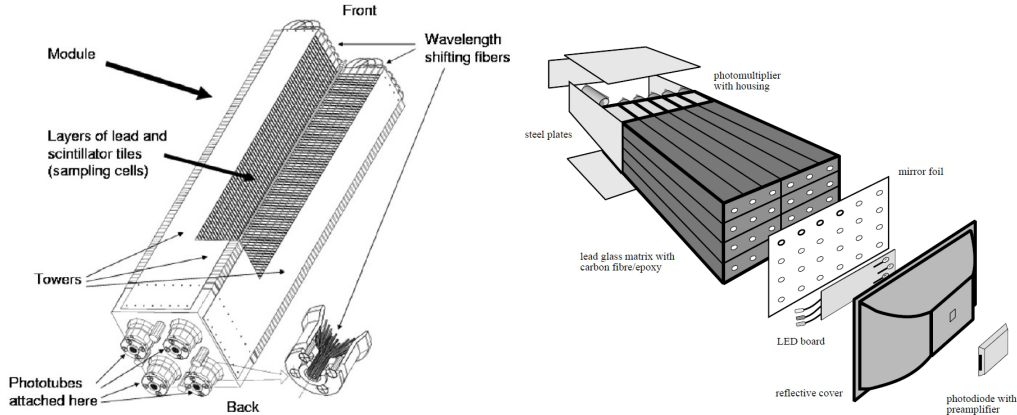
Figure 2.13: Left: view of PbSc structure. Right: view of PbGl structure.

2.6.2 Electromagnetic Calorimeter

The Electromagnetic Calorimeter [36] is used for electron identification, spatial position, energy and time-of-flight measurement. An EMCal wall sitting at the outmost of each Central Arm completes the PHENIX spectrometer in central rapidity. Each wall covers $70° < \theta < 110°$ in rapidity and $90°$ in azimuth. The wall in the West Arm is made of four sectors of Pb-Scintillator (PbSc) sampling calorimeter while the East wall consists of two Pb-Scintillator and two Pb-Glass (PbGl) Cherenkov calorimeter sectors.

The PbSc is a shashlik type sampling calorimeter that covers approximately 48 m^2 in acceptance. It comprises of 15,552 5×5 cm^2 individual towers, each made of 66 sampling cells containing tiles of alternating lead and scintillator. 4 such towers are mechanically grouped into a module, and 36 modules make a supermodule. There are 18 supermodules in each of the 6 PbSc sectors. The cells in each tower are optically connected via 36 longitudinally penetrating wavelength shifting fibers to phototubes for light read-out.

The active depth for an individual tower is 37.5 cm, with a radiation length of $X_0 = 18$. The energy resolution for PbSc is $8.1\%/\sqrt{E} \oplus 2.1\%$ while the timing resolution is approximately 450 ps for electromagnetic showers.

The lower two EMCal sectors on the east arm are PbGl calorimeters, with the PHENIX Time-of-Flight East detector placed in front. A basic PbGl module is 4 $cm \times 4$ cm in cross section and 40 cm in length, and is connected to 84 photomultipliers for read out. The radiation length is
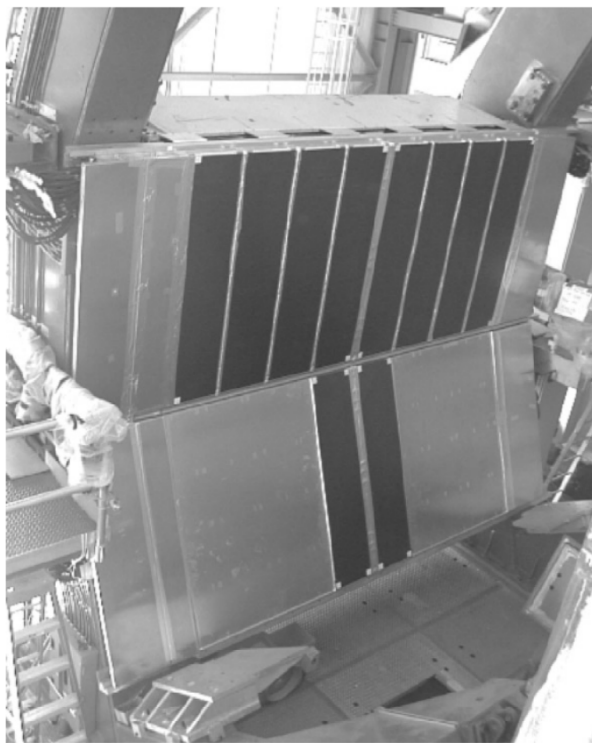
Figure 2.14: The 10 panels of ToF East detector.

$14.4X_0$. A PbGl supermodule is made by a 6×4 module array, physically held together by carbon fiber and epoxy resin. Finally, a sector contains 192 such supermodules arranged in a 16×12 array.

The PbGl has an energy resolution of $5.9\%/\sqrt{E} \oplus 0.8\%$ and a timing resolution of $\sim 700~ps$.

2.6.3   Time of Flight East Detector

The Time-of-Flight East (ToFE) detector [33] is crucial for separating hadron species. However it is also useful in e/π separation. It is mounted 5.1 m from the collision point, in between the PC3 and the PbGl in the East Arm. Its acceptance covers an η range of $70° < \theta < 110°$ and $30°$ in azimuthal direction. It consists of 10 panels of ToF walls, with 96 segments in each ToF wall. Every segment contains a plastic scintillator slat and PMTs which are connected to read-outs at both ends.
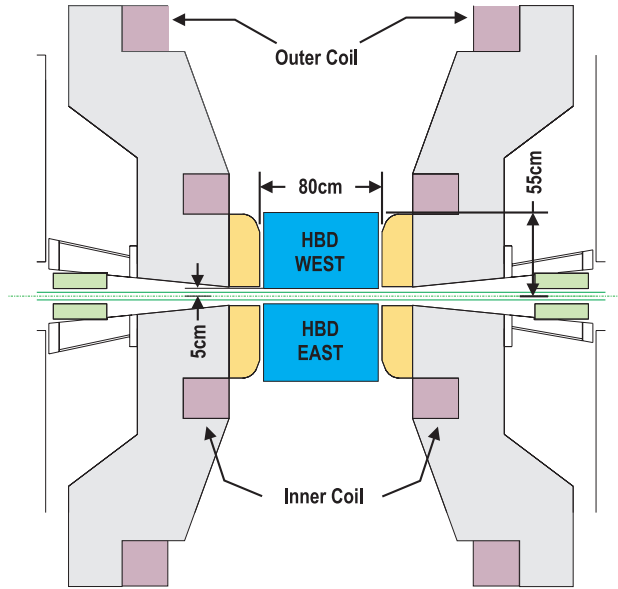
Figure 2.15: HBD location in PHENIX.

Fig. 2.14 shows a photo of the TOF East detector with the 10 panels mounted on PHENIX East Arm. It has a timing resolution of ~ 150 ps.

2.7 Hadron Blind Detector

As mentioned at the end of the first chapter, PHENIX has successfully collected a substantial amount of data of $p + p$ and $Au + Au$ collisions with an HBD upgrade in 2009 and 2010. The Hadron Blind Detector [35] upgrade was introduced to reduce the huge combinatorial background in dielectron spectra measurements.

2.7.1 HBD Design and Construction

A huge combinatorial background arises from random pairing of e^+ and e^- tracks in an event. The majority of these tracks are background electrons from π^0 Dalitz decays and photon conversions. If electrons from these sources can be identified and rejected, the dielectron measurement would benefit from an improved S/B ratio.

For this purpose, a novel detector named the Hadron Blind Detector

56
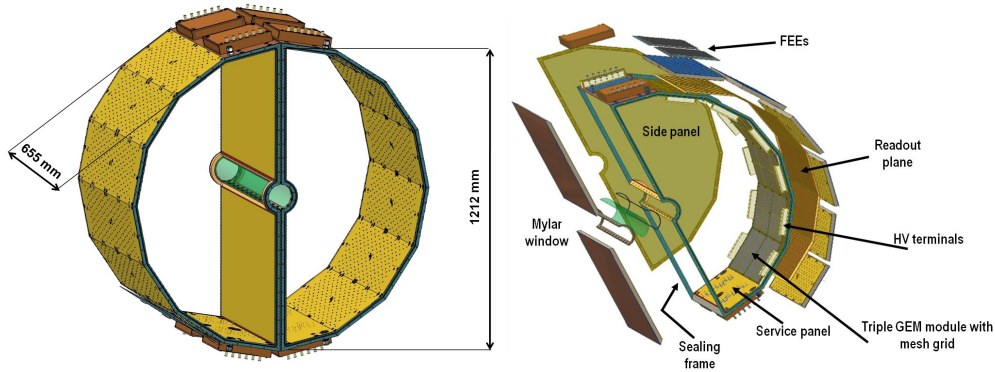
Figure 2.16: HBD schemic view

(HBD) was designed and constructed by PHENIX. It uses the opening angle between electron pairs to recognize electrons from π^0 Dalitz decays and photon conversions, as those electron pairs have very small opening angles, whereas the pairs from vector meson decays, i.e. the signals, have significantly larger pair opening angles.

The HBD must function in a field-free region so that the pair opening angle is not altered by the magnetic field. Fig. 2.15 shows the location of the HBD, together with the inner and outer coils in the PHENIX central magnet. The magnetic field configuration for HBD operation must be the "+-" mode, as shown in the right panel in Fig. 2.3. This setting creates a field free space inside the HBD to preserve the opening angle between electron pairs, and a uniform magnetic field outside HBD up to the drift chamber.

The HBD is a windowless proximity focused Cherenkov detector operating in pure CF_4 gas as radiator, with triple GEM stacks as active modules. It has two identical halves for each PHENIX central arm, named the HBD West and HBD East. Each has a half cylinder shape. Installed together, the detector wraps around the beam pipe to form a cylinder with $\sim 60~cm$ in radius and 65.5 cm along the beam direction. Fig. 2.16 illustrates the HBD structures. The left panel is a 3-D drawing of the HBD shell made of honeycomb, and the right is a break down of its various components. The detector consists of an entrance window situated just outside the beam pipe with a radius of 5 cm, a gas volume filled with CF_4 with a radiator length of 50 cm, triple GEM photon detectors installed in the inner surface of the HBD shell, and read-out pre-amplifiers at the outer shell. "GEM" stands for Gas Electron
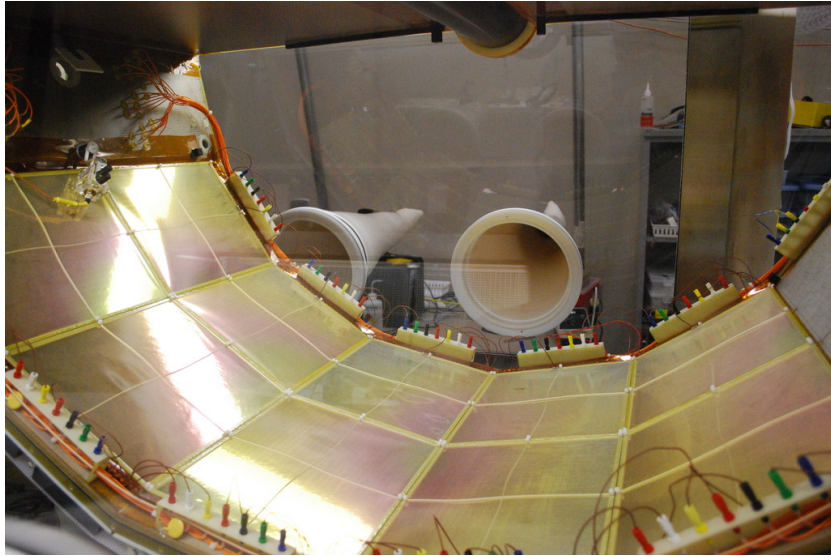
Figure 2.17: Photo of the completed HBD interior.

Multiplier, and three layers of the GEM make a triple GEM stack. There are 12 panels in each HBD side, 6 in ϕ and 2 in z direction. During data taking in Run9 and Run10, 10 panels in each side were installed with triple GEM photon detecting modules. This configuration provides an acceptance of 112.5° in azimuth and ±0.45 units in pseudorapidity, which exceeds the central arm acceptance of 90° in ϕ and ±0.35 in η.

Each GEM module measures 23 cm in width and 27 cm in length. It contains one gold GEM foil in the top, stacked together with two copper GEM foils in the middle and bottom. The GEM foil is made of 50 μm thick kapton foil coated with metal. Arrays of $60 - 80$ μm diameter holes with 140 μm pitch are chemically etched into the GEM foils. A 300 nm thick layer of CsI, which acts as the photocathode, is evaporated onto the gold surface at the top of the GEM stack. As CsI is not chemically stable on top of copper, the gold GEM which is coated with a layer of Ni on top of its copper surface and then a layer of gold on top of Ni, is chemically inert, and is chosen instead of the more common copper GEM to host the CsI photocathode. Finally, a mesh grid is installed above the CsI coated top GEM foil and this completes a photon sensitive triple GEM module. Fig. 2.17 is a photo of the completed HBD interior with 10 triple GEM modules installed. The irredescent color on the GEM surface comes from the CsI film.
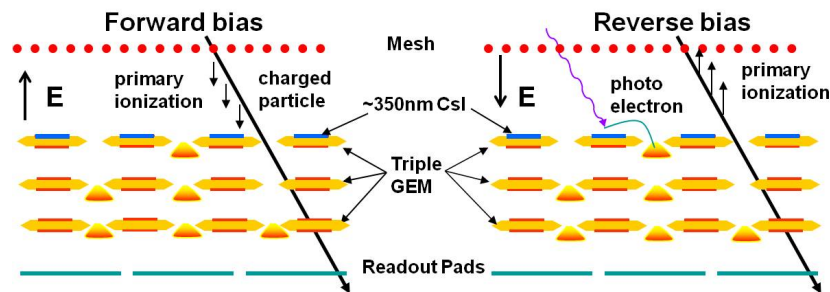
Figure 2.18: Schematic side view of a Triple GEM stack in Forward bias mode and Reverse bias mode.

Beneath the triple GEM stack, the inner surface of the HBD shell is paved with hexagonal read-out pads. The side length of the hexagon is 1.55 cm, corresponding to an area of $\sim 6.2~cm^2$. Beneath a triple GEM module there are 96 pads, which are connected via wires to the readout board in the exterior of the HBD shell. Pre-amplifiers are mounted onto the readout board for signal extraction.

In total, each HBD side weighs less than 10 kg. Taking the total material budget which includes the detector vessel, CF_4 gas, GEM stacks, read-out board and preamplifiers into account, the radiation length for the entire detector comes to 2.40%.

2.7.2   HBD Operating Modes

The HBD detects Cherenkov light emitted from high velocity charged particles transversing the CF_4 radiator. Similar to the RICH, electrons emit Cherenkov radiation inside the HBD while charged hadrons do not under $\sim 4 GeV$. The Cherenkov light shines directly onto the CsI layer on top of the triple GEM stacks in a round blob slightly larger than a readout pad. (The blob size is estimated to be $\sim 9.9~cm^2$). The produced photo electrons are pulled towards the bottom GEM by an electric field. When crossing the GEM foils through the holes, strong electric field inside the GEM induces electron avalanches. After three stages of multiplication at the GEM foils, the signal is collected by the readout pads. During Run9 and Run10, the HBD was operated at a gain of ~ 4000, with the voltage across each GEM foil set at $\Delta V_{GEM} \sim 470~V$.

The HBD can operate in the Forward Bias (FB) mode or the Reverse Bias

(RB) mode, as illustrated by Fig. 2.18. The hadron blindness is activated in the reverse bias mode, where the mesh is set at a lower negative voltage with respect to the top GEM. For the forward bias mode, the mesh has a higher negative voltage. The electric field in the drift region between the mesh and the top GEM, as a result, points to opposite directions for the two modes. When charged particles pass through the CF_4, the electrons from primary ionization in the drift region are pulled towards different destinations. For the forward bias mode, the ionization electrons drift towards the triple GEM. Their signals are amplified and collected by the pads. On the other hand, for the reverse bias mode, the ionization electrons are repelled from the GEMs and are collected by the mesh. Consequently the readout pads are much less susceptible to ionization from charged tracks. When running in reverse bias mode, the HBD sees little trace of the hadron tracks aside from weak scintillation light. Fig. 2.19 compares the HBD responses to PHENIX central arm identified hadrons in Forward Bias (blue) and Reverse Bias (red) modes. The Forward Bias response displays a Landau distribution representing the energy loss of minimum ionization particles. The Reverse Bias response is much lower, as the ionization electrons are absorbed by the mesh.

The reverse bias is the normal HBD operating mode. The relative voltage between the mesh and the top GEM is optimized so that the maximum hadron rejection is achieved while the photoelectron collection efficiency is also maximized. In practice, the relative voltage is selected individually for each GEM module, after running a voltage scan from $+5$ to -20 V, and has a value at typically ~ -10 V.

2.7.3   HBD Signals

The expected number of photoelectrons N_{pe} of the actual HBD is calculated to be $N_{pe} = 20.3 \pm 2.8$. Therefore, for a single electron, the most probable HBD response is ~ 20 photoelectrons, distributed over a small cluster of $2 \sim 3$ pads. For a pair of electrons, when they are close to each other, typically with an opening angle of < 200 $mrad$, their Cherenkov blobs overlap on the triple GEM modules, and induce an HBD response whose number of photoelectrons is expected to be doubled. When a pair of electrons has large enough opening angle, the case is similar to two single electrons. Two separate clusters are found, with 20 p.e. in each cluster.

Fig. 2.20 displays the HBD responses to open (left panel) and close (right panel) electron pairs. PHENIX central arm reconstructed electron/positron
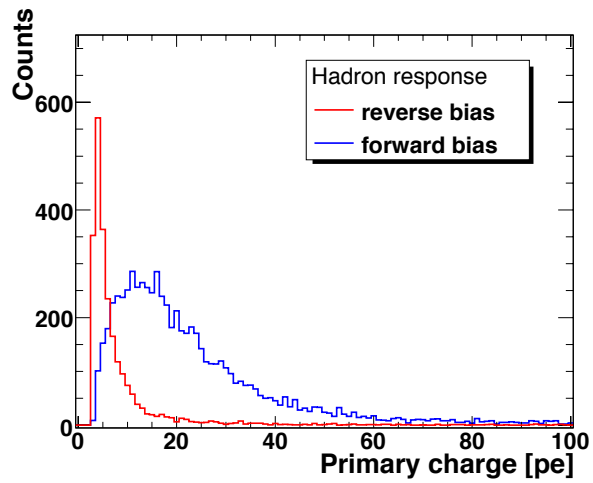
Figure 2.19: HBD responses to charged hadrons in Forward Bias mode and Reverse Bias mode [35].
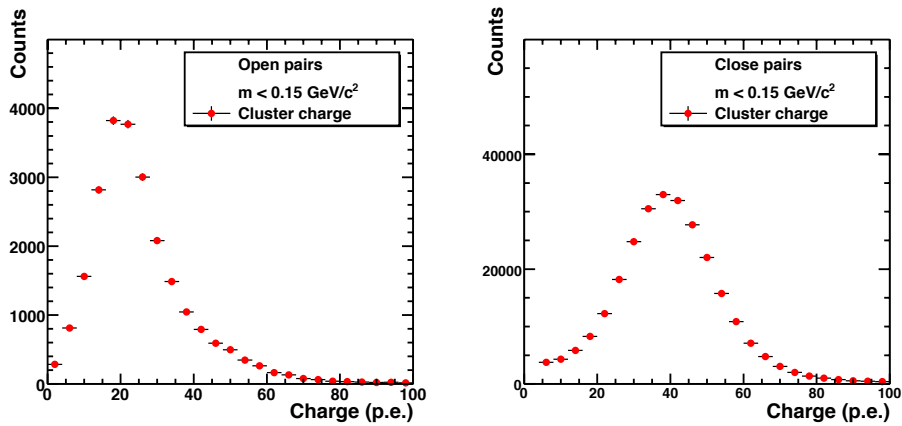
Figure 2.20: HBD single and double response [35].

tracks are matched to HBD clusters within 3σ between the track projections on the HBD and the centers of gravity of the clusters, in both ϕ and z directions. The pairs are required to have $m < 150 \ MeV$, where combinatorial background is small. Open pairs are selected when the electron and positron point to different HBD clusters. On the other hand, when the electron and positron point to the same HBD cluster, the pair is interpreted as a close pair. Fig. 2.20 demonstrates that the HBD has good ability to distinguish open (peaks at $\sim 20 \ p.e.$) and close (peaks at $\sim 40 \ p.e.$) pairs, and this is important in rejecting background for dielectron mass spectrum measurement.

Chapter 3

Analysis

3.1 Analysis Overview

We will describe in detail how the Run10 $Au + Au$ data were analyzed to extract the dielectron invariant mass spectra in the present chapter. As discussed in the first chapter, there exist already a number of dielectron mass spectra measurements with PHENIX for different systems. This newest PHENIX measurement, however, did not simply copy the analysis method of a past measurement. In addition to the use of a HBD, meaningful improvements were made to electron identification and background subtraction. The former raised the electron purity in central events substantially by incorporating the time-of-flight information from the EMCal or ToFE, while the latter demonstrates a deepened understanding of the numerous background sources and an ability to control them to high precision. This lies at the core of this analysis, which suffers from very small signal to background ratio.

The stream of the analysis is as follows:

We first selected good collision events, which were recorded while all detector systems relevant to the analysis were performing in a stable and healthy state. Runs taken with significant detector failures were rejected. Next, electron candidate tracks were selected from the events. Cuts on HBD signals were introduced to reject, a) charged hadrons and late conversion electrons[1], b) electrons likely to come from π^0 Dalitz decays and early conversions[2]. A real challenge of the analysis is to identify the various background

---

[1]Conversions which happen after the GEM modules, are termed late conversions. They mostly take place in the HBD backplane.

[2]Conversions which happen before the GEM modules are early conversions. They come from the beampipe, the HBD entrance window, and the CF_4 gas.

sources, and to reproduce them as accurately as possible both in magnitude and in shape as a function of mass and p_T. Finally, with the background pairs removed, the raw spectra are efficiency corrected to the ideal PHENIX acceptance. Simulations of dielectron mass spectra, using the various meson yields measured by PHENIX as dielectron sources and assuming that all the mesons decay in vacuum, give an expectation of the spectra when the hot medium effects were not present. The simulation, known as the cocktail thanks to its numerous components of dielectron source, is compared to the final corrected spectra. Any discrepancy between the measured spectra and the vacuum expectation, would point to medium modification of the corresponding dielectron source.

In the following sections aspects of the analysis are recounted, starting with the event selection, followed by electron identification, the HBD clusterizer, pair cuts, background normalization strategy and efficiency correction. The systematic uncertainties will be discussed in the last section. The final dielectron invariant mass spectra will be shown in the next chapter, together with comparison to the cocktails and results from a parallel analysis by Yosuke Wanatabe in the Weizmann Institution in Rehovot, Israel [89].

3.2 Event Selection

The analysis uses the PHENIX data taken in Run10 (year 2010) of $Au + Au$ collisions at $\sqrt{s} = 200\ GeV$. The events selected for analysis satisfy the following criteria:

- The event is recorded using a minimum bias trigger.

- It falls into one of the five centrality classes 0-10%, 10-20%, 20-40%, 40-60%, and 60-92%

- The collision position along the beam direction satisfies $|bbcz| < 20.0$ cm

- It is recorded without major detector failures, i.e. no large dead areas in the DC/PC/RICH/EMCal

- The event has no two electron candidates sharing a hit in HBD, PC1, RICH or EMCal. This is a condition required by the pair cuts, which will be treated in more detail in Sec. 3.4.

3.2.1 Trigger choice

Most events in the run10 data are written with the available bandwidth with minimum bias (MB) trigger. When the event rate is too high to record in MB, additional MB trigger sets with scale down of 2 and 3 were added. All three types were valid for the analysis.

3.2.2 Centrality Classes

The analysis is done using 5 centrality classes: 0-10%, 10-20%, 20-40%, 40-60%, and 60-92%. These are the same centrality bins used by the other PHENIX analyses [10, 89] for dielectron spectra in $Au + Au$ collisions at $\sqrt{s}$ = 200 GeV so that it is much easier to make direct comparison with results from those analyses.

Table. 3.1 lists the average number of participants N_{part} and binary collisions N_{coll} in each centrality class, with the associated systematic uncertainties in the parenthesis. The values are obtained from a Glauber model calculation [93] [28].

Centrality	$N_{part}(syst)$	$N_{coll}(syst)$
0-10%	324.0(5.7)	951.1(98.6)
10-20%	231.0(7.3)	590.1(61.1)
20-40%	135.6(7.0)	282.4(28.4)
40-60%	56.0(5.3)	82.6(9.3)
60-92%	12.5(2.6)	12.1(3.1)
0-92%	106.3(5.0)	251.1(26.7)

Table 3.1: The average number of participants N_{part} and binary collisions N_{coll} for each centrality class, with the associated systematic uncertainties in the parenthesis. The numbers are obtained from a Glauber model calculation [93] [28].

3.2.3   Event Vertex Cut

Due to the limited span of the HBD in the z direction, the HBD works best for events whose vertex are within $bbc_z < 20$ cm. Additionally, events occurring outside this ± 20 cm window suffer a significant increase of conversion electrons in the central arm. This can be seen in Fig. 3.1, where the number of identified electron tracks per event is plotted as a function of bbc_z. This increase of background at high $|bbc_z|$ leads to the decision to only analyze events within the window $|bbc_z| < 20.0$ cm.

3.2.4   Quality Assurance

For quality assurance, fiducial acceptance maps of key detectors were visually inspected for each individual run. The inspected detectors included the Drift Chamber, the Pad Chamber, RICH and the EMCal, all of which were used for electron identification.

The traditional approach was to look at the number of electrons per event as a function of run number, and drop the runs that showed significant deviation from the average. The current approach of looking directly into individual detector's active areas offered detailed information on hardware failures. There are a number of runs being rejected for missing significant DC, RICH, EMCal or HBD sectors. Fig. 3.2 gives an example of a typical bad run where the southwest and northwest sectors (upper left and upper right panels in Fig. 3.2) of RICH are dead during the run.

The PC, RICH and EMCal were mostly stable during the entire length
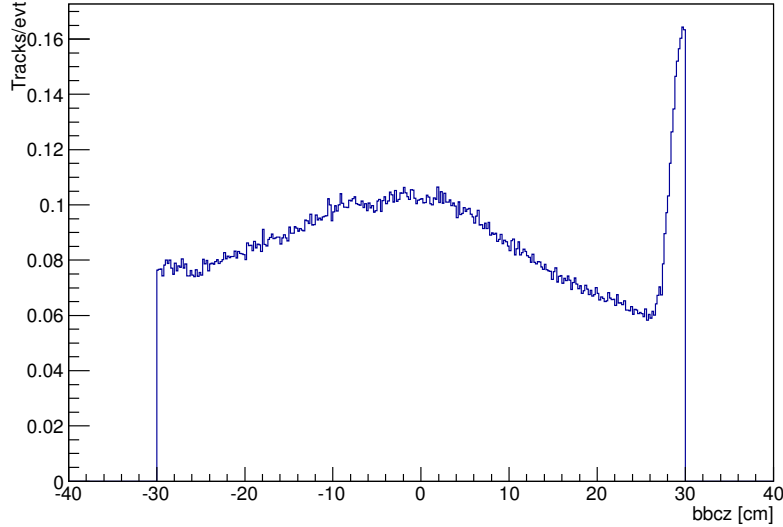
Figure 3.1: Z vertex dependence of electron multiplicity

of the run. The Drift Chamber, however, showed changing dead channels over time. Hence among a total of 880 runs, the ones that passed QA were classified into four run groups based on their DC acceptance. All runs within each run group share an identical DC dead channel map. The DC acceptance for each of the four run groups, plotted as the read-out board number versus α plane, can be seen in the Fig. 3.3. The board number represents the DC module channels and α is the track inclination angle in the DC, as defined in Sec. 2.5.1. Furthermore, a large number of runs whose DC acceptance did not match any of the four run groups, but were close enough that they can be unified by applying fiducial cuts were placed in a separate fifth run group.

Table. 3.2 lists the number of runs, and the total number of events for each run group, together with statistics thrown out because of RICH or other detector failures. Thus, the good events used for data analysis amount to 4.8×10^9.
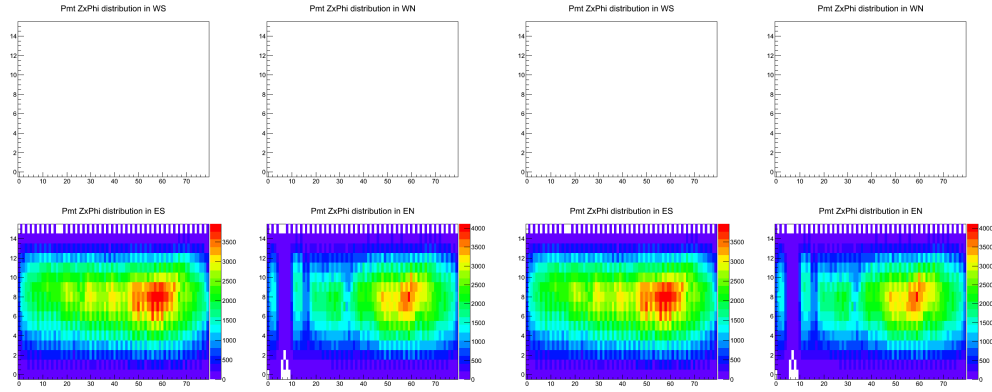
Figure 3.2: A few runs were found with partially dysfunctional RICH. The empty panels denote dead RICH sectors. All such runs were rejected. The list of runs with this condition in the RICH are also listed in the QA appendix.

Run Group	number of runs in run group	Number of events in run group
Run G1	132 runs	512M events
Run G2	221 runs	1.36B events
Run G3	188 runs	1.50B events
Run G4	99 runs	758M events
Run G5	106 runs	681M events
Rich problem	45 runs	336M events
Bad runs	95 runs	437M events

Table 3.2: The number of runs and the number of events distributed in 5 run groups used for the analysis. Additionally statistics from the two problematic run groups - one with a bad RICH sector, the other with miscellaneous problems - are listed. These two run groups are rejected.
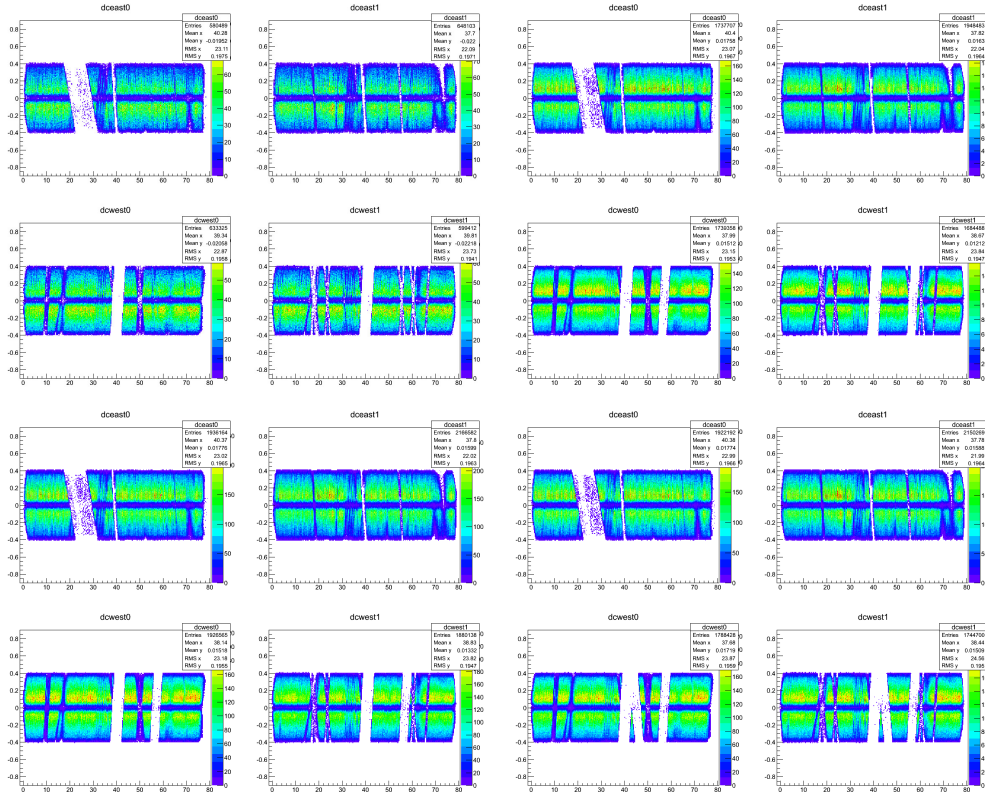
Figure 3.3: From top left to bottom right: DC dead maps in the east north, east south, west north and west south arms in run groups 1, 2, 3 and 4. each plot is a scatter of the α of unidentified charged tracks in CNT files plotted as a function of board number. The board number is in its turn a simple function of the ϕ angle where the track crosses the reference radius in the DC.

3.3 Electron Identification

This section describes the cuts used for electron identification. A series of conventional 1-Dimentional cuts of the central arm detectors are employed for basic electron ID. In addition to the usual set of central arm detector cuts adopted by most PHENIX electron analyses, Time of Flight measured from the EMCal or ToFE has proven to be an effective tool for further cleaning the sample by reducing hadron contamination. This tool is especially effective for low p_T tracks, which constitute a major fraction of the total electron yield.

In addition to the electron identification and HBD cuts, acceptance cuts were also applied to the tracks to mask out inactive detector areas, as well as the edge of the PHENIX acceptance. There are three cuts involved in the acceptance. The first is the PHENIX central arm acceptance, otherwise known as the "Butsyk aperture", which removes the outer edges of the acceptance to avoid edge effects in the individual detectors. More details will be given more details in Sec. 3.6.1. The second is the DC dead maps, which masks the dead areas in the Drift Chamber, as shown in Fig. 3.3, which held responsible for the majority of total dead detector areas in the PHENIX central arms. The third is an HBD dead map, removing one failed GEM module out of a total of 20, covering ∼5% of total acceptance.

Furthermore, the HBD was constructed in order to provide not only additional rejection of charged hadrons, but also identification of electrons from conversions of photons and Dalitz decays of neutral pions. Those electron tracks form a significant contributor to the combinatorial background in the measurement. We will present a cluster searching algorithm developed for HBD signal extraction in a high occupancy environment, as is the case in a most central $Au + Au$ collision. The efficiency and the rejection power of the HBD will be discussed later in the section.

3.3.1 Standard Electron Identification Variables

The standard electron identification cuts rely on the rejection power of the RICH and the EMCal. For the RICH, the cuts take into account the Cherenkov light produced in the RICH close to the track projection, ring position matching and ring shape matching. For the EMCal, matching between the track's momentum and the energy deposited into the EMCal is required. The cuts are as follows:

- $p_T \geqslant$ **0.2 GeV**/c^2 Minimum accepted track p_T is 0.2 GeV/c^2. Lower p_T tracks would curl around in the magnetic field and could not be reconstructed.

- **ecore > 0.15 GeV** Minimum cluster energy deposit into the EMCal associated with track is 0.15 GeV.

- **n0$\geqslant$3** The *n0* is the number of hit PMTs in a ring shaped region around the track projection. The ring region has an inner radius of 3.4 cm and outer radius of 8.4 cm, as a Cherenkov ring from an electron is typically 5.9 cm in radius. The cut $n0 \geqslant 3$ requires that 3 or more PMTs detect Cherenkov light in the Cherenkov ring region.

- **disp<5.5** The *disp* is also a RICH variable, it stands for the displacement between the track projection in RICH and the reconstructed ring center from the hit PMTs. $disp < 5.5$ requires that the associated reconstructed ring center is less than 5.5 cm away from the track projection.

- χ^2/**npe0<20** The χ^2 is a measure of how well the hit PMTs spatial distribution resembles a ring. The *npe0* is the number of photo electrons in the given ring. This cut checks the likelihood that the associated hits indeed exhibit a ring shape, as opposed to random associations with little discernible pattern.

- **npe0 >0** The total number of photo electrons in the associated ring is greater than zero.

- **-2.0 < dep < 2.0** The *dep* is a standardized E/p cut, defined as $\frac{E/p-1}{\sigma_{E/p}}$, where E is the energy measured by the EMCal, p is the three-momentum measured by the drift chamber and the PC1, and $\sigma_{E/p}$ is the width of electron E/p peak. For electrons with $m_e = 0.511 \ MeV$, $E \simeq p$, resulting in a gaussian-like E/p distribution, with a peak locating at 1 where the measured momentum matches with the measured energy. For a charged hadron, a substantial fraction of the energy would escapes the EMCal, leading to a measured energy considerably less than the measured momentum. As a result, the E/p for hadrons is closer to 0 than 1. The dep variable standardized the E/p gaussian-like distribution so that electrons of any p_T form a gaussian distribution centered at $dep = 0$ with a width of 1. The dep for hadrons $\ll 0$.

71

- $\sqrt{\sigma_{\Delta\phi}^2 + \sigma_{\Delta z}^2} < 3.0$ The EMCal matching cut requires the track projection to EMCal to be close to the associated EMCal cluster within 3 units of standard deviations (3σ) in a circle in the ($\Delta\phi_{EMC}, \Delta z_{EMC}$) space.

3.3.2 Time of Flight cuts

The time of flight cut was introduced as a means to further reduce hadron contamination in the sample. The dep cut which requires a match between the track momentum and the energy deposited into the EMCal has less discriminating power at low p_T. For very low momentum hadrons with small energy, showering in the EMCal costs a significant fraction of the total energy, so that the energy deposited in the EMCal is comparable to the momentum. Thus low p_T hadrons are more likely to pass the dep cut than hadrons with higher momentum, causing increased hadron contamination at low p_T. As many tracks in the sample are low p_T tracks, it is necessary to include an additional cut which has more hadron discrimination at lower p_T.

We took the time of flight and the path length from the PHENIX track reconstruction algorithm, with the time measured from the EMCal, or from the TOF East detector when available, and reconstructed m^2, where $m^2 = p^2(\frac{ct}{L} - 1)$. p denotes track momentum, t is the time of flight, L is track path length and c is the speed of light. The hadrons, which were mainly composed of charged pions, showed a peak at $m_\pi^2 = [0.14~GeV/c^2]^2 \sim 0.02$ $[GeV/c^2]^2$, whereas electron tracks were peaked at $m_e^2 \simeq 0.0~[GeV/c^2]^2$, as shown in the following Fig. 3.4 and Fig. 3.5. The TOF East detector, installed in front of the PbGl sectors in EMCal, has much better resolution but covers much smaller acceptance than the PbSc sectors in EMCal. The PbSc time of flight resolution, though not as good, was enough to distinguish electrons and hadrons up to ~ 0.5 GeV/c. The m^2 resolution was best at low p_T, where electron and hadron peaks were distinct. As p_T increased, the widths of the two distributions broadened, until the two peaks finally merged into one. The TOF cut had best hadron rejection at low p_T and offered additional discrimination power in the region where the normal dep cut was less effective.

Fig. 3.4 and Fig. 3.5 show the m^2 distributions of charged tracks after passing all central arm eID cuts and the HBD charge cut, which will be detailed in the next section, from the TOF East and the EMCal, respectively.
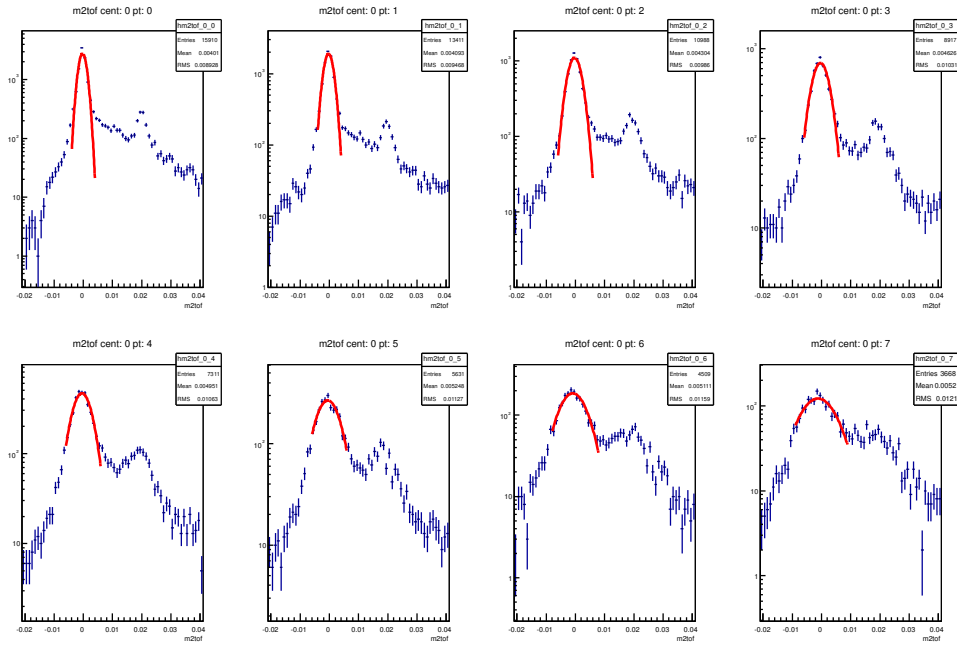
Figure 3.4: TOF East m^2 distributions of charged tracks after passing Central Arm standard eID cuts ahd HBD charge cuts, for events in 0-10% centrality. In 8 p_T slices with a width of $\Delta p_T = 0.05\ GeV/c$. From top left to lower right, the p_T slices are 0.2-0.25, 0.25-0.30, 0.30-0.35, 0.35-0.40, 0.40-0.45, 0.45-0.50, 0.50-0.55, 0.55-0.60 GeV/c.
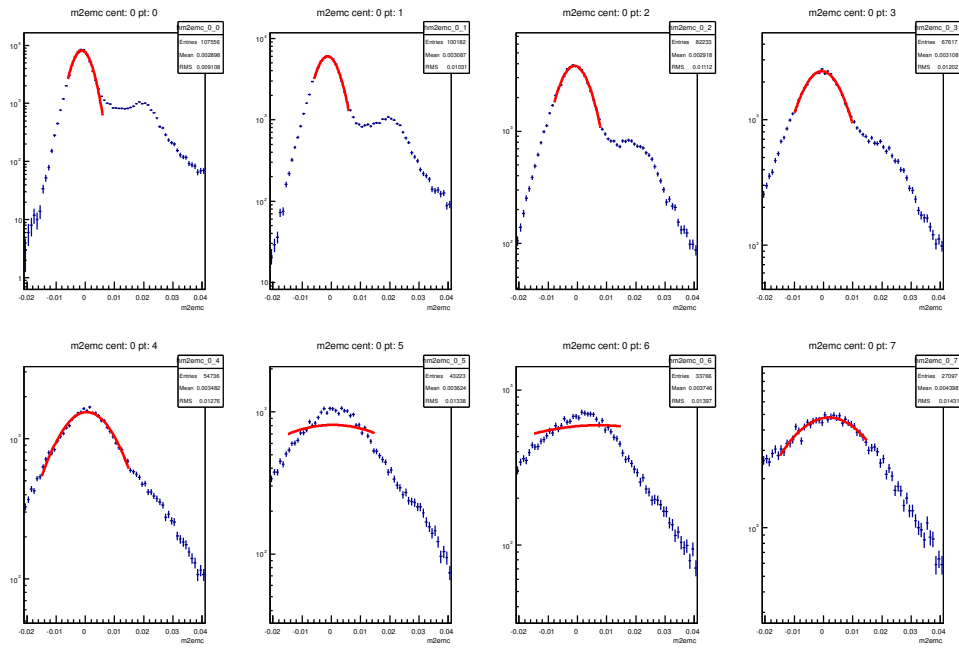
Figure 3.5: EMCal m^2 distributions of charged tracks after passing Central Arm standard eID cuts ahd HBD charge cuts, for events in 0-10% centrality. In 8 p_T slices with a width of $\Delta p_T = 0.05\ GeV/c$. From top left to lower right, the p_T slices are 0.2-0.25, 0.25-0.30, 0.30-0.35, 0.35-0.40, 0.40-0.45, 0.45-0.50, 0.50-0.55, 0.55-0.60 GeV/c.

The distributions are plotted in 8 p_T slices. For each p_T slice, the width σ of the electron peak was obtained by making Gaussian fits at $m^2 = 0$. The fits worked well between 0.2 GeV/c and 0.6 GeV/c for the TOF East (Fig. 3.4), or between 0.2 and 0.45 GeV/c for the EMCal (Fig. 3.5). As the EMCal(Fig.3.5) has poorer timing resolution, the fits collapsed in the last three panels, where track p_T exceeded 0.45 GeV/c causing the electron and pion peak to merge into each other. The p_T dependence of σ was found by fitting σ vs. p_T, as shown in Fig. 3.6 where the red curves represent the fitting results.
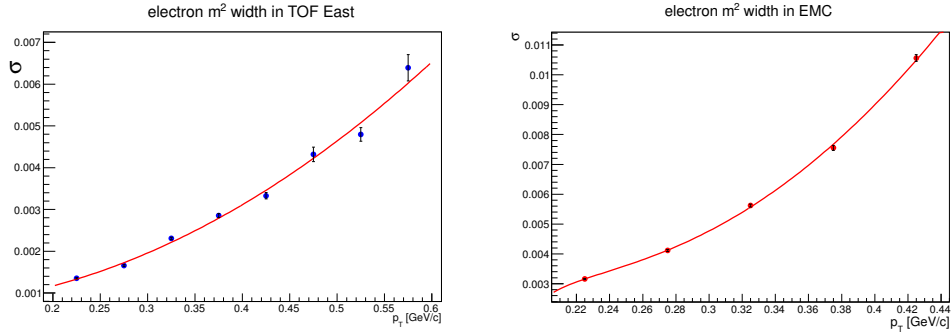
Figure 3.6: Upper panel: σ vs. p_T with TOF East. Lower panel: σ vs. p_T with EMCal.

A p_T dependent upper cut at 1.5 σ away from the electron peak was applied to the tracks. The level of hadron contamination in the sample was studied by the technique of swapping tracks. A swapped track is a fake track created by swapping a real track to the opposite arm by artificially changing the track projection in RICH from (x, y, z) to (-x, y, z), so that the RICH response at the swapped projection is merely that of background noise. In this sense, a swapped track was similar to a charged hadron, which did not induce RICH signals, and in principle both should be rejected by RICH cuts. Once in a while, however, a swapped track (or a charged hadron) can accidentally align parallel to a real electron in RICH and becomes falsely associated with the real one's Cherenkov light, as such is misidentified as an electron. Applying eID cuts to a set of real tracks and their swapped partners, a first order estimation on the level of misidentified hadrons in the track sample can be deduced from comparing the numbers of surviving tracks in both cases.
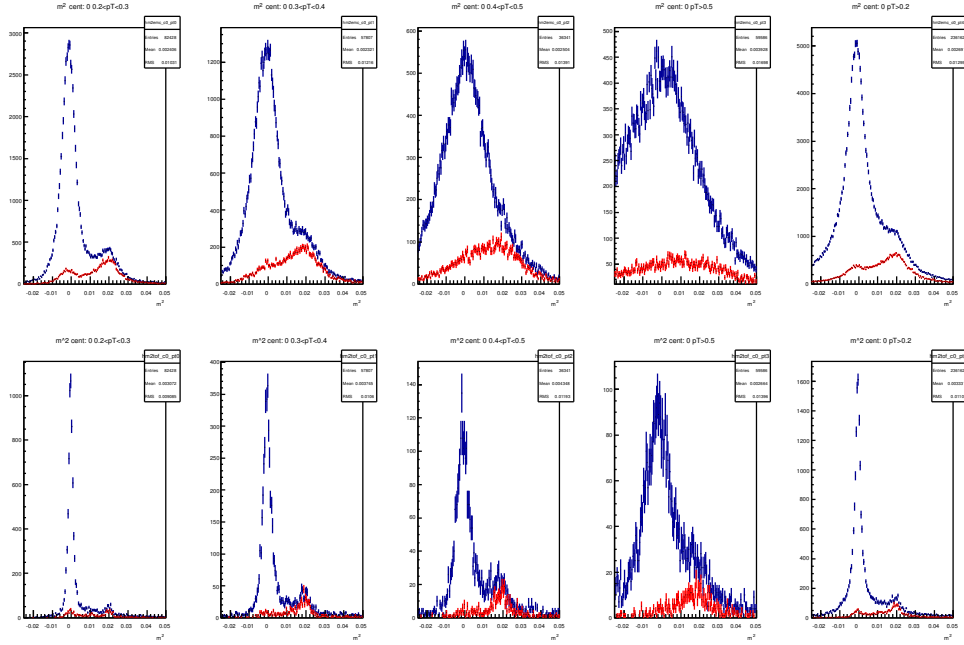
Figure 3.7: Centrality $0 - 10\%$. Upper panel: m^2 distribution for all tracks(blue) and swapped tracks(red). All central arm eID cuts and HBD cuts are applied. The upper five panels show m^2 from EMCal, and the lower five panels are m^2 from TOF East. From left to right, the p_T selections are: $0.2 < p_T < 0.3 \ GeV/c$, $0.3 < p_T < 0.4 \ GeV/c$, $0.4 < p_T < 0.5 \ GeV/c$, $p_T > 0.5 \ GeV/c$ and $p_T > 0.2 \ GeV/c$.

Fig. 3.7 illustrates the m^2 distribution for all real tracks and swapped tracks that have passed central arm eID cuts and HBD cuts. The 5 panels represent 5 p_T selections: $0.2 < p_T < 0.3$ GeV/c, $0.3 < p_T < 0.4$ GeV/c, $0.4 < p_T < 0.5$ GeV/c, $p_T > 0.5$ GeV/c and $p_T > 0.2$ GeV/c. The upper panels are for EMCal m^2 and the lower panels are TOF East m^2. The red swapped distributions indicate the hadron contamination contained in the blue (real) distributions.
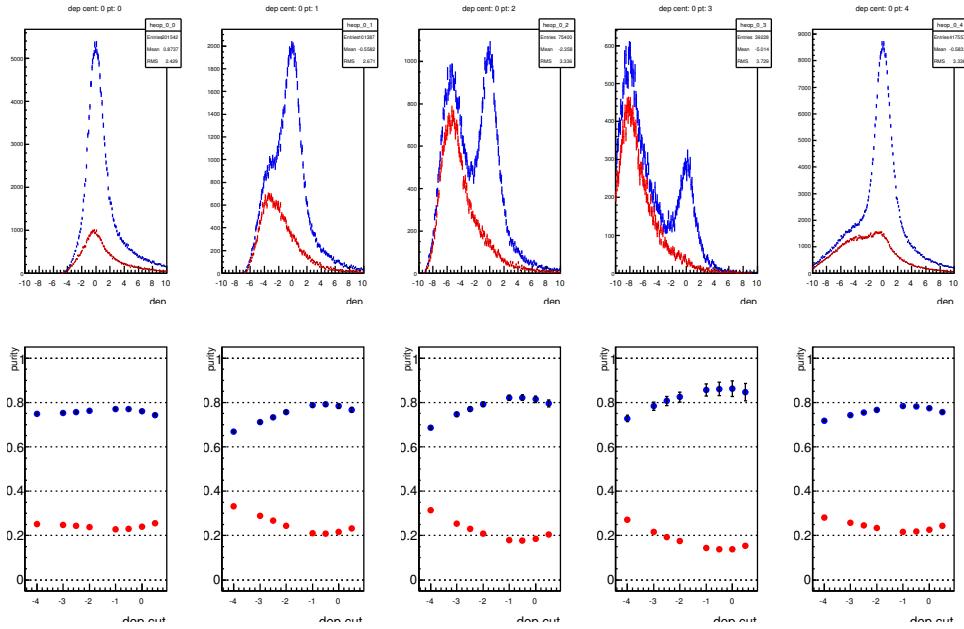
Figure 3.8: Centrality bin $0 - 10\%$. Upper panels: the dep distribution for all tracks(blue) and swapped tracks(red) after passing all central arm eID cuts plus HBD cuts, except dep cut. No TOF cut is applied to the tracks. 5 panels are made for 5 p_T selections. From left to right: $0.2 < p_T < 0.4$ GeV/c, $0.4 < p_T < 0.6$ GeV/c, $0.6 < p_T < 1.0$ GeV/c, $p_T > 1.0$ GeV/c and $p_T > 0.2$ GeV/c. The lower panels show the electron purity(blue) and hadron contamination(red) vs. lower dep cut value, with an upper dep cut fixed at 2.0. The horizontal axis shows the lower dep cut value. The analysis uses $-2.0 < dep < 2.0$.

In Figure. 3.8, the upper panels show the dep distribution in $0 - 10\%$ centrality bin for all tracks(blue) and swapped tracks(red) after passing all central arm eID cuts and HBD cuts, except dep cut. No TOF cut is applied

77

Centrality	purity without TOF cut	purity with TOF cut
0-10%	76.5%	86.2%
10-20%	84.5%	91.8%
20-40%	91.7%	96.2%
40-60%	97.2%	98.8%
60-92%	99.3%	99.5%

Table 3.3: Table of electron purity in five centrality bins. All other eID cuts are already applied to the tracks. The left column lists the electron purity when TOF cut was not applied, while the right column shows the improved purity after appling TOF cut.

to the tracks. 5 panels are made for 5 p_T selections, which are from left to right: $0.2 < p_T < 0.4\ GeV/c$, $0.4 < p_T < 0.6\ GeV/c$, $0.6 < p_T < 1.0\ GeV/c$, $p_T > 1.0\ GeV/c$ and $p_T > 0.2\ GeV/c$. The lower panels show the electron purity (blue) and hadron contamination (red) vs. the lower dep cut value at the corresponding p_T selection, when the upper dep cut is fixed at 2.0. The electron purity is calculated directly from the plot above. In the analysis, the *dep* cut is chosen at $-2.0 < dep < 2.0$. Thus the electron purity in the analysis for $0 - 10\%$ is shown at approximately $\sim 78\%$ before the TOF cut. Fig. 3.9 shows the same set of plots, but now with TOF cut applied. It can be seen that the hadron contamination is improved for all p_T slices, particularly for the lower p_T tracks. Now the electron purity in the analysis is increased to $\sim 88\%$.

Table. 3.3 lists the electron purity in five centrality bins. The left column lists the purity with all electron ID cuts and HBD charge cut applied, except for the TOF cut. The right column shows the purity obtained when TOF cut is applied in addition to all other track cuts. The single track efficiency loss from the one-sided 1.5σ cut is $\sim 6.7\%$, yet the purity increased from 76.5% to 86.2% for the most central bin. In fact, the TOF cut brought an improvement in electron purity seen in all centralities (Table. 3.3), with the biggest benefit in the most central events.
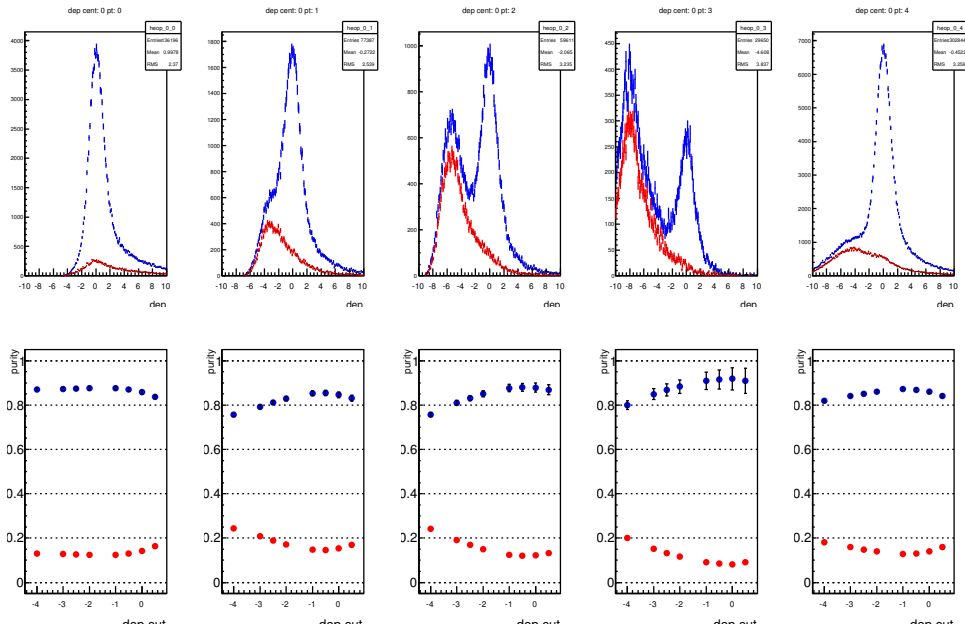
Figure 3.9: Centrality bin $0-10\%$. Upper panels: the dep distribution for all tracks(blue) and swapped tracks(red) after passing all central arm eID cuts + HBD cuts + TOF cut, except dep cut. 5 panels are made for 5 $p_T$selections. From left to right: $0.2 < p_T < 0.4\ GeV/c$, $0.4 < p_T < 0.6\ GeV/c$, $0.6 < p_T < 1.0\ GeV/c$, $p_T > 1.0\ GeV/c$ and $p_T > 0.2\ GeV/c$. The lower panels show the electron purity(blue) and hadron contamination(red) vs. lower dep cut value, with an upper dep cut fixed at 2.0. The horizontal axis shows the lower dep cut value. The analysis uses $-2.0 < dep < 2.0$

79

3.3.3 HBD cuts

HBD Local Background Subtraction Clusterizer

The HBD as a novel detector, requires a specifically designed algorithm to look for the Cherenkov light blobs deposited onto the HBD GEM stacks by electrons. The algorithm searches for clusters of photoelectrons from the read out hexagonal pads in the HBD backplane. The area of a typical light blob from an electron is slightly larger than one readout pad, so that a compact triple, i.e. three pads close to each other, is the basic cluster searching unit in the algorithm. In $Au + Au$ collisions, especially in the central events, the HBD was operating in a high multiplicity environment. Even though the scintillation light from charged hadrons typically induces only a small response in the HBD, the scintillation becomes a significant background when the multiplicity is high. In a most central event, most of a HBD GEM stack was lit up by the scintillation and the background level could reach as high as 10 p.e. per pad [41]. Therefore, the question of how to distinguish authentic clusters from the scintillation background becomes important for central $Au + Au$ collisions.

The algorithm used in this analysis is called the Local Background Subtraction. The name is descriptive of the how the algorithm operates: subtracting an estimate of the background based on the *typical* illumination in the neighborhood. The word typical will be quantified shortly.

The main assumption of the LBS algorithm is that the scintillation background that underlies events varies continuously over the HBD fiducial surface. As such, the best place to look for an estimate of the scintillation background affecting any specific area is in its immediate neighborhood. A weak demonstration of this assumption is the existence of a correlation between the area (a) normalized charge (q) measured by the first neighbors and second neighbors of all possible triplets. Fig. 3.10 shows a scatter plot of q/a of first neighbors of all possible triplets accumulated over several events. The correlation is apparent and from here on the working assumption is that the background in the central compact triplet (charge=qt, area=at) can be estimated from the average signal measured in the surrounding first neighbors (charge=qfn, area=afn) and second neighbors (charge=qsn, area=asn). The background in the central compact triplet can then be estimated as

$$bkg = at \times \left(wfn \times \frac{qfn}{afn} + wsn \times \frac{qsn}{asn} \right) \tag{3.1}$$

where wfn and wsn are weights for the first and second neighbors that should add up to 1. A weight of 0.5 for both gives equal weight to the estimation of the background using those two groups. This background is local to the triplet under consideration, and averaged over $9 + 15 = 24$ independent samples from the surrounding pads which reduces the error due to the statistical fluctuation.

An implicit simplification used in the above discussion is that there is no second electron falling into the neighboring pads so that the first and second neighbors read solely background scintillation. In reality, chances are that a nearby electron deposits its Cherenkov light into the neighboring pads, and causes an overestimation of the local background. This would lead to a pair of nearby electrons canceling out the net charge of each other. Therefore, the pads that are pointed to by any candidate electron need to be excluded from the local background estimation beforehand to avoid this undesirable effect. This is done as a preparation step for every event before running the actual algorithm.
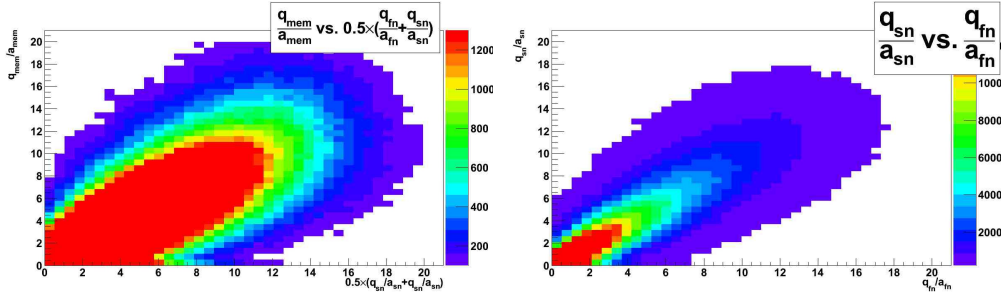
Figure 3.10: Left: Correlation between the average charge density measured in the localized three pad area (q_{mem}/a_{mem}, where q_{mem} is charge in the triplet and a_{mem} is the triplet area) vs the charge density measured in the first and second neighbors (q_{fn}/a_{fn} and q_{sn}/a_{sn} are the charge density for the first and the second neighbors respectively). Right: Correlation between the average charge density measured in first neighbors vs average charge density in second neighbors.

The actual algorithm used proceeds in three steps. First, the pedestal is subtracted from the actual charge measured in all triplets to calculate the net signal of the triplet. Then triplets are culled by any desired condition on topology (here just a condition on the net charge is used). The remaining compact triplets will be used as pre-clusters to build actual clusters with.

Once a selection of good compact triplets is done from set of all possible compact triplets, any merging algorithm can be run to combine all overlapping compact triplets. Below is a little bit more detail on each one of these steps of cluster reconstruction in the HBD.

- Step 0: In preparation for cluster searching, all pads pointed to by electron candidate tracks are ruled out from background estimation. In each event, any track that is associated with a hit in the RICH ring ($n0 \geq 0$) is picked out, the three closest pads to its projection on the HBD are tagged and excluded from use during background estimation for the event.

- Step 1: The first step is forming all possible *compact* triplets of pads. By compact, we mean where each member hexagonal pad of the triplet shares one side with each of the two other members of the triplet, as depicted on the left side of Fig. 3.11. For each event the total charge [3] inside the triplet area (q_t) as well as the median charge per pad in the first (q_{fn}) and second neighbors (q_{sn}) around the triplet area are evaluated for all triplets inside the HBD. The first and second neighbors of a triplet are depicted in Fig. 3.11. The 'net' charge of the triplet is evaluated as

$$q_{net} = q_t - A_t \times \frac{q_{fn} + q_{sn}}{2} \tag{3.2}$$

- Step 2: Filtering of triplets based on the distribution of charge. Triplets unlikely to be coming from Cherenkov light must be rejected. For this the charge calculated in step 1 is used to remove all triplets where the net charge (as defined by equation 3.2) doesn't fall within a window (between 0 and 60 pe). The reason for this choice is that the mean charge expected from a single electron is of the order of about 20 pe and that from a double hit is about 40 pe. Including fluctuations, this window can safely catch any triplet that received a charge from Cherenkov

---

[3]When calculating the charge of triplets, we exclude the use of pads that have uncharacteristically large charges. It was shown that excessively high charged pads are the result of electronic noise. The cutoff on the single pad charge was placed at 100 p.e. after calibration. The effect of this cutoff on the acceptance can be quantified as a function of cutoff value for different centralities. As shown in Fig. 3.11 right, the acceptance loss for a cap of 60 p.e. which is used in this analysis is less than a percent.
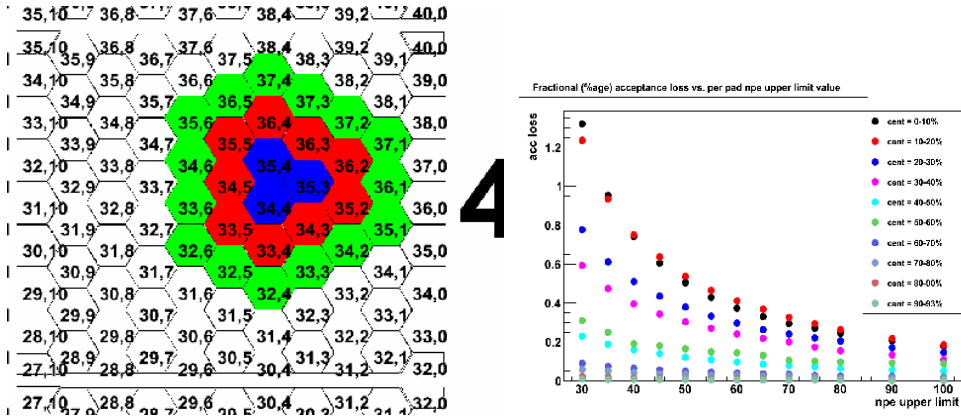
Figure 3.11: Left: Definition of triplet, first neighbor and second neighbor in the HBD pad plane. Right: Fraction of active area of HBD lost on average due to an upper limit cut on the charge measured by a pad.

light in the absence of any scintillation background. However in central events where we have significant background fluctuations from scintillation, the subtraction can result in throwing away some triplets due to over-subtraction. But this is the price to pay for a more controlled charge measurement that doesn't depend on centrality.

- Step 3 Remaining triplets after filtering are merged based on track projection. The identified electron tracks are projected onto the HBD surface to find triplets whose center of gravity is within a settable radius [4] (called the merging radius below). All triplets with a center of gravity within the merging radius of the track projection are combined to form a cluster for that track. Once a cluster is thus formed, the neighbor finding algorithm is called on the merged cluster again (which this time has an arbitrary shape because it's a superposition of a non predefined number of triplets). The net charge of the cluster is calculated as with the triplets by subtracting from the full charge on the merged cluster a background charge estimate calculated as the median of the the first and second neighbors charge per pad, and correcting by the area of the cluster as in

---

[4]This condition is a shape cut because triplets where the largest amount of charge was deposited in the pad pointed to by the track projection are favored over triplets where the charge distribution moves the center of gravity away from the track projection.

$$q_r = q_{totclust} - A_{clust} \times \frac{<q_{fn}> + <q_{sn}>}{2} \qquad (3.3)$$

where $Q_{totclust}$ is the total charge measured in the cluster area, and A_{clust} is the number of pads in the cluster. $<q_f>$ and $<q_s>$ are the median charge per pad in the first and second neighbors. Notice that the net charge has an index, that from here on will be used to denote the size of the merging radius. $Q_{1\ cm}^{HBD}$ would for example be used to denote the charge of the cluster associated with the track when using a merging radius of 1 cm.

Detector Efficiency and Rejection

The outcome of the HBD cluster reconstruction for any electron candidate track can be classified into three categories.

- No associated HBD cluster or cluster with very low net charge (often < 5 *p.e.*). The HBD response to the track is consistent with mere background scintillation with little evidence of Cherenkov light. In such a case, the electron candidate track could be, a) a misidentified hadron which leaves no Cherenkov light in the HBD; b) a secondary electron created by a photon conversion, which occurred behind the HBD GEM stacks - most often at the HBD backplane where readout pre-amplifiers are installed, these are referred to as late conversion electrons; c) a true single electron, whose Cherenkov signal is overwhelmed by upward fluctuation of high scintillation background, in a high multiplicity, most central collision event. Cases a) and b) are background tracks to be rejected. Case c) causes efficiency loss in the most central events.

- Single electron cluster. These clusters have net charge around 20 *p.e.*, as expected from the Cherenkov light deposit in the HBD from a single electron track. These single electrons are from a variety of sources, such as open Dalitz decays of light mesons, semi-leptonic decays of open heavy flavors, and charmonium decays. They are signal electrons to be kept.

- Double electron cluster. The net charge is around 40 *p.e.*, as these are from overlapping Cherenkov light of two electrons flying together. The sources of the double electron clusters are, a) photon conversions

84

taking place in front of the HBD GEM modules where the magnetic field is absent, often at the beam pipe, the HBD entrance window, or in the CF_4 gas, these electrons are referred to as early conversion electrons; b) closed Dalitz decay of light mesons, mostly the π^0. Both should be rejected, though for slightly different reasons. The former are simply secondary tracks, while the latter are background to the final dielectron spectra. Both considerably deteriorate the S/B ratio of the measurement.

The HBD cluster charge distribution of electron candidate tracks in peripheral events is shown in Fig. 3.12. The sharp peak close to 0 p.e. is the background scintillation response. The tracks associated with these clusters are mostly HBD backplane conversion electrons and misidentified hadrons which do not deposit Cherenkov light inside the HBD. A small, broader peak is visible at ~ 20 $p.e.$. It corresponds to the single electron clusters. At around 40 p.e., distributions of single electron clusters and double electron clusters are merged and there is little distinct peak of double electron clusters. For a first look, we roughly decompose the cluster distribution using 2 Gaussian distributions between 5 and 50 p.e., as shown in Fig. 3.12. Thus we obtain a single electron distribution centered at 17.7 ± 2.4 $p.e.$ and a double peak at 36.6 ± 1.1 $p.e.$, which are reasonably within expectations.

A more careful study of the HBD responses to single and double electrons as computed by the LBS cluster algorithm is presented in Fig. 3.13. In order to get a clean sample of single and double signals, Run9 $p + p$ data is used, as it has proven difficult to completely remove conversion electrons in the Run10 $Au + Au$ data which has higher multiplicity without including HBD cut. The single electrons are selected from open Dalitz pairs, by requiring electron pair mass $m_{ee} < 150$ MeV and pair opening angle > 300 $mrad$. The double electrons are selected from closed Dalitz pairs, with the requirements that the pair mass $m_{ee} < 150$ MeV and pair opening angle < 20 $mrad$. The single electrons exhibit a peak at 19.1 ± 0.5 $p.e.$, and the double electron signal peaks at 34.3 ± 0.1 $p.e.$.

The HBD performance is highly dependent on the event occupancy of the detector. As mentioned previously, the background scintillation light increases when the collisions become more central. In a high occupancy, most central event, the background scintillation can reach as high as 10 p.e. per pad. Once in a while true Cherenkov signals get drowned in an upward fluctuation of local scintillation light, leading to efficiency loss. On the other
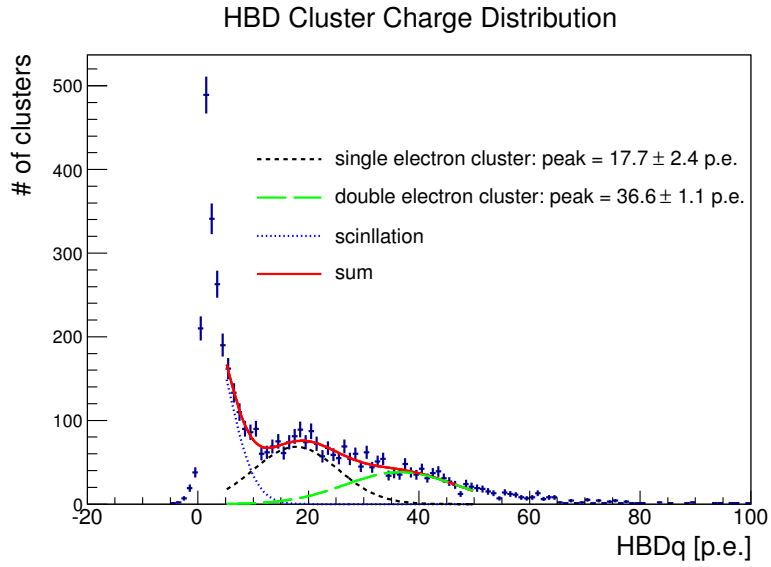
Figure 3.12: HBD cluster charge distribution of electron candidate tracks in peripheral events (centrality 60-92%).
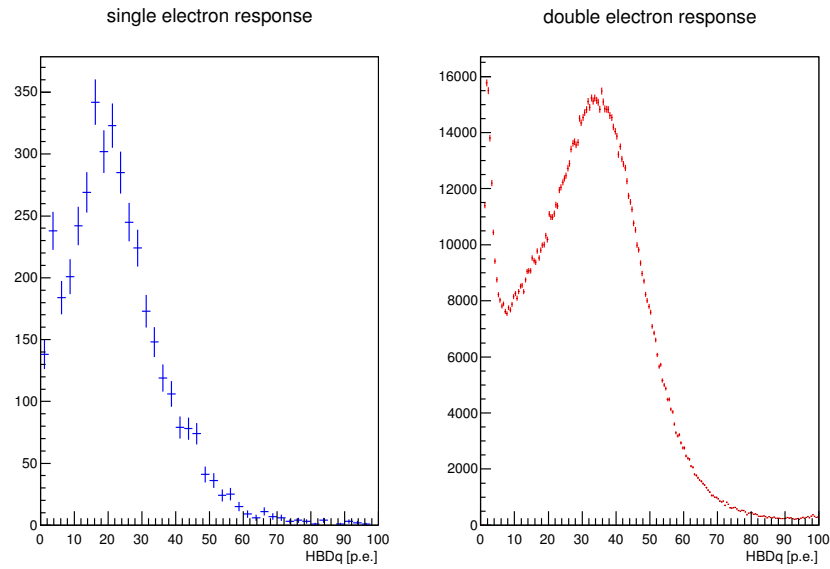
Figure 3.13: HBD single electron response(left) and double electron response(right), plotted using run9 $p + p$ data.

hand, conversions at the HBD back-plane, which produce no signal inside the HBD, can be occasionally associated with fake clusters resulting from background fluctuations. This weakens the rejection power for back-plane conversions.

For this reason an HBD-only embedding was implemented and integrated into the efficiency calculation chain, to allow the calculation of efficiency as a function of centrality. In the embedding, the simulated HBD responses to Monte Carlo electron tracks are embedded into real HBD data of a chosen centrality, to replicate the case of electron Cherenkov blobs falling amid centrality dependent scintillation light. Then the clusters are reconstructed by running the LBS algorithm on the embedded HBD data. The HBD efficiency calculated this way implicitly contains the HBD centrality-dependent efficiency.

The single track HBD efficiency as a function of centrality and merging radius is shown in Fig. 3.14. It is calculated for full HBD acceptance and avoiding areas at the edge of HBD acceptance. The single track efficiency (blue) is shown as a function of merging radius in 10% centrality bins. The centrality increases from top left panel to the bottom right. The efficiency curves saturate when the merging radius reaches $\sim 1.5~cm$. The saturated efficiency decreases when the collisions become central, as the signals grow more likely to be overwhelmed by scintillation. In addition to the efficiency, the embedding simulation was used to calculate the rejection factor for HBD back-plane conversions, which are a major source of the combinatorial background. Due to fake cluster formation, the misidentification rate for such back-plane conversion electrons (which otherwise shouldn't produce any signal in the HBD) increases with centrality.

A cluster merging radius, which is in essence, a cluster matching cut, was chosen to be 1.5 cm. The cluster charge was set to a lower threshold at 10 p.e. to reject hadrons and early conversion electrons, and an upper threshold of 40 p.e. to reject closed electron pairs that produce overlap clusters.
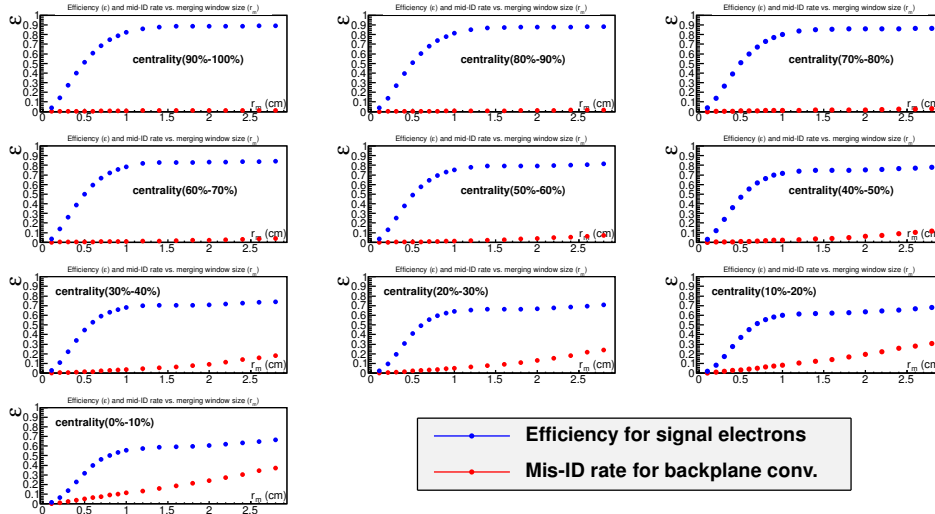
Figure 3.14: single electron efficiency (blue) and back-plane conversion electron misidentification (red) rate.

3.4 Pair Cuts

It is briefly mentioned in Sec. 3.2 that one of the event selection criteria is passing the pair cuts, or the proximity cuts. By name, the cuts check the distance of a pair of tracks, and if the pair is found to be too close in space, the entire event is thrown out.

There are two major reasons for adopting proximity cuts in the analysis. The first one is to eliminate background contamination (mostly charged hadrons) caused by specific detector configurations. The second reason has to do with the event mixing technique, which is used for background subtraction and will be described in the upcoming section.

In the RICH, Cherenkov light emitted from electrons is reflected by the RICH mirrors and is focused into a ring of light on arrays of photo multipliers. The position on the PMT arrays is solely determined by the entrance angle of the track, rather than the track's spatial coordinates. When, by mere chance, a charged hadron flying parallel to an electron enters the RICH - the likelihood is not negligible and it increases with event multiplicity - the Cherenkov ring radiated by the electron will also be associated with the charged hadron, as RICH is sensitive only to angles. As a result, the charged hadron is indistinguishable from a true electron, and is misidentified as such.

The effect is particularly unwelcome for most central events, as the possibility of finding parallel electron and hadron pairs is highest there thanks to the high multiplicity. Thus, a RICH proximity cut, which prevent pairs from getting too close to each other in RICH projections, is necessary to keep high electron purity in the sample.

As in many other pair analyses, we use the technique of event mixing to estimate background. The event mixing, of which there is a detailed account in the next section, constructs electron pairs exclusively from two different events, with the aim to replicate the shape of the combinatorial background. This approach requires the exactly same cuts to be applied for both the mixed events (BG) and the real events (FG), in order to insure that the mixed events could precisely reproduce the combinatorial shape in the foreground. However, when two tracks happen to be close enough to each other in any individual detector surface, a discrepancy will appear betwwen the FG and the BG. For the FG pairs, i.e. actual close pairs in a detector in a real event, the signals they produce in the detector will physically interfere with each other, whereas this is not the case for the artificial close pairs in the BG. Thus, close pairs in any detector should be removed from both FG and BG to avoid this discrepancy.

In general, overlap in the spatial dimension at certain detector elements in reality results in very localized pairs in pair mass vs. p_T space, as those pairs fit very specific spatial requirements.

There are a few ways in which a proximity cut can be implemented. After consideration of signal to background, the best method to handle them was found to be throwing out whole events in case any pair of tracks passing the identification cuts is found to overlap in any one of the detectors RICH, EMCal, DC/PC and HBD. The check on the presence of overlapping pairs is done after the single electron identification cuts and the HBD cut have already been applied. For both real events and mixed events, all possible pairings within the event are required to pass the proximity cuts.

The cut values are determined by plotting a "poor man's" efficiency [5] corrected yield in the region of the mass axis where the cuts remove pairs, and

---

[5]The efficiency is estimated roughly as the fraction of pairs lost in the unlike sign mixed event background when this cut is applied as compared to when it is not applied. In order to make sure that we're seeing only the efficiency loss due to this proximity cut and not others, event-wise rejections are not applied to mixed events, and the proximity cut is applied only as a pair cut. In actual analysis, all proximity cuts are applied as event-wise cuts.

plotting this yield as a function of cut values. Such proximity cuts typically decrease the yield, take it below the saturation value and then raise back up to the nominal pair yield value when the separation between two tracks required by the cuts is big enough. The reason that the corrected yield dips before it comes back up and plateaus is because at some separation typically of the size of a cluster in a given detector, hits from two such neighboring electrons interfere destructively (by distorting shape of cluster) and result in a reduced yield as compared to when they are closer and their clusters are mostly adding up without shape distortion.

As an example, Fig. 3.15 left shows the pair cut efficiency corrected yield in the mass region around 200 MeV (where pairs affected by EMCal proximity cut sit, as shown in the right of Fig. 3.15) as a function of the EMCal proximity cut ($\Delta_{EMC} = \sqrt{(\Delta y)^2 + (\Delta z)^2}$, where y and z are the indices of the central tower of the cluster associated with the electrons). The yield goes down, and raises back up until it plateaus around a cut of Δ_{EMCal} of 2.5. The cut value of 2.5 is chosen this way, in order to insure that signals in each leg of any actual electron pair that pass the cuts do not interfere. In other words a separation of at least 2.5 towers is required between the central towers of two electron clusters. Similar studies were made for the RICH and PC1, and the final proximity cuts in the three detectors were set to:
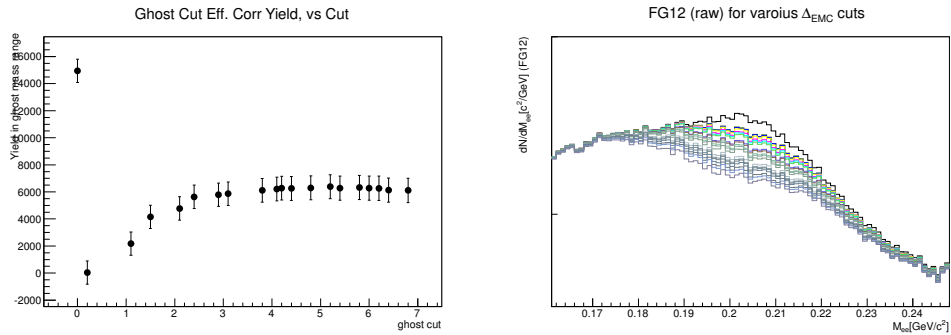
Figure 3.15: Left: The poor man's efficiency corrected yield as a function of Δ_{emc} cut, the EMCal proximity cut. Right: The uncorrected signals for all the Δ_{emc} cuts used in this study. One sees clearly that the effect of EMCal proximity cut is very localized at $190 < M_{ee} < 220\ MeV/c^2$.

- RICH: $\sqrt{\frac{\Delta cross_\phi}{0.01\ rad}^2 + \frac{\Delta cross_z}{3.6\ cm}^2} > 10.0$, where $\Delta cross_\phi$ is the separation in the ϕ direction between two track projections on the RICH photomulti-

90

plier plane, and $\Delta cross_z$ is the same separation in the z direction. The ϕ direction is "sigmalized" to 0.01 radian and the z direction difference is "sigmalized" to 3.6 cm.

- EMCal $\Delta_{EMC} = \sqrt{(\Delta y)^2 + (\Delta z)^2} > 2.5$: As described in previous paragraph

- DC/PC $\sqrt{\frac{\Delta pc1_{phi}}{0.02\ rad}^2 + \frac{\Delta pc1_z}{5\ cm}^2} > 1.0$

- HBD pair opening angle $> 0.1\ rad$

The pair cuts at RICH, EMCal and DC/PC are standard pair proximity cuts adopted regularly in PHENIX pair analyses. The cut at the HBD, is introduced specifically to Run10 data because of the detector's presence in the run. Its inclusion has a similar reason to the RICH proximity cut, and is used to prevent a charged hadron or a back-plane conversion electron from accidentally pointing to an authentic HBD cluster produced by a close-by signal electron, and thereby being misidentified as a true signal. Without the cut, a localized enhancement was seen in both unlike and like sign foreground in the very low mass region, which cannot be reproduced by the mixed background, indicating extra pair yields arising from false electron candidates.

3.5   Background Subtraction

Before going into details of the method, we will first introduce some conventions.

In the following, common PHENIX convention will be used in referring to Foreground pairs (FG) as the set of all possible pairs of electrons *within* a physical event. Physical event is meant as opposed to mixed events. There are three categories depending on the charge (++, +- or −). Like sign pairs of positrons in the foreground will be referred to as FG11 whereas like sign of electrons will referred to as FG22. Unlike sign electron-positron pairs in the foreground will be denoted FG12.

Mixed event background will be used to refer to the combinatorial background estimation obtained by combining tracks from multiple events into one fictitious event, and generating pairs with tracks from two different events. Such pairs are denoted BG11, BG22 and BG12 following the same convention as for FG pairs.

3.5.1   Strategy Overview

Background Components

We deal with a number of sources of background in the present analysis. Every source of background is estimated to the best of our knowledge, and then is subtracted individually. The uncertainty in the estimation we attempt to propagate into the systematic uncertainty of the final spectra.

The background sources can be classified into two categories, the uncorrelated and the correlated. As such, the two categories invite two different treatments. As we make all possible pairings from all electron candidates within an event, it is unavoidable that two candidates, with no relation between them whatsoever, are paired together. This forms the the biggest background source of all,the combinatorial background, which arises from random pairing of unrelated electrons and positrons, and it falls into the first category. The second category contains several different sources. Generally speaking, those pairs are kinematically correlated, some through a common physical origin, such as electrons or positrons produced in the same di-jet system or by decay from a common ancestor meson, and some through the PHENIX spectrometer configuration, such as the electron-hadron pairs. They are often seen as localized distributions in the pair invariant mass spec-

tra.

Below is a list of electron pair sources (not necessarily background) treated in the analysis.

- combinatorial background (*uncorrelated background*)

- cross pairs (*correlated background*)

- jet pairs (*correlated background*)

- e-h pairs (*correlated background*)

- b-$\bar{b}$ pairs (*correlated component of like sign foreground*)

Background Subtraction Strategy

Thus, the total yield of unlike sign pairs can be decomposed as the following,

$$FG12 = Sig12 + CB12 + CP12 + JP12 + EH12 \qquad (3.4)$$

where symbols $Sig12$, $CB12$, $CP12$, $JP12$ and $EH12$ stand for unlike sign signals, combinatorial background, cross pairs, jet pairs and e-h pairs, respectively. Likewise, the yield of like sign pairs can also be decomposed in much the same way. Given the knowledge that real signal pairs only populate the unlike sign space, the like sign yield is written as,

$$FG1122 = CB1122 + CP1122 + JP1122 + EH1122 + BB1122 \qquad (3.5)$$

where 1122 denotes the sum of 11 (positron-positron) and 22 (electron-electron) pairs, and BB represents correlated pairs decayed from heavy quark $b - \bar{b}$ pairs. Note that heavy flavor $c - \bar{c}$ decays do not contribute to like sign yield. In the unlike sign space, both charm and bottom decay products are part of the signal, and we do not list them separately.

We infer from Eq. 3.5 that when all the like sign background sources are correctly reproduced and subtracted, the residue yield must come to zero at all invariant mass within statistical uncertainty, as there is no signal in the like sign. Thus the like sign spectra can be utilized as a yardstick, by which to judge the accuracy of the background estimation, and therefore the

credibility of the final spectra. A blind analysis procedure is devised accordingly, that the unlike sign spectra is to be kept intentionally unknown until background normalization for the various background sources is fixed using the like-sign spectra only, at that point, we unveil the unlike sign spectra and apply component-by-component background subtraction. Considering the difficulty of extracting tiny signals from an overwhelming background, the blind procedure ensures the subtraction to be free of bias arising from expectation of the final result.

Background Subtraction Procedures

The background sources are treated component by component. For the uncorrelated, i.e. the combinatorial background, we adopt the event mixing technique which generates artificial pairs with no relation whatsoever. The mixed pairs, however, must be corrected to replicate elliptic flow modulation in real life. For the correlated, Monte Carlo simulations are used to generate each individual source, to which absolute normalization is initially applied.

After the mass distribution of every single background source is reproduced by the calculation, we fit them to the like sign spectra to obtain the normalizations that describes the spectra best. Once the like sign spectra are described to a satisfactory degree, we then introduce a κ factor which is key to translate the background subtraction from the like sign space to the unlike sign.

Spectra of raw signal are obtained after the background is subtracted. It then needs to be efficiency corrected to represent the dielectron pair yields in the ideal PHENIX acceptance, which will be the topic of the next section.

Hence the discussion in the section will follow step-by-step in the ordering below,

- Combinatorail background with flow modulation

- Cross pairs

- Jet pairs

- e-h pairs

- b-$\bar{b}$ pairs

- Normalization in the like-sign space

94

- Normalization in the unlike-sign space

- Raw spectra

3.5.2 Combinatorial Background and Event Mixing

We make all possible pairings from the electrons and positrons detected in an event. Among those pairs, there are real pairs from the same parent, correlated pairs that do not share parents but share common ancestors, and dominantly, unrelated pairs that are arbitrarily paired, and do not carry any physics information at all. The last category is the combinatorial background. By its very nature, the level of the combinatoric rises approximately with event multiplicity squared. In the most central events, the combinatorial background reaches such a height that the S/B ratio dips below 1:1000 at certain mass regions. A plot of S/B as a function of pair mass for all five centrality classes (Fig. 3.53) will be shown later in Sec. 3.5.9. It is of utmost importance for this analysis to replicate the combinatorial background to high precision, both in multiplicity and in spectral shape. It is the most critical background component of all.

Event Mixing

The combinatorial background is dealt with by the technique of event mixing. We resort to a standard PHENIX event mixing machinery, nicknamed CabanaBoy, to handle the issue. Within the CabanaBoy framework, a list of electrons that has passed single electron identification cuts (cf. Sec. 3.3) was taken to construct the foreground first, then proceeded to create mixed event background. Pair cuts were checked for every pair in each event, both real and mixed. If a pair failed the cut, the entire event was rejected.

Mixed events were made by picking random electrons from different events. The number of electrons in such an event was controlled by the real electron multiplicity distribution in a given centrality. Within a mixed event, every track was picked from a different event in order to ensure that no pair could have any sort of correlation. When an mixed event failed one of the pair cuts, another was constructed to take its place.

During the event mixing, events were grouped into pools that share similar properties, such as centrality, BBC measured z vertex (bbcz), and event plane orientation measured by RXNP. Mixing could only take place within

one such pool. This is to ensure that only events with close enough topology are mixed, so that pairs that are impossible in real events (FG) will not be produced in the event mixing procedure. We used 20 equal pools between -20 cm and +20 cm in bbcz range, and 20 pools in centrality from 0% to 100%. However we did not divide the reaction plane direction into multiple pools, and the reason will be discussed later in the section on the elliptic flow modulations.

The number of events in each pool is termed pool depth. If the depth of a given pool is shallow, i.e. small number of events are contained in the pool, there would be relatively limited choices of tracks in forming a mixed event. When the choices are exhausted, no new mixed event satisfying the pair requirements could be made. This may lead to the undesirable effect of the natural fractions of like and unlike sign pairs being disturbed. The "2 square root relation", shorthanded as "2sqrt relation" and whose details can be found in Sec. 3.5.8, mandates the balance in quantity between the unlike and like sign pairs, and is important in background subtraction in the unlike sign. In order for the 2sqrt relation to hold true, a deep pool depth is required. Thus, after some study, the pool depth is set to 5000 for mixing.

Elliptic Flow Modulation of the Combinatorial Background

Even though the combinatorial background is composed of pairs made from random track pairing, simply being within the same event means the tracks still share some sort of intrinsic correlation. Importantly, the elliptic flow, which rearranges the angular distribution of all tracks within an event, has an overall influence on the shape of the combinatorial background. It, for example, introduces a depletion at 90 degrees in pair opening angle, and enhancement around 0 and 180 degrees. This slight modification in pair opening angle distribution is reflected in the distortion of the pair m vs. p_T spectral shape.

A mixed event, however, combines electrons from different events with different reaction plane orientations, and is oblivious to any effect from the flow. An adjustment for flow must be introduced, to account for the elliptic flow's modulation of the combinatorial background to get the correct combinatorial shape.

Pooling in reaction plane ideally could be able to reproduce the flow effect in the mixed events, as mixing would only happen with events of very close reaction plane orientations. If events with random reaction plane orienta-
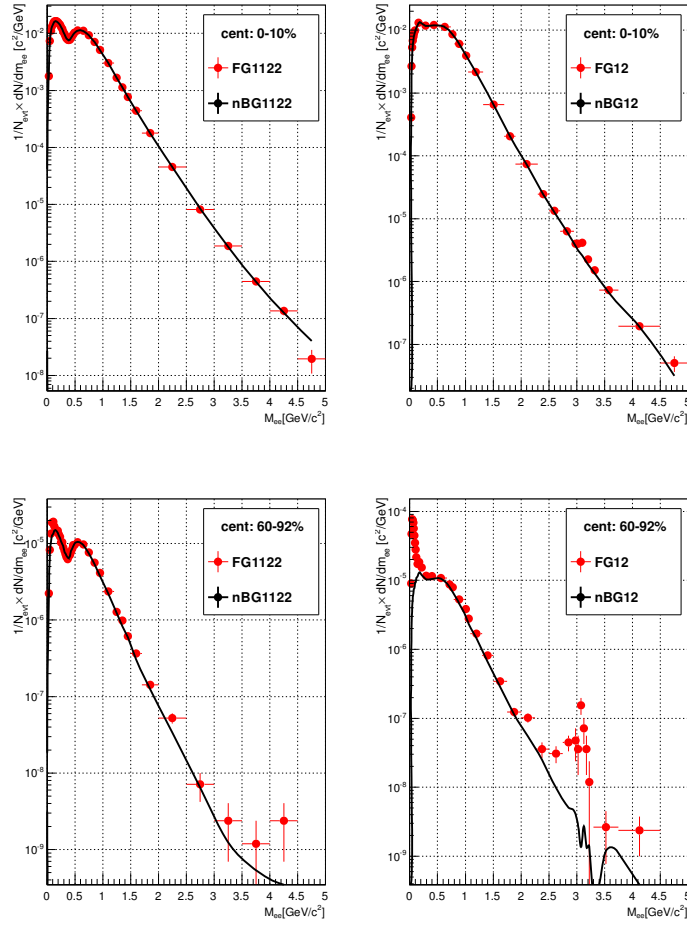
Figure 3.16: Foreground pairs (red) and mixed background pairs (black) in the like and unlike sign for centrality bin 0-10% and 60-92%.

tions are mixed, flow is washed out in consequence. However, due to finite resolution from the reaction plane detector, pooling in reaction plane could not be made fine enough , and it fails to emulate the full flow effect as some of the modulation is washed out. Thus another method was introduced to solve this problem.

A weighting factor was applied for each mixed pair. The weight was written as

$$weight = 1 + 2v_{2,1}(cent, p_{T,1})v_{2,2}(cent, p_{T,2})cos(2\Delta\phi) \qquad (3.6)$$

where $v_{2,1}(cent, p_{T,1})$ and $v_{2,2}(cent, p_{T,2})$ are the elliptic flow v_2 of electron 1 and 2, whose values vary as a function of centrality and p_T, and $\Delta\phi$ is the azimuthal angle between the two electrons. Mathematically, this weighting factor fully corrects the elliptic flow's modulation on the background shape. A derivation can be found in Ref. [89].

We measured the inclusive electron v_2 with the set of single electron identification cuts as detailed in Sec. 3.3. The v_2 was measured as a function of electron p_T, in 10% centrality bins when centrality is more peripheral than 10%. For the most central events with centrality less than 10%, v_2 was measured in 2% centrality bins. As the combinatorial background is most significant in the 0-10% bin, it is preferable to describe the combinatoric to the best achievable precision. The 2% centrality bins gave a more realistic v_2 dependence on centrality in the most central events, rather than simply using the v_2 value averaged over the entire 0-10% bin.

Fig. 3.17 compares the inclusive electron v_2 we measured from Run10 data (in black and white) to published inclusive electron v_2 of Run7 measurement [12] (in blue). The upper two panels are v_2 from $0-10\%$ and $10-20\%$ bins, respectively. The lower left panel shows Run7 v_2 in $20-40\%$ bin compared to Run10 values in $20-30\%$ and $30-40\%$. The lower right panel presents Run7 in $40-60\%$ and Run10 in $40-50\%$ and $50-60\%$. The Run10 and Run7 results of inclusive electron v_2 exhibit nice agreement.

Then, for each measured centrality, the v_2 vs. p_T plots were fitted with a smooth function eq. 3.7 which approached a finite limit at positive infinite.

$$v_2 = Aatan(a_0 p_T) + a_1(p_T^2 + a_2 p_T)e^{-a_3 p_T}; \qquad (3.7)$$

Given a centrality and track p_T, electron v_2 can be obtained from the above function.
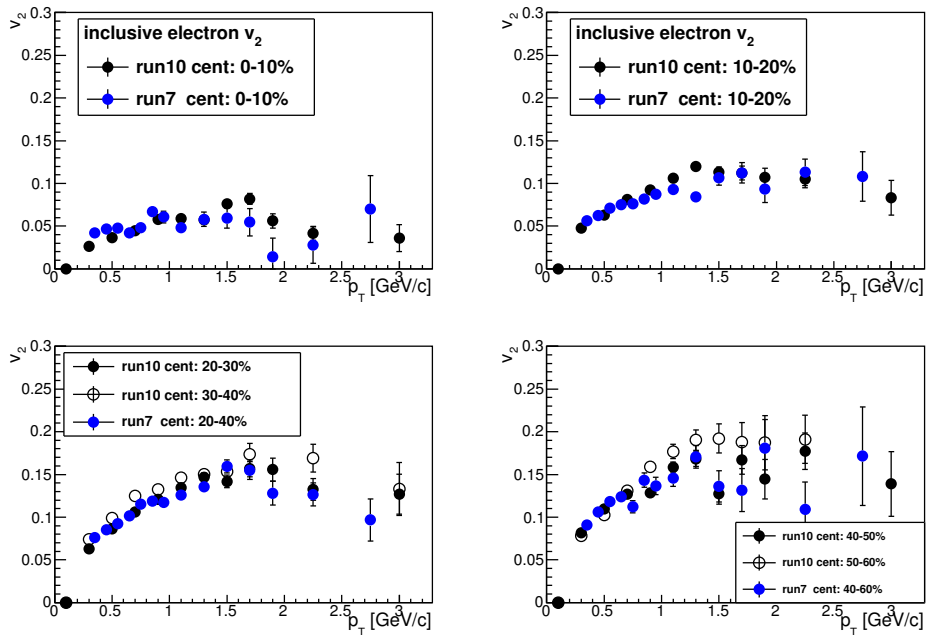
Figure 3.17: Measured run 10 inclusive electron v_2 (in black and white) with electron ID cuts described in Sec. 3.3, compared to published run 7 v_2 of the inclusive electrons (in blue).

Fig. 3.18 and Fig. 3.19 display the inclusive electron v_2 in the chosen centrality bins, and the corresponding fitting functions (plotted in red) used to calculate the flow weight in event mixing. The black curves above and below the red curves denote 10% systematic uncertainty in the electron v_2 measurement. Fig. 3.18 shows the flow fitting functions in 2% centrality bins for $0 - 10\%$ events. Fig. 3.19 presents the functions in 10% centrality bins for more peripheral events.
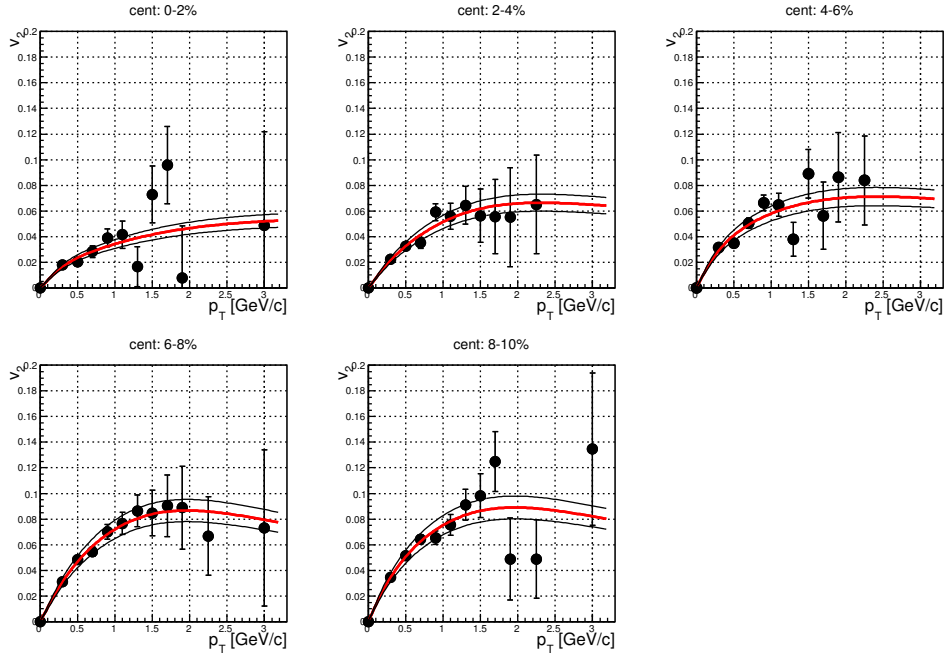
Figure 3.18: Fitting functions for inclusive electron v_2 vs p_T in 0-2%, 2-4%, 4-6%, 6-8% and 8-10% bins. The band denotes 10% systematic uncertainty [12].

Fig. 3.20 shows the ratio of flow modulated mixed background to one without the modulation in blue. The red histogram is the ratio of mixed background using reaction plane pooling with 8 pools[6], to the same unweighted mixed background. The ratio from reaction plane pooling is closer to 1, due to limited reaction plane detector resolution, meaning the flow effect is under corrected.

_____

[6]More reaction plane pools do not improve the situation, as the useful number of pools is limited by the RXNP resolution.
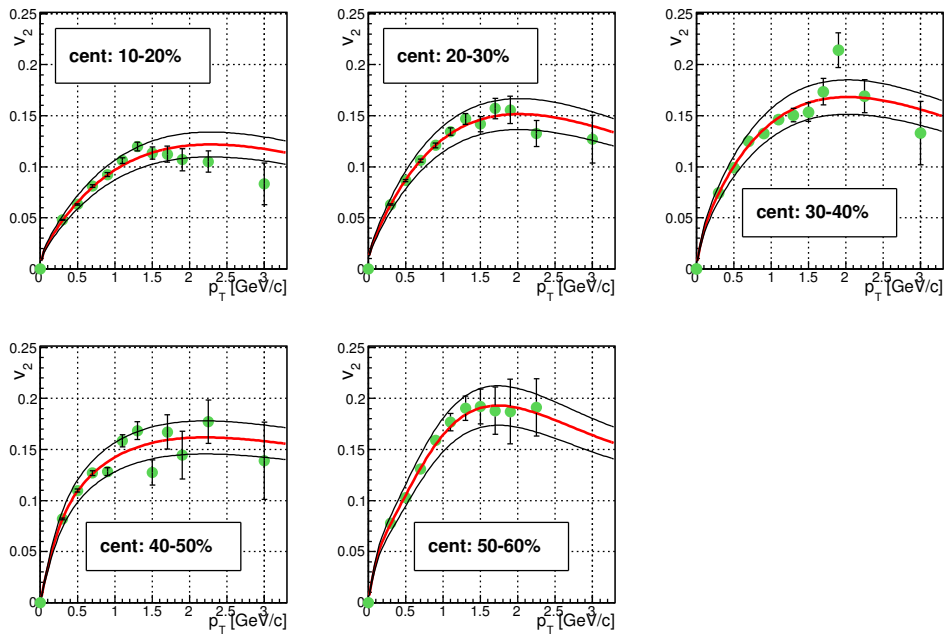
Figure 3.19: Fitting functions for inclusive electron v_2 vs p_T in 10-20%, 20-30%, 30-40%, 40-50% and 50-60% bins. The band denotes 10% systematic uncertainty [12].

As we were limited by statistics in the 60-92% centrality bin, the uncertainty of v_2 became large. However, the signal to background ratio was best in the 60-92% bin, and the combinatorial background was not as overwhelmingly dominant as in the most central events, therefore significantly less precision in reproducing the combinatorial background is required. Besides, the flow's modulation had an effect of 0.4% at largest, as seen in Fig. 3.20. In the most peripheral events where the combinatorial background was relatively small, it was not an important effect. Given the large uncertainty of v_2, we decided not to apply the flow weighting for the 60-92% bin.
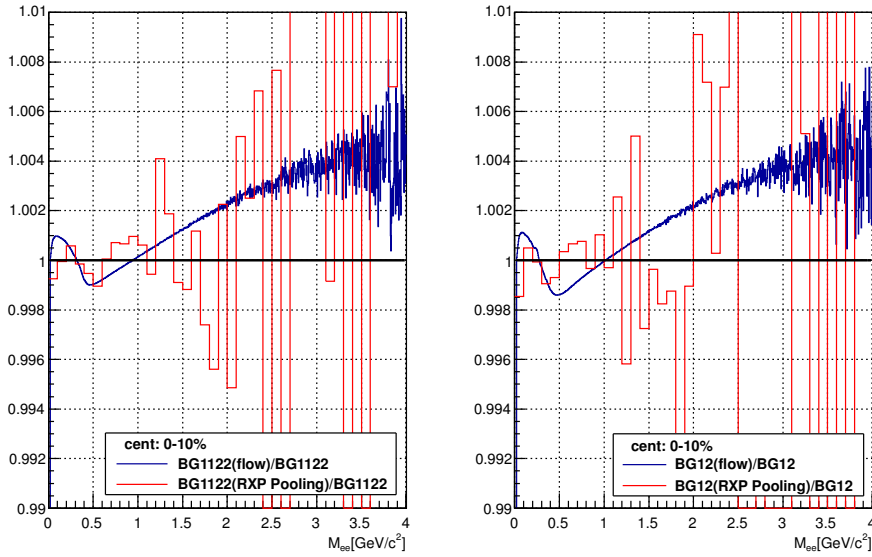
Figure 3.20: Ratio of flow modulated mixed background to unweighted mixed background in the like and unlike sign. Plotted with the 0-10% centrality bin.

3.5.3 Cross Pairs

A cross pair is a background pair, in which the electron and the positron are coming from different parents, which however originate from the same meson. A π^0 meson, for example, decays into two photons. When both photons convert, the electron from photon 1 can pair with the positron from

photon 2, thus forming a cross pair. In the case of a π^0 Dalitz decay, the photon conversion electron(positron) can form a pair with the virtual photon decay positron(electron). Such a pair intrinsically contains the kinematics of meson decay, and forms specific structures in the dielectron mass spectra. This correlated component of the background cannot be subtracted using event mixing, which reproduces uncorrelated background only. Two main contributors of the cross pairs are π^0 and η mesons. Both mesons undergo double photon decay and Dalitz decay with significant branching ratios.

We analyzed a set of simulation produced by the Weizmann Institute of Science [89] to calculate the cross pairs from the two kinds of mesons. The π^0 and the η mesons are generated by a particle generating package named EXODUS, which is specifically designed to produce various electron-producing mesons for $Au + Au$ and $p + p$ collisions in PHENIX with realistic, PHENIX measured p_T distributions, and then to handle the meson decays into photons and electrons realistically [7] Only a single meson was generated per event, to eliminate any combinatorial pairs in the output. The mesons are generated uniformly between $|bbcz| < 30$ cm, with flat distributions in $|\eta| < 0.6$ and $0 \leqslant \phi \leqslant 2\pi$. Only relevant decay channels were turned on. The produced decay photons and electrons were fed into PISA, a machinery of GEANT4 simulation for the full PHENIX configuration, to emulate detector response, track reconstruction, etc. To increase the statistics, the cross section for photon conversion in PISA was turned up by a factor of 20. This unnatural modification was corrected by applying a weighting factor, which was dependent on the radius between the vertex and the conversion point, to the conversion electrons.

The electron tracks in the Weizmann simulation were then embedded into the real data in the HBD detector to account for the HBD efficiency in different centrality bins. The HBD LBS clusterizer described in sec. 3.3.3 was run to find HBD clusters with embedded HBD charge. The full set of electron identification cuts, HBD cut, and PHENIX acceptance cut (including dead map cuts which masked dead regions in major detectors), as well as all pair cuts, were then applied to the simulation tracks. The cross pairs were selected by requiring that the two electron legs should have different creation points. For absolute normalization, we used PHENIX measured $\frac{dN^{\pi^0}}{dy}$ and $\frac{dN^{\eta}}{dy}$ for pion and η multiplicity in each centrality, respectively. Fig. 3.21 is a plot of

---

[7]For more detailed discussion on EXODUS simulation of meson decays, please refer to Sec. 3.7 on the hadronic cocktails.

the invariant mass distribution of cross pairs in like and unlike sign for the 0-10% centrality bin. The π^0 cross pairs show up in a peak just below the pion mass, likewise, the η cross pairs are smaller and broader contributions below the η mass.
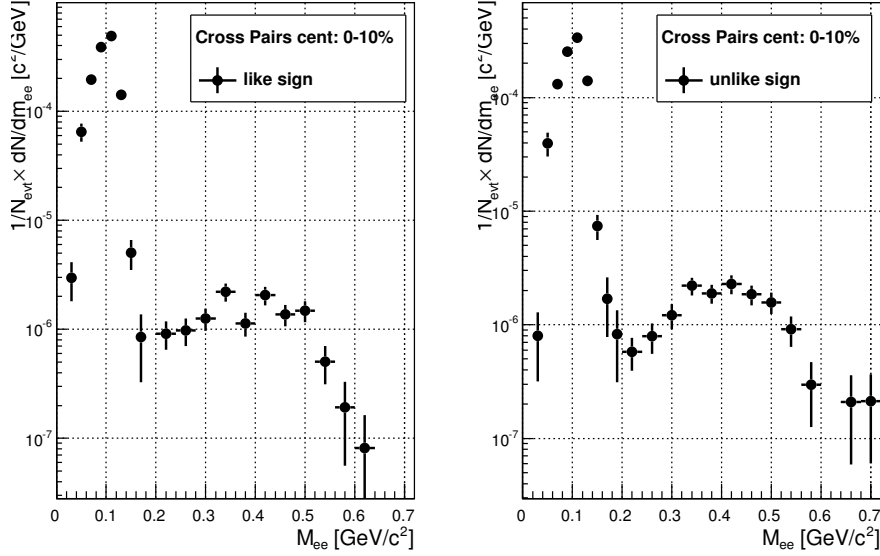
Figure 3.21: Absolutely normalized cross pair distribution in the like and unlike sign for centrality bin 0-10%.

3.5.4 Jet Pairs

A jet pair is formed by two electrons created in a di-jet system. The two electrons, though decayed from different mesons, are kinematically correlated by originating from a single hard scattering event. They populate a much wider region in pair mass vs. p_T space than the cross pairs do. Pairs from the same side of a di-jet system are denoted near side jet pairs, whereas the ones from opposite sides are away side pairs.

The simulation for jets was produced by the Weizmann Institute [89] and analyzed in Stony Brook. A $p+p$ event generator PYTHIA [116] generated triggered events with a threshold for minimum parton p_T at 2 GeV/c, with a flat $bbcz$ distribution within $|bbcz| < 30$ cm. The π^0 and η mesons from these

PYTHIA events were fed into full PISA simulation, again with the 20 times larger than normal cross section of photon conversion for sufficient statistics. The natural branching ratios of relevant meson decay channels were adjusted as well, in order to obtain reasonable statistics for decay channels of naturally small branching ratio. Both the enhanced conversion cross section and adjusted branching ratio were corrected by weighting electron tracks by their ancestry information.

As PYTHIA utilizes a wide variety of setting parameters, it is useful to present a list of the exact settings for the event generation, which is done in the framework of PYTHIA version 6.319 with CTEQ5L parton distribution functions [116].

The following hard QCD processes are turned on inside PYTHIA, where $f_{i,j,k}$ represents a fermion with flavor i, j, k and $\bar{f}_{i,j,k}$ is its corresponding antiparticle. g stands for a gluon.

- MSUB 11: $f_i f_j \rightarrow f_i f_j$

- MSUB 12: $f_i \bar{f}_i \rightarrow f_k \bar{f}_k$

- MSUB 13: $f_i \bar{f}_i \rightarrow gg$

- MSUB 28: $f_i g \rightarrow f_i g$

- MSUB 53: $gg \rightarrow f_k \bar{f}_k$

- MSUB 68: $gg \rightarrow gg$

Together with other kinematic setting parameters:

- MSTP(91)=1, PARP(91)=1.5: Primordial k_T distribution with a Gaussion width set to 1.5 GeV/c.

- MSTP(33)=1, PARP(31)=1.0: K-factor set to 1.0.

- CKIN(3)=2.0: Minimum parton p_T set to 2.0 GeV/c.

Additionally, Table. 3.4 lists the π^0 and η meson decay channels and their modified branching ratio used in the simulations.

As in the case of cross pairs, the jet simulation was again embedded into the HBD and the tracks that passed the full set of analysis cuts (single track, acceptance and pair cuts) were taken to construct pairs. However, there was

process	natural BR	modified BR
$\pi^0 \to \gamma\gamma$	98.802	70.05
$\pi^0 \to ee\gamma$	1.198	29.95
$\eta \to \gamma\gamma$	39.31	23.12
$\eta \to 3\pi^0$	32.57	19.17
$\eta \to \pi^+\pi^-\pi^0$	22.74	13.41
$\eta \to \pi^+\pi^-\gamma$	4.60	2.78
$\eta \to ee\gamma$	0.69	41.40
$\eta \to \mu\mu\gamma$	0.09	0.12

Table 3.4: List of Branching Ratio modifications in PYTHIA simluations.

a combinatorial background to be subtracted in the case of jet pairs. In fact, cross pairs also exist in the jet simulations, but they can be eliminated by requiring the electrons to decay from different mesons. To deal with the combinatorial background, we used the framework of CabanaBoy for event mixing. The mixed background was normalized at $\simeq \pi/2$ in $\Delta\phi$, as shown in Fig. 3.22.

The absolute normalization for the jet pairs involved a few factors. Firstly, the triggered PYTHIA $p + p$ events (by requiring minimum parton p_T of 2.0 GeV/c) were normalized to minimum bias $p + p$ events, by normalizing the PYTHIA π^0 yield per event to PHENIX measured π^0 yield in $p + p$ collisions [6]. Fig. 3.23 shows PHENIX published π^0 yield in $p + p$ collisions (red points) and the normalized PYTHIA π^0 yield (in blue) in $|\eta| < 0.35$. Secondly, the jet yield was scaled by the number of nucleon-nucleon collisions for individual centrality bins, as jets are hard processes, which scale with the number of collisions. Lastly, jet suppression in $Au + Au$ collisions must be taken into consideration.

A suppression factor $R_{AA} \times I_{AA}$ was applied to the near side and away side jet pairs respectively. If the angle $\Delta\phi$ between the parent mesons is less than $\pi/2$, the pair was determined to be a near side pair, otherwise it was away side. The values for R_{AA} and I_{AA} were approximated from PHENIX measurements of pions in Ref. [8,9,13]. Table. 3.5 lists the values chosen. As p_T of the parent mesons were mostly under 2 GeV/c, the suppression factor I_{AA} were actually measured to be greater than 1. The published measurement of the suppression factors had quite large uncertainty in this lower p_T region, but it can be compensated by the fitting method described in Sec. 3.5.7.
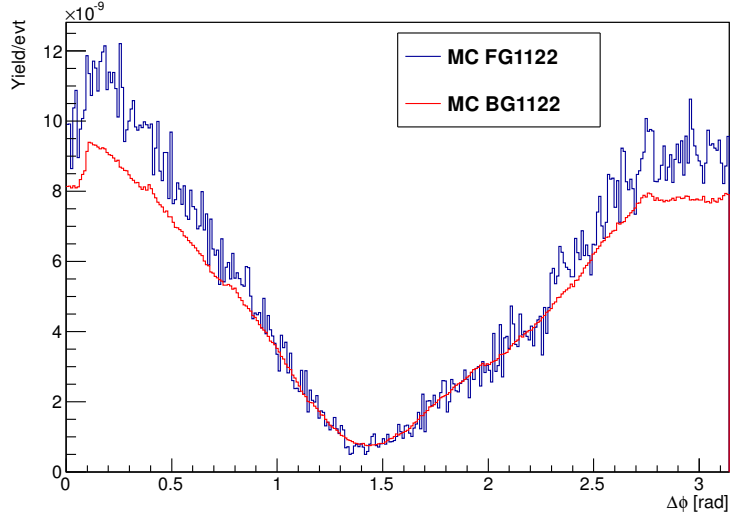
Figure 3.22: Normalization of jet mixed background at $\simeq \pi/2$ in $\Delta\phi$ in the like sign pairs.
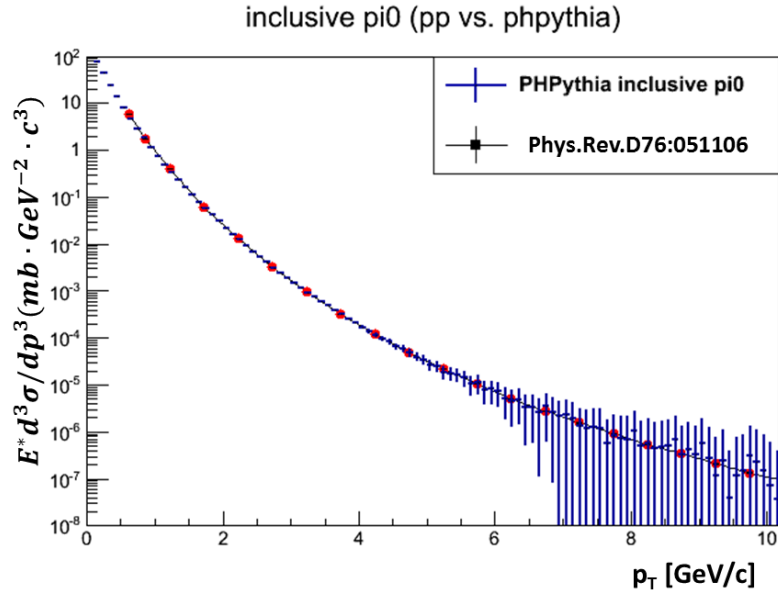
Figure 3.23: Normalization of π^0 yield in PYTHIA to PHENIX measured π^0 yield in $p + p$ collisions [6].

107

centrality	R_{AA}	Near Side I_{AA}	Away Side R_{AA}
0-10%	0.4	2.2	3.23
10-20%	0.45	2.2	3.23
20-40%	0.52	2.23	2.71
40-60%	0.65	1.54	1.61
60-92%	0.75	1.13	1.09

Table 3.5: List of R_{AA} and I_{AA} values used in jet normalization.

Fig. 3.24 shows absolutely normalized jet pair distributions for 0-10% centrality.
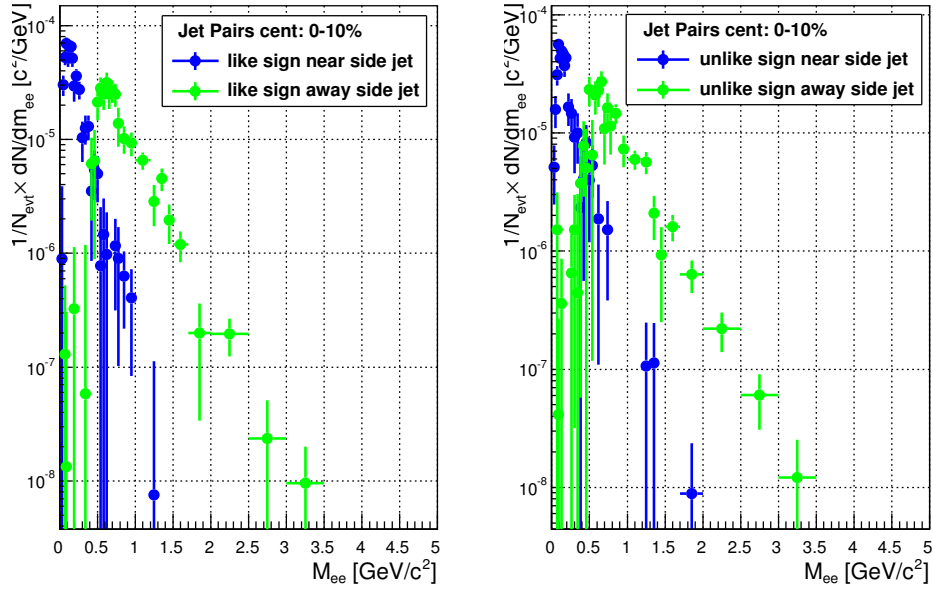
Figure 3.24: Absolutely normalized near side and away side jet pairs in the like and unlike sign for centrality bin 0-10%.

3.5.5 Electron-Hadron Pairs

As discussed with the time of flight cut in Sec. 3.3.2, the hadron contamination in the sample was $\sim 13\%$ for the most central events, and the number

decreased when centrality for more peripheral collisions. The hadrons can form a special kind of correlation with electrons through the configuration of PHENIX detector system. This shows up as another source of correlated background in the data.
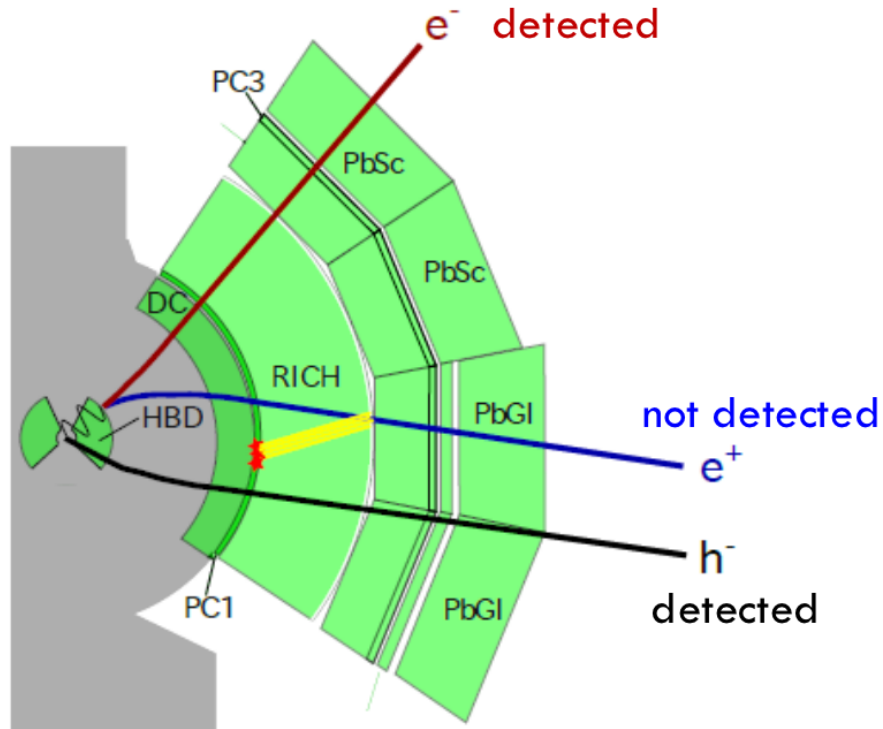
Figure 3.25: Illustration of an e-h pair correlated through the RICH [18]. The hadron h^- shares the Cherenkov signal produced by the undetected parallel e^+, and forms a correlated like-sign pair with the detected e^-.

If we were to scrutinize how hadrons can be mistaken for electrons, the misidentified hadrons in the sample must have had shared the Cherenkov light in the RICH with a true electron flying parallel. Having passed the RICH proximity pair cut, which checks for any parallel electrons, implies that the parallel electron was not identified due to the finite electron identification efficiency in PHENIX. Flying through a dead area in the tracking detectors is one reason for losing electrons. When the parallel electron was from a photon

conversion, it was likely to be rejected by the HBD already. In the case when the undetected electron was created in a pair, for example from a photon conversion, and one electron was detected, the hadron must form a correlation with the detected electron by flying parallel to its undetected sibling. This kind of correlation was established simply by the detector system, instead of by kinematic properties. To illustrate this, Fig. 3.25 shows two electrons created in pair plus a misidentified hadron. The detected charged hadron h^-, by simply flying parallel to the undetected e^+, establishes a sort of correlation with the detected e^-.

This correlated source is different from the electron-hadron pairs from semileptonic heavy flavor decays, where both the electrons and the hadrons are decay products. Such a source is negligible because the decay hadrons are eliminated by the electron identification cuts.[8]

Full embedding simulation into PISA was undertaken to study the e-h correlations. Unfortunately this involved a large amount of coding and debugging, and could not be finished within a reasonable time frame. Weizmann's study of embedding cross pair tracks into the RICH detector was used instead (Ref. [89]). It embedded Monte Carlo electron tracks from the cross pair simulation into the RICH detector, merged the MC RICH ring into real RICH data in $Au + Au$ collisions, applied electron identification cuts to the embedded RICH variables for the MC electrons as well as real hadrons in the data, and extracted pairs with one reconstructed MC electron and one real hadron from the $Au + Au$ event. The result is normalized by measured $\pi^0 \ dN/dy$ values.

The Weizmann analysis and this present analysis used different electron identification cuts which may lead to different efficiency, however, the difference was compensated by the components-fitting normalization technique described in Sec. 3.5.7, and is within the systematic uncertainty. Fig. 3.26 is the plot of e-h pairs for the 5 centrality bins. The level of hadron contamination improves when going from the most central to most peripheral events. With the elimination of hadrons when collisions become more peripheral,

---

[8]Assuming same acceptance for the unlike and like sign heavy flavor e-h pairs for approximation, the unlike and the like sign e-h yields should be similar. We infer from Fig. 3.51 that heavy flavor decay electron-positron pairs are only a small contribution at $m_{ee} < 1 \ GeV/c^2$. Now if we were to replace one decay electron with a decay hadron to estimate the e-h contribution, we should keep in mind that with the eID cuts the hadron survival rate is a few magnitudes lower than the electron efficiency. We can therefore estimate that the contribution from heavy flavor decay e-h pairs is negligible.

the yield of e-h pairs gradually declined. The unlike and the like sign e-h pairs are also shown to have quite different mass distributions. The unlike sign pairs have smaller opening angles than the like sign pairs, leading to a distribution at lower mass than that of the like sign.
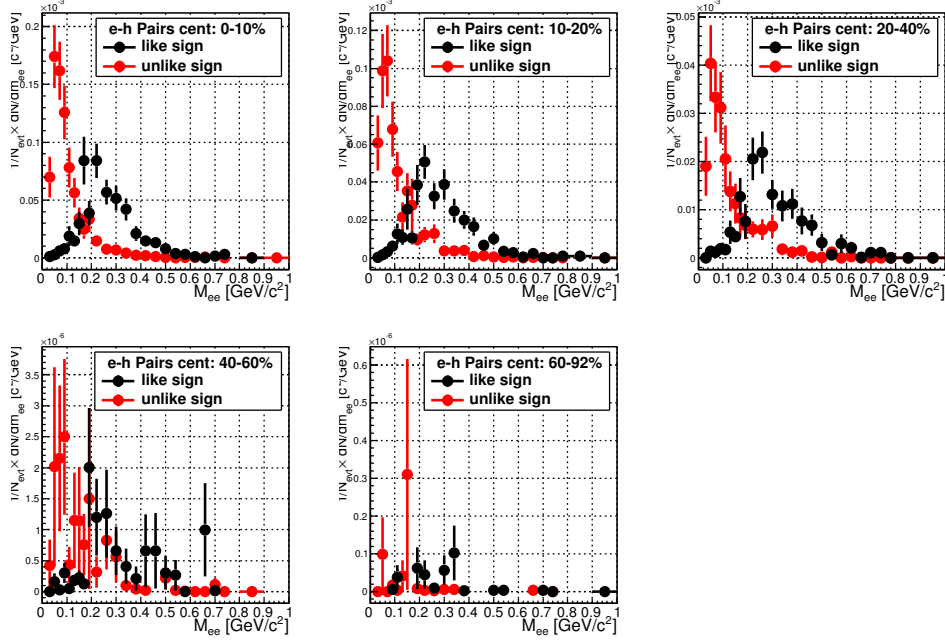
Figure 3.26: Distributions of absolutely normalized e-h pairs in the like (black) and unlike (red) sign for centrality bins 0-10%, 10-20%, 20-40%, 40-60%, 60-92%. There is strong dependence on centrality.

3.5.6 Heavy Flavor Pairs

$c\bar{c}$ and $b\bar{b}$ events contribute to the dielectron mass spectra via semi-leptonic decays from D and B mesons. $c\bar{c}$ events do not populate like sign space, for direct semi-leptonic decays $D \rightarrow e^+X$ and $\bar{D} \rightarrow e^-X$ can only produce unlike sign pairs. On the other hand, Ref. [19] estimates that approximately 1/3 of the ee pairs from $b\bar{b}$ events are like sign pairs, due to the longer decay chains of B mesons. Table.3.6 lists the most relevant B decay channels with the effective branching ratios [19].

111

B decay modes	effective BR
$B \to e^+ X$	11%
$B \to \bar{D}X \to e^- X$	8.5%
$B \to \bar{D}e^+ X \to e^+ e^- X$	0.8%

Table 3.6: List of the most relevant B meson decay channels and the corresponding effective branching ratios, which are averaged over all possible meson combinations. [19]

The dielectron pairs produced by heavy flavors are not considered "background". The unlike pairs constitute part of the dielectron signals. The like sign pairs (from $b\bar{b}$) manifest as a component of the correlated like sign spectra. The $b\bar{b}$ pairs are simulated to complete the picture of the like sign dielectron composition, and are used as a correlated like sign background component in the components fitting normalization method, as described in Sec. 3.5.7 with details.

The $b\bar{b}$ pairs were generated by MC@NLO simulation [71] [111], a next-to-leading-order event generator, following the procedures described in Ref. [19] in details. The generator properly handles the particle-antiparticle oscillations between B^0 and $\bar{B}^0$, which change one of the charges in an ee pair. The simulations were generated with a $b\bar{b}$ cross section of $3.4\mu b$ for $p+p$ collisions, as obtained in the work Ref. [19]. We used the number of binary collisions N_{coll} to scale the MC to $Au + Au$ multiplicity for any given centrality.

Fig. 3.27 is the bottom pair distribution for most central events. As noted above, the like sign yield is $\sim 1/3$ of the unlike sign yield. At $m_{ee} < 2\,GeV/c^2$, due to the very small yield, the bottom pairs are negligible compared to other correlated like sign sources. At m_{ee} above $2\,GeV/c^2$, however, the bottom becomes a significant component. It is worth noting that, although the bottom pairs are treated as one of the like sign background sources in the components fitting method, the unlike sign bottom pairs are part of the dielectron signal, and should *not* be subtracted from the unlike sign spectra. Therefore only the left panel in Fig. 3.27 (the like sign pairs) are used in the actual analysis.
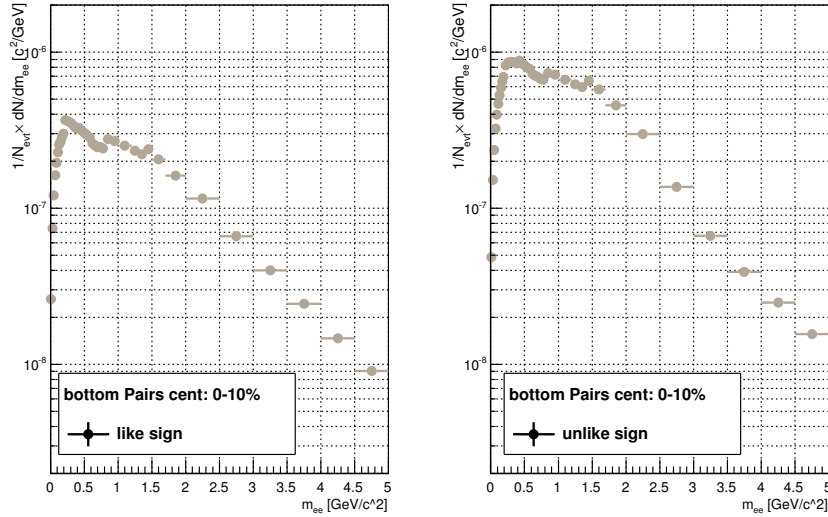
Figure 3.27: Distributions of absolutely normalized heavy flavor electron pairs from $b\bar{b}$ in the like and unlike sign for centrality bin 0-10%.

3.5.7 Normalization in the Like Sign Spectra

The strategy of the blind analysis, was to find the optimal normalization in the like sign space, then to go and see what happens with this normalization in the unlike sign spectra after subtracting the background. The first step for normalization, therefore, was to determine the background levels from the various sources in the like sign space.

Absolute Normalization

The first step for like sign normalization is to absolutely normalize the various background components in the like sign. One purpose is to verify that the absolute normalization is able to give a good enough description of the like sign yield, and to convince ourselves that we have sufficient knowledge of the background components. The absolute normalization is relatively straightforward for the correlated components calculated from simulation, by using past PHENIX measurements, and it is already described in the previous sections. The level of combinatorial background, however, is determined differently.

The absolute normalization for the mixed pairs was done by first subtracting all correlated pairs, namely the cross, the jet, and e-h pairs, all absolutely normalized. Bottom's contribution is negligible compared to these sources. The normalization factor for BG1122 is then found by taking the integral of the entire m vs. p_T space:

$$N_{\text{like}} = \sqrt{\frac{\int_{\text{m,pt}} \text{FG11} \times \int_{\text{m,pt}} \text{FG22}}{\int_{\text{m,pt}} \text{BG11} \times \int_{\text{m,pt}} \text{BG22}}} \tag{3.8}$$

Fig. 3.28 shows the fair agreement between like sign spectrum in 0-10% and the absolutely normalized background sources. It confirms we have good understanding of the background components, and are able to reproduce the background shape and magnitude by calculation. However, accounting for the uncertainty in the normalization factors, the shape of the Monte Carlo background sources does not perfectly match the like sign shape. As we aim to describe the background sources accurately, we can take advantage of the background information in the shape of FG1122, and adjust the normalization factors for the background sources to fit FG1122.

The Component Fitting Method

The cross pairs and e-h pairs are two localized distributions at different mass regions that are easy to identify in the like sign space. The jet pair pairs has a double-hump structure in mass, and is spread in all m vs. p_T space. Comparing to the other correlated sources, $b - \bar{b}$ pairs' contribution only becomes signifcant at above ~ 2 GeV/c^2. We made use of these attributes when fitting FG1122 in the invariant mass space with the sum of the background components.

There were 6 components used for fitting FG1122. Here the jet pairs are split into same side jet component and away side jet component because I_{AA} in the jet suppression factor $R_{AA} \times I_{AA}$ is physically and numerically different for the same and the away side.

- BG1122 with flow modulation

- Cross pairs

- Same side jet pairs

Figure 3.28: Like Sign yield after subtracting absolutely normalized mixed background, compared to absolutely normalized correlated background sources. Centrailty bins: 0-10%.

Figure 3.29: Like Sign yield after subtracting absolutely normalized mixed background, compared to absolutely normalized correlated background sources. Centrailty bins: 60-92%.

- Away side jet pairs

- e-h pairs

- $b\bar{b}$ pairs

Mathematically, the fitting procedure can be described by the following equation,

$$FG1122 = a_0 BG1122 + a_1 CP1122 + a_2 JP1122^{same} + \\ a_3 JP1122^{away} + a_4 EH1122 + a_5 BB1122 \quad (3.9)$$

where a_i denotes the normalization factor for the corresponding component, which was ready absolutely normalized in the first step. Hence, a_i represents the relative individual component yield to the component's absolutely normalized yield. In the case of $a_i = 1, i = 0, 1, 2, ...5$, we return to the case of absolute normalization. From Eq. 3.9 we also obtain,

$$FG1122 - a_0 BG1122 = a_1 CP1122 + a_2 JP1122^{same} + \\ a_3 JP1122^{away} + a_4 EH1122 + a_5 BB1122 \quad (3.10)$$

Fig. 3.30 to Fig. 3.34 show the various components in like-sign spectra, normalized by the fitting result, in the 5 centrality bins. The blue points represent $FG1122 - a_1 BG1122$, which is the left-hand side of Eq. 3.10, the like-sign remnant after subtracting the normalized combinatorial background $a_1 BG1122$. The Cross pairs are plotted in magenta lines, the near side jet in green, the away side jet in blue, the e-h in cyan and $b - \bar{b}$ in black. The red histogram is the sum of all the correlated sources, i.e. the right-hand side of Eq. 3.10. When normalized correctly, the red histogram should match the blue points at all masses. Good agreement between the red histogram and the blue points can be seen at all masses in all five centrality bins, as shown in Fig. 3.30 to Fig. 3.34.

Tables of the fitting factors and their statistical uncertainties for the 5 centrality bins can be found in Table. 3.7:

The ratio of like sign foreground to background gives a measure of how well the foreground is described by the normalized backgrounds. Fig. 3.35 shows the like sign foreground divided by the sum of all background sources,
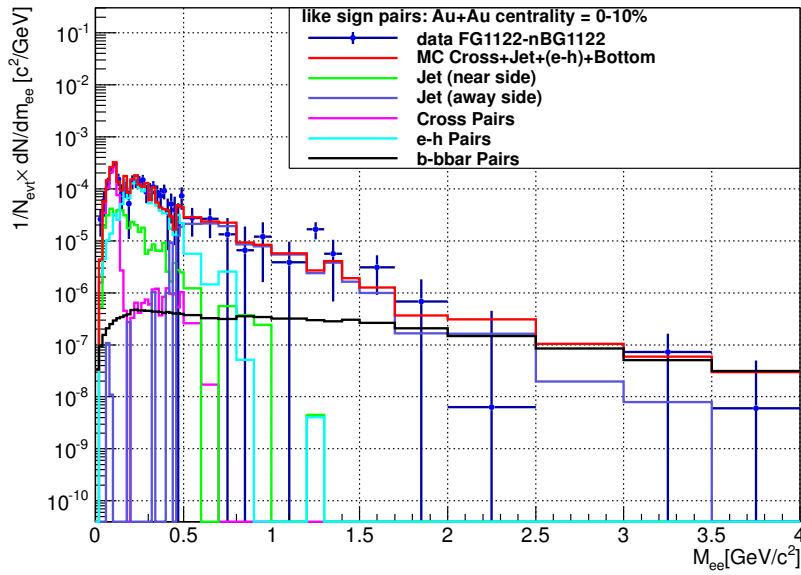
Figure 3.30: Like Sign yield after subtracting normalized mixed background, compared to various correlated background sources. Components fitting procedures were used for the normalization. For centrality bin 0-10%.
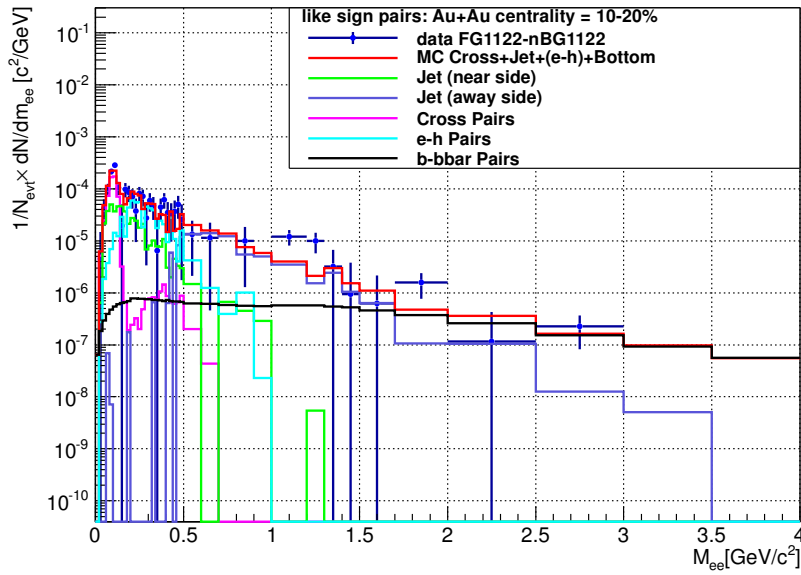
Figure 3.31: Like Sign yield after subtracting normalized mixed background, compared to various correlated background sources. Components fitting procedures were used for the normalization. For centrality bin 10-20%.
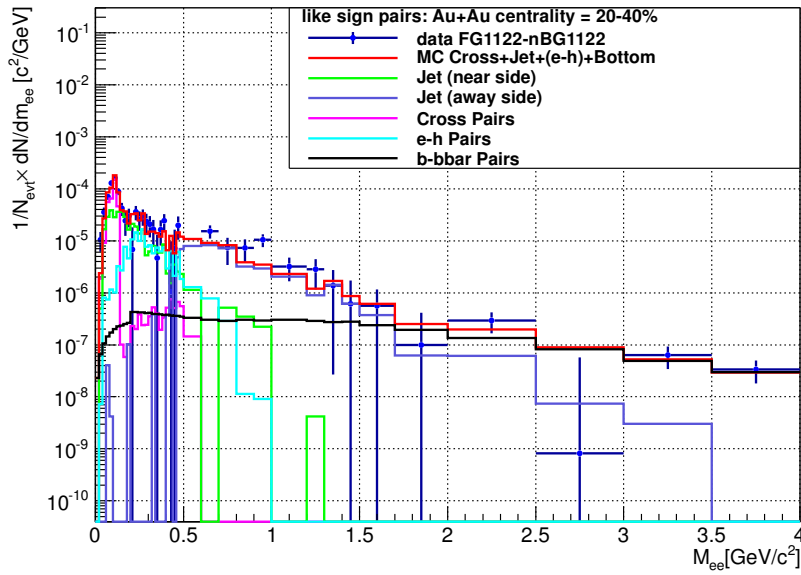
Figure 3.32: Like Sign yield after subtracting normalized mixed background, compared to various correlated background sources. Components fitting procedures were used for the normalization. For centrality bin 20-40%.
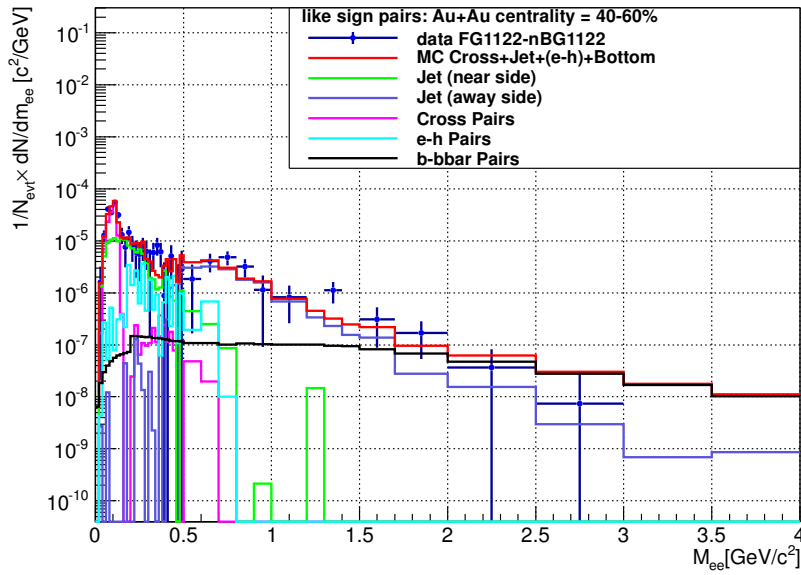
Figure 3.33: Like Sign yield after subtracting normalized mixed background, compared to various correlated background sources. Components fitting procedures were used for the normalization. For centrality bin 40-60%.
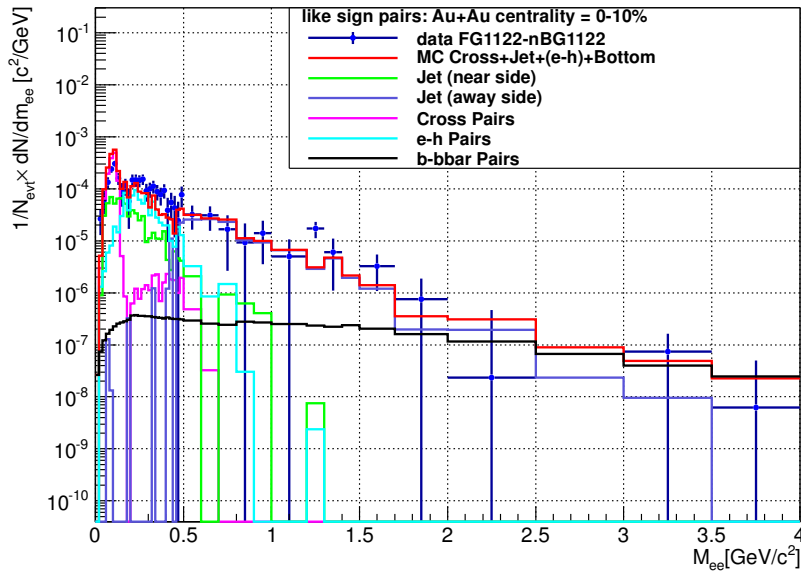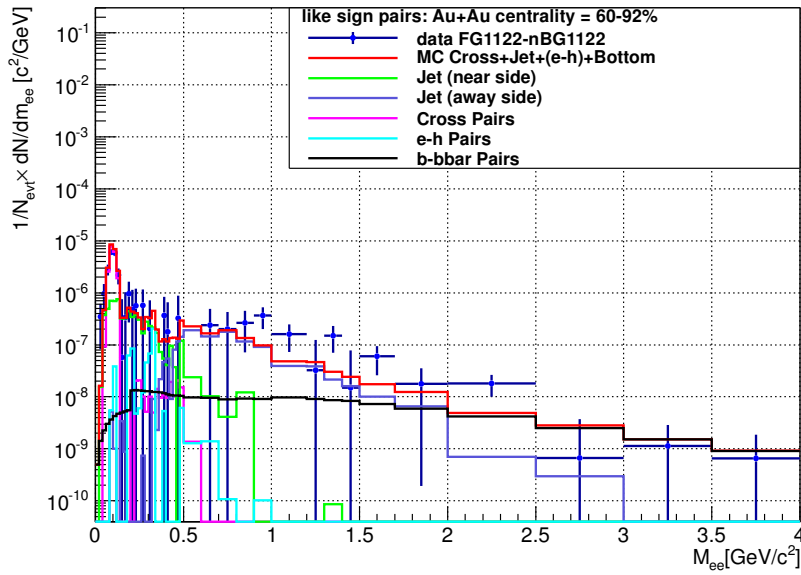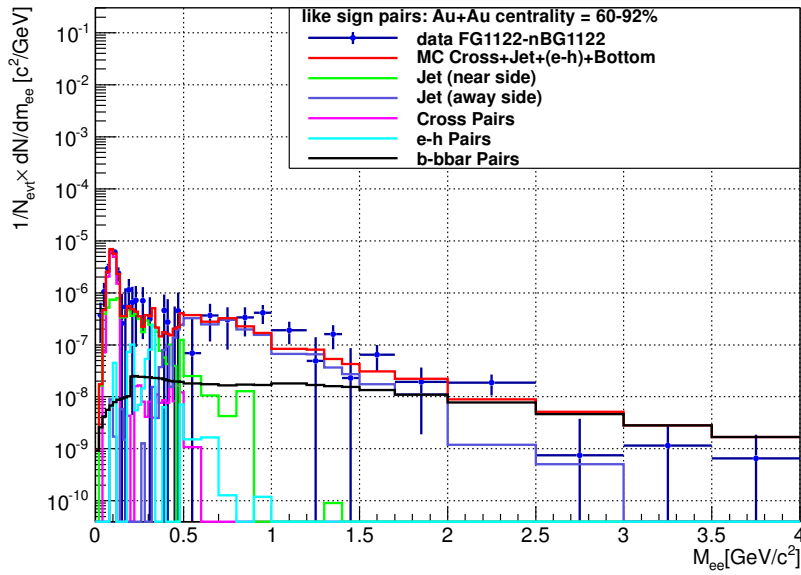
Figure 3.34: Like Sign yield after subtracting normalized mixed background, compared to various correlated background sources. Components fitting procedures were used for the normalization. For centrality bin 60-92%.

normalized by the fitting method, in five centrality bins. The left panel shows the mass range in $0.2 < m_{ee} < 1 \ GeV/c^2$ and the right panel shows $0 < m_{ee} < 3 \ GeV/c^2$. In the most central bin, the FG/BG ratio is mostly within 0.1% around 1. As collisions become more peripheral, the combinatoral background is greatly reduced, leading to higher S/B ratio. As a result, the scale on the ratio plots increases when the collisions become more peripheral, reflecting the decreasing combinatorial background. The grey bands around 1 represent the uncertainty on the combinatorial background normalization. Overall there is little evident deviation from unity in all centrality classes.

As a comparison between component-fitting method and absolute normalization, Fig. 3.36 shows the foreground to background ratio obtained from the two methods. The solid red points are made with the fitting method while the open red points are by absolute normalization. The difference between the two methods are especially visible in the most central and the $40 - 60\%$ bins, where the fitting method gives a better description of the foreground than the absolute normalization. Fitting is beneficial for the most central bin, where the background is largest, and most difficult to control.
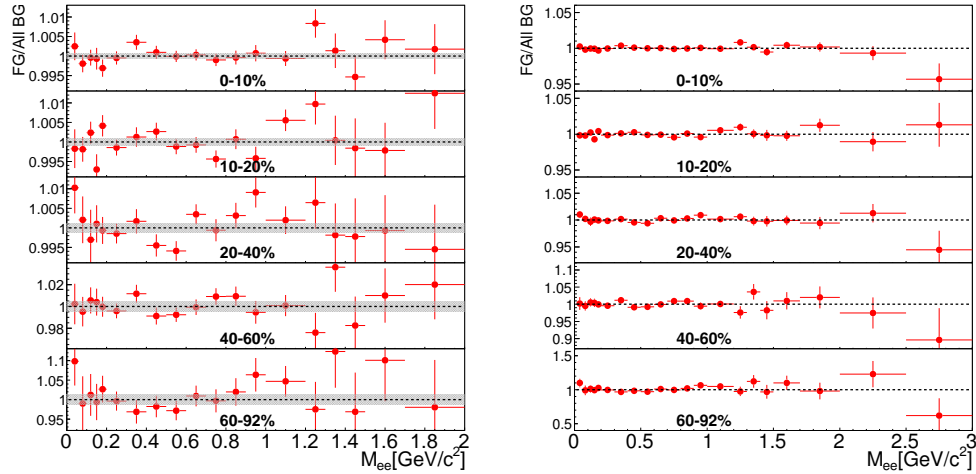
Figure 3.35: Ratio of like sign foreground to sum of all background for the five centrality bins.

Figure. 3.37 illustrates the normalized background sources in comparison to the foreground like sign spectrum in minimum bias collisions, where the open circles are the foreground pairs, the black line on the same level
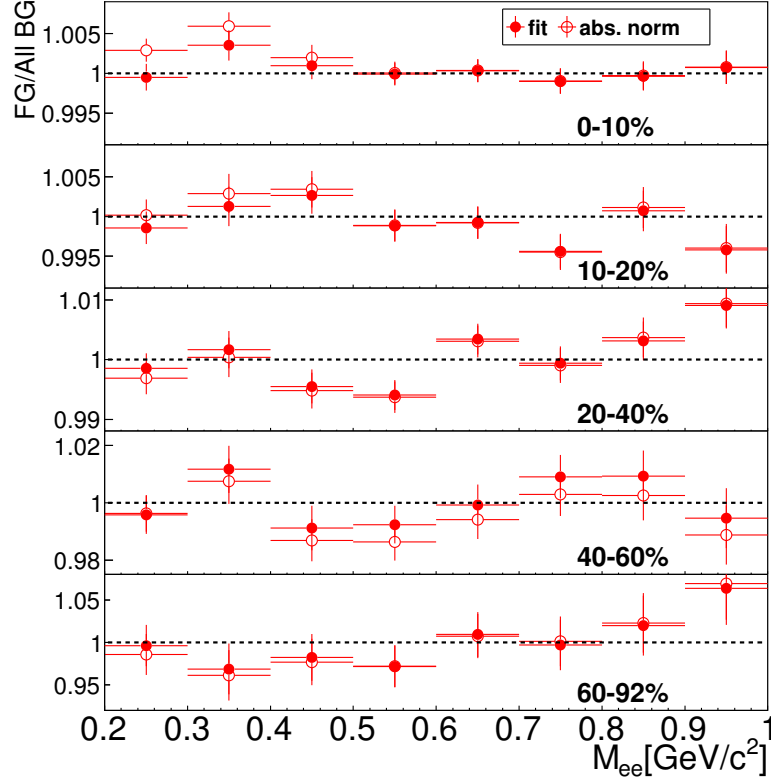
Figure 3.36: Ratio of like sign foreground to sum of all background for the five centrality bins.

Cent	BG1122	CP	EH	JP(near)	JP(away)	BB
0-10%	1.00038	0.532203	1.71226	0.594841	0.831325	1.27822
	±0.000619	±0.0279	±0.185	±0.090	±0.239	±0.639
10-20%	1.00104	0.600961	1.12556	0.915615	0.684522	2.407
	±0.000804	±0.0667	±0.213	±0.266	±0.165	±0.519
20-40%	1.00165	0.842717	0.608176	1.03532	0.711795	1.99709
	±0.00117	±0.0760	±0.0976	±0.201	±0.162	±0.621
40-60%	0.990063	1.20664	1.70529	1.5458	1.29431	1.88279
	±0.00460	±0.0913	±0.735	±0.353	±0.437	±0.783
60-92%	0.986472	0.795212	1.18032	1.05101	1.708	1.8528
	±0.0120	±0.0762	±0.612	±0.434	±0.606	±0.865

Table 3.7: Fitting factors for the like sign background components.

124

of the foreground yield is the combinatorial background, towering over all other background sources. The red, blue and green are cross pairs, jet pairs and e-h pairs respectively, which exhibit distinct structures in mass and are significantly smaller contributors. The purple dotted line represent the very small $b - \bar{b}$ contribution.
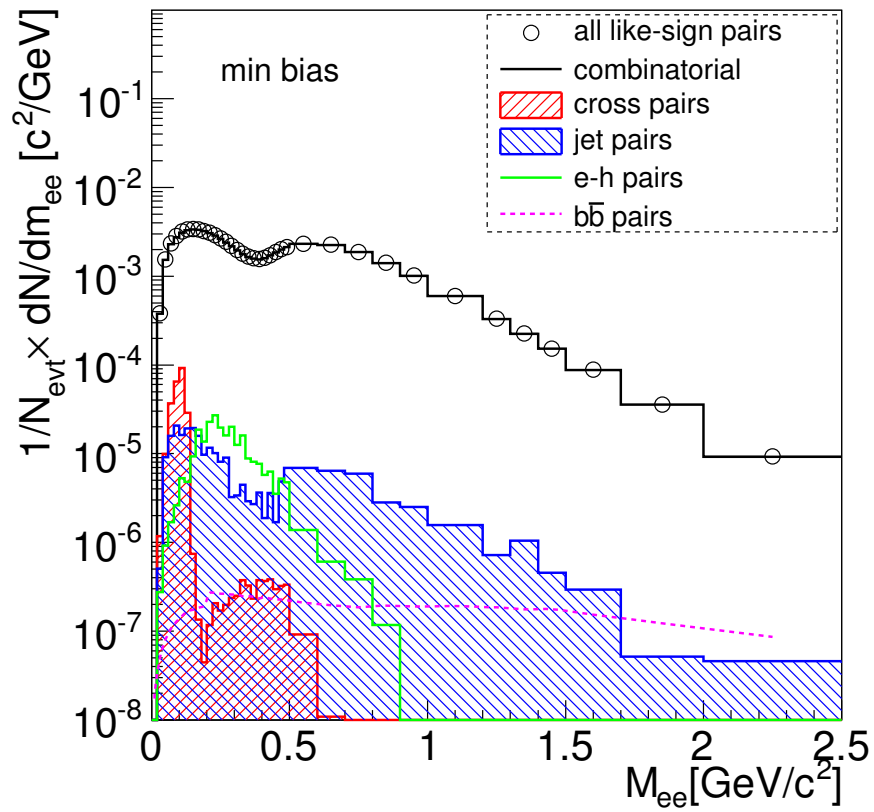
Figure 3.37: Normalized like-sign background components in minimum bias collisions.

3.5.8 Normalization in the Unlike Sign and κ Correction

Once the like sign has been normalized, one needs to calculate the normalization for the unlike sign. Before going directly into action, any difference between the like sign and unlike sign mixed background must be examined.

Twice Square Root Relation

As a starting point, a previous study in Ref. [10] has proven that for uncorrelated electron-positron pairs, the unlike-sign background is the geometric mean of the like-sign pairs, regardless of the primary multiplicity:

$$BG_{+-} = 2\sqrt{BG_{++}BG_{--}} \tag{3.11}$$

This is known as the twice square root relation between the unlike and like sign pairs. A sufficient but not necessary condition for the like sign normalization to work properly in the unlike sign space is that the 2 square root relation is held true for both uncorrelated foreground (denoted by FG') and mixed event background pairs, i.e.

$$\int FG'12 = 2 \times \sqrt{\int FG'11 \times \int FG'22}$$

and at the same time,

$$\int BG12 = 2 \times \sqrt{\int BG11 \times \int BG22}$$

(The relation is shorthanded sometimes as the $2 \times \sqrt{}$ normalization). Then,

$$\int FG'12 = 2 \times \sqrt{\int FG'11 \times \int FG'22}$$

$$= 2 \times \sqrt{\int FG'11 \times \int FG'22} \times \frac{\int BG12}{2\sqrt{\int BG11 \times \int BG22}}$$

$$= \frac{\sqrt{\int FG'11 \times \int FG'22}}{\sqrt{\int BG11 \times \int BG22}} \times \int BG12$$

$$= N_{like} \times \int BG12 \quad (3.12)$$

where N_{like} is the normalization factor for the like sign combinatorial background, which equals a_0 in Sec. 3.5.7.

(Upon close inspection of the above derivation, it is easy to see that, if the factor 2 were replaced by a factor f for *both FG and BG simultaneously* so that f is canceled, Eq. 3.12 would hold true regardless. In other words, if the 2 square root relation were broken by the same amount for both FG and BG, Eq. 3.12 would still work.)

Unfortunately, the pair cuts, which were used to reject overlapping tracks and misidentified $\pi^{\pm}$ tracks, breaks this 2 square root relation in the uncorrelated foreground, yet preserves the relation in the mixed background. As was done in FG, the same set of pair cuts is applied when generating the mixed background. When a mixed event failed the pair cut, the Matathias Pool (which handles the mixing) in CabanaBoy, would regenerate a new event until the pair cuts were satisfied to replace the failed one. This ensured the mixed background always satisfied the $2 \times \sqrt{}$ relation, provided the pool was deep enough, i.e. there were sufficient tracks to choose from. For this reason, a pool depth of 5000 was tested and used in the analysis. The flow modulation of the mixed background was also found to impact the $2 \times \sqrt{}$ relation, however the effect is very small. This is not surprising, as the flow weight was very close to 1. The deviation was found to be 0.037% in 0-10% centrality bin, and to increase to 0.27% in 40-60% bin. This is within acceptable precision. Furthermore, in the analysis done by Yosuke Watanabe [89], he has demonstrated by a Toy Monte Carlo that the flow causes the same amount of deviation in both the foreground and the background pairs, so that the

effect is canceled in the normalization factor. We therefore ignored the effect from the flow weighting in the background normalization, which accounts for its effect on the background shape.

To restore the broken $2 \times \sqrt{}$ relation in the uncorrelated FG, one can calculate empirically the factor by which the ratio $\int FG'12 / (2 \times \sqrt{\int FG'11 \times \int FG'22})$ is broken. To that end one needs to calculate the factor (called κ), so that, $\int (FG'12) = \kappa \times 2 \times \sqrt{\int FG'11 \times \int FG'22}$.

Then, the normalization factor for the mixed background in the unlike sign is given by

$$
\begin{aligned}
\int FG'12 &= \kappa \times 2 \sqrt{\int FG'11 \times \int FG'22} \\
&= \kappa \times 2 \sqrt{\int FG'11 \times \int FG'22} \times \frac{\int BG12}{2\sqrt{\int BG11 \times \int BG22}} \\
&= \kappa \times \frac{\sqrt{\int FG'11 \times \int FG'22}}{\sqrt{\int BG11 \times \int BG22}} \times \int BG12 \\
&= \kappa \times N_{like} \times \int BG12 \quad (3.13)
\end{aligned}
$$

Therefore we get:

$$
N_{unlike} = \kappa \times N_{like} \tag{3.14}
$$

where

$$
N_{like} = \frac{\sqrt{\int FG'11 \times \int FG'22}}{\sqrt{\int BG11 \times \int BG22}} \tag{3.15}
$$

Calculation of κ

Suppose, if the loss in efficiency in the uncorrelated part of the unlike sign spectra (denoted uFG12 to differentiate from total foreground FG12) is κ_{12} and that for the two like signs uFG11 and uFG22 is κ_{11} and κ_{22} respectively,

then, the fact that with no pair cuts the $2 \times \sqrt{}$ normalization should hold implies that

$$\frac{\int uFG12}{\kappa_{12}} = 2 \times \sqrt{\frac{\int uFG11}{\kappa_{11}} \times \frac{\int uFG22}{\kappa_{22}}} \tag{3.16}$$

or

$$\int uFG12 = \frac{\kappa_{12}}{\sqrt{\kappa_{11} \times \kappa_{22}}} \times 2 \times \sqrt{\int uFG11 \times \int uFG22} \tag{3.17}$$

where

$$\kappa = \frac{\kappa_{12}}{\sqrt{\kappa_{11} \times \kappa22}} \tag{3.18}$$

can be calculated empirically by weighted averaging the pair cut survival probability in real data events as a function of event topology (how many electrons and positrons the events contains). The survival probability of a given pair naturally depends on the number of electrons and positrons available in the event the pair came from, which indirectly depends on multiplicity. The higher the multiplicity, the higher the chance of getting an overlapping pair in the event. The pair cut survival probabilities ($s_{12}(n_1, n_2)$, $s_{11}(n_1, n_2)$ and $s_{22}(n_1, n_2)$) are thus calculated for events of every possible topology (n_1 electrons and n_2 positrons). The weights are calculated from the experimental frequency distribution of events as a function of the number of electron and positrons they contain ($p(n_1, n_2)$).

The weighted average of survival probabilities (or κ_{ij}'s) are then evaluated using:

$$\kappa_{12} = \frac{\sum n_1 n_2 \cdot s_{12}(n_1, n_2) \cdot p(n_1, n_2)}{\sum n_1 n_2 \cdot p(n_1, n_2)}$$

$$\kappa_{11} = \frac{\sum n_1(n_1 - 1) \cdot s_{11}(n_1, n_2) \cdot p(n_1, n_2)}{\sum n_1(n_1 - 1) \cdot p(n_1, n_2)}$$

$$\kappa_{22} = \frac{\sum n_2(n_2 - 1) \cdot s_{22}(n_1, n_2) \cdot p(n_1, n_2)}{\sum n_2(n_2 - 1) \cdot p(n_1, n_2)}$$

They can be used to calculate the κ factor as in equation 3.18. Technically, the survival rates $s_{ij}(n_1, n_2)$ and event frequency $p(n_1, n_2)$ were obtained from
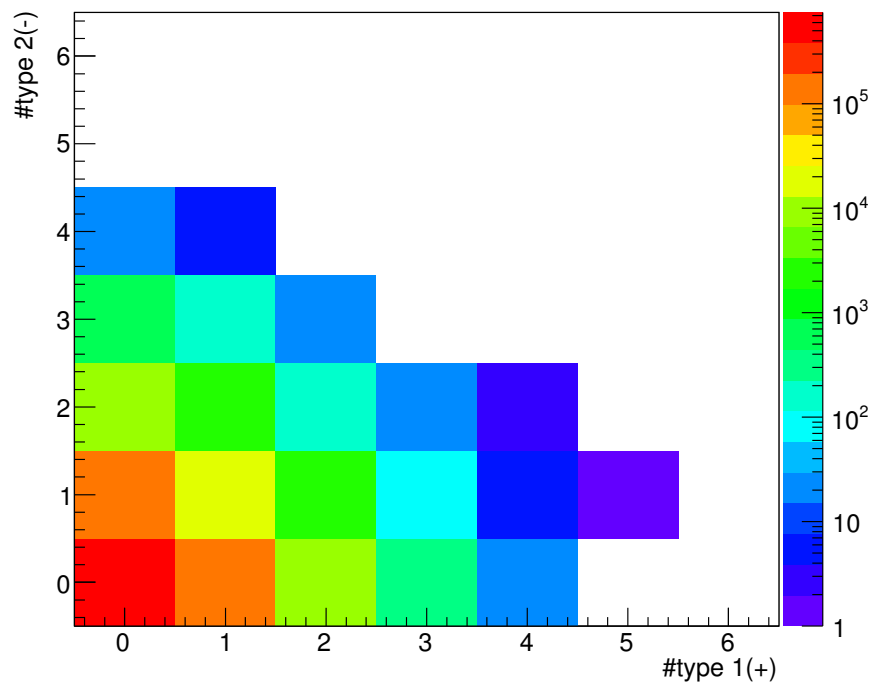
Figure 3.38: Distribution of events with a given number of electrons and positrons

CabanaBoy event mixing which provided uncorrelated pairs. Fig. 3.38 shows the event distribution with n_1 type1(electron) and n_2 type2(positron) tracks, in which each grid at location (x,y) represents the events containing x type1 (+) and y type2 (-) electrons. Fig. 3.38 would yield the event probability distribution $p(n_1, n_2)$ when divided by the total number of events. Table 3.8 shows values of κ that were calculated using this procedure for each centrality.
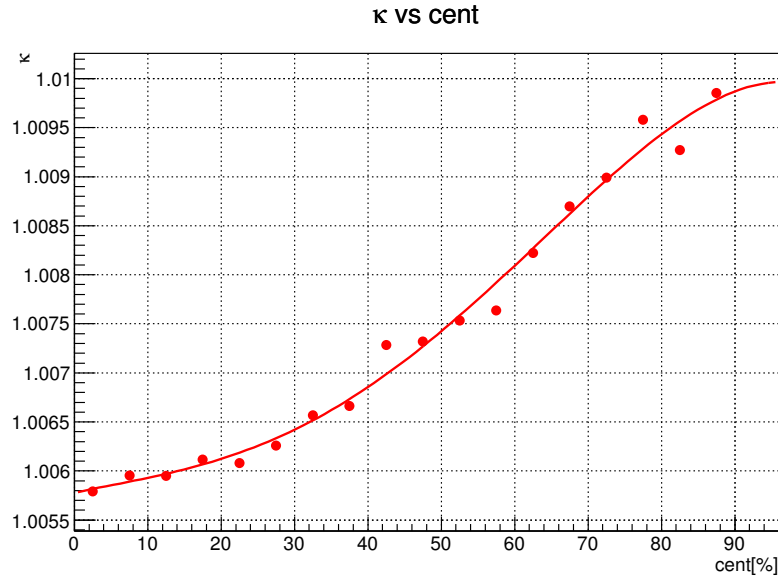
Figure 3.39: κ values calculated in 10% centrality bins.

κ increases with centrality, as can be seen from Fig. 3.39, and it is also found to have a dependence on event vertex position along the beam direction z. Fig. 3.40 shows the variation of κ in 4 z vertex bins. The solid horizontal line in each panel represents κ calculated from event vertex position $-20\ cm < bbcz < 20\ cm$, which marks the κ applied in the analysis. The variation was taken as a source of systematic uncertainty. κ was also applied in 10% centrality bins, to account for the centrality dependence.

Fig. 3.39 presents the κ calculated in 5% centrality bins as a function of centrality. It shows a clear rising trend when centrality increases. The points are fitted with a 4th order polynomial, and κ was extracted from the fitting function for every 10% centrality bin.
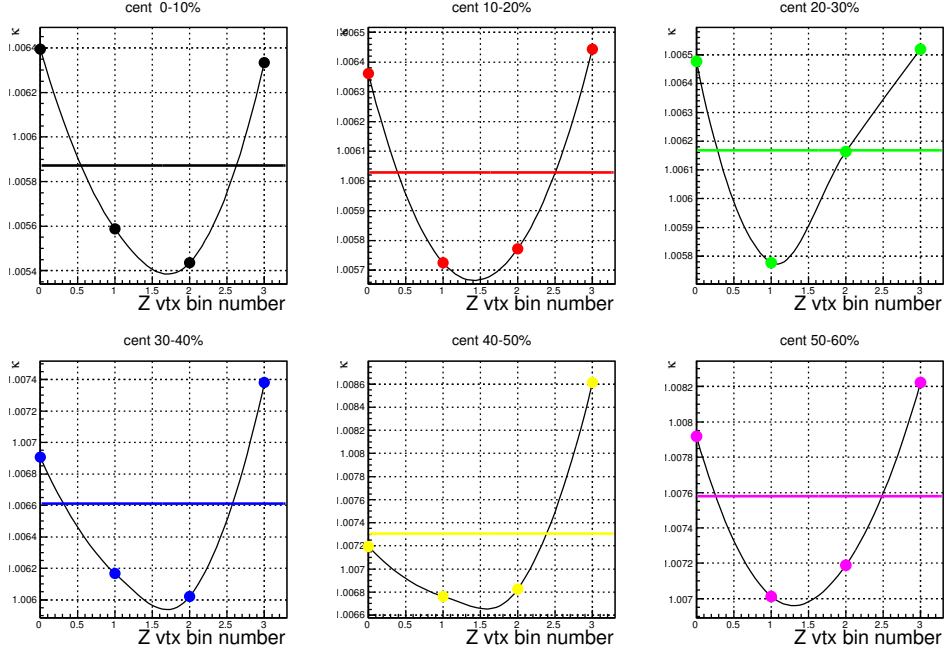
Figure 3.40: variation of κ with z vtx bins.

centrality	κ	$\Delta\kappa$
0-10%	1.00585	0.0006
10-20%	1.00602	0.0006
20-30%	1.00626	0.0005
30-40%	1.00662	0.0005
40-50%	1.00712	0.0004
50-60%	1.00775	0.0005
60-70%	1.00845	0.0008
70-80%	1.00913	0.0008
80-92%	1.00996	0.0010

Table 3.8: κ values used in the analysis in 10% centrality bins. The variation of κ over event z vertex $\Delta\kappa$ is implemented in the systematic uncertainty.

3.5.9 Raw Subtracted Spectra

After subtracting all known backgrounds, the raw spectra without correction are plotted below in Fig. 3.41. Next it is necessary to make efficiency correction for the PHENIX acceptance.

At this point, it would be useful to compare the residual unlike sign background to all subtracted background. The unlike sign residual background can be roughly estimated from the like sign residual background,

$$\Delta N_{like} = FG1122 - a_0 BG1122 - a_1 CP1122-$$
$$a_2 JP1122^{same} - a_3 JP1122^{away} - a_4 EH1122 - a_5 BB1122 \quad (3.19)$$

by applying a corrector for acceptance difference. The magnetic field opens up the like and unlike sign pairs differently, leading to different acceptance for the two types of pairs. A correction factor $\alpha(m) = BG12(m)/BG1122(m)$ was used to correct the acceptance difference. Hence, the residual unlike sign background can be estimated by

$$\Delta N_{unlike}(m) = \alpha(m) \times \Delta N_{like}(m)$$

.

Figure. 3.42 shows the ratio of unlike sign residue background to all subtracted background in 5 centrality bins. The left panel shows the mass range up to 3 GeV and the right panel shows the mass range between $0.2 < m < 1.0 \ GeV$ for a more detailed look in this important region. It is seen that the residue backgrounds in all centrality bins are flat in mass and consistent with 0.
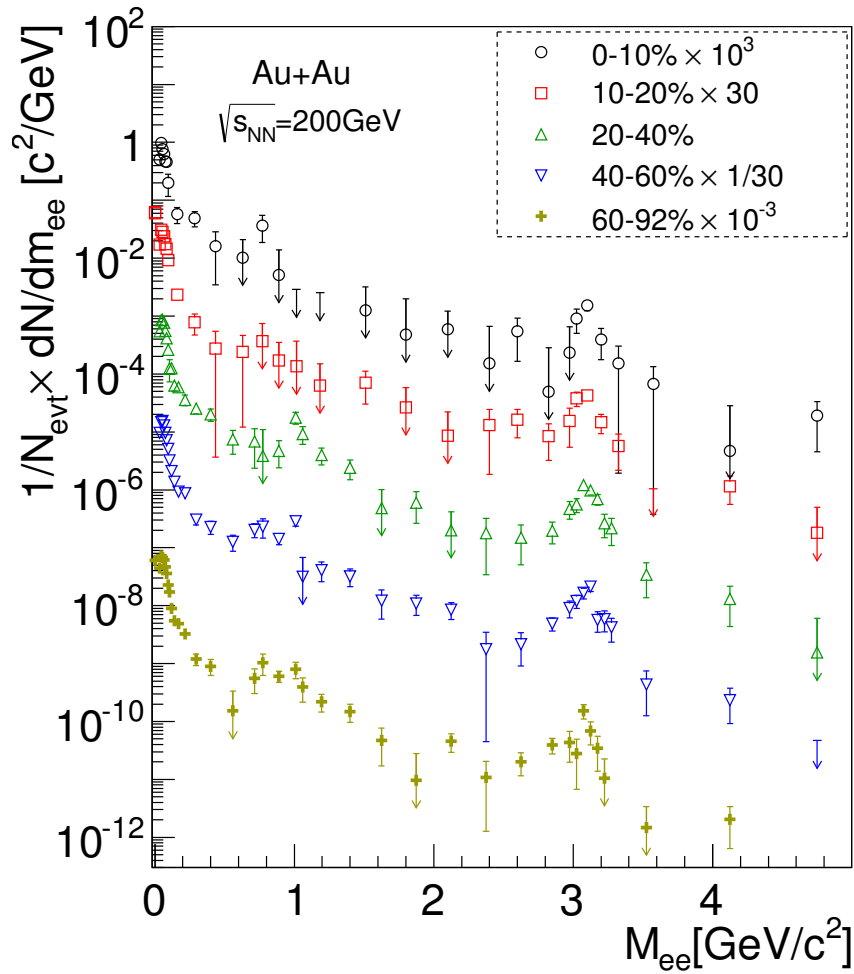
Figure 3.41: Raw unlike sign spectra after subtracting all background components in 0-10%, 10-20%, 20-40%, 40-60% and 60-92% centrality bin.
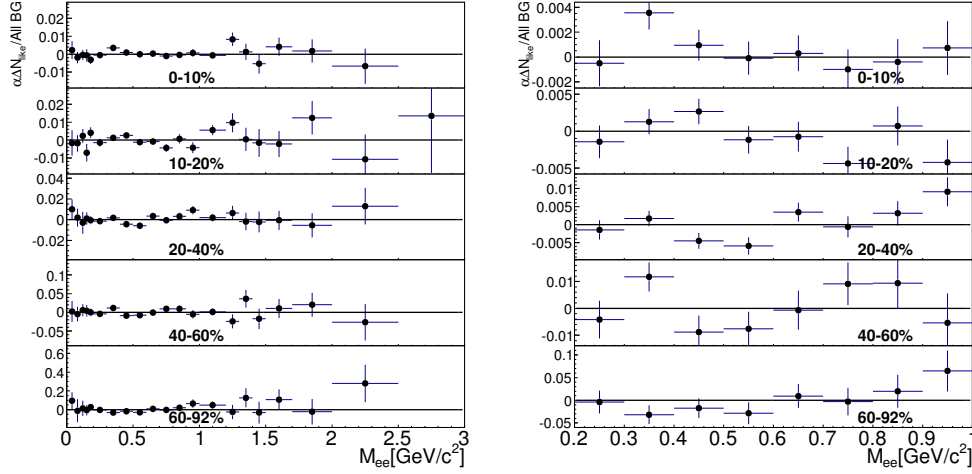
Figure 3.42: Unlike sign residue background to all background ratio in 0-10%, 10-20%, 20-40%, 40-60% and 60-92% centrality bins. The Unlike sign residue background is estimated from α corrected like sign residue background. The left panel shows the ratio in mass range $0 < m_{ee} < 3\ GeV/c^2$. The right panel shows it in $0.2 < m_{ee} < 1.0\ GeV/c^2$.

3.6   Efficiency Correction

The total efficiency can be decomposed into three components, and be studied separately,

$$\epsilon_{pair}^{total} = \epsilon_{pair}^{cut} \cdot \epsilon_{pair}^{embed} \cdot \epsilon_{pair}^{TOF} \tag{3.20}$$

The first term describes the effect of all the cuts (except for the TOF cut) in the track reconstruction. The second term is the central arm "embedding efficiency", which results from the effect of particle occupancy on the track reconstruction and is dependent upon the event centrality. The last term evaluates the efficiency of the TOF cut, which had to be calculated separately because the variable was not reproduced by the PISA simulation package.

3.6.1   Cut Efficiency For Dielectron Pairs

We used standard PISA simulation package for run 10 to calculate this efficiency ϵ_{pair}^{cut}.

135

Event Generation was done by using technique described in Ref. [81] [82] (analysis of dielectron spectra in $d + Au$ collisions) which consists of generating electron positron pairs flat in the $m, p_T, \eta, \phi, \theta^*, \phi^*$ space. For normalization, only events with at least two electrons that fall into the PHENIX central arm acceptance (in ϕ vs. α[9] 2-D space as shown in Fig. 3.43, also called the Butsyk aperture) are kept aside. The m vs p_T spectrum of this normalization sample is of course not flat and shows the features expected from a two-arm spectrometer (valley at $m \approx p_T$). This normalization distribution is shown on the right panel of Fig. 3.43. In order to avoid dealing with edge effects, the acceptance into which the correction is done is slightly narrower than the fuzzy edges seen in the data at the edges of the various detectors. With this choice, the generated tracks are produced with a slightly wider acceptance than actual PHENIX, and then are passed through the full GEANT4 PHENIX detector simulation chain. At the end when both the numerator and denominator mass vs p_T distributions are calculated, they are filtered through the narrower acceptance, which is also applied to the real data and is defined by equations Eq. 3.21 for the west arm and Eq. 3.22 for the east arm.

$$(-0.570 < \phi + \frac{q \times 0.118}{p_T} < 0.983) \; and \; (-0.570 < \phi + \frac{q \times 0.060}{p_T} < 0.983) \tag{3.21}$$

$$(2.153 < \phi + \frac{q \times 0.118}{p_T} < 3.718) \; and \; (2.153 < \phi + \frac{q \times 0.060}{p_T} < 3.718) \tag{3.22}$$

PISA + Reconstruction simulation the GEANT part of this MC is done using the official Run10 PISA simulation setup. Full HBD including support structures is simulated. The simulation was done with perfect detector configuration. The DC/PC1 dead maps and the HBD dead map, which held responsible for the majority of dead areas, were applied to the reconstructed tracks after simulation. The time of flight variable of EMCal and ToFE detector could not be reproduced by the PISA simulation. Since the TOF cut is a simple sigmalized cut with an efficiency of $\sim 87\%$, independent of p_T and centrality, the TOF efficiency ϵ_{pair}^{TOF} is applied as a multiplicative factor. It was estimated separately in Sec. 3.6.3.

---

[9]α describes the angle between a straight line which connects the vertex to the track position at the middle of the DC and the tangential line to the track at the DC middle.
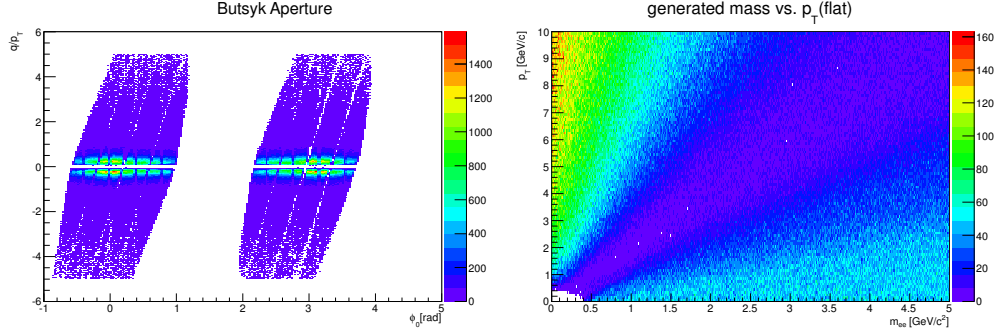
Figure 3.43: Top: The Butsyk acceptance plot. This acceptance is determined by the magnetic field configuration (+- and -+) for run 10. Bottom: The flat generated pairs after filtering through Butsyk aperture. Notice the valley at $mass \approx p_T$

HBD Embedding. Simulated HBD responses to MC electron tracks are embedded into real HBD data of a chosen centrality. This imitates electron Cherenkov blobs falling amid centrality-dependent scintillation light inside the HBD. The LBS algorithm reconstructs HBD signal clusters from the embedded data. The same procedure is also used for determining the HBD efficiency and is described in Sec. 3.3.3.

Pair Efficiency Weighting

The efficiency is applied in the mass projection. Because the electron pairs were generated flat in $(m, p_T, \eta, \phi, \theta^*, \phi^*)$ space, weighting must be applied to achieve a realistic pair m vs. p_T distribution. Otherwise, in regions of very steep variations of efficiency or pair yield, it could lead to mistakes in the efficiency. In the m vs. p_T 2-dimensional space, in the mass dimension, a hadronic cocktail filling a fine binned histogram (with 1 MeV bins in mass) was generated to use as a weighting function. The meson resonance peaks on the cocktail were removed to avoid weighting bias due to detector resolution. The mass regions where the peaks sit are interpolated with smooth curves. In the p_T dimension, to realistically describe the pair p_T distribution at mass m, a Hagedorn function,

$$cocktail H(p_T) = \frac{c}{(exp(-ap_T - bp_T^2) + p_T/p_0)^n} \tag{3.23}$$

is used for mass < 140 MeV, and a modified Hagedorm function, in which p_T in Eq. 3.23 is replaced with $\sqrt{p_T^2 + m^2 - m_\pi^2}$, is used for mass > 140 MeV[10]. The functions are parameterized to describe the PHENIX measured $Au + Au$ meson data (see Tab. 3.10 for exact parameter values). The actual procedure for a pair of m^0 and p_T^0 is

- Obtain the modified Hagedorn function at m^0, which can be denoted by $H_{m^0}(p_T)$.

- Calculate the mean of function $H_{m^0}(p_T)$: $< p_T^{H_{m^0}} >$. Normalize $H_{m^0}(p_T)$ such that the mean equals the cocktail yield at given mass m^0: $N_0 \times < p_T^{H_{m^0}} >= Cocktail(m^0)$, where N_0 is the normalization factor and Cocktail(m) is the cocktail yield at mass m.

- The weight for the pair is then calculated as $w(m^0, p_T^0) = N_0 \times H_{m^0}(p_T^0)$

The numerator, m vs. p_T distribution (fully reconstructed pairs, passing the full set of analysis cuts which include Butsyk aperture, detector dead map cut, single, HBD and pair cuts), and denominator, m vs. p_T (generated pairs passing Butsyk aperture), are then filled from the reconstructed and generated pairs respectively, using the above weighting function, and projected onto the pair mass axis. Fig. 3.44 presents the unweighted and weighted mass spectrum for the generated and reconstructed tracks. The ratio of the numerator to the denominator is used as the efficiency for cuts and reconstruction ϵ_{pair}^{cut}, and is shown in Fig. 3.50 as a function of mass for the 5 centrality bins in the analysis.

Figure. 3.45 shows the comparison of eID variables between the simulation and data from $60 - 92\%$ centrality bin. The data generally are well described by the simulation. The vertical lines denote the cut values on the variables. For comparison to the HBD charge of single electrons (the 2nd panel from left in the second row), one MC electron track was generated for every event and embedded into $60 - 92\%$ data to account for the background scintillation in real $Au + Au$ collisions. The blue curve is HBD charge from open Dalitz electron pairs in $60 - 92\%$ data. The pairs are selected by all central arm eID

---

[10]In the intermediate mass, the contribution from open charm becomes significant. We tested the weighting method by replacing the modified Hagedorn function with open charm decay electron p_T distribution produced from MC@NLO, in the mass range $1.5 < m < 2.5$. The resulting efficiency is very similar to the Hagedorn result.
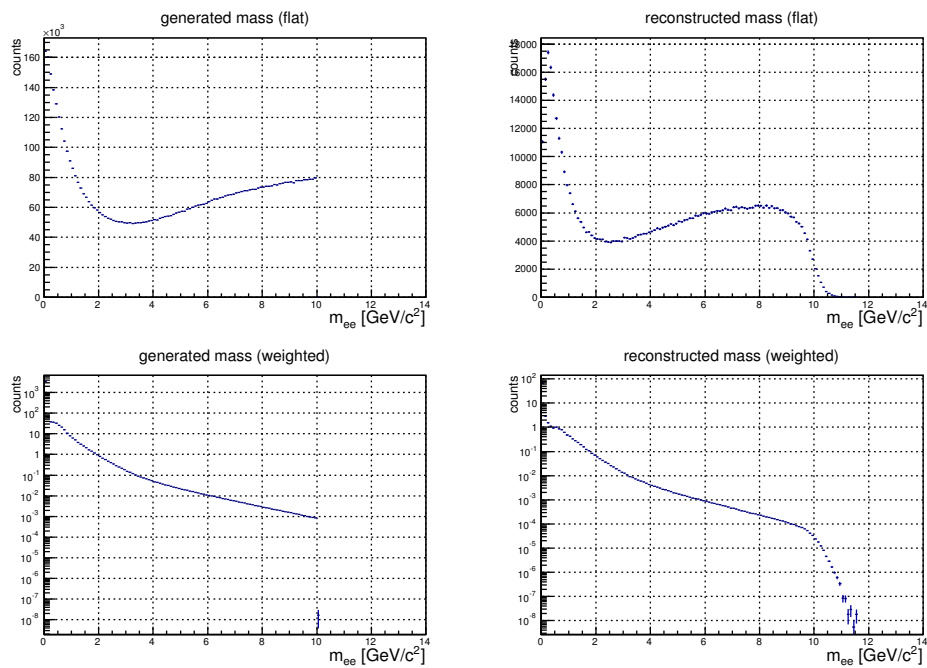
Figure 3.44: Upper left: Unweighted generated pair mass spectrum. Upper right: Unweighted reconstructed pair mass spectrum. Lower left: weighted generated pair mass spectrum. Lower right: weighted reconstructed pair mass spectrum.

cuts, a mass cut of $30 < m < 100\ MeV$ and a ϕ_V[11] cut of $1.0 < \phi_V < 2.3\ rad$. However it is still difficult to get a clean sample of single electrons from data without using HBD information. An extra conversion peak at HBD $q \sim 5\ p.e.$ can be seen in the data. A comparison of the MC HBD charge to single electron HBD charge in $p+p$ collisions, where conversion electrons are fewer, is therefore presented in Fig. 3.46.
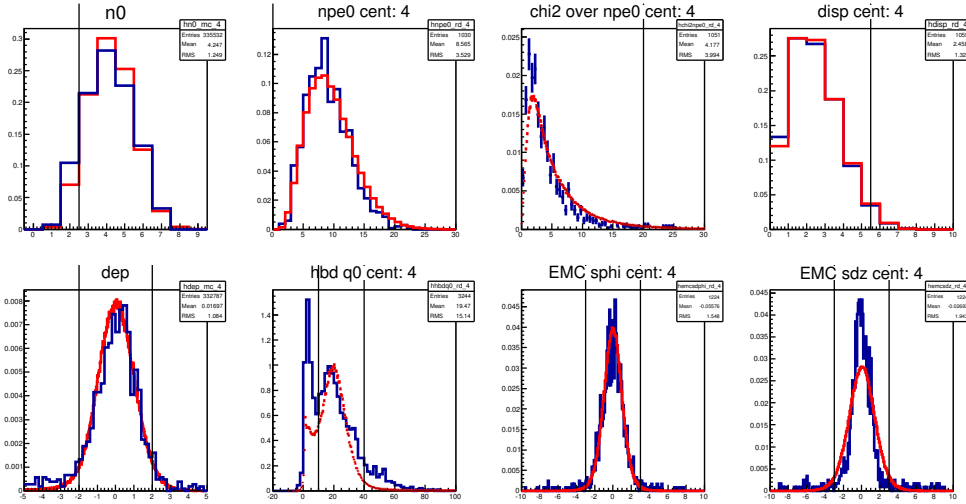
Figure 3.45: Comparison of eID variables between simulation and data from $60 - 92\%$ centrality bin.

In Fig. 3.46, the red curve is the single electron HBD charge in simulation without embedding, as the background in $p+p$ is low. The blue is made by open Dalitz pairs in $p+p$, where the pairs are selected by $m < 150 MeV$ and opening angle $> 300\ mrad$ after passing standard central arm eID cuts. The HBD charge shows reasonable agreement between the data and the simulation. Fig. 3.47 demonstrates the good agreement of HBD cluster matching between data(blue) and HBD-embedded MC(red).

---

[11]The opening angle between a pair projected onto the direction parallel to the magnetic field. As magnetic field does not bend charged tracks in the direction of its field lines, conversion pairs exhibit near-0 ϕ_V angles.
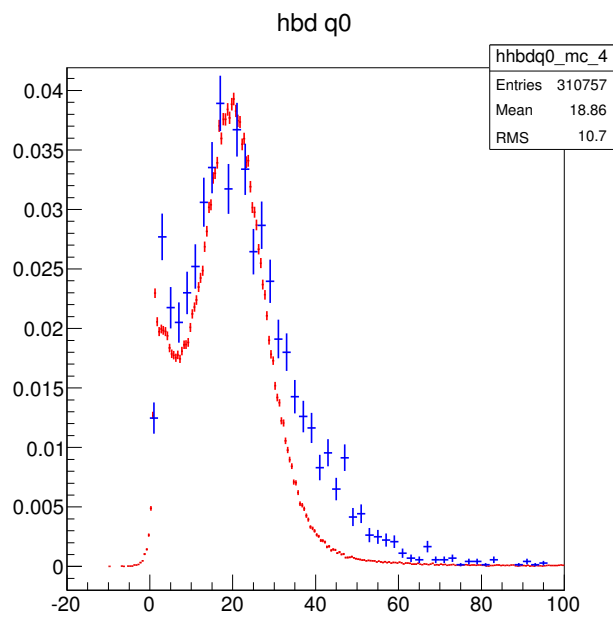
Figure 3.46: Comparison of single electron HBD charge in MC and in $p + p$ collisions.
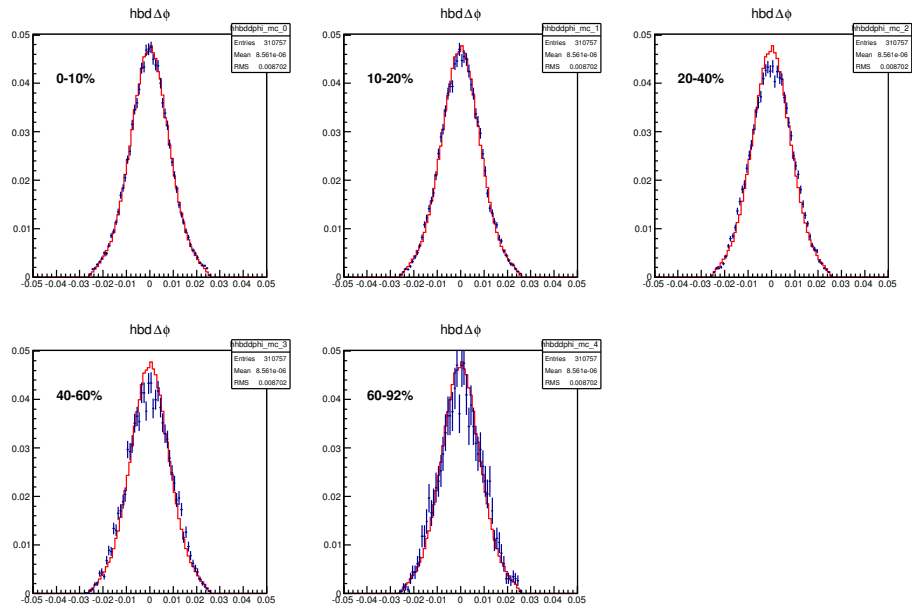
Figure 3.47: Comparison of single electron HBD matching in HBD-embedded MC(red) and in $Au + Au$ collisions(blue) in the 5 centrality classes.

142

3.6.2 Central Arm Embedding

The occupancy of charged particles in the detectors affects the track reconstruction efficiency. When occupancy is high, a fraction of tracks get lost by the reconstruction algorithm. The corresponding efficiency ϵ_{pair}^{embed} is thus studied by a standard PHENIX central arm embedding strategy. It embeds simulated tracks into measured events in all relevant central arm detectors, then reconstructs these tracks using the standard analysis chain. For the present analysis, we used the central arm embedding files produced by the Weizmann group (Ref. [89]), which contains information on the MC tracks reconstructed without embedding and the same set of reconstructed MC tracks from embedded events[12]. The same set of central arm cuts (except for TOF, which was treated separately) were then applied to both groups of reconstructed tracks. The resulting efficiency $\epsilon_{single}^{embed}$ for single tracks is listed in Table. 3.9. It decreases as the collisions get central and multiplicity increases. The numbers are also compared to the results of past PHENIX electron analysis, Ref. [12], which used very similar cuts. The numbers between the two analyses are consistent.

For systematic uncertainty studies, we used a tighter and a looser set of central arm cuts by varying the two most important electron identification variables: n0 and dep, as shown in Table. 3.9. The looser set of cuts exhibits little significant difference in centrality dependence compared to the normal cuts, while the tighter set displays a slightly stronger centrality dependence.

We note that the reconstruction efficiency $\epsilon_{single}^{embed}$ found with the central arm embedding, while strongly dependent on centrality, exhibits no measurable p_T dependence, and therefore can be applied as a multiplicative correction for each centrality class, as has been done in previous PHENIX analyses. For pair efficiency, ϵ_{pair}^{embed} is simply the square of $\epsilon_{single}^{embed}$ and it varies from 57.6% to 92.5% going from central to peripheral collisions. In the most central events in 0-10% bin, the variation of pair efficiency between the three sets of cuts is roughly $\pm$ 4.5%; for the 10-20% bin, a variation of $\pm 3\%$ is observed, and for all other bins the variation is negligible.

---

[12]Special care was taken to make sure that the RICH reconstruction algorithm, which was slightly modified by the Weizmann group [89], was corrected to stay consistent with the present analysis. This is confirmed by ensuring that after embedding, the tracks have the same or larger number of photomultipliers assigned as in the case of our analysis.

	n0	dep	EMC match	disp	$\frac{\chi^2}{npe0}$	0-10%	10-20%	20-40%	40-60%	60-92%
default	> 2	$\|\| < 2$	< 3	< 5.5	< 20	.759	.823	.882	.932	.962
tight	> 3	$\|\| < 1.5$	< 3	< 5.5	< 20	.719	.805	.868	.929	.961
loose	> 1	$\|\| < 2.5$	< 3	< 5.5	< 20	.777	.843	.882	.932	.958
Ref. [12]	> 3	$-2 << 3$	< 2	< 5	< 10	.771	.835	.90	.952	982

Table 3.9: Central arm embedding efficiency for different cut settings and centrality bins. Given is the reduction of the single track efficiency once embedded in events of a certain centrality class. we compare the default cuts used in our analysis to tighter and loser cuts. We also compare our result to the results from Ref. [12].

3.6.3 Correction for the TOF cut

The efficiency for the TOF cut was verified using data. For a single sided 1.5 σ cut on each track, one expects a 87.0% efficiency for the pairs following a normal distribution, considering the cut was placed at 1.5σ at the upper side, accepting 93.3% of single tracks. We have compared the foreground pairs for an analysis with a 1.5 σ cut to a 2.5 σ cut. The data as a function of mass and the ratio of the data sets is shown in Fig. 3.48 for the most peripheral event class. The ratio is consistent with 87%, as expected. There may be a small mass dependence which indicates that for momenta above about 1 GeV/c the width of the ToF distribution is underestimated and fewer tracks are lost. This may lead to an up to 10% underestimate estimate of the efficiency above 1 GeV/c, which we include in the systematic uncertainty.

The left panel in Figure. 3.48 shows the unlike sign foreground in the most peripheral bin, where electron purity is highest ($> 99\%$ as shown in Table. 3.3 in Sec. 3.3.2). The red points are made with 1.5σ TOF cut, and the blue are made with 2.5σ TOF cut. The pair efficiency expected for the 1.5σ cut is 87.0% while for the 2.5σ cut is 98.8%. The right panel is the FG12 ratio of 1.5σ over 2.5σ. We fit the ratio with a constant from 0 to 2 GeV/c^2 in mass, as shown in the red dashed line. The constant is determined to be 0.886 ± 0.008, which is consistent with $87.0\%/98.8\% = 0.881$. .

In addition to the 1.5σ cut, we discovered that a fraction of low momentum electrons did not have reasonable time of flight values in the PbSc. The tof values are above 30ns for those tracks, which is clearly too slow for a dis-
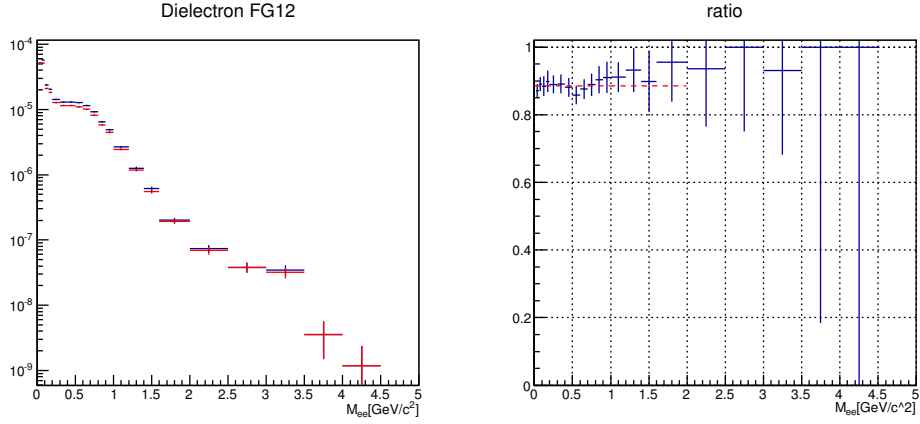
Figure 3.48: Left panel: FG12 in $60 - 92\%$ bin with TOF cut at 1.5σ(red) and at 2.5σ(blue). Right panel: $60 - 92\%$ bin FG12 ratio of 1.5σ and 2.5σ.

tance of ~ 6m from the event vertex to the EMCal. Fig. 3.49 shows the ratio of electrons tracks in PbSc with good tof ($< 30ns$) over all tracks in PbSc, as a function of momentum. The ratio is found to be centrality independent. The red curve is a fit through the ratio vs. momentum and the efficiency loss is corrected by implementing the fit into efficiency calculation.

The efficiency correction is done in mass dimension only. The raw subtracted yields are divided by the total efficiency to obtain the efficiency corrected yields. The final total efficiency for the five centrality bins are shown in Fig. 3.50
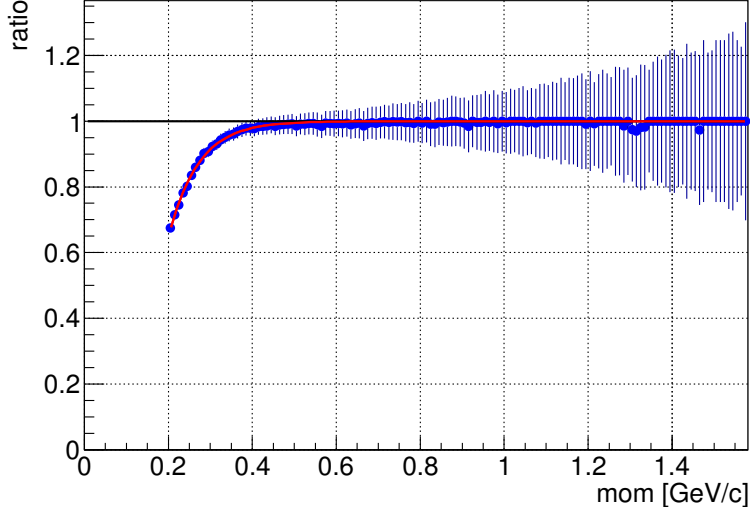
Figure 3.49: The ratio of tracks in PbSC with tof < 30ns over all tracks in PbSc, as a function of momentum in minimum bias collisions. The red curve denotes a fit to the points. The ratio is found to be centrality independent.

3.7 Hadronic Cocktails

This analysis is done in parallel to Yosuke Watanabe's dielectron analysis, described in Ref. [89] [18]. When comparing results from the two analyses, we decided both results should compare to the same hadronic cocktail generated by the Weizmann group. The MC generation is described in detail in Ref. [89] [18]. Here we include a sketch of the procedures.

The hadronic cocktail is generated with EXODUS, PYTHIA [116] and MC@NLO [71] [111]. The EXODUS simulation handles the photonic and non-photonic decay electrons from a variety of neutral mesons. The electron pairs from semi-leptonic decays of open heavy flavor (charm and bottom), are generated by PYTHIA. The hadrons have uniform distribution over both pseudorapidity $|\eta| < 0.35$ and azithmuthal angle $0 < \phi < 2\pi$. The simulations are filtered through the ideal PHENIX acceptance and smeared with the detector resolution.

The EXODUS package produces decay electrons from the various decay channels of meson sources, which include π^0, η, ρ, ω, η', ϕ and J/ψ. The dominant π^0 spectrum is the primary input the EXODUS relies on, and

146
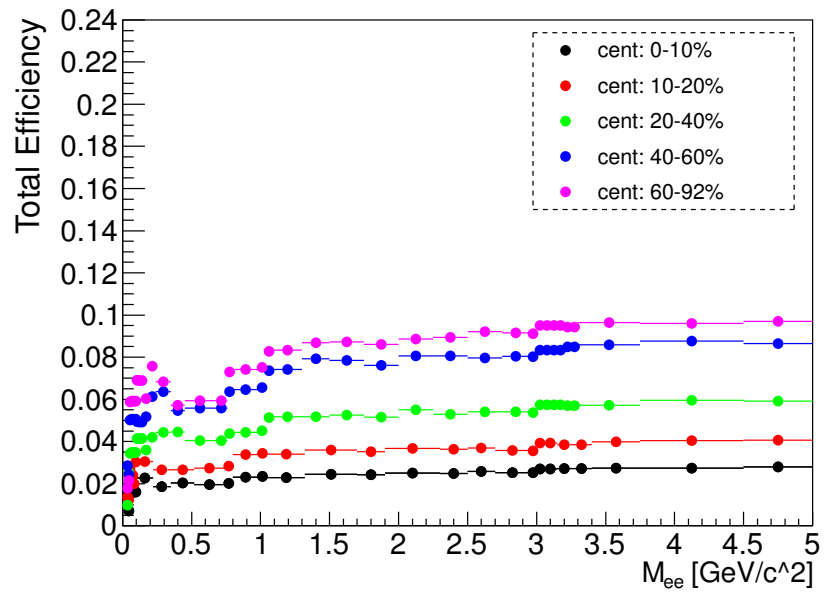
Figure 3.50: Pair efficiency as a function of pair invariant mass. For centrality 0-10%, 10-20%, 20-40%, 40-60% and 60-92%.

centrality	c	a	b	p_0	n	$\frac{dN_\pi}{dy}$
0-10%	1331	0.57	0.19	0.74	8.4	219
10-20%	1001	0.53	0.16	0.75	8.3	153
20-40%	634	0.43	0.11	0.79	8.5	88
40-60%	313	0.36	0.13	0.76	8.4	33
60-92%	81.9	0.33	0.088	0.74	8.4	6.4

Table 3.10: Pion input parameters for EXODUS.

is generated from realistic p_T distribtutions, characterized by a Hagedorn function:

$$E\frac{d^3\sigma}{d^3p} = \frac{c}{(exp(-ap_T - bp_T^2) + p_T/p_0)^n} \qquad (3.24)$$

The parameters a, b, c, p_0 and n are fixed by fitting simultaneously to published PHENIX π^0 [9,27] and π^+ π^- [26] measurements. The values used are listed in Table. 3.10. dN_π/dy is estimated by integrating the function over p_T.

The p_T distributions of other light mesons are obtained by m_T scaling [10] of the Haggedorn function eq. 3.24, namely, the p_T in eq. 3.24 is replaced by $\sqrt{p_T^2 + m_{meson}^2 - m_\pi^2}$. The p_T distribution is normalized by the ratio of the meson's invariant yield to that of π^0 at high p_T. The ratios are given in Table 3.11. The numbers listed are measured in $p + p$ collisions, however, in $Au + Au$ collisions the suppression of mesons at high p_T are similar to π^0, so the relative yield of various mesons to π^0 is believed to be the same as in $p + p$ collisions. Tab. 3.12 lists the rapidity density dN/dy of light mesons as the input parameters to EXODUS in the five centrality selections.

The J/ψ produced by EXODUS also uses m_T scaling from the π^0 p_T spectrum in $p + p$ collisions. The produced decay electrons are then fed into a full PISA simulation to reproduce the detector resolution and the line shape. The resulting spectrum is normalized to the measured $p + p$ cross section, and then scaled to $Au + Au$ situation by the number of binary collisions N_{coll} and the suppression factor R_{AA} for individual centrality class.

The electron pairs originating from open heavy flavor semi-leptonic decays are handled by MC@NLO [71,111] and PYTHIA [116]. The MC@NLO is a next-to-leading-order Monte Carlo simulation which produces hard scattering events. Herwig [63] subsequently takes those events for fragmentation in

meson	η	ρ	ω	η'	ϕ
meson/π^0	0.48	1.00	0.90	0.25	0.40

Table 3.11: meson to π^0 ratio in $p + p$ collisions at high p_T ($p_T \geq 5 \; GeV/c$).

centrality	π^0	η	ρ	ω	η'	ϕ
0-10%	219	30	30	26	4.3	5.6
10-20%	153	21	21	18	3.0	3.9
20-40%	88	11	11	10	1.7	2.2
40-60%	33	3.8	3.9	3.4	0.56	0.76
60-92%	6.4	0.65	0.65	0.55	0.089	0.12

Table 3.12: dN/dy of light mesons as inputs to EXODUS in the five centrality classes.

vacuum. On the other hand, PYTHIA uses leading-order perturbative QCD for heavy flavor production. The PYTHIA and the MC@NLO simulations are passed through ideal PHENIX acceptance in "+-" field, which is described in Sec. 3.6.1. The open heavy flavor contributions from both generators are first normalized to $p + p$ cross sections, and are scaled by a factor of N_{coll} for $Au + Au$ collisions.

Ref. [19] presents estimates of the cross sections of $c\bar{c}$ and $b\bar{b}$ in $p+p$ events, deduced from fitting $d + Au$ dielectron mass spectra at $m > 1.15 GeV/c^2$ with simulated heavy flavor spectra generated by PYTHIA and MC@NLO, and then scaled down to $p + p$ multiplicity. The $b\bar{b}$ cross section is found to be $1.36\pm0.32(stat)\pm0.44(syst)\mu b$. However for $c\bar{c}$, the cross section is generator dependent. PYTHIA yields a cross section of $106 \pm 9(stat) \pm 33(syst)\mu b$ whereas it is $287\pm29(stat)\pm100(syst)$ for MC@NLO. The difference, though not significant at higher mass above $1.5 \; GeV/c^2$, leads to a visible difference at lower mass region in $0.5 < m < 1.0 \; GeV/c^2$.

The total cocktail is normalized by fitting the sum of the cocktail and direct virtual photon to the precisely measured e^+e^- data in a restricted phase space, given by $m_{ee} < 1 GeV/c^2$ and $p_T/m_{ee} > 5$, where the yields are predominantly π^0 Dalitz decays, with a small contribution of direct virtual photons and smaller still, η Dalitz decays. All three show a $1/m_{ee}$ dependence in their mass spectra and their relative magnitudes are known from PHENIX measurements [11] [16] [14].

Fig. 3.51 shows the hadronic cocktail generated for minimum bias $Au+Au$
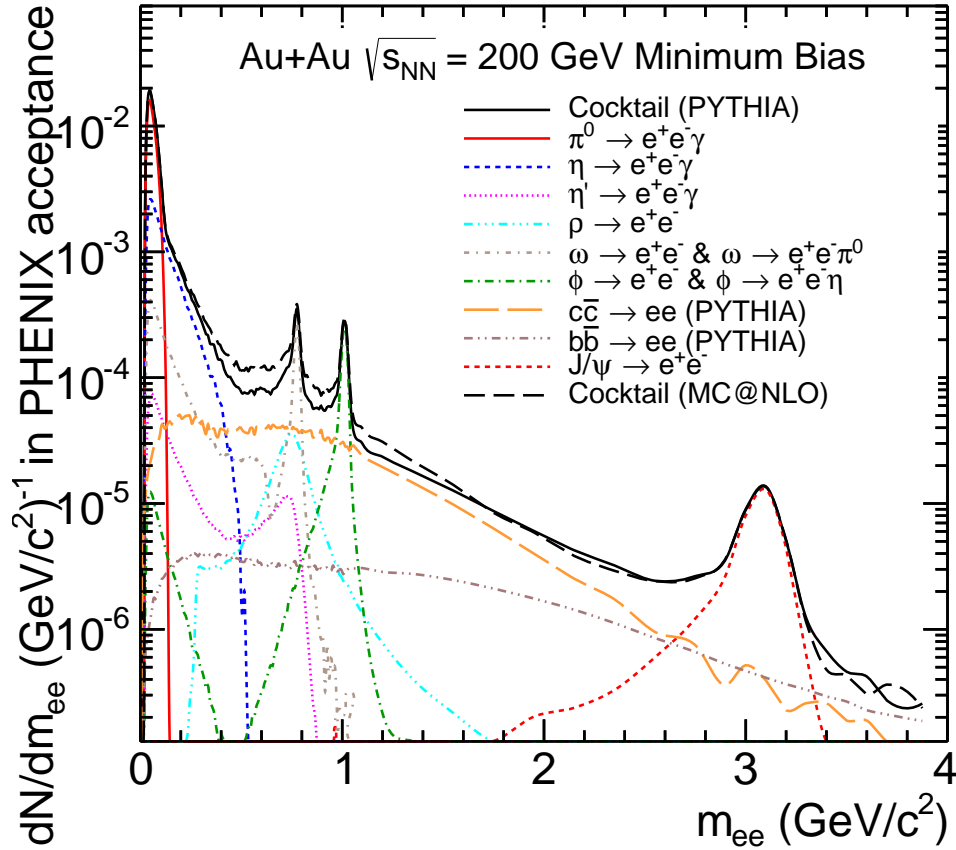
Figure 3.51: Cocktail generated for Minimum Bias $Au + Au$ events [18].

collsions [18]. The various cocktail ingredients are represented by the colored curves. The solid black line denotes the sum of all components with open heavy flavor generated by PYTHIA. The dashed black line has PYTHIA replaced with MC@NLO. The two exhibit a noticeable difference at the region $0.5 < m_{ee} < 1.2 \ GeV/c^2$, due to the intrinsic difference in the generators. In keeping with all previous published PHENIX dielectron measurements, we decide to use the PYTHIA result as was done in the previous PHENIX measured dielectron spectra in $Au + Au$ collisions.

The systematic uncertainties on the various cocktail components are evaluated and propagated to determine the total systematic uncertainty of the cocktail. They include,

- *Light meson to π^0 ratio.* We used the same systematic uncertainties as Ref. [10]. They are 30% for η, ω and ϕ. For ρ it is 33%, and 100% for η'.

- *Direct Photon.* The systematic uncertainties for dN/dy of direct photons are centrality dependent. They range from 24% to 70% from central to peripheral events. The values are evaluated in Ref. [17].

- *Open heavy flavor $c\bar{c}$ and $b\bar{b}$.* The systematic uncertainty for the cross sections of $c\bar{c}$ and $b\bar{b}$ are estimated in Ref. [19]. We assign 33 μb for $c\bar{c}$ uncertainty and 0.44 μb for $b\bar{b}$. The systematic uncertainties on N_{coll} for all centrality classes are listed in Table. 3.1. The uncertainties on the cross sections and N_{coll} are summed in quadrature.

- *J/Ψ.* 14% systematic uncertainty on J/Ψ cross section in $p+p$ collisions is obtained from Ref. [15]. Centrality dependent systematic uncertainties on J/Ψ R_{AA} ranges from 22% to 35%, as estimated by Ref. [7]. The uncertainties are added in quadrature.

Fig. 3.52 shows the systematic uncertainties on the individual cocktail ingredients. The total systematic uncertainty is determined by their quadratic sum, and is denoted by the green line. It is slightly mass dependent and is approximately 25% in the entire mass range shown.

3.7.1 Signal To Background Ratio

Now that we have all the ingredients, it is suitable to give an estimation of the signal to background ratio in the analysis. The estimation is made by dividing the hadronic cocktail, which is approximately the signal expectation, by the efficiency corrected total background, thus we obtain Fig. 3.53, which plots the Cocktail to Background ratio (C/B) vs. mass for the five centrality classes and the minimum bias events. At mass outside the ρ mass region, $S/B \sim C/B$. At $m_{ee} \sim 600 \ MeV/c^2$, $S/B \simeq C/B \times f^{enh}$, where f^{enh} is the enhancement factor at ρ mass.

As expected, the most central bin 0-10% where the multiplicity is highest, exhibits the smallest overall S/B ratio, whereas the most peripheral bin 60-92% shows the largest. All centrality bins show the smallest S/B ratio at $m_{ee} \sim 600 \ MeV/c^2$, indicating this is the mass region most affected by
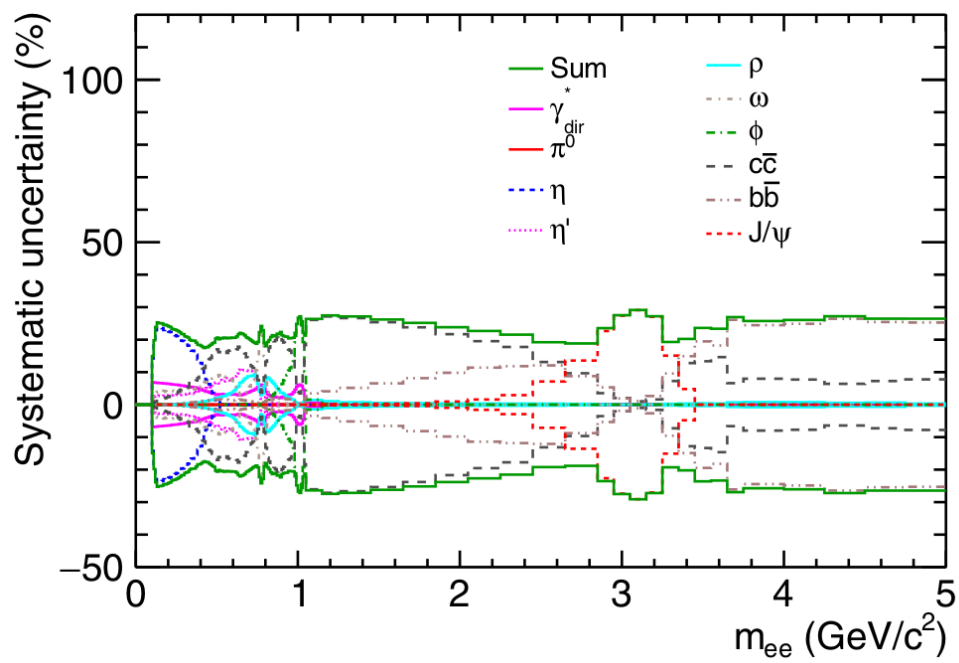
Figure 3.52: Systematic uncertainty on the total cocktail and its components in minimum bias $Au + Au$ collisions. [18].

the large size of the background. Taking into account the low mass enhancement observed by experiments at around $m_{ee} \sim 600 \ MeV$ in $Au + Au$ collisions, with an observed enhancement factor f^{enh} around 2 for minimum bias events [18] [4] [2], we estimate that, in the most central events the worst S/B ratio drops to $\sim 1 : 800$, in the most peripheral events the S/B reaches the minimum of $\sim 1 : 30$, while the minimum S/B is approximately $1 : 500$ for minimum bias events.

In the mass region of $0.15 < m_{ee} < 0.75 \ GeV/c^2$, the parallel analysis reaches a C/B ratio of $1/250$ for minimum bias events [18], while in the previous PHENIX measurement, the C/B over the same mass window is estimated to be $1/600$ [10] [18]. In comparison, we estimate a C/B value of $\sim 1/375$ for the present analysis at the same mass range and the same multiplicity. The new measurement demonstrates improved signal sensitivity compared to the previous one. On the other hand, the C/B ratio of present analysis is a factor of 1.5 lower than the parallel analysis. This is due to the superior electron identification adopted by the Weizmann group, who has developed and optimized three different eID neural networks and is able to achieve an electron purity of above 95% for all centralities. More details in the parallel analysis will be described in Sec. 4.2.

We can also compare S/B to the plot of the ratio of residual background to total background in Fig. 3.42. For the most central events in the 0-10% bin, at $m_{ee} \simeq 600 MeV/c^2$ where the situation is the worst, the S/B reaches a minimum of $1/800 = 0.00125$, more than two times the ratio of residual background to total background, 0.0006. We can use this information to make a rough estimation on the systematic uncertainty from the background subtraction on the worst point of the mass spectrum, and it leads us to a $\sim 48\%$ systematic uncertainty on the final result. This is acceptable, considering we do not suffer so severely from S/B elsewhere. We conclude that after much effort we have achieved acceptable precision of background control.
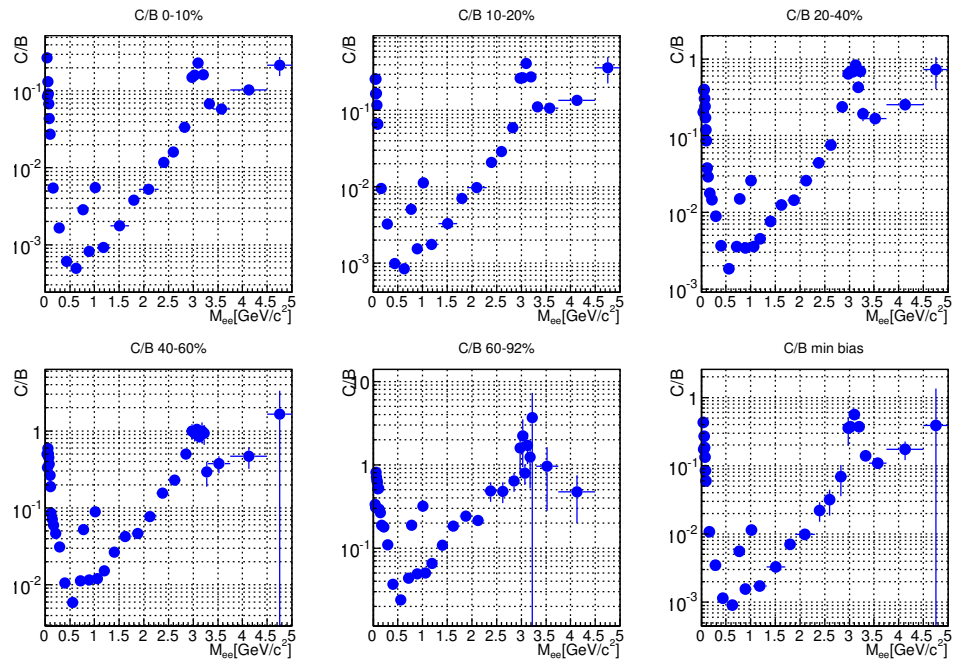
Figure 3.53: Cocktail To Background ratio as an estimation for Signal To Background ratio in centrality 0-10%, 10-20%, 20-40%, 40-60%, 60-92%

uncertainty source	N_{like}	cross pairs	e-h pairs	jet(near)	jet(away)
most affected mass regions (GeV/c^2)	0.4-2.0	0.1-0.2	0-0.25	0.1-0.4	0.5-2.5
$0 - 10\%$	27%	2%	10%	4%	15%
$10 - 20\%$	23%	3%	6%	10%	9%
$20 - 40\%$	10%	5%	1%	6%	5%
$40 - 60\%$	11%	2%	1%	6%	12%
$60 - 92\%$	8%	1%	$< 1\%$	3%	12%

Table 3.13: Systematic uncertainty on the final spectra due to the statistical uncertainties of the various background components in the background subtraction. The numbers listed are calculated as $\Delta Y(m_{ee})/Y(m_{ee})$ where $Y(m_{ee})$ denotes the yield of the corrected spectra at m_{ee}, and are averaged in the mass windows listed in the second row.

3.8 Systematic Uncertainty

3.8.1 Systematics in Background Normalization

The major contributor to the systematic uncertainty comes from the background normalization, due to the high level of the combinatoric. Four factors of uncertainty in the normalization was taken into account:

- Statistical uncertainty in determination of the normalization factors of the various components, among which the combinatorial normalization factor plays the pivotal role.

- Background shape difference between absolute normalization and the component fitting normalization.

- Uncertainty from the flow modulation due to the uncertainty in the measured v_2 values.

- Variation of κ with z vertex.

The statistical uncertainty of the normalization factors are given in Table. 3.7. The systematic uncertainty resulting from the statistical errors of the various components and their most affected regions are listed in Tab. 3.13.

	$0-10\%$	$10-20\%$	$20-40\%$	$40-60\%$	$60-92\%$
$\Delta Y(m_{ee})^{norm}/Y(m_{ee})$	7.7%	6.5%	6.9%	7.9%	$< 5\%$

Table 3.14: Shape difference caused systematic uncertainty $\Delta Y(mee)^{norm}/Y(m_{ee})$, where $Y(m_{ee})$ denotes the yields at mass m_{ee} of the corrected dielectron spectra. The numbers listed are averaged in mass region $0.3 < m < 2.0 GeV/c^2$

	$0-10\%$	$10-20\%$	$20-40\%$	$40-60\%$
$\Delta Y(m_{ee})^{flow}/Y(m_{ee})$	7.3%	7.9%	7.9%	4%

Table 3.15: Systematic uncertainty of flow $\Delta Y(mee)^{flow}/Y(m_{ee})$, where $Y(m_{ee})$ denotes the yields at mass m_{ee} of the corrected dielectron spectra. The numbers listed are averaged in $500 < M < 700 MeV/c^2$ and $1.0 < M < 2.5 GeV/c^2$, where the shape difference caused by flow modification is biggest.

The background shape difference was given by taking the difference between absolute normalization results and the component fitting normalization results. As discussed in Sec. 3.5.7, the fitting factor for each component denotes the deviation from the absolute normalization. The uncertainties in the correlated background sources are therefore given by the difference between absolute normalization and the best fit result. The uncertainties are calculated bin-by-bin for the final spectra. This systematic uncertainty in the mass region $0.2 < m < 2.0 GeV/c^2$ is shown in Tab. 3.14. At higher mass, the uncertainty becomes smaller.

The uncertainty from flow was not included in the background shape because of the way the flow effect is implemented. The Run7 single electron flow measurement estimated a 10% uncertainty in Ref. [12]. Therefore, we scaled the flow v_2 vs. p_T curves up and down by 10%, then used the two curves as the upper and lower flow limit to weight the mixed events. Fig. 3.18 and Fig. 3.19 illustrate the upper and lower flow curves used in calculating this uncertainty. The component fitting normalization was performed separately for each case. Because of the shape dependence, they gave an upper and a lower uncertainty for each bin in the final spectra. The flow gives the biggest uncertainty in $500 < m < 700\ MeV/c^2$, and in $1.0 < m < 2.5 GeV/c^2$. The biggest uncertainty for each centrality bin is listed in Tab. 3.15.

As mentioned in Sec. 3.5.8, the κ factor has a variation with respect to

	$0-10\%$	$10-20\%$	$20-40\%$	$40-60\%$	$60-92\%$
$\Delta Y(m_{ee})^{\kappa}/Y(m_{ee})$	16.4%	7.7%	5%	2%	$<1\%$

Table 3.16: Systematic uncertainty from κ $\Delta Y(mee)^{\kappa}/Y(m_{ee})$, where $Y(m_{ee})$ denotes the yields at mass m_{ee} of the corrected dielectron spectra. The numbers listed are averaged in mass region $0.3 < m < 2.0 GeV/c^2$

the event z vertex. Fig. 3.40 shows a study of κ variation as a function of z vertex bin number in 6 centrality bins. The z vertex ranges from -20 cm to 20cm, and it is sectioned into 4 bins, with a bin width of 5 cm each. The four points connected by a curve show κ calculated from each z vertex bin. The solid horizontal line in each panel represents κ calculated from $-20\ cm < zvtx < 20\ cm$, and it is the value used in the analysis. A list of κ deviation for each centrality can be found in Table. 3.8. Since κ does not affect normalization in the like sign, the systematic uncertainty was found by subtracting the unlike sign mixed background using the upper and lower κ values. Table. 3.16 lists the systematic uncertainty on the final spectra from κ for the five centrality bins in mass range $0.3 < m < 2.0 GeV/c^2$.

3.8.2 Systematics in Efficiency

In addition to the systematic uncertainty from background subtraction three variations of eID cuts are used to identify uncertainties in efficiency calculation. The three eID cut variations are

- Cut1: Tightened HBD cut $15 < HBDq < 40$

- Cut2: Loosened central arm eID cuts $n0 > 1$ and $|dep| < 2.5$

- Cut3: Tightened central arm eID cuts $n0 > 3$ and $|dep| < 1.5$

The efficiency corrected yields in the Dalitz region $m < 100 MeV$ are compared to the ones with normal eID cuts. The ratio averaged over all centrality bins are given with RMS in Table. 3.18. We quote 12% as the total systematic for efficiency correction.

Finally, we list in Tab. 3.19 the various sources of systematic uncertainties other than from the background normalization, which already occupy a few tables in the previous section Sec. 3.8.1.

Cut	0-10%	10-20%	20-40%	40-60%	60-92%
Dalitz Region					
Cut 1	1.09925	0.812753	0.963346	1.00951	1.02993
Cut 2	1.10724	1.01145	1.15683	1.04054	1.07781
Cut 3	0.935029	1.24518	0.887367	0.86762	1.17674
J/ψ Region					
Cut 1	1.19842	0.891088	1.04001	0.91326	0.812464
Cut 2	1.15679	1.09566	1.03517	0.977274	1.08059
Cut 3	1.03152	0.935457	0.955832	0.925778	0.937298

Table 3.17: Ratio of corrected yields of cut variations to that of the normal cuts, in the Dalitz and J/ψ region for the five centrality bins.

	mean	RMS	raw yield (Cut Variation/Normal Cut) in 0-10%
Cut1	0.98	0.12	0.527
Cut2	1.07	0.056	1.619
Cut3	0.99	0.12	0.428

Table 3.18: Ratio of Dalitz region yields of 3 eID cut variations to normal cut. The mean and RMS for all centrality bins for each cut variation. In the last column, the ratios represent the change of total raw yields with respect to the raw yield with the normal cut. The numbers listed are calculated from $0 - 10\%$ before efficiency correction.

	0-10%	10-20%	20-40%	40-60%	60-92%
eID	12%	12%	12%	12%	12%
embedding	4.5%	3.0%	-	-	-
TOF m>1GeV/c^2	10%	10%	10%	10%	10%

Table 3.19: Summary of systematic uncertainty sources as $\Delta Y(m_{ee})/Y(m_{ee})$ except from the background normalization.

3.8.3 Total Systematic Uncertainty

The systematic uncertainty sources are independent and their uncertainties are uncorrelated. The total systematic uncertainty is obtained by summing all sources in quadrature. Fig. 3.54 illustrates the total systematic uncertainty and its various components in minimum bias collisions. The dark red solid color denotes the total systematic uncertainty. The uncertainty from the absolute normalization is shown in orange. The flow uncertainty is in green. The uncertainty from κ is drawn in pink, while the one caused by the statistical uncertainty in the normalization factor a_0 of the combinatorial background is in black. The uncertainties from the efficiency ϵ_{pair}^{eID} and ϵ_{pair}^{TOF} are drawn in blue and purple, respectively. The uncertainty of ϵ_{pair}^{embed} is small as seen in the previous section, and we therefore ignore it.
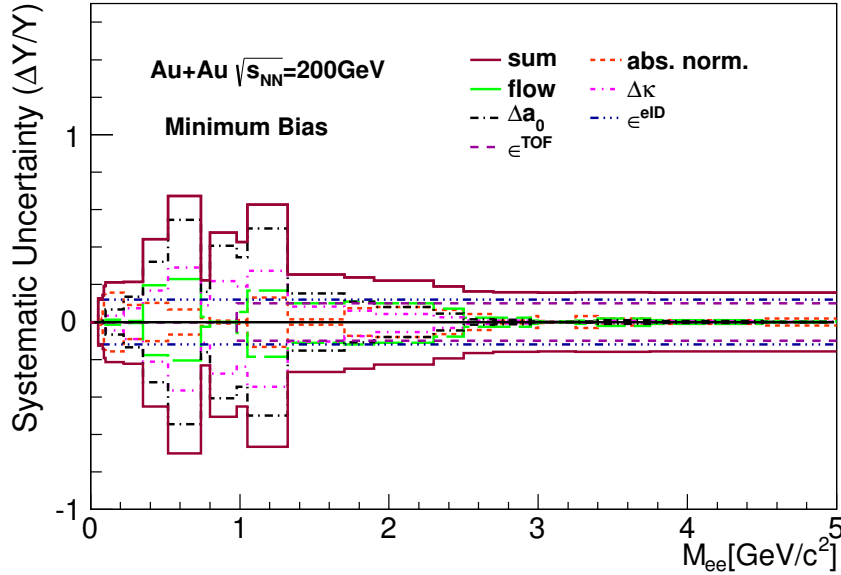
Figure 3.54: Various systematic uncertainty components and their quadratic sum as the total systematic uncertainty in minimum bias collisions.

It can be seen from Fig. 3.54 that the total systematic uncertainty is largest in $0.4 < m_{ee} < 1.3 \ GeV/c^2$, where S/B is low. At $m_{ee} < 0.4 \ GeV/c^2$, the systematic uncertainties from the difference in normalization methods (absolute normalization and component-fitting) and ϵ_{pair}^{eID} are important. The

total systematic is at approximately 20%. At mass region $0.4 < m_{ee} <$ 1.3 GeV/c^2, the dominating systematic uncertainty is from the statistical uncertainty in the combinatorial background normalization factor a_0. Uncertainty in κ is the second important source. The biggest total systematic uncertainty is found in this region, at $m_{ee} \sim 600~MeV/c^2$, where the total uncertainty reaches $\sim 65\%$. At $m_{ee} > 1.3~GeV/c^2$, uncertainties in ϵ_{pair}^{eID} and ϵ_{pair}^{TOF} are the main systematic sources. The total uncertainty is relatively flat with mass, and is approximately between 15% and 20%.

Fig. 3.55 plots the total systematic uncertainty together with the efficiency corrected dielectron mass spectra in the five centrality classes. The systematic uncertainties are represented by the shaded boxes at each data points. From top to bottom, the centrality selections are 0-10%, 10-20%, 20-40%, 40-60% and 60-92%. Similar to the minimum bias events, the total systematic uncertainty is largest in the region $0.4 < m_{ee} < 1.3~GeV/c^2$ due to the small S/B. In the mass regions $m_{ee} < 0.4~GeV/c^2$ and $m_{ee} > 1.3~GeV/c^2$, the total systematic uncertainty is approximately 20%, and the corresponding boxes in Fig. 3.55 are roughly the same size as the data points.
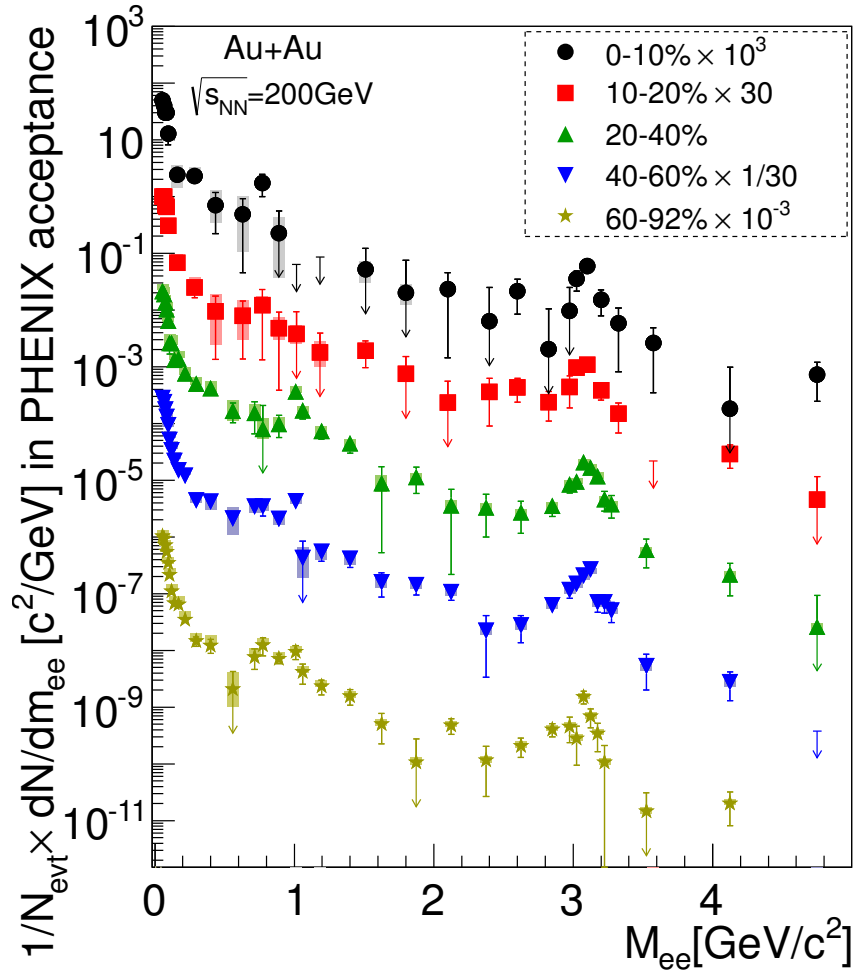
Figure 3.55: The efficiency corrected invariant mass spectra with corresponding total systematic uncertainties. From top to bottom the centrality selections are 0-10%, 10-20%, 20-40%, 40-60% and 60-92%.

Chapter 4

Fully Corrected Dielectron Mass Spectra

In this chapter, we will present the final dielectron invariant mass spectra. We will first compare the spectra to the hadronic cocktails, which represent the spectrum expectation when all dielectrons decay in vacuum. Any difference between the data and the cocktail would be indicative of additional sources or medium modifications of hadrons. In the Low Mass Region, we are particularly interested in any observation of enhancement in the ρ region, where medium modification of the ρ mesons due to the Chiral Symmetry Restoration plays a possible role. In the Intermediate Mass Region, the yields are believed to be dominated by open charm contributions.

Secondly, the final spectra will be compared to an independent parallel analysis [89] carried out by Yosuke Watanabe and the group in the Weizmann Institute of Science. The two analyses adopted different analysis strategies. The most significant difference comes from the electron identification technique, as the other analysis employs the Neural Networks for electron identification. There are also smaller differences in almost every step of the analysis stream. We will make a comparison of the analysis methods as well as the final results.

4.1 Comparison To The Hadronic Cocktails

The fully corrected dielectron invariant mass spectrum is shown in Fig. 4.1 for minimum bias $Au + Au$ collisions at $\sqrt{s_{NN}} = 200 \ GeV$, together with the expectation from hadronic decay dielectrons, namely the hadronic cocktail. Sec. 3.7 has described how the cocktail was constructed from a variety of meson sources, generated according to PHENIX measured yields and p_T distributions, and combined with heavy flavor contributions simulated by PYTHIA. The various colored lines denote all the sources in the cocktail including the π^0, η and η' Dalitz decay, vector meson decays from ρ, ω, ϕ and J/Ψ, and open heavy flavor contributions from $c\bar{c}$ and $b\bar{b}$.

The data points in black are the dielectron invariant pair mass spectrum corrected to ideal PHENIX acceptance at midrapidity of $|y| < 0.35$. The vertical lines represent the statistical errors, and the shaded boxes show the systematic errors, as discussed earlier in Sec. 3.8. The yellow band around the cocktail represents the uncertainty in the cocktail calculations.

The spectrum includes a lower track p_T cut at 0.2 GeV/c, and an opening angle cut for pairs of $\Theta_{oa} > 0.1 \ rad$. The lower panel in Fig. 4.1 shows the ratio of the data points to the cocktail. Again, the yellow band denotes the uncertainty on the cocktail. It can be seen that over nearly the entire mass range, the data points are in excellent agreement with the total cocktail, plotted as a solid black line, with the exception of a clearly visible enhancement appearing at around $m_{ee} \sim 500 \ MeV/c^2$. The ω is visible in the data and agrees nicely with the cocktail. However the ϕ meson is unfortunately not as clear as ω, due to a downward fluctuation. The J/ψ resonance peak is also well described by the cocktail, both in magnitude and in width, which contains the PHENIX detector resolution. Of particular interest, the yield between $0.3 < m_{ee} < 0.76 \ GeV/c^2$ exhibits an enhancement, meeting the expectation arising from both theoretical calculations of modified ρ spectral function in the hot medium and past heavy ion dilepton mass spectra measurements. It is heartening to see this enhancement confirmed by this new and improved PHENIX measurement.

For the intermediate mass region between the ϕ and the J/Ψ resonances, within the uncertainties, no marked deviation from the cocktail is observed, either in yield or in the line shape. The dominating component in the cocktail in this mass region is the semi-leptonic decay products from open charm mesons. As described in Sec. 3.7, the component is simulated by PYTHIA, which produces MC $c\bar{c}$ events in $p + p$ collisions, and is then normalized by

the average number of binary collision N_{coll} for $Au + Au$ multiplicity. The $c\bar{c}$ cross section for $p+p$ collisions is deduced in Ref. [19], by fitting the PYTHIA MC output to the measured dielectron mass spectrum in $d + Au$ collisions for $m_{ee} > 1.15\ GeV/c^2$. The resulting cross section is scaled by the average number of binary collisions in $d + Au$ to yield the equivalent $p + p$ cross section. The contribution from $b\bar{b}$, which forms a smaller component in this mass region, is treated following the same procedures [19]. We should note that, by using PYTHIA, the correlations between the $c\bar{c}$ pairs in $Au + Au$ collisions are assumed to be the same as in $p + p$. This assumption, however, is not supported by experimental evidence, as medium effects such as heavy quark energy loss and collective flow were reported [12]. This should affect the opening angle distribution of the $c\bar{c}$ pairs and should be reflected in the mass spectra. Lacking a generator which models the medium effects on heavy quarks, Ref. [18] studies the other extreme case where medium effects completely break the correlation between $c\bar{c}$ pairs. Randomly picking electron pairs from a measured heavy flavor decay single electron p_T distribution and uniform rapidity and azimuth distributions, it is found that the random $c\bar{c}$ pairs produce slightly softer mass spectra, as well as lower yields which lead to 70% larger enhancement factor[1] in the intermediate mass region. Keeping this consideration in mind, we conclude that the data agrees with the cocktail expectation in this mass range.

Fig. 4.2 shows the final dielectron spectra compared to the corresponding cocktails in the five centrality bins 0-10%, 10-20%, 20-40%, 40-60% and 60-92%. An enhancement is clearly visible at around $m_{ee} \sim 500\ MeV/c^2$ in the more central bins. In the most peripheral 60-92% centrality bin, where the event multiplicity is lowest, the point at $m_{ee} \sim 600 MeV/c^2$ happens to dip below the cocktail expectation, though its relatively large uncertainty still touches the cocktail. Except for the enhancement region, the spectra in all centrality bins display generally good agreement with the cocktails. In the intermediate mass region, we observe reasonable agreement between data and the cocktails in all five centrality classes. In that region, the data points may hint at a very subtle enhancement and a very slightly steeper slope, but they are consistent with the hadronic cocktails. For the light vector mesons ω and ϕ, due to limited statistics, we have varying degrees of success. Spectra in centraliy bins 0-10%, 10-20% show visible ω peaks yet ϕ is barely visible. In

---

[1]The enhancement factor is defined by the ratio of the yields in data to the yields in the cocktail in the mass region $1.2 < m_{ee} < 2.8\ GeV/c^2$. See Sec. 4.1 for more details.
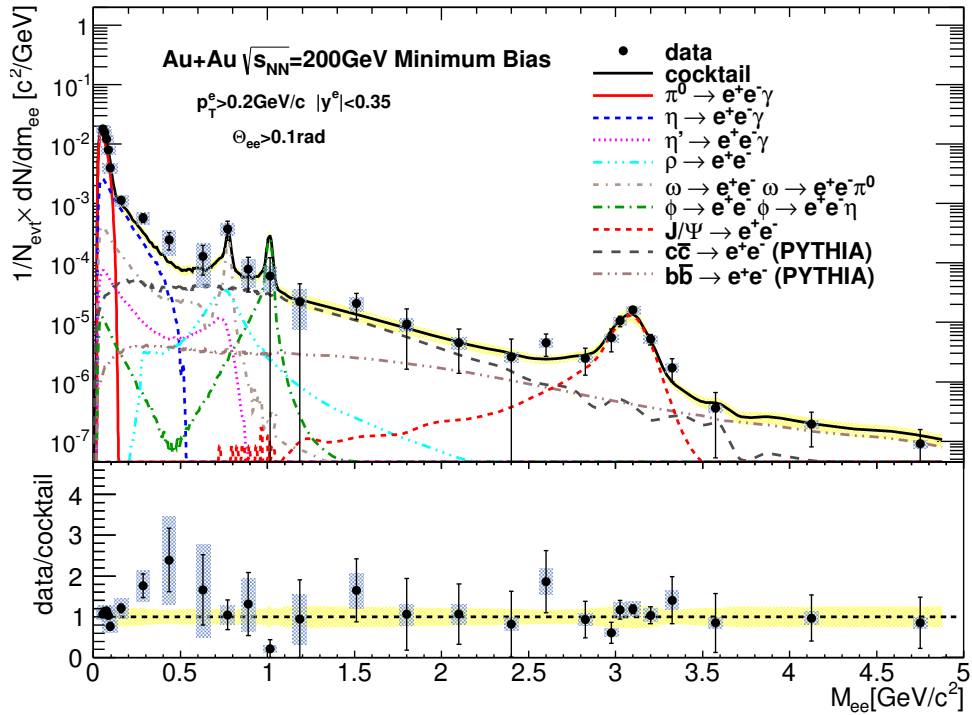
Figure 4.1: Fully corrected dielectron invariant mass spectra in minimum bias 0-92%, compared to the hadronic cocktail. The lower panel shows the ratio of the spectra to the cocktail. The shaded blue bands around the black data points denote the systematic errors from the measurement. The yellow around the cocktail represents the uncertainty of the cocktail.

centrality bin 20-40% we have a clearly peaked ϕ resonance, yet the ω peak is not quite there. The two most peripheral bins, 40-60% and 60-92%, where S/B are best, manage to capture both resonance peaks. The J/ψ peaks are well reproduced in both the magnitude and width for all centrality classes.
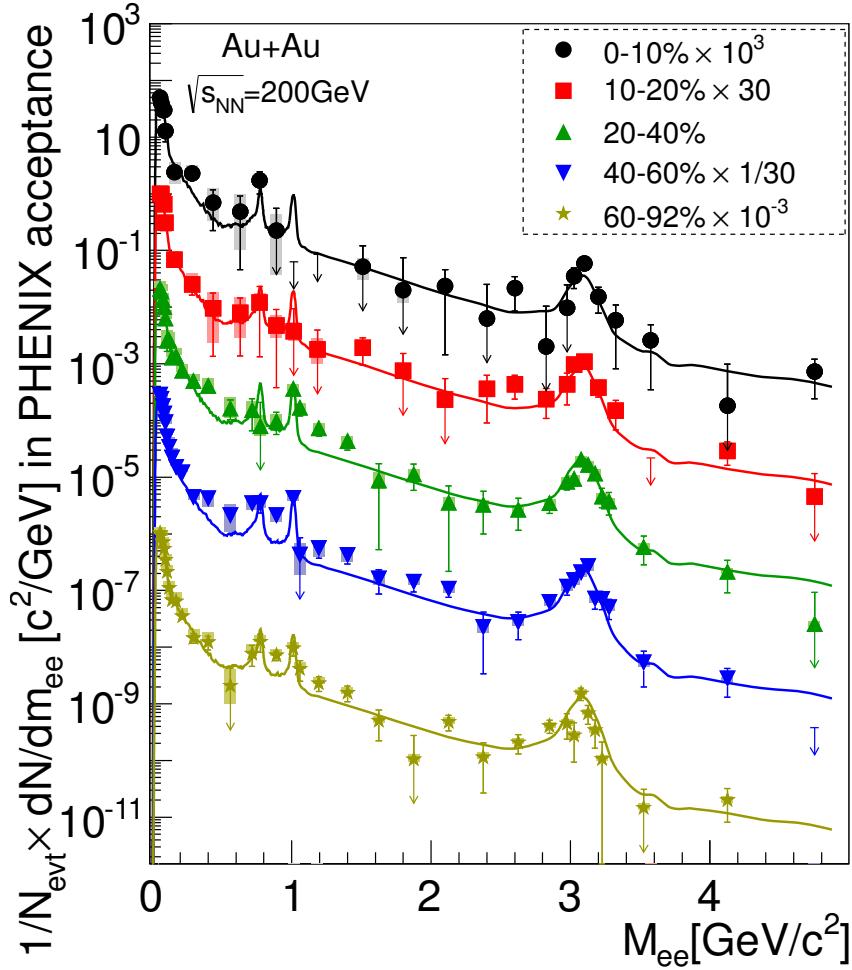
Figure 4.2: Fully corrected dielectron invariant mass spectra in centrality bin from top to bottom: 0-10%, 10-20%, 20-40%, 40-60% and 60-92% compared to the corresponding hadronic cocktails.

The Low Mass Region

Here we will concentrate on the low mass region, where the dielectron yields are composed of a number of sources. The decay electrons from light mesons η, η', ρ, ω, ϕ and contributions from open charm decays make the total yields. As discussed in Sec. 1.1.3, it is predicted that modification of ρ mesons in the QGP boundary will lead to a change of the ρ spectral function, which will in turn be visible from the Low Mass Region of the dielectron spectra.

We have seen in Fig. 4.1 that there is a noticeable enhancement taking place in the low mass region between 0.3 and 0.76 GeV/c^2. In Fig. 4.2, the enhancement appears to be more visible in the more central collisions, while the most peripheral bin exhibits no marked evidence of excess. We calculated the enhancement factor in the region $0.3 < m_{ee} < 0.76\ GeV/c^2$, defined as the ratio of the yield of the final spectra to the yield of the corresponding cocktail in the predefined mass region. The enhancement factor as a function of the number of participants (N_{part}) is plotted in Fig. 4.3, where the vertical lines on the black points show the statistical errors while the squares show the systematic uncertainty. To estimate the systematic uncertainty, the systematic uncertainty on the dielectron yield in $0.3 < m_{ee} < 0.76\ GeV/c^2$ from each systematic uncertainty source is determined separately. Sec. 3.8 contains a discussion of all systematic uncertainty sources. The total systematic uncertainty is calculated as the quadratic sum, and is then divided by the total cocktail yield in the same mass window. The grey band around 1.0 represents the uncertainty in the hadronic cocktails. The major contributors to the uncertainty on the cocktail in this mass region come from the yields of the light mesons and direct photons, as well as $c\bar{c}$ cross section, as shown in Fig. 3.52 and described in Sec. 3.7.

In the most central events, where N_{part} is largest, we obtain an enhancement factor reaching $2.10 \pm 0.91^{stat} \pm 1.16^{syst} \pm 0.20^{cocktail}$. The second most central bin, 10-20% centrality, exhibits a downward fluctuation in the dielectron yield. Considering the small S/B ratio ($\sim 1/700$ at $m_{ee} \sim 600 MeV/c^2$ as estimated from Fig. 3.53) in this centrality bin, a fluctuation in the foreground yields could potentially cause a considerable effect in the signal after background subtraction, and this is reflected by the large statistical uncertainty assigned to the point. The excess is also visible for the 20-40% and 40-60% centrality bins. Little enhancement is observed for the most peripheral bin, which is the most $p+p$ like. Table. 4.1 lists the enhancement factor

found for all centrality bins.

For minimum bias events, we obtain an enhancement factor of $1.79 \pm 0.40^{stat} \pm 0.81^{syst} \pm 0.20^{cocktail}$, which is in agreement with the result from an independent parallel analysis using the same dataset [18] [89]. We will give a detailed description of the parallel analysis in the coming section. The parallel analysis concludes an enhancement factor of $2.3 \pm 0.4^{stat} \pm 0.4^{syst} \pm 0.2^{cocktail}$ for minimum bias $Au+Au$ events in the same mass region, when compared to the same set of hadronic cocktails which includes a charm component calculated by PYTHIA.[2] The enhancement factor derived from the present work is slightly less than the alternative analysis, however the two are consistent within uncertainties.

The STAR Collaboration's measurement of $Au + Au$ dielectron spectra at $\sqrt{s} = 200\ GeV$ [4] [2] yields an enhancement factor of $1.77 \pm 0.11^{stat} \pm 0.24^{syst} \pm 0.33^{model}$ in $0.3 < m_{ee} < 0.76\ GeV/c^2$ for min bias events, when comparing to a ρ-less cocktail. While this number is completely consistent with our result, the lack of ρ meson contribution in the STAR cocktail leads to $\sim 10\%$ decrease in their cocktail yield in this mass region. On the other hand, the charm component in the STAR cocktail is generated by PYTHIA with a different charm cross section $d\sigma_{c\bar{c}}/dy = 171 \pm 26\mu b$, which is greater than our charm cross section of $106\ \mu b$. Thus the two differences in the STAR cocktail tend to cancel. Taking account of the uncertainty and subtle differences in the cocktails, we can conclude the excess factor is consistent with the STAR result.

On the other hand, this enhancement factor is markedly smaller than the previous PHENIX dielectron measurement in $Au + Au$ collisions, which derived a factor of $4.7 \pm 0.4(\text{stat}) \pm 1.5(\text{syst}) \pm 0.9(\text{model})$ [10]. As the present analysis is a substantial upgrade from the previous one, there are a number of evident improvements upon the previous analysis, as follows:

- The new data utilizes the hardware upgrade of the HBD, which improves the ability to distinguish hadrons from electrons, as well as to identify conversion electrons and π^0 Dalitz decay pairs. These constitute a significant source of the combinatorial background, and the HBD reduces the total background.

---

[2]When comparing to a hadronic cocktail whose open charm component is calculated by MC@NLO, the parallel analysis finds an enhancement factor of $1.7 \pm 0.3^{stat} \pm 0.3^{syst} \pm 0.2^{model}$.

- The new analysis has analyzed a total of 4.8×10^9 events, as opposed to the 8×10^8 events analyzed in the previous measurement.

- The improved electron identification with the HBD and the TOF has raised the electron purity in the most central events (0-10%) from 70% to the present 87%.

- Tighter pair cuts are applied than in the previous analysis.

- The new analysis introduced the modulation due to transverse anisotropy into the combinatorial background, as the the elliptic flow inherent in heavy ion collisions has a non-trivial effect upon the shape of the combinatorial background. Without correcting for flow, the mixed events are unable to reproduce the combinatorial background within a satisfactory precision.

- The background from correlated electron-hadron pairs is identified and treated in the new analysis. This particular background contribution arises from mis-identified hadrons correlated with certain electrons in the sample. This background source peaks below 100 MeV for unlike sign pairs and between 200-300 Mev for like sign pairs. Previously this background sources was not considered.

- The contribution of away-side jet pairs are calculated by simulation and subtracted from the final spectra. The away side jet contribution was considered negligible in the previous analysis and was not treated. Even though the away side jet yield is small compared to the combinatorial background, it becomes the main correlated background source at $0.5 < m_{ee} < 1\ GeV/c^2$ as Fig. 3.37 illustrates. The subtraction of the away side jet pairs allows for a more accurate treatment of the total background.

- The current analysis normalizes all like sign components simultaneously over the full mass range. It gives a good description of the entire like sign spectra and takes into account every background source. The previous analysis first normalized the combinatorial background in the region $m_{ee} > 0.7\ GeV/c^2$, where the correlated pairs were considered " small enough". Then the simulated cross and near side jet pairs were fitted to the remaining like sign spectra. The new normalization has achieved a significant improvement in the background description.
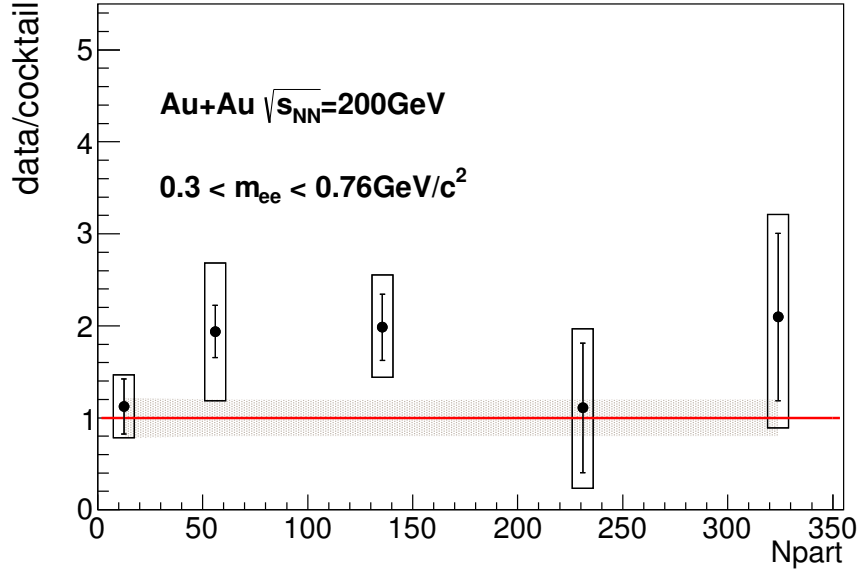
Figure 4.3: The enhancement factor in the low mass region $0.3 < m_{ee} < 0.76 \, GeV/c^2$, defined by the ratio of the yields of data to that of the cocktail in the given mass window. The vertical lines on the data points show the statistical uncertainty. The black squares represent the systematic uncertainty. The shaded grey band around 1.0 denotes the uncertainty from the hadronic cocktail.

The present analysis do not observe the large enhancement the previous PHENIX measurement reported. Many of the above improvements affect the yield in the ρ mass region, although their effects are not always in the same direction nor in the same magnitude. The loose pair cuts, for instance, could lead to excess yield in the mass region in question. On the other hand, not correcting for the flow can impact the yield in both directions, depending on how exactly the combinatorial background is normalized. With the background normalization method adopted by the previous measurement, it tends to oversubtract the background. The most significant effects come from the hadron contamination, the tighter pair cuts and the correlated electron-hadron pairs. Given the numerous improvements listed above, we regard the new result an improvement upon the previous one.

centrality	enhancement factor $\pm$ stat $\pm$ syst $\pm$ cocktail
0-10%	$2.10 \pm 0.91 \pm 1.16 \pm 0.20$
10-20%	$1.11 \pm 0.70 \pm 0.87 \pm 0.20$
20-40%	$1.98 \pm 0.36 \pm 0.56 \pm 0.20$
40-60%	$1.94 \pm 0.28 \pm 0.75 \pm 0.20$
60-92%	$1.12 \pm 0.30 \pm 0.34 \pm 0.20$
MB	$1.79 \pm 0.40 \pm 0.81 \pm 0.20$

Table 4.1: Table of enhancement factor derived for mass window $0.3 < m_{ee} < 0.76 \ GeV/c^2$ for all centrality classes.

The Intermediate Mass Region

The intermediate mass region is believed to be dominated by $D\bar{D}$ semi-leptonic decay pairs, with smaller contributions from $B\bar{B}$ and Drell-Yan processes. Thermal radiation of QGP, is also theoretically anticipated to fall into this region, though its small yield is overwhelmed by other sources.

Table. 4.2 presents the enhancement factor, defined as the ratio of the yields measured to those from the cocktail expectation in the mass window $1.2 < m_{ee} < 2.8 \ GeV/c^2$, for all the centrality classes. The factors are plotted as a function of the number of participants in Fig. 4.4. The vertical lines on the data points are the statistical errors while the squares show the systematic errors. To determine the systematic uncertainty, we first calculate separately the systematic uncertainty on the dielectron yield in $1.2 < m_{ee} < 2.8 \ GeV/c^2$ from each systematic uncertainty source. The sources are described in Sec. 3.8. The total systematic uncertainty is added in quadrature, and divided by the total cocktail yield in the same mass window. The shaded grey band around 1.0 is the uncertainty from the cocktail, whose heavy flavor contributions are produced from PYTHIA simulations. As discussed in Sec. 3.7, the uncertainty on the cocktail in this mass region (see Fig. 3.52) is dominated by the uncertainty on the $c\bar{c}$ cross section, with smaller contributions from the uncertainty on the $b\bar{b}$ cross section and on the J/Ψ.

For all centrality classes, the enhancement factors are slightly above and still consistent with 1.0, within the uncertainties. There may be a hint of enhancement in the intermediate mass region. Yet given the statistical and systematic uncertainties, we can also conclude that no clear enhancement is observed.

centrality	enhancement factor $\pm$ stat $\pm$ syst $\pm$ cocktail
0-10%	$1.27 \pm 0.96 \pm 0.44 \pm 0.25$
10-20%	$1.42 \pm 0.70 \pm 0.37 \pm 0.25$
20-40%	$1.31 \pm 0.38 \pm 0.29 \pm 0.25$
40-60%	$1.55 \pm 0.30 \pm 0.35 \pm 0.25$
60-92%	$1.34 \pm 0.27 \pm 0.22 \pm 0.32$
MB	$1.34 \pm 0.43 \pm 0.35 \pm 0.25$

Table 4.2: Table of enhancement factor derived for mass window $1.2 < m_{ee} < 2.8\ GeV/c^2$ for all centrality classes.
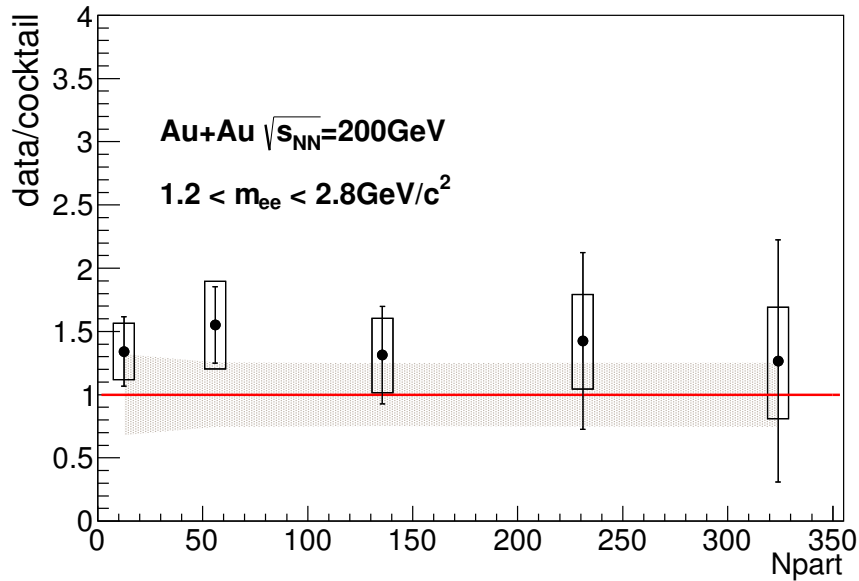
Figure 4.4: The enhancement factor in the intermediate mass region $1.2 < m_{ee} < 2.8\ GeV/c^2$, defined by the ratio of the yields of data to that of the cocktail in the given mass window. The vertical lines on the data points show the statistical uncertainty. The black squares represent the systematic uncertainty. The shaded grey band around 1.0 denotes the uncertainty from the hadronic cocktail.

4.2 Comparison To The Parallel Analysis

This analysis was done in parallel with an independent effort by Yosuke Watanabe from the Weizmann Institute of Science, whose work is recently published in Ref. [18]. There are many differences between the analysis approaches adopted by the two sides. In the section, we will briefly explain these differences in each analysis step, as well as the procedures that are the same, and then we will compare the final spectra produced by the two analyses.

The two analyses adopt the same PHENIX acceptance aperture cut and the same set of pair cuts, so that the results can be directly comparable in the same phase space. Additionally, the two streams also adopt the same set of detector fiducial cuts which mask inactive detector areas, though the final spectra are corrected to ideal PHENIX acceptance. The Weizmann events were selected with slightly looser *bbcz* range, yielding 5.6×10^9 MB events, which corresponds to $\sim 15\%$ more events than the present work. The centrality class selection is identical in the other analysis.

The main feature of the parallel analysis is that it adopts an electron identification procedure consisting of three neural networks. The neural networks use standard electron identification variables, n0, disp, chi2/npe0, emcsdr, prob, dep, sigmalized time-of-flight from PbSc or ToF-E, and HBD variables produced by their separately developed HBD algorithm, which includes quantities such as the HBD cluster charge, cluster size (the number of pads occupied by the cluster), the maximum charge on a single pad in the cluster, etc., and then produce a single output variable between 0 (background) and 1 (signal), which denotes the likelihood of the given track being a true signal. The neural networks are used to achieve electron/hadron separation as well as HBD single/double hit separation. It allows the electron sample to achieve an electron purity of greater than 95% for all centralities.

For the combinatorial background, the alternative analysis also employs the CabanaBoy mixing machine with Matathias Pool for event mixing, with the mixed events weighted to describe the azimuthal anisotropy as detailed in Eq. 3.6. For the correlated backgrounds, both analyses utilized the simulation produced by the Weizmann Institute for the cross and the jet pairs, applying their own separate electron identification method and analysis chain. The simulations for e-h pairs and bottom pairs are shared between the two analyses, with systematic uncertainties assigned to cover the different electron identification efficiency. In the parallel analysis, the correlated backgrounds

are absolutely normalized, and the mixed events were normalized to foreground in a centrality-dependent $\Delta\phi_0^{pair}$ window around $\pi/2$ in the like sign space.

For efficiency correction, instead of generating uniform distribution of e^+e^- pairs, the alternative analysis generated realistic electron cocktail that was processed through the PHENIX GEANT4 simulation. The resulting tracks are subject to the same analyzing cuts such as the eID, detector fiducial cuts and pair cuts. This produces the efficiency due to electron identification, detector live area and pair cuts. The efficiency resulting from the HBD is dealt with by the procedure of embedding into the HBD detector.

To summarize, a comparison of the procedures from the two analyses is listed in Table. 4.3.

Fig. 4.5 compares of the final results between the two parallel analyses. The closed symbols denote the alternative analysis and the open symbols represent the results from this dissertation. For all five centrality classes presented, the two analyses exhibit complete agreement with each other within uncertainties. The alternative analysis tends to have smaller uncertainty, as the neural networks are optimized to achieve the highest possible figure of merits, while this optimization is not available to the conventional approach of 1-Dimensional electron selection cuts adopted in this work.

χ^2 values are calculated for the five centrality classes show in Fig. 4.5, to quantify the agreement between the two results. Using the parallel analysis as the model to test results of the main analysis, the χ^2 is calculated as

$$\chi^2 = \sum_i \frac{(Y_i^m - Y_i^p)^2}{\sigma_i^2}$$

where Y_i^m and Y_i^p stand for the yield at the ith point of the main and the parallel analysis, respectively. We consider the statistical and systematic uncertainty on the ith point from the main analyses, and use the larger of the two uncertainties for the value of σ_i. In the places where the two analyses do not use the same mass values, interpolation on the main analysis points is adopted to make estimations on yields at the same mass values used in the parallel analysis. Table. 4.4 displays the resulting χ^2, the number of degrees of freedom and the reduced $\chi_{red}^2 = \chi^2/NDF$ obtained from the two results.

The χ^2/NDF values obtained are smaller than 1. On the one hand, the small values indicate that the results from the two analyses are in good agreement within the experimental uncertainty. On the other hand, $\chi^2/NDF < 1$

	Stony Brook Analysis	Weizmann Analysis
HBD Algorithm	HBD LBS Clusterizer	Neural Networks + HbdMinPadClusterizer + HbdWisClusterizer
eID	LBS + Central Arm eID cuts + TOF	Neural Networks
Combinatorial background	Event mixing with Matathias Pool with regeneration Weighted by flow	Event mixing with Matathias Pool without regeneration Weighted by flow
Correlated Backgrounds	Cross Pair(PISA) Jet(PYTHIA+PISA) e-h(RICH embedding) bottom(MCNLO)	Cross(PISA) Jet(PYTHIA+PISA) e-h(RICH embedding) bottom(MCNLO)
Normalization	Components fitting in like sign space κ correct to unlike	Absolute Normalization for correlated components
Efficiency	Monte Carlo pairs in flat (m, p_T) weighted with realistic distribution ϵ applied in mass direction	Realistic cocktails ϵ applied in (m, p_T)

Table 4.3: Comparison of analysis strategies between the present work and the parallel analysis, labeled the Stony Brook and the Weizmann analysis respectively.

centrality	χ^2	NDF	χ^2/NDF	P
0-10%	7.959	24	0.332	0.995
10-20%	9.573	23	0.416	0.975
20-40%	7.797	30	0.260	0.995
40-60%	12.002	34	0.353	0.995
60-92%	14.348	34	0.422	0.995

Table 4.4: Table of χ^2, the number of degrees of freedom, the reduced χ^2_{red} between the two analyses for centrality bins 0-10%, 10-20%, 20-40%, 40-60% and 60-92%. The last column 'P' stands for the possibility that the two distributions are identical, obtained from a standard χ^2 distribution table.

suggests that the model is over-fitting data, or overestimated uncertainty. As both analyses are done on the same run10 data set, the fluctuations and uncertainties in both works are largely correlated. The small χ^2/NDF values reflect the shared fluctuations between the two sets of spectra. It also suggests the possibility that we have assigned conservative experimental uncertainty to the final spectra. Because of the small χ^2 values, the possibility that the two results have complete agreement, obtained from a standard χ^2 distribution table, is better than 0.975 for all centralities. Keeping in mind that the χ^2/NDF is reduced by common fluctuations, the possibility tends to be an overestimation. However, despite this, the values of χ^2/NDF also indicates that the average deviation between the two results at each data point is less than 1 sigma. We can safely conclude that we have very good agreement between the results from the two analyses.
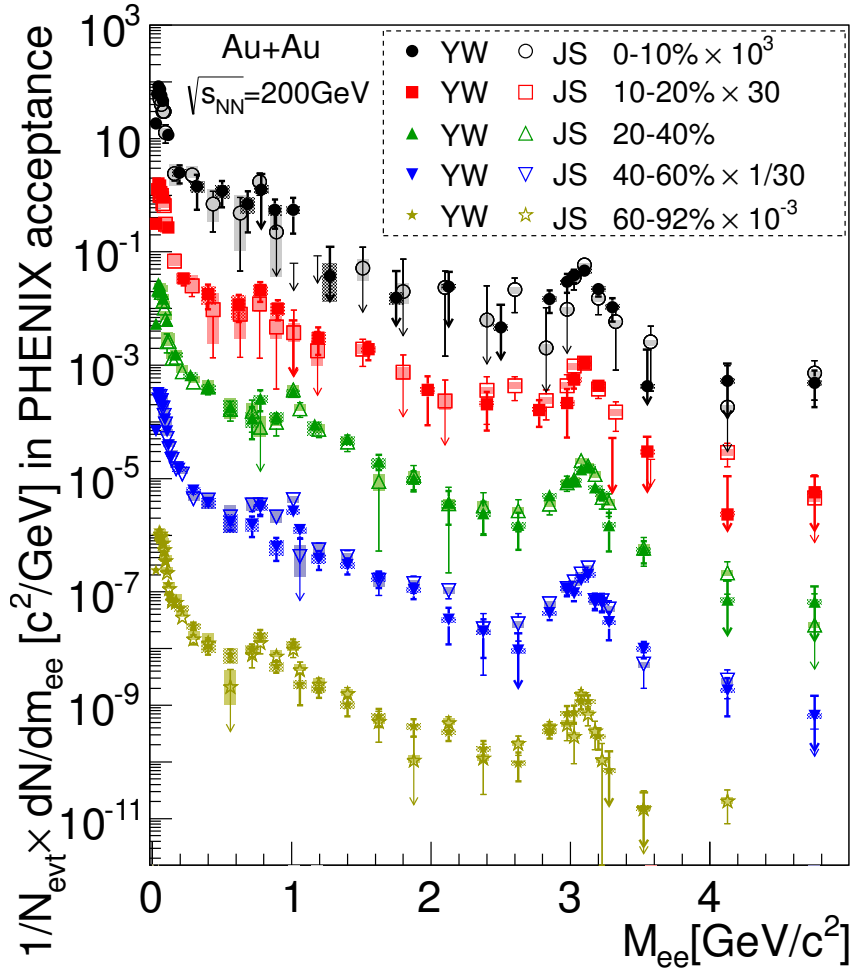
Figure 4.5: Comparison of two sets of final spectra following different analysis streams with Run10 $Au + Au$ data at $\sqrt{s_{NN}} = 200 \ GeV$. From top to bottom, centrality classes compared are 0-10%, 10-20%, 20-40%, 40-60% and 60-92%. The open symbols labeled 'JS' stand for the results obtained by this dissertation work, the closed symbols labeled 'YW' shows the ones from the alternative analysis.

Chapter 5

Comparison To Theoretical Calculations

Now, it is time for us to return to the chief motivation of initiating such a complex measurement. The main aim of the dielectron mass spectra measurement, of course, is to study the predicted chiral symmetry restoration occurring at the phase boundary when hadronic matter transits into the deconfined regime of the quark gluon plasma. The chiral symmetry, which governs the dynamics of light quarks, u, d, and s, is spontaneously broken in the QCD vacuum for the finite chiral condensate, and its restoration is anticipated to coincide with the QGP phase transition where the chiral condensate is predicted to suffer a considerable drop at $T \sim T_c$ and to vanish at high temperature $T \sim 1.5T_c$ [59] [100]. The dynamics of light vector mesons will be affected by the chiral symmetry restoration. As the chiral condensate is not an observable, we can look for evidence of the chiral symmetry restoration in the modification of light vector mesons, ω, ρ, and ϕ. The modification will be reflected in the vector meson resonance peaks in the spectral function, such as mass shift, change of peak width, suppression or enhancement. The vector mesons decay into dilepton pairs. Signs of vector meson modification in the hot and dense medium are carried unaffected by the final state strong interactions via the dilepton pairs to our detecting system. The ρ meson is a particularly sensitive probe, since it predominantly decays inside the hot medium so that its in-medium modification can be directly reflected by its decay dilepton pairs.

The measured dielectron mass spectrum is a sum of dielectron emissions from every source over the entire evolution of the heavy ion collisions. Accordingly, theoretical calculations need to reproduce the emissions during the whole time span of the collisions, then the sum of all relevant sources can be compared directly to the measured spectra.

We will first introduce the theoretical models treating the ρ meson in-medium modification in Sec. 5.1, and then proceed to present the comparison of the final spectra to certain chosen theoretical calculations in Sec. 5.2.

5.1 Theoretical Models On Dilepton Productions

As discussed in Sec. 1.1.3, there are two frequently mentioned scenarios dealing with the in-medium properties of the ρ meson, the dropping mass scenario [48] [49] [88], and the collisional broadening scenario [106] [103]. The dropping mass scenario uses the degeneracy of vector and axial-vector mesons under the condition of conserved chiral symmetry and proposes that, most of the ρ meson in-medium mass is dynamically generated by the $\langle \bar{q}q \rangle$ quark condensate, and as $\langle \bar{q}q \rangle$ goes to zero, the ρ in-medium mass drops to zero. [49]. The collisional broadening scenario is a more "conventional" approach based on ρ meson scattering on constituents of a hadronic medium. The calculations find that the ρ spectral function is broadened by many-body collisions, but with little shift in the resonance mass. Both scenarios produce an enhancement at around and below the ρ mass in the dilepton invariant mass spectrum. The high precision in the SPS NA60 dimuon data in $In+In$ collisions at 158GeV [38] [39] [96] [37] has revealed an excellent agreement with the collisional broadening case while ruling out results from the dropping of ρ mass.

Calculations of dilepton rates at the RHIC energy of $\sqrt{s} = 200\ GeV$ have been actively pursued for more than a decade. For thermal radiation from the hadronic phase, the main contributions are pion annihilation $\pi^+\pi^- \to l^+l^-$, kaon annihilation and hadron collisions. According to the vector-meson dominance model [112] [113] [105], these two-body annihilation processes are coupled with an intermediate vector meson, e.g. $\pi^+\pi^- \to \rho \to \gamma^* \to l^+l^-$, thus the dilepton emission can be regarded as in-medium vector-meson spectroscopy [100]. For the emissions from the Quark-Gluon Plasma, according to perturbative QCD, the leading order contribution is the quark-antiquark annihilation. Higher order processes at definite temperature and chemical potential are studied extensively [45] [94]. As the QGP phase resides at higher temperature than the hadronic phase, the emissions from QGP are expected to form a harder distribution, and it is predicted to be substantial compared to other sources at $M > 1.5\ GeV/c^2$. There are efforts using thermal lattice QCD to calculate the dilepton rates in a nonperturbative way [65] [46].

Two approaches have achieved consistent success in predicting dilepton mass spectra in different experiments and collisions. One is a macroscopic effective many-body model developed following the work of R. Rapp, J.

Wambach, H. van Hees et al. [103] [106] [99] [102], the other is the PHSD, or, the parton-hadron-string dynamics transport approach [86] [56] [47], led by W. Cassinga, E.L. Bratkovskaya, and O. Linnyk.

The Effective Many-Body Collisional Approach

The calculation of the dilepton emission rate in this model is based on the retarded electromagnetic current-current correlator Π_{em} in the general form of the dilepton thermal rate in a hot and dense medium of temperature T and baryon density μ_B,

$$\frac{d^8 N_{l+l-}}{d^4 x d^4 q} = -\frac{\alpha_{EM}^2}{\pi^3 M^2} f^B(q_0; T) Im\Pi_{em}(q_0, \mathbf{q}; \mu_B, T) \tag{5.1}$$

where f^B is the thermal Bose distribution and $q_0 = \sqrt{M^2 + q^2}$ is the lepton pair energy. Because of the vector dominance model (VDM), the correlator can be written in the form of the imaginary parts of the vector meson propagators,

$$Im\Pi_{em} = \sum_{V=\rho,\omega,\phi} \frac{(m_V^{(0)})^4}{g_V^2} Im D_V \tag{5.2}$$

where the predominant ρ meson propagator D_ρ, taking into account of ρ's various interactions with the medium, takes the form of,

$$D_\rho^{L,T} = \frac{1}{M^2 - (m_\rho^{(0)})^2 - \Sigma_{\rho\pi\pi}^{L,T} - \Sigma_{\rho M}^{L,T} - \Sigma_{\rho B}^{L,T}} \tag{5.3}$$

The letters L and T denote the longitudinal and transverse projections. The terms in the ρ in-medium selfenergy give consideration to the three types of ρ-medium interactions. The $\Sigma_{\rho\pi\pi}$ term is pion cloud modifications on ρ. The term $\Sigma_{\rho M}$ constitutes the ρ interactions with the most abundant mesons surrounding it, namely the π, K, $\bar{K}$ and ρ mesons. $\Sigma_{\rho B}$ accounts for ρ interaction with most abundant baryons, such as N, $\Delta(1232)$, N(1440) and N(1520). The interaction vertices are constrained by experimental data.

The resulting spectral function of ρ displays considerable broadening and essentially no mass shift. The broadening increases with the temperature and density. The total baryon density in the system is found to have a driving effect in the broadening of the spectral function, and thus is responsible for

the low mass enhancement at $m_{ee} \sim 0.4 \; GeV/c^2$.

Then, for the thermal emissions in the Quark-Gluon-Plasma phase, the calculations employ perturbative QCD and compute the leading order $q\bar{q} \to l^+l^-$ annihilation, the result of which can be considered as a lower limit of true QGP thermal radiation. The argument of the "parton-hadron" duality [100], which states that the dilepton rates from hadronic thermal radiation extrapolated upwards to $T \sim T_c$ is equivalent to the ones from partonic thermal radiations extrapolated downwards to T_c, can be useful when calculating dilepton production down to masses about 1.1 GeV. The dilepton rates for the QGP, thus can be expressed in the following form,

$$
\begin{aligned}
\frac{d^8 N_{\mu\mu}}{d^4 x d^4 q} = \frac{\alpha^2}{4\pi^4} \frac{T}{q} f^B(q_0; T) \sum_{q=u,d,s} e_q^2 \\
\times \, ln \frac{(x_- + y)(x_+ + exp[-\mu_q/T])}{(x_+ + y)(x_- + exp[-\mu_q/T])}
\end{aligned}
\tag{5.4}
$$

where $x_\pm = exp[-(q_0 \pm q)/2T]$.

The dilepton production rates must be incorporated into a medium evolution model to properly account for the dilepton yields in the whole time span of the system, and to be directly comparable to experimental measurements. The key ingredients are relativistic hydrodynamics which describes the space-time expansion of the medium, and the medium equation of state. Before the recent development of finite temperature lattice QCD calculation, the model used a simplified thermal fireball model parameterized to resemble hydrodynamic calculations, and a bag-model Equation of State. It assumed a cylindrically expanding fireball with isotropic temperature and density.

Recently the model has been updated by the latest lattice QCD data which gives parameterization of a nonperturbative thermal QGP EoS, and an ideal hydro calculation which changed the chosen pseudo-critical temperature T_{pc} to 170 MeV and the chemical freeze-out temperature T_{ch} to 160 MeV. Additionally, the QGP thermal radiation during the partonic phase is also updated with the lQCD EoS [108].

The model has successfully reproduced the low mass dilepton enhancement in a number of dilepton measurements in heavy ion collisions, those includes the CERES/NA45 e^+e^- invariant mass spectra in Pb(158AGeV)-

Au collisions [100] [61] [60], and the NA60 dimuon spectra of In(158AGeV)-In collisions [100] [64]. For RHIC energies, it had success in reproducing the low mass excess in the dielectron mass spectra in $Au + Au$ collisions at $\sqrt{s} = 200$ GeV, 62.4 GeV and 19.6 GeV measured by the STAR collaboration [108].

The Parton-Hadron-String Dynamic Approach

The Parton-Hadron-String Dynamic model [86] [56] [47] is a microscopic off-shell transport approach which gives a consistent description of the full evolution of the heavy ion collision. It models the initial hard scattering and string formation, an explicit partonic phase, the dynamics of hadronization, and the subsequent hadronic interactions. This dynamical approach for the strongly interacting and non-equilibrium system is based on the Kadanoff-Baym (KB) equations [43] [79] [78]. The KB theory treats the field quanta in terms of dressed propagators with complex self energies. The real part of the self-energy is related to mean-field potentials, while the imaginary part contains the lifetime information on time-like "particles". The time evolution of the system can be fully described by off-shell transport equations once the complex self-energies are obtained.

The description of the partonic phase is based on a Dynamical QuasiParticle Model, DQPM [52] [51], which relies on single particle Green functions to describe QCD properties. The DQPM is phenomenologically parameterized to match the lattice QCD results for quark-gluon-plasma in thermal equilibrium. Thus, the model calculates off-shell cross sections of dilepton production in strongly interacting QGP (sQGP), using the parametrizations from the DQPM. The processes responsible for dilepton production include the leading order Born $q + \bar{q}$ annihilation, gluon Compton scattering $q + g \rightarrow \gamma^* + q$ and $\bar{q} + g \rightarrow \gamma^* + \bar{q}$, gluon bremsstrahlung during quark - antiquark annihilation $q + \bar{q} \rightarrow g + \gamma^*$.

For the dilepton production in the hadronic phase, the PHSD model is akin to the HSD transport model [66] [54]. Ref. [57] describes in detail the implementation of hadronic decays into dileptons in HSD, based on transport equations derived from Kadanoff-Baym equations. In addition to off-shell propagation for vector mesons, the model incorporates modifications of vector-meson spectral functions which cover possible scenarios for in-medium modification of the vector mesons. The collisional broadening of the vector meson spectral functions is introduced into the model using the vector meson width:

$$\Gamma_V^*(M, |\vec{p}|, \rho_N) = \Gamma_V(M) + \Gamma_{coll}(M, |\vec{p}|, \rho_N)$$

where $\Gamma_V(M)$ is the total width of the vector mesons in the vacuum. $\vec{p}$ is the three-momentum. The collisional width is approximated by

$$\Gamma_{coll}(M, |\vec{p}|, \rho_N) = \gamma \rho_N \langle v \sigma_{VN}^{tot} \rangle \approx \alpha_{coll} \frac{\rho_N}{\rho_0}$$

where $v = |\vec{p}|/E$ is the velocity (E is the energy). $\gamma = 1/(1-v^2)$. ρ_N is the nuclear density, $\rho_0 = 0.16 fm^{-3}$ is the normal nuclear density. σ_{VN}^{tot} is the total cross section of meson-nucleon interaction. The ρ_N dependent coefficient α_{coll} can be extracted in the PHSD model from vector-meson collision rate in $In + In$ collisions at 158A GeV [85]. For ρ mesons $\alpha_{coll} \approx 150\ MeV$, and $\alpha_{coll} \approx 70\ MeV$ for ω mesons.

The dropping mass scenario can also be implemented into the PHSD model by introducing the Brown-Rho scaling [48] [49] to the in-medium vector meson pole masses:

$$M_0^*(\rho_N) = \frac{M_0}{(1 + \alpha \rho_N/\rho_0)}$$

where $\alpha \approx 0.16\ fm^{-3}$ for ρ mesons and $\alpha \approx 0.12\ fm^{-3}$ for ω mesons [85].

Thus the different scenarios of the medium effects on the vector mesons are easily studied with the PHSD. The dilepton production mechanisms involved in the PHSD include the hadronic decays into lepton pairs, namely, π, η, η', ω, Δ, a_1 Dalitz decays, and direct decays $\rho \rightarrow l^+l^-$, $\omega \rightarrow l^+l^-$, $\phi \rightarrow l^+l^-$. For PHSD, secondary multiple meson interactions $\pi\omega \rightarrow l^+l^-$, $\pi\rho \rightarrow l^+l^-$, $\pi a_1 \rightarrow l^+l^-$, $\rho\rho \rightarrow l^+l^-$ are also implemented.

When employing the broadened ρ spectral function, the PHSD model achieves fairly good agreement with $Au+Au$ dielectron invariant mass spectra at $\sqrt{s} = 200\ GeV$ measured by STAR [4]. According to the PHSD results, the observed STAR low mass enhancement can be explained by decays of the π^0, η, η', ω, ρ, ϕ and a_1 mesons, as well as Δ and open charm decays, while collisional broadening of the ρ meson is incorporated.

5.2 Final Spectra Compared to Models

5.2.1 Comparison To The Effective Many-Body Collisional Approach

Now we compare the final spectra in our measurement to the calculation results from the effective many-body collisional model. Here we use the theoretical calculation from R. Rapp; the method and ingredients are described in the last section and a comprehensive description can be found in Ref. [108].

Fig. 5.1 is the dielectron invariant mass spectrum in minimum bias $Au + Au$ collisions at $\sqrt{s} = 200 \ GeV$ data compared to the collisional broadening model results. The data are plotted in black points with vertical lines denoting statistical uncertainty and black squares representing the systematic uncertainty. The solid black curve is the sum of three calculated contributions. The first is the hadronic cocktail with the ρ contribution subtracted, and is illustrated in dashed green lines in the plot. The second and the third components are results from the ρ broadening model. The red curve depicts the dielectron yields from the ρ, whose spectral function suffers significant in-medium broadening due to many-body collisions. The dash-dotted blue is the quark-gluon-plasma thermal radiation based on a nonperturbative lattice QCD equation of state, whose contribution is well below the ρ-less cocktail and the ρ at around the ρ mass region $m_{ee} \sim 500 MeV$. The QGP is a smoothly falling distribution with little distinctive structure. The ρ shape, when compared to the vacuum ρ expectation displayed in the full cocktail in Fig. 4.1, presents a much flattened resonance structure, and it has been referred to accordingly as the 'melting ρ'. Another distinct difference between the in-medium and vacuum ρ shape, is that the in-medium ρ reveals significant dielectron yield at low mass $m_{ee} < 0.2 GeV/c^2$, whereas the vacuum ρ contribution is almost gone at $m_{ee} < 0.2 GeV/c^2$.

The data and the theoretical sum of the components, i.e. the black curve, exhibit good agreement. In the mass range between $0.2 < m_{ee} < 0.9 MeV/c^2$, the theoretical expectation gives a fair description of the data points. In the mass regions outside this $0.2 < m_{ee} < 0.9 MeV/c^2$ window, the yields of the QGP and the broadened ρ are no longer significant compared to the cocktail, as a result, the agreement between data and the summed expectation there is rather due to the cocktail.

To quantify the agreement between the data and the model calculation, we use the χ^2 test. In order to obtain sufficient points, we take a slightly
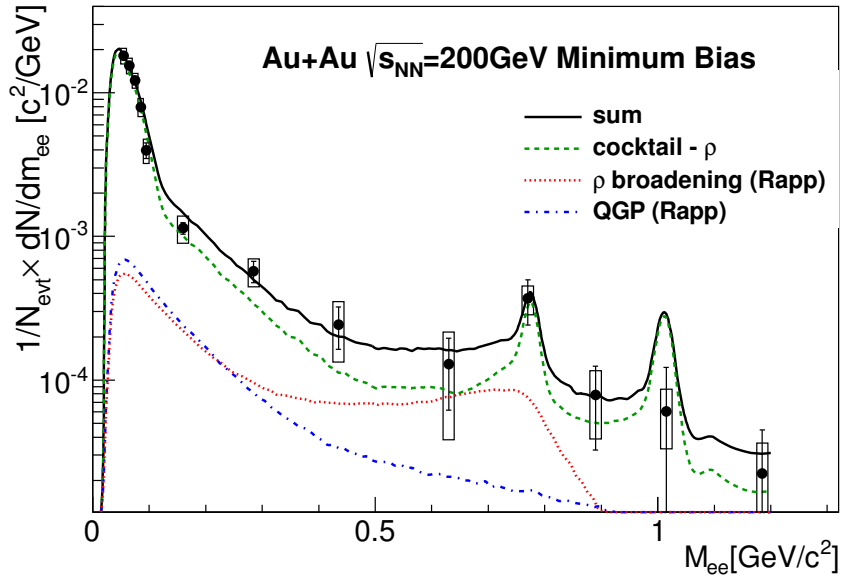
Figure 5.1: Dielectron invariant mass spectrum in minimum bias $Au + Au$ collisions at $\sqrt{s} = 200\ GeV$, compared to the collisional broadening model calculation by R. Rapp. Data is shown in black points, with systematic errors denoted by the black frames. The blue dotted curve is the QGP radiation calculation, and the red dotted line is the ρ contribution resulting from a broadened ρ spectral function. The dashed green is a ρ-less cocktail. The black solid curve is the sum of the ρ-less cocktail, the broadened ρ contribution and the QGP radiation

Mass Window	χ^2	ndf	χ^2/ndf	p-value
$0.15 < m_{ee} < 1.0\ GeV/c^2$	6.7	6	1.11	0.35

Table 5.1: Table of χ^2 for comparison between data and collisional broadening model for min bias $Au+Au$ dielectron mass spectrum in mass window $0.15 < m_{ee} < 1.0\ GeV/c^2$.

wider mass window of $0.15 < m_{ee} < 1.0\ GeV/c^2$. We use the statistical uncertainty as it is mostly comparable to the systematical uncertainty in this mass region, and obtain, $\chi^2/ndf = 6.7/6$, with a corresponding p-value of 0.35, listed in Tab. 5.1.

In Fig. 5.2, we present the comparison of dielectron pair p_T distribution in the low mass window $0.3 < m_{ee} < 0.76\ GeV/c^2$ between data and the Rapp ρ broadening model in minimum bias $Au + Au$ collisions. Just as in Fig. 5.1, the theoretical expectations are drawn in three components, and their sum is shown in the solid black line. The cocktail excluding ρ is shown as the dashed green curve, the broadened ρ p_T distribution is shown in red, and the QGP thermal radiation, which is the smallest contribution, is drawn in blue. The data points are shown in blue, with the shaded light blue bands presenting systematic uncertainty.

We note reasonable agreement between the measurement and the theoretical calculation in the pair p_T distribution. For p_T up to 10.0 GeV/c inside the mass window $0.3 < m_{ee} < 0.76\ GeV/c^2$, using statistical errors which exceeds the systematical uncertainty, the comparison yields a χ^2 value of 17.9 with 13 degrees of freedom. We obtain the corresponding p-value of 0.16. The numbers are listed in Tab. 5.2.

Mass Window	χ^2	ndf	χ^2/ndf	p-value
$0.30 < m_{ee} < 0.76\ GeV/c^2$	17.9	13	1.38	0.16

Table 5.2: Table of χ^2 for comparison between data and collisional broadening model for min bias $Au + Au$ dielectron p_T spectrum in mass window $0.3 < m_{ee} < 0.76\ GeV/c^2$. The p_T range is under 10 GeV/c.

In Fig. 5.3 we present the excess yields in the mass window $0.3 < m_{ee} < 0.76\ GeV/c^2$ as a function of N_{part}, which also represents the centrality. The

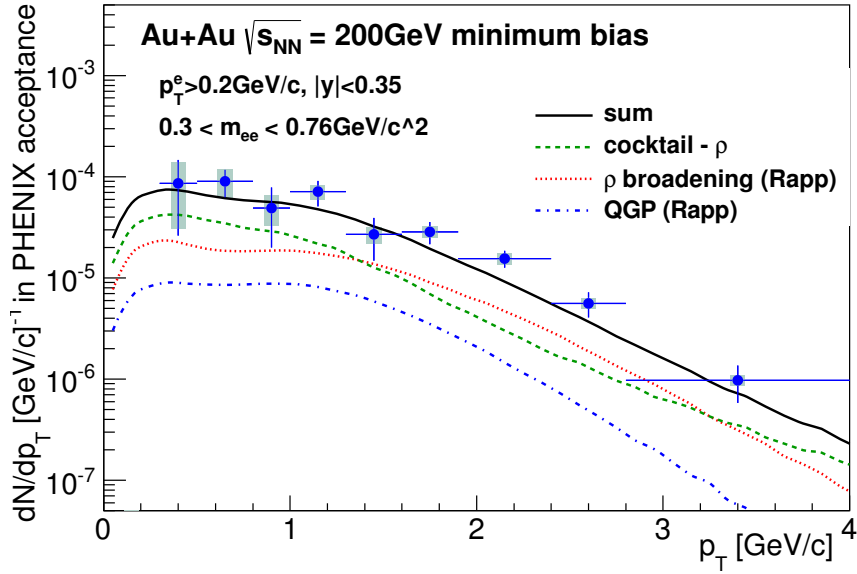Figure 5.2: Minimum bias dielectron p_T distribution in mass window $0.3 < m_{ee} < 0.76 \ GeV/c^2$, compared to theoretical calculations by R. Rapp, which includes QGP thermal radiation in dotted blue, and the broadened ρ contribution in dotted red. The other contributions are contained in a ρ-less cocktail denoted by dashed green. The black curve is the sum of the three theoretical contributions.

excess yields are calculated as the measured spectra yield minus the ρ-less cocktail in the given mass window. The quantity plotted on the vertical axis in Fig. 5.3 is the ratio of the excess yield divided by N_{part}. The data points are plotted in black with the squares denoting the systematic uncertainty. As seen in the last chapter, the excess yields, when divided into centrality classes, suffer large uncertainty, both statistically and systematically. As at the mass windows $0.3 < m_{ee} < 0.76\ GeV/c^2$ the S/B ratio of the measurements reaches its minimum, and small fluctuations or uncertainty in the background subtraction can cause a large impact in the excess yields.

The dotted black curve on Fig. 5.3 is the result from the Rapp model, which is a power law scaling of N_{part} ($Y_M/N_{part} \propto N_{part}^\alpha$). The model predicts $\alpha \simeq 0.45$ with 10% uncertainty, and is closed to the experimentally measured value for integrated thermal photon yields [108].

Within large uncertainty, we conclude that the data is consistent with the model prediction.

5.2.2 Comparison To PHSD Model

Fig. 5.4 compares the minimum bias $Au + Au$ data to the predictions of the PHSD model in the low mass region. The black points denotes the measured spectrum, with black squares representing the systematic uncertainty and the vertical black bars showing the statistical uncertainty. The PHSD calculates the dielectron yields from a variety of light meson decay sources, which include the Dalitz decays from π^0, η, η', ω, Δ and a_1, as well as direct decays from ω, ρ and ϕ. The QGP radiation computed by the PHSD is shown in dashed blue color. The contributions from semi-leptonic decays of $c\bar{c}$ and $b\bar{b}$ are the PYTHIA simulation used in the cocktail (Sec. 3.7), and are illustrated in the dark dashed curve. These various dielectron sources are represented by curves of different colors. The solid black curve is the sum of all sources. Comparing to the vacuum hadronic cocktail in Fig. 4.1, which is generated by EXODUS as described in detail in Sec. **??**, the PHSD calculations incorporates contributions from Δ and a_1 Dalitz decays, and collisional broadening of ρ mesons. Both the Δ and a_1 are shown to populate the low mass region at $m_{ee} < 0.7\ GeV/c^2$ with insignificant contributions. The Δ contributes less than one tenth of the total dielectron yields at the relevant mass region, while the a_1 yields $< 0.1\%$ of the total. The ρ direct decays illustrated in light blue incorporates collisional broadening of the
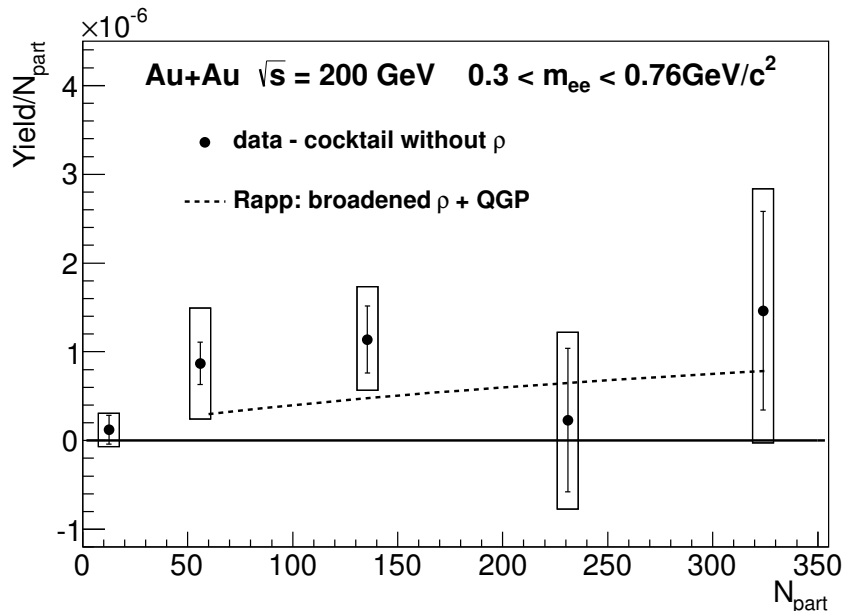
Figure 5.3: The excess yields in the mass window $0.3 < m_{ee} < 0.76\ GeV/c^2$, defined by the data minus the ρ-less cocktail in the given mass region. The figure is plotted as the excess yields divided by N_{part}, as a function of N_{part} (centrality). The dotted black line is theoretical result of emissions from broaden ρ and the QGP by R. Rapp.

Mass Window	χ^2	ndf	χ^2/ndf	p-value
$0.15 < m_{ee} < 1.0\ GeV/c^2$	6.68	6	1.113	0.351

Table 5.3: Table of χ^2 for comparison between data and PHSD model of min bias $Au + Au$ dielectron mass spectrum in mass window $0.15 < m_{ee} < 1.0\ GeV/c^2$.

in-medium ρ spectral function. It shows a much flattened and broader distribution than the vacuum ρ in the hadronic cocktails. In the ρ mass region $0.3 < m_{ee} < 0.76\ GeV/c^2$, the ρ is shown to be the dominating dielectron source. It can be seen in Fig. 5.4 that the data and the PHSD calculations have reasonable agreement. In the excess region in particular, the sum of the predominant ρ and other smaller contributions gives a fair description of the data.

Similar to what is done for the comparison with the collisional broadening model, we calculate χ^2 in mass region $0.15 < m_{ee} < 1.0\ GeV/c^2$ using the statistical uncertainties on the data points. Table. 5.3 lists the resulting $\chi^2/ndf = 6.68/6$, with a corresponding p-value of 0.351 for the PHSD model.

Fig. 5.5 presents the comparison of data and the PHSD model for pair p_T distribution within the ρ mass windows $0.30 < m_{ee} < 0.76\ GeV/c^2$. The blue points are the data, with the shaded light blue bars illustrating the systematic errors. The various dielectron sources calculated by the PHSD as described above, are plotted in different colors. The sum of all components, represented by the black curve, is visibly lower than the data p_T distribution at $0.6 < p_T < 2.5\ GeV/c$. Comparing to the collisional broadening model result by R. Rapp shown in Fig. 5.2, which has obtained a fair agreement with the data, the PHSD calculation exhibits a generally different shape in p_T. The p_T integrated dilepton yields in the given mass window $0.30 < m_{ee} < 0.76\ GeV/c^2$ obtained by the Rapp model is $\sim 92.6\%$ of that of the PHSD calculation. Despite similar total yields given by the two models, the PHSD shows markedly more yields at the lowest p_T where $p_T < 0.4\ GeV/c$. In p_T range $0.6 < p_T < 2.5\ GeV/c$, the PHSD underestimates the data approximately by almost a factor of ~ 2, whereas the Rapp model shows a fair agreement with the data. At higher p_T where $p_T > 2.5\ GeV/c$, both models can describe the data within uncertainties. In particular, the p_T distribution of the ρ meson, which is the biggest contributor to the total yield, is given
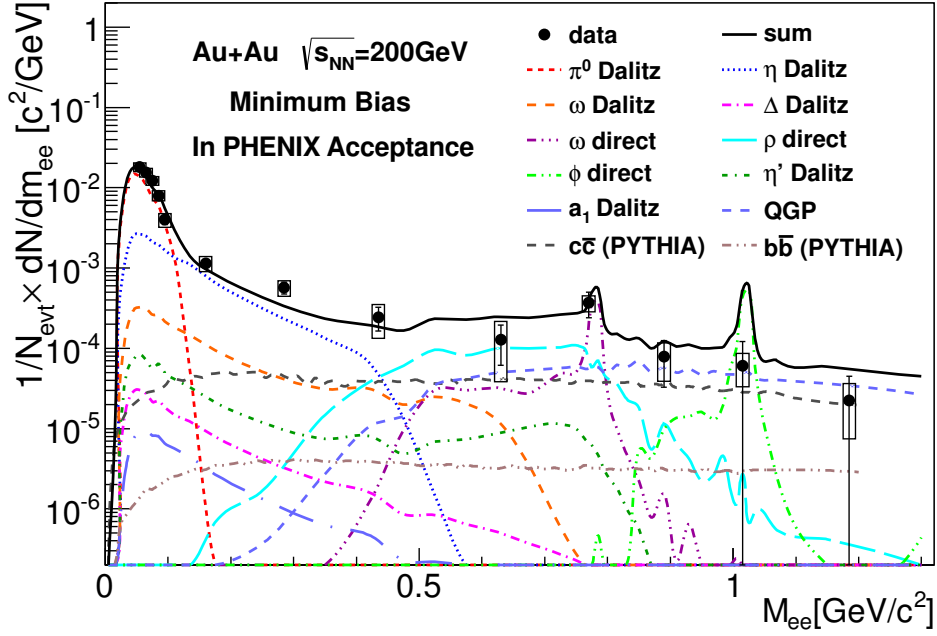
Figure 5.4: Dielectron invariant mass spectrum in minimum bias $Au + Au$ collisions at $\sqrt{s} = 200 \ GeV$, compared to the PHSD model calculation by O. Linnyk et. al. Data is shown in black points, with systematic errors denoted by the black frames. The PHSD predictions are presented in a variety of dielectron decay sources of light mesons and heavy quarks. The meson sources calculated by PHSD include the Dalitz decays of π^0, η, η', ω, Δ and a_1 mesons, as well as direct decays from ω, ρ and ϕ. The heavy quark contribution computed by PHSD is shown in dark dashed curve. The black solid curve denotes the sum of all sources.

different shapes by the two models. Although both models incorporate the broadening of the ρ spectral function into the calculations, it appears that their different treatments of the dilepton production (ρ meson in particular) have led to somewhat different p_T distributions of dielectrons from ρ, despite the fact that both models describe the invariant mass spectrum reasonably well.

Table. 5.4 presents the χ^2 calculated for the comparison between the data and the PHSD pair p_T distribution up to $p_T < 10\ GeV/c$ in the ρ mass window $0.30 < m_{ee} < 0.76\ GeV/c$. Similar to Tab. 5.2, we use statistical errors which are larger than the systematic errors, and obtain $\chi^2/ndf = 45.88/13$, with a corresponding p-value of 1.5×10^{-5}. Although the PHSD calculation reaches reasonable agreement with the data in the minimum bias invariant mass spectrum, a comparison of the pair p_T distribution in the ρ mass region shows that it does not hold good consistency with the data in the p_T direction.

The author of the PHSD model attributes the inconsistency to "missing string rotation" in the calculation. She explains the issue as follows: strings are pulled between the leading quarks and antiquarks in high energy collisions of hadrons. In these initial collisions, the strings are almost co-linear with the z-axis, and inside PHSD they are assumed to be exactly co-linear. On the other hand, at RHIC energy the secondary hadronic collisions of high invariant energy are numerous and important. These proceed in PHSD also through the string formation. However, the approximation that the string is co-linear with the z-axis is no longer valid for these secondary collisions. The author noticed that this approximation rendered the hadron p_T distribution very soft, and this in turn, made the hadron decay dielectron p_T too soft. The solution is to rotate the strings properly to the orientation of the colliding hadrons in PHSD.

Mass Window	χ^2	ndf	χ^2/ndf	p-value
$0.30 < m_{ee} < 0.76\ GeV/c^2$	45.88	13	3.53	1.5×10^{-5}

Table 5.4: Table of χ^2 for comparison between data and PHSD model for min bias $Au + Au$ dielectron p_T spectrum in mass window $0.3 < m_{ee} < 0.76\ GeV/c^2$. The p_T range is under 10 GeV/c.
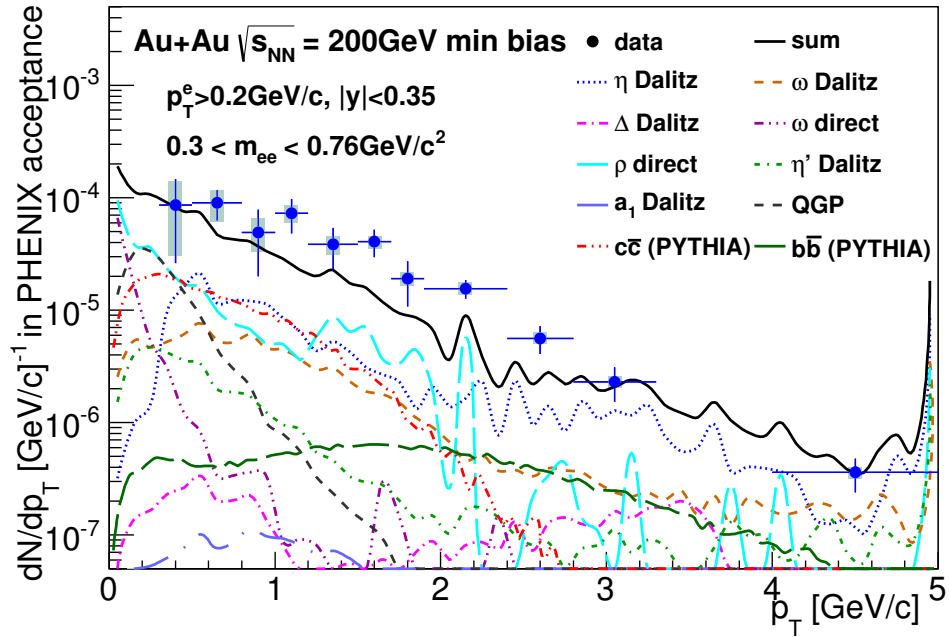
Figure 5.5: Minimum bias dielectron p_T distribution in mass window $0.3 < m_{ee} < 0.76\ GeV/c^2$, compared to theoretical calculations by PHSD, which includes the Dalitz decays of π^0, η, η', ω, Δ and a_1 mesons, direct decays from ω, ρ and ϕ, and open heavy flavor semi-leptonic decays. The black curve is the sum of all theoretical contributions. Data is shown in blue points, with systematic errors denoted by light blue bands.

5.2.3 Summary

Now we have obtained the final dielectron invariant spectra of $Au + Au$ collisions at $\sqrt{s} = 200~GeV$. Comparison with the hadronic cocktail, which represents the expected spectra when all meson decays take place in vacuum, reaches good agreement in all mass regions except the ρ region between $0.2 < m_{ee} < 0.76~GeV/c^2$. The very low mass region where $m_{ee} < 150~MeV/c^2$, is dominated by Dalitz decays from π^0, together with a small contribution from η Dalitz decays. The spectrum is in good agreement with the cocktail within uncertainties. As the Dalitz decays of the long lived π^0 and η are supposed to happen after freeze-out, the agreement between the spectra and the cocktail is expected, and it has confirmed the PHENIX measurements of pion spectra whose results are used as inputs to generate the cocktail.

The wide and prominent resonance structure of J/Ψ is well described by the cocktail, both in magnitude and in width. The suppression of J/Ψ production in $Au + Au$ collisions, incorporated into the hadronic cocktail by the suppression factor $R_{AA}^{J/\Psi}$ measured by PHENIX, is confirmed by the final J/Ψ yield. As the J/Ψ mostly decays after freeze-out due to its long lifetime, its spectral function is unaffected by the hot and dense medium and retains its vacuum properties. The width of the resonance reflects intrinsic PHENIX detector resolution and is well described by the hadronic cocktail.

The Dalitz region at $m_{ee} < 150~MeV/c^2$ and the J/Ψ resonance region can serve the purpose of sanity check for the final dieletron spectra. The high mass region at above the J/Ψ mass $3.5 < m_{ee} < 5~GeV/c^2$ are governed by open heavy flavor contributions, especially from open bottom decays. The Drell-Yan processes are still negligible at this mass range. The final spectra start to suffer from loss of statistics, but still agree with the cocktail. In this region, the predominant semi-leptonic open bottom decays in the cocktail depend on the $b\bar{b}$ cross section, which is calculated from measured $b\bar{b}$ cross section in $d + Au$ collsions, and scaled by the average number of binary collisions $N_{coll}^{AuAu}/N_{coll}^{dAu}$ to acquire the equivalent $Au+Au$ cross section. Within large uncertainties, the data points are consistent with the cross section estimation.

The intermediate mass region is dominated by open charm semi-leptonic decay pairs. We observe agreement with the cocktail. The QGP thermal radiation, which is theoretically predicted to make a small contribution in this region, remains out of reach due to experimental uncertainties, of which the statistical uncertainty dominates. When integrating the yields between $1.2 <$

$m_{ee} < 2.8\ GeV/c^2$, a slight enhancement seems to appear. However, within uncertainties, the yields are still consistent with the cocktail prediction.

For the low mass region, resonance peaks of ω and ϕ are observed. The two resonances exhibit no noticeable mass shift, and their exact widths are unfortunately out of reach, due to limited statistics. Having relatively long lifetimes, the two vector mesons decay into dileptons mostly outside of the medium, making their resonance structure less sensitive to the medium effects than the short-lived ρ meson.

The enhancement at and below ρ mass is noticeable in minimum bias and in the more central collisions. The magnitude of the excess is in consistency with the recent STAR result. It is also markedly smaller than the previous PHENIX measurement. This reduced enhancement we attribute to a substantially upgraded analysis strategy and the HBD. The new result is an improvement upon the previous one.

Cross checking with an independent parallel analysis on the same data set, with a different analysis approach, the results from the two analyses exhibit very good agreement over the full mass range in all centrality classes. It strengthens the credibility of our result.

The result is compared to two theoretical calculations, the effective many-body collisional broadening approach and the PHSD approach. The minimum bias invariant mass spectrum at the low mass region is in fair agreement with both model calculations, yielding comparable χ^2/ndf values. The minimum bias pair p_T distribution in the ρ mass region $0.30 < m_{ee} < 0.76\ GeV/c$, however, is consistent with the collisional broadening model, whereas it is not so well described by the PHSD approach. We also find that, the centrality dependence of the excess, plotted as the excess yield as a function of N_{part}, is consistent with the collisional broadening model within uncertainties. On the other hand, we do not have such centrality dependent calculations from the PHSD model, and no similar comparison is made.

In the low mass region, we have come to a fair agreement between the data and the effective many-body collisional model by R. Rapp, in the minimum bias mass spectrum, the p_T distribution in the ρ mass region, and the centrality dependence of the excess. At the same time, we find that the PHSD model implementing ρ broadening also gives fair description of the mass spectrum, although the p_T distribution is not so well reproduced. One would ponder the question what our findings signify? Have we observed chiral symmetry restoration? The rejection of the dropping ρ mass scenario

and the general success of the collisional broadening scenario in various collision systems points to the fact that the connection between ρ and the chiral symmetry restoration is not as explicit as the ρ mass dropping. The present dielectron measurement contributes to a collection of dilepton invariant mass spectra data on a variety of collision systems, which seems to confirm collectively that a strongly broadened ρ spectral function is involved during the QGP-hadron phase transition. Then how is the broadening of light vector meson spectral functions linked with the chiral symmetry as well as the chiral condensate of quarks and gluons? There are arguments [100] suggesting that the many-body effects may encode the mechanics of the chiral symmetry restoration, though to what extent is quite unknown at present, and a "careful and exhaustive treatment of hadronic many-body effects is an inevitable ingredient for evaluating mechanisms of χSR" [100].

On the other hand, we notice that the QGP radiation shape is markedly different in the two models, as seen in the Fig. 5.1 and Fig. 5.4. In the effective many-body collisional model, the QGP produces more low mass pairs under $m_{ee} < 500 MeV/c^2$. Yet at $m_{ee} > 1\ GeV/c^2$, the PHSD QGP radiation becomes larger than the many-body model, moreover, the PHSD QGP component is above the charm yields computed by PYTHIA in this mass region. The difference has to be originated from the two different treatments of the partonic emission. In the many-body collisional model, perturbative QCD is used to compute the leading order $q\bar{b} \to l^+l^-$, which gives a lower limit of true QGP emission. Whereas the PHSD calculates strongly interacting QGP and includes three additional processes $q + g \to \gamma^* + q$, $\bar{q} + g \to \gamma^* + \bar{q}$ and $q + \bar{q} \to g + \gamma^*$. This procedure yields a QGP contribution comparable to D-meson decays in the intermediate mass region, as noted by the authors in Ref. [86]. On the experimental side, however, a hint of enhancement with a factor of $1.34 \pm 0.43^{stat} \pm 0.35^{syst} \pm 0.25^{cocktail}$ over the cocktail, which is dominantly D-meson decay, is observed in the intermediate mass region in minimum bias events. Yet given the limited statistical and systematical precision in the experiment, a meaningful measurement of the thermal radiation from the QGP remains elusive. An accurate subtraction of the charm component in the IMR is necessary to measure the QGP thermal radiation, which would help discriminate the two theoretical models. We look forward to future measurements with significantly improved precision in the IMR to bring discoveries on the eagerly anticipated QGP radiation.

Chapter 6

Conclusion

Measurements of dielectron invariant mass spectra in $Au + Au$ collisions at $\sqrt{s} = 200$ GeV were carried out in this thesis work. Compared to the previous PHENIX measurement, it benefited from a much larger data set, a detector upgrade of the Hadron Blind Detector, and a substantially improved analysis method. Studying the spectra can shed light on the medium modification of the light vector mesons, the ρ meson in particular, whose in-medium properties are closely related to the chiral symmetry restoration. Furthermore, the analysis is aimed to resolve the "PHENIX puzzle", referring to the large dielectron excess around the ρ mass, observed by the previous PHENIX measurement with a magnitude too large to be reproduced by any theoretical calculation. The magnitude also exceeds the result from STAR experiment, whose measurement of dielectron mass spectra in $Au + Au$ collisions at $\sqrt{s} = 200$ GeV yields a smaller enhancement at the ρ mass.

Electrons were measured with the PHENIX Central Arm Spectrometer. It consists of two central arms, each covering 90° in the azimuth and $|\eta| < 0.35$ in pseudorapidity. Each arm is equipped with a layer of Drift Chamber(DC) and 2 layers of Pad Chamber(PC1, PC3) for charged particle tracking, a Ring Imaging Cherenkov Counter(RICH) and an Electromagnetic Calorimeter (EMCal) for electron identification. In addition to the standard electron identification, the new dielectron measurement benefited from the installation of the Hadron Blind Detector. The HBD, a windowless Cherenkov detector, was installed in year 2009 and 2010, with the 2009 $p+p$ data serving as a proof of principle prior to taking 2010 $Au + Au$ data. Using the opening angle between an electron pair, the detector identified background electrons produced from photon conversions and π^0 Dalitz decays, thereby reducing the huge combinatorial background which plagues dielectron measurement

in central, high multiplicity events.

An HBD clusterizing algorithm was developed to extract HBD signals, which were utilized to distinguish a) the Cherenkov signals from single electrons and the scintillation light caused by charged hadrons; b) the double Cherenkov signals from pairs of close electrons with small opening angles (photon conversion pairs and closed Dalitz pairs predominantly from π^0), and the signals from single electrons. After applying a series of standard 1-dimensional electron identification cuts, the electron sample was further cleaned by applying a cut on the time-of-flight from the EMCal (or ToFE when available), as well as cuts on the HBD cluster charge. A purity of 87% in the most central collisions (0-10% centrality) was achieved, which was a substantial improvement compared to the 30% hadron contamination in central $Au + Au$ collisions reported by the previous PHENIX measurement [10].

The principal difficulty of measuring $Au + Au$ dielectron spectra arose from the overwhelming combinatorial background, resulting in small signal to background ratio. In the present analysis, we estimated a S/B ratio of $\sim 1/500$ at $m_{ee} \sim 600 MeV/c^2$ for minimum bias collisions. Consequently an accurate description of the background sources was crucial to the analysis. The method of background subtraction has undertaken significant improvements upon the previous measurement. We adopted a blind analysis strategy: only after fixing the normalization of all background sources so that a satisfactory description of the like sign pairs was achieved, the analysis was extended to unlike sign pairs.

Compared to the previous analysis, the new subtraction method took into consideration the effect of collective flow in the underlying events on the combinatorial background, the contributions from away side jet pairs, electron-hadron pairs and bottom pairs, and used a normalization method of fitting all components simultaneously. The comprehensive study of the background sources, together with normalizing each background component by fitting the like-sign pair distribution, led to a sufficiently accurate background description.

The systematic uncertainty was dominated by the uncertainty in the background subtraction due to the overwhelming background level. Systematic uncertainty sources in the background normalization included the statistical uncertainty in the normalization factors, uncertainty of the flow and κ factor, and uncertainty from two different normalization methods, i.e. the absolute normalization and the component fitting method. Other systematic error sources included the uncertainties in the decomposed efficiencies, ϵ_{pair}^{cut}, ϵ_{pair}^{embed}

and ϵ_{pair}^{TOF}.

The final dielectron invariant mass spectra are compared to the hadronic cocktail, which is the expected dielectron spectrum in vacuum, free of any medium effect. In the central events, the measured spectra obtain good agreement with the hadronic cocktail in all mass range except for the ρ mass region at $0.3 < m_{ee} < 0.76\, GeV/c^2$, where an enhancement of dielectron yield is manifest. The ρ enhancement tends to decrease when the collisions become peripheral. In the most peripheral collisions which are very similar to $p + p$ collisions, the measured spectrum is consistent with the hadronic cocktail in the full mass range. The enhancement factor for minimum bias collisions at the ρ region is measured to be $1.79 \pm 0.40^{stat} \pm 0.81^{syst} \pm 0.20^{cocktail}$, which is in agreement with the STAR experiment, who reported an enhancement factor of $1.77 \pm 0.11^{stat} \pm 0.24^{syst} \pm 0.33^{cocktail}$. The excess is smaller than the previous PHENIX measurement by 1.6σ, which yields a factor of $4.7 \pm 0.4^{stat} \pm 1.5^{syst} \pm 0.9^{cocktail}$. At the intermediate mass region where contribution of the QGP thermal radiation is predicted, no significant enhancement is observed within statistical uncertainties.

We therefore do not confirm the large excess at the ρ region as is reported by the previous PHENIX measurement. The new analysis has significantly upgraded the analysis method. The differences include substantially reduced hadron contamination, higher S/B ratio, tighter pair cuts and a more comprehensive and elaborate treatment of the background sources, taking into account the flow modulation of the combinatorial background, the electron-hadron pairs and the away side jet pairs. Among the differences, the hadron contamination, the pair cuts and the flow have the biggest effect.

A parallel analysis on the same data has been carried out by a second group independently. It used neural networks to identify electrons, and had a number of smaller differences in the analysis chain. The work has been published in Ref. [18]. The results of the two analyses are cross checked and they exhibit very good agreement with each other in all centrality classes, confirming the validity of the present analysis.

Two theoretical models based on the "collisional broadening" scenario are selected to compare with the data. In the collisional broadening scenario, the ρ in-medium spectral function is broadened by many-body collisions governed by vector-meson dominance. The first model is an effective many-body collisional approach which calculates dilepton production rate based on the retarded electromagnetic current-current correlator in a general form of the dilepton thermal rate in a hot and dense medium. The comparisons of the

minimum bias mass spectrum at the low mass region, the dielectron minimum bias p_T distribution in the ρ region $0.3 < m_{ee} < 0.76\ GeV/c^2$, and the centrality dependency of the ρ excess yields show good agreement between the data and the model.

The second model is the Parton-Hadron-String-Dynamics (PHSD) approach, which is a microscopic off-shell transport model describing the full evolution of a heavy ion collision from the initial hard scattering and string formation, an explicit partonic phase, the hadronization, to the subsequent hadronic interactions. It calculates the dielectron spectra with a comprehensive list of dielectron production sources. The "collisional broadening" scenario is implemented in the light vector meson spectral functions. When comparing to the data, the minimum bias invariant mass spectrum also obtains fair agreement in the low mass region. Similar to the first model, the PHSD shows equally good description of the ρ enhancement. When comparing to the pair p_T distribution in the same ρ region $0.3 < m_{ee} < 0.76\ GeV/c^2$, however, the PHSD exhibits a different overall shape than the data. The source of the inconsistency is explained by the author as follows: the strings formed during secondary hadron collisions need to be rotated properly inside the model. When neglected for approximation, hadron p_T distribution becomes too soft and thus affects the dielectrons p_T distribution.

Finally, we have addressed the interesting physics described in the first chapter. The analysis on the dielectron invariant mass spectra of $Au + Au$ collisions at $\sqrt{s} = 200\ GeV$ using the PHENIX 2010 data with the HBD upgrade has led to a substantially improved measurement upon the previous PHENIX result, thus has helped resolve the "PHENIX puzzle". The new result is consistent with the parallel analysis as well as the STAR measurement, and is well described by two different main-stream theoretical models, both based on the widely accepted "collisional broadening" scenario. The thermal radiation from the partonic phase remains elusive within the current statistical uncertainties. Future measurements with significantly improved precision will hopefully shed light on the QGP thermal radiation.

Bibliography

[1] L Adamczyk, G Agakishiev, MM Aggarwal, Z Ahammed, AV Alakhverdyants, I Alekseev, J Alford, BD Anderson, CD Anson, D Arkhipkin, et al. Di-electron spectrum at mid-rapidity in p+p collisions at $\sqrt{s} = 200$gev. *Physical Review C*, 86(2):024906, 2012.

[2] L. Adamczyk et al. Dielectron Mass Spectra from Au+Au Collisions at $\sqrt{s_{\mathrm{NN}}} = 200$ GeV. *Phys. Rev. Lett.*, 113(2):022301, 2014. [Addendum: Phys. Rev. Lett.113,no.4,049903(2014)].

[3] L. Adamczyk et al. Energy dependence of acceptance-corrected dielectron excess mass spectrum at mid-rapidity in Au+Au collisions at $\sqrt{s_{NN}} = 19.6$ and 200 GeV. *Phys. Lett.*, B750:64–71, 2015.

[4] L. Adamczyk et al. Measurements of Dielectron Production in Au+Au Collisions at $\sqrt{s_{\mathrm{NN}}} = 200$ GeV from the STAR Experiment. *Phys. Rev.*, C92(2):024912, 2015.

[5] D. Adamova and others (CERES Collaboration). *Phys.Rev.Lett*, 91, 2003.

[6] A. Adare et al. "inclusive cross section and double helicity asymmetry for π^0 production in $p+p$ collisions at $\sqrt{s}$ =200 gev: Implications for the polarized gluon distribution in the proton". *Phys. Rev. D*, 76(5):051106, 2007.

[7] A. Adare et al. j/ψ production versus centrality, transverse momentum, and rapidity in Au + Au collisions at $\sqrt{s_{NN}} = 200$ GeV. *Phys. Rev. Lett.*, 98:232301, Jun 2007.

[8] A. Adare et al. "dihadron azimuthal correlations in $au + au$ collisions at $\sqrt{s_{NN}}$=200 gev". *Phys. Rev. C*, 78(1):014901, 2008.

[9] A. Adare et al. "suppression pattern of neutral pions at high transverse momentum in $au+au$ collisions at $\sqrt{s_{NN}} = 200$ gev and constraints on medium transport coefficients". *Phys. Rev. Lett*, 101(23):232301, 2008.

[10] A. Adare et al. Detailed measurement of the $e+e-$ pair continuum in $p+p$ and $au+au$ collisions at $\sqrt{s_{NN}} =200$ gev and implications for direct photon production. *Phys. Rev. C*, 81(3):034911, 2010.

[11] A. Adare et al. Enhanced production of direct photons in au+au collisions at $\sqrt{s_{NN}} =200$ gev and implications for the initial temperature. *Phys. Rev. Lett.*, 104, 2010.

[12] A. Adare et al. "heavy quark production in $p+p$ and energy loss and flow of heavy quarks in $au+au$ collisions at $\sqrt{s_{NN}} = 200$ gev". *Phys. Rev. C*, 84(4):044905, 2010.

[13] A. Adare et al. "transition in yield and azimuthal shape modification in dihadron correlations in relativistic heavy ion collisions". *Phys. Rev. Lett*, 104(25):252301, 2010.

[14] A. Adare et al. Transverse momentum dependence of η meson suppression in au+au collisions at $\sqrt{s_{NN}} = 200$ gev. *Phys. Rev. C*, 82:011902, Jul 2010.

[15] A. Adare et al. Ground and excited state charmonium production in $p+p$ collisions at $\sqrt{s} = 200$ GeV. *Phys. Rev. D*, 85:092004, May 2012.

[16] A. Adare et al. Centrality dependence of low-momentum direct-photon production in au+au collisions at $\sqrt{s_{NN}} =200$ gev. *Phys. Rev. C*, 91, 2015.

[17] A. Adare et al. Centrality dependence of low-momentum direct-photon production in Au + Au collisions at $\sqrt{s_{NN}} = 200$GeV. *Phys. Rev. C*, 91:064904, Jun 2015.

[18] A. Adare et al. Dielectron production in Au+Au collisions at $\sqrt{s_{NN}}$=200 GeV. 2015.

[19] A. Adare et al. "the cross-section for $b\bar{b}$ production via dielectrons $ind+au$ collisions at $\sqrt{s_{NN}} = 200$ gev". *Phys. Rev. C*, 91(1):014907, 2015.

[20] A. Adare and others (PHENIX Collaboration). *Phys.Lett.B*, 670, 2009.

[21] K. Adcox et al. Construction and performance of the PHENIX pad chambers. *Nucl. Instrum. Meth.*, A497:263–293, 2003.

[22] K. Adcox et al. PHENIX central arm tracking detectors. *Nucl. Instrum. Meth.*, A499:489–507, 2003.

[23] K. Adcox et al. PHENIX detector overview. *Nucl. Instrum. Meth.*, A499:469–479, 2003.

[24] C. Adler, A. Denisov, E. Garcia, M. Murray, H. Strobele, and S. White. The RHIC zero-degree calorimeters. *Nucl. Instrum. Meth.*, A499:433–436, 2003.

[25] Clemens Adler, Alexei Denisov, Edmundo Garcia, Michael J. Murray, Herbert Strobele, and Sebastian N. White. The RHIC zero degree calorimeter. *Nucl. Instrum. Meth.*, A470:488–499, 2001.

[26] S. Adler et al. "identified charged particle spectra and yields in $au + au$ collisions at $\sqrt{s_{NN}} = 200$ gev". *Phys. Rev. C*, 69(3):034909, 2004.

[27] S. Adler et al. "a detailed study of high-pt neutral pion suppression and azimuthal anisotropy in $au + au$ collisions at $\sqrt{s_{NN}} = 200$ gev". *Phys. Rev. C*, 76(3):034904, 2007.

[28] S. S. Adler et al. Transverse-energy distributions at midrapidity in $p + p$, $d + $ Au, and Au $+$ Au collisions at $\sqrt{s_{\mathrm{NN}}} = 62.4\breve{\ }200$ gev and implications for particle-production models. *Phys. Rev. C*, 89:044905, Apr 2014.

[29] G. Agakishiev and others (HADES Collaboration). *Phys.Rev.Lett.*, 98, 2007.

[30] G. Agakishiev and others (HADES Collaboration). *Phys.Lett.B*, 663, 2008.

[31] G. Agakishiev and others (HADES Collaboration). *Phys.Rev.C*, 84, 2011.

[32] G. Agakishiev and others (HADES Collaboration). *Eur.Phys.J.A*, 48, 2012.

204

[33] M. Aizawa et al. PHENIX central arm particle ID detectors. *Nucl. Instrum. Meth.*, A499:508–520, 2003.

[34] M. Allen et al. PHENIX inner detectors. *Nucl. Instrum. Meth.*, A499:549–559, 2003.

[35] W. Anderson et al. Design, Construction, Operation and Performance of a Hadron Blind Detector for the PHENIX Experiment. *Nucl. Instrum. Meth.*, A646:35–58, 2011.

[36] L. Aphecetche et al. PHENIX calorimeter. *Nucl. Instrum. Meth.*, A499:521–536, 2003.

[37] R. Arnaldi and others (NA60 Collaboration). *Phys.Rev.Lett.*, 100, 2008.

[38] R. Arnaldi and others (NA60 Collaboration). *Eur.Phys.J.C*, 59, 2009.

[39] R. Arnaldi and others (NA60 Collaboration). *Eur.Phys.J.C*, 61, 2009.

[40] S. H. Aronson et al. PHENIX magnet system. *Nucl. Instrum. Meth.*, A499:480–488, 2003.

[41] E. Atomssa. Presentation on plhf meeting.

[42] J. Badier et al. *Z. Phys. C*, 20, 1983.

[43] R Bersohn. Quantum statistical mechanics. lp kadanoff and g. baym. benjamin, new york, 1962. 203 pp. illus. paper, 4.95; *cloth*,6.95, 1963.

[44] J. D. Bjorken. *Phys. Rev. D*, 27, 1983.

[45] Eric Braaten, Robert D. Pisarski, and Tzu Chiang Yuan. Production of soft dileptons in the quark-gluon plasma. *Phys. Rev. Lett.*, 64:2242–2245, May 1990.

[46] BastianB. Brandt, Anthony Francis, HarveyB. Meyer, and Hartmut Wittig. Thermal correlators in the ρ channel of two-flavor qcd. *Journal of High Energy Physics*, 2013(3), 2013.

[47] E.L. Bratkovskaya, W. Cassing, V.P. Konchakovski, and O. Linnyk. Parton–hadron-string dynamics at relativistic collider energies. *Nuclear Physics A*, 856(1):162 – 182, 2011.

[48] G.E. Brown and M. Rho. *Phys. Rev. Lett.*, 66, 1991.

[49] G.E. Brown and M. Rho. *Phys. Rept.*, 269, 1996.

[50] Sarah Campbell. "ph.d. dissertation".

[51] W Cassing. Dynamical quasiparticles properties and effective interactions in the sqgp. *Nuclear Physics A*, 795(1):70–97, 2007.

[52] W Cassing. Qcd thermodynamics and confinement from a dynamical quasiparticle point of view. *Nuclear Physics A*, 791(3):365–381, 2007.

[53] W. Cassing and E.L. Bratkovskaya. *Phys.Rep.*, 308, 1999.

[54] W. Cassing and E.L. Bratkovskaya. Hadronic and electromagnetic probes of hot and dense nuclear matter1. *Physics Reports*, 308(2–3):65 – 233, 1999.

[55] W. Cassing and E.L. Bratkovskaya. *Nucl.Phys.A*, 831, 2009.

[56] W. Cassing and E.L. Bratkovskaya. Parton–hadron–string dynamics: An off-shell transport approach for relativistic energies. *Nuclear Physics A*, 831(3–4):215 – 242, 2009.

[57] W Cassing and S Juchem. Semiclassical transport of particles with dynamical spectral functions. *Nuclear Physics A*, 665(3):377–400, 2000.

[58] Simon Turbide Charles Gale. *Nucl.Phys.A*, 793, 2007.

[59] M. Cheng et al. The QCD equation of state with almost physical quark masses. *Phys. Rev.*, D77:014511, 2008.

[60] CERES Collaboration. Modification of the ρ meson detected by low-mass electron–positron pairs in central pbau collisions at. *Physics Letters B*, 666(5):425 – 429, 2008.

[61] CERES Collaboration et al. e^+e^--pair production in pb-au collisions at 158 gev per nucleon. *The European Physical Journal C-Particles and Fields*, 41(4):475–513, 2005.

[62] The NA38/NA50 Collaborations. *Nucl.Phys.A*, 698, 2002.

[63] G. Corcella and B. Webber. *JHEP*, 0101, 2010.

[64] S. Damjanovic. Na60 results on the ρ spectral function in in-in collisions. *Nuclear Physics A*, 783(1–4):327 – 334, 2007. Proceedings of the 2nd International Conference on Hard and Electromagnetic Probes of High-Energy Nuclear Collisions Hard Probes 2006.

[65] H.-T. Ding, A. Francis, O. Kaczmarek, F. Karsch, E. Laermann, and W. Soeldner. Thermal dilepton rate and electrical conductivity: An analysis of vector current correlation functions in quenched lattice qcd. *Phys. Rev. D*, 83:034504, Feb 2011.

[66] W. Ehehalt and W. Cassing. Relativistic transport approach for nucleus-nucleus collisions from {SIS} to {SPS} energies. *Nuclear Physics A*, 602(3–4):449 – 486, 1996.

[67] Bazavov et al. Equation of state and qcd transition at finite temperature. *Phys. Rev. D*, 80:014504, Jul 2009.

[68] K.A. Olive et al. (Particle Data Group). *Chinese Physics C*, 38, 2014.

[69] PHENIX Collaboration (K. Adcox et al.). *Nucl.Phys.A*, 757, 2005.

[70] A. Martin for CERES Collaboration. http://arxiv.org/abs/0802.2679. *Proceedings of 4th International Workshop on Critical Point and Onset Deconfinement, Darmstadt, Germany, 9-13 Jul 2007*, 2007.

[71] S. Frixione and B. Webber. *JHEP*, 0206, 2002.

[72] G.Agakichiev and others (CERES Collaboration). *Phys.Rev.Lett.*, 75, 1995.

[73] G.Agakichiev and others (CERES Collaboration). *Eur.Phys.Jour.C*, 4, 1998.

[74] Björn Schenke Ralf Rapp Sangyong Jeon Gojko Vujanovic, Clint Young and Charles Gale. Dilepton emission in high-energy heavy-ion collisions with viscous hydrodynamics. *Phys.Rev.C*, 89, 2014.

[75] U. Heller. *PoS LAT2006:011*, 2006.

[76] R. Rapp Hendrik van Hees. *Nucl.Phys.A*, 806, 2008.

[77] Paul M. Hohler and R. Rapp. *Phys. Lett. B*, 731, 2014.

[78] S Juchem, W Cassing, and C Greiner. Nonequilibrium quantum-field dynamics and off-shell transport for $\phi 4$-theory in $2+1$ dimensions. *Nuclear Physics A*, 743(1):92–126, 2004.

[79] Sascha Juchem, Wolfgang Cassing, and Carsten Greiner. Quantum dynamics and thermalization for out-of-equilibrium $\varphi\ 4$ theory. *Physical Review D*, 69(2):025006, 2004.

[80] Y. Miake K. Yagi, T. Hatsuda. *Quark-Gluon Plasma: From Big Bang to Little Bang*. Cambridge University Press, 2006.

[81] Jason Kamin. Analysis note for $d + au$ dielectron spectra. *PHENIX Analysis Note 858*.

[82] Jason Kamin. "ph.d. dissertation".

[83] Frithjof Karsch. *Lattice QCD at high temperature and density*. Springer, 2002.

[84] E.L. Bratkovskaya. W. Cassing V.P. Konchakovski and O. Linnyk. *Nucl.Phys.A*, 856, 2011.

[85] O Linnyk, EL Bratkovskaya, V Ozvenchuk, W Cassing, and CM Ko. Dilepton production in nucleus-nucleus collisions at top cern super proton synchrotron energy of 158 a gev within the parton-hadron-string dynamics transport approach. *Physical Review C*, 84(5):054917, 2011.

[86] O. Linnyk, W. Cassing, J. Manninen, E. L. Bratkovskaya, and C. M. Ko. Analysis of dilepton production in Au + Au collisions at $\sqrt{\mathbf{s_{NN}}} = \mathbf{200}$ gev within the parton-hadron-string dynamics transport approach. *Phys. Rev. C*, 85:024910, Feb 2012.

[87] C. Spieles S.A. Bass C. Ernst S. Soff L. Bravina M. Belkacem H. Weber H. Stöcker W. Greiner M. Bleicher, E. Zabrodin. *J.Phys.G*, 25, 1999.

[88] C. Sasaki M. Harada. *Phys. Rev. D*, 73, 2006.

[89] M. Makek et al. Phenix analysis note 1204: Dielectron production in $au + au$ collisions at $\sqrt{s_{NN}}$=200 gev with the hadron blind detector.

[90] M. Masera. *Nucl.Phys.A*, 590, 1995.

[91] T. Matsui and H. Satz. *Phys.Lett.B*, 178, 1986.

[92] R. Peschanski Michal P. Heller, Romuald A. Janik. *Acta Phys.Polon.B*, 39, 2008.

[93] Michael L. Miller, Klaus Reygers, Stephen J. Sanders, and Peter Steinberg. Glauber modeling in high-energy nuclear collisions. *Annual Review of Nuclear and Particle Science*, 57(1):205–243, 2007.

[94] T. Munehisa and Y. Munehisa. *Nucl.Phys.A*, 435, 1985.

[95] The NA38 and NA50 Collaborations. *Eur.Phys.J.C*, 14, 2000.

[96] H. J. Specht NA60 Collaboration. http://arxiv.org/abs/1011.0615. *AIP Conf.Proc.*, 1322, 2010.

[97] R.J. Porter and others (DLS Collaboration). *Phys.Rev.Lett*, 79, 1997.

[98] G. Chanfray R. Rapp and J. Wambach. *Nucl.Phys.A*, 617, 1997.

[99] H. van Hees R. Rapp, J. Wambach. *Relativistic Heavy-Ion Physics.* edited by R.Stock and Landolt Bornstein (Springer), 2010.

[100] J. Wambach R. Rapp and H. van Hees. The chiral restoration transition of qcd and low mass dileptons. *arXiv:0901.3289*, 2009.

[101] Michael Strickland Radoslaw Ryblewski. *Arxiv preprint hep-ph*, http://arxiv.org/abs/1505.04018, 2015.

[102] R. Rapp. *Phys.Rev.C*, 63, 2001.

[103] R. Rapp. *AIP Conf.Proc.*, 1322, 2010.

[104] R. Rapp. *PoS CPOD2013*, 2013.

[105] R. Rapp and J. Wambach. *Eur. Phys. J. A*, 6, 1999.

[106] R. Rapp and J. Wambach. *Adv.Nucl.Phys*, 25, 2000.

[107] R. Rapp and J. Wambach. *Advances in Nuclear Physics*, chapter Chiral Symmetry Restoration and Dileptons in Relativistic Heavy-Ion Collisions, pages 1–205. Springer US, Boston, MA, 2002.

[108] Ralf Rapp. Dilepton spectroscopy of qcd matter at collider energies. *Advances in High Energy Physics*, 2013, 2013.

[109] Ralf Rapp and Hendrik van Hees. Thermal dileptons as fireball thermometer and chronometer. *Arxiv preprint hep-ph*, http://arxiv.org/abs/1411.4612, 2014.

[110] E. Richardson et al. A Reaction Plane Detector for PHENIX at RHIC. *Nucl. Instrum. Meth.*, A636:99–107, 2011.

[111] P. Nason S. Frixione and B. Webber. *JHEP*, 0308, 2002.

[112] JJ Sakurai. Vector-meson dominance and high-energy electron-proton inelastic scattering. *Physical Review Letters*, 22(18):981, 1969.

[113] Jun John Sakurai. *Currents and mesons.* University of Chicago press, 1969.

[114] Dieter Schildknecht. Vector meson dominance. *arXiv preprint hep-ph/0511090*, 2005.

[115] MA Stephanov. Qcd phase diagram: an overview. *arXiv preprint hep-lat/0701002*, 2006.

[116] C. Friberg L. Lnnblad G. Miu S. Mrenna T. Sjostrand, P. Edn and E. Norrbin. *Comput. Phys. Commun.*, 135, 2001.

[117] R. Vogt. *Phys.Rept.*, 310, 1999.

[118] Cheuk-Yin Wong. *Introduction to High-Energy Heavy-Ion Collisions.* World Scientific, 1994.